UNIVERSIDAD COMPLUTENSE DE MADRID

FACULTAD DE CIENCIAS GEOLÓGICAS

DEPARTAMENTO DE GEODINÁMICA

TESIS DOCTORAL

ASPECTOS TÉRMICOS Y MECÁNICOS DE LA GEODINÁMICA DE LA LITOSFERA

MEMORIA PARA OPTAR AL GRADO DE DOCTOR

PRESENTADA POR

ALBERTO JIMÉNEZ DÍAZ

Directores

Javier Ruiz Pérez
Rosa Tejero López
Ramón Capote del Villar

Madrid, 2015

ASPECTOS TÉRMICOS Y MECÁNICOS DE LA GEODINÁMICA DE LA LITOSFERA

TESIS DOCTORAL

Alberto Jiménez Díaz

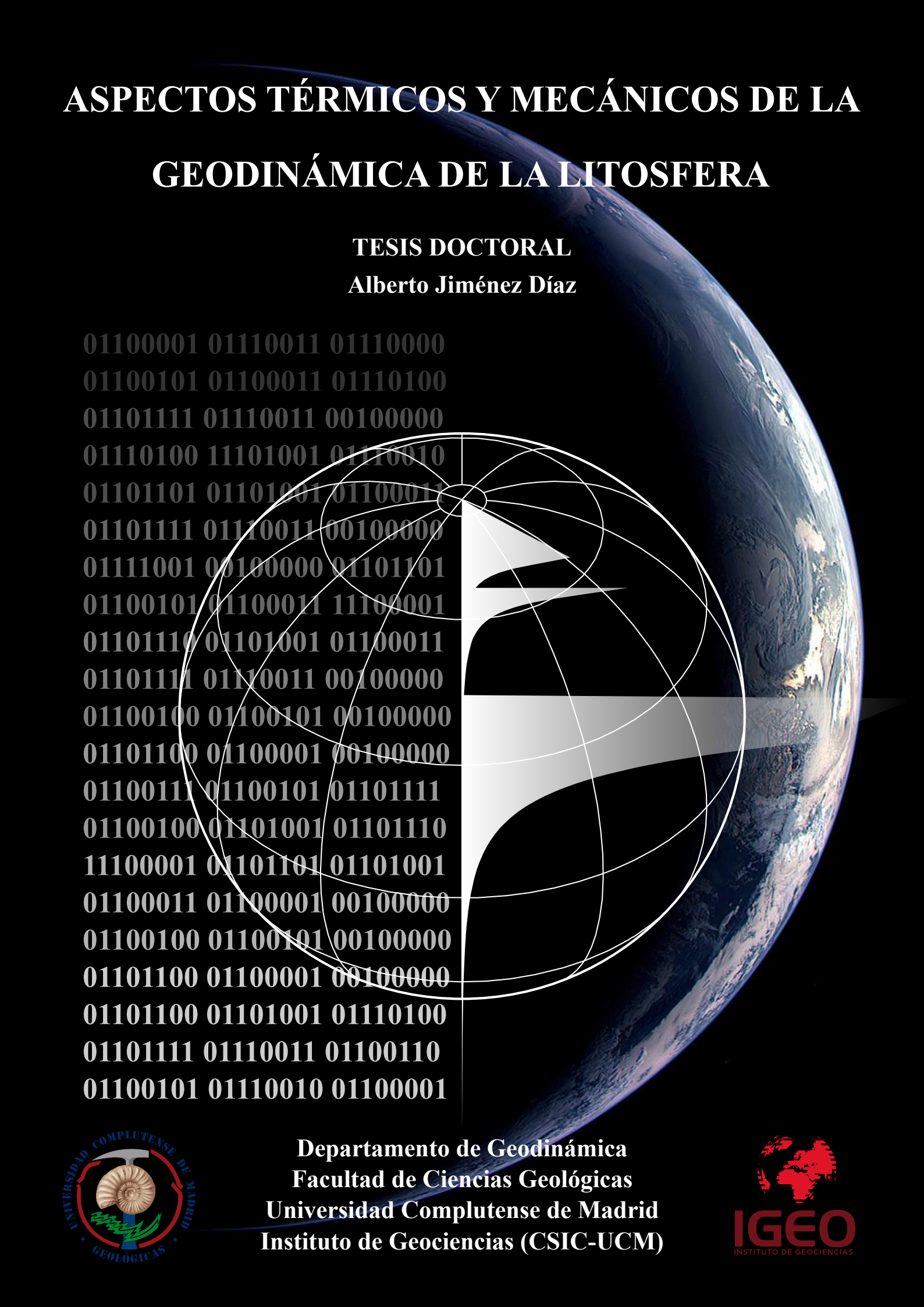

Departamento de Geodinámica
Facultad de Ciencias Geológicas
Universidad Complutense de Madrid
Instituto de Geociencias (CSIC-UCM)

ASPECTOS TÉRMICOS Y MECÁNICOS DE LA GEODINÁMICA DE LA LITOSFERA

TESIS DOCTORAL

ALBERTO JIMÉNEZ DÍAZ

MEMORIA PRESENTADA PARA OPTAR AL GRADO DE DOCTOR

MADRID, FEBRERO DE 2015

Dirigida por el Dr. Javier Ruiz Pérez, la Dra. Rosa Tejero López y el Dr. Ramón Capote del Villar

Departamento de Geodinámica

Facultad de Ciencias Geológicas

Universidad Complutense de Madrid

Departamento de Dinámica Terrestre y Observación de la Tierra

Instituto de Geociencias (CSIC-UCM)

ASPECTOS TÉRMICOS Y MECÁNICOS DE LA GEODINÁMICA DE LA LITOSFERA

TESIS DOCTORAL

ALBERTO JIMÉNEZ DÍAZ

MEMORIA PRESENTADA PARA OPTAR AL GRADO DE DOCTOR

MADRID, FEBRERO DE 2015

Tesis Doctoral realizada en el Departamento de Geodinámica de la Universidad Complutense de Madrid, y en el Departamento de Dinámica Terrestre y Observación de la Tierra del Instituto de Geociencias (CSIC-UCM), bajo la dirección del Dr. Javier Ruiz Pérez, la Dra. Rosa Tejero López y el Dr. Ramón Capote del Villar.

Vº Bº de los directores de la Tesis:

Dr. Javier Ruiz Pérez Dra. Rosa Tejero López Dr. Ramón Capote del Villar

A María José

(...) Tan insistente fue la computadora en su intento por comunicarse con Eleanor Arroway, que fue casi como si transmitiera una urgente necesidad personal de compartir con ella el descubrimiento.
La anomalía quedó al descubierto dentro de la aritmética en base 11, con totalidad de ceros y unos. Comparado con lo que se había recibido de Vega, eso podía ser, en el mejor de los casos, un mensaje simple, pero su importancia en el campo de la estadística era inmensa. El programa reagrupó las cifras formando una trama cuadrada, de igual número de dígitos en sentido horizontal y vertical. La primera línea era una sucesión continua de ceros, de izquierda a derecha. En la segunda aparecía un único uno, justo en el centro, y ceros a ambos lados. Luego de varias líneas se formó un inconfundible arco, compuesto por unos. Rápidamente se construyó una sencilla figura geométrica, rica en promesas. Emergió luego la última línea de la figura, toda de ceros, también con un cero por centro.
Oculto en el cambiante esquema de las cifras, en lo más recóndito del número irracional, se hallaba un círculo perfecto, trazado mediante unidades dentro de un campo de ceros.
El universo había sido creado ex profeso, manifestaba el círculo. En cualquier galaxia que nos encontremos, tomamos la circunferencia de un círculo, la dividimos por su diámetro y descubrimos un milagro: otro círculo que se remonta kilómetros y kilómetros después de la coma decimal. Más adentro, habría mensajes más completos. Ya no importa qué aspecto tenemos, de qué estamos hechos ni de dónde provenimos. En tanto y en cuanto habitemos en este universo y poseamos un mínimo talento para la matemática, tarde o temprano lo descubriremos porque ya está aquí, en el interior de todas las cosas. No es necesario salir de nuestro planeta para hallarlo. En la textura del espacio y en la naturaleza de la materia, al igual que en una gran obra de arte, siempre figura, en letras pequeñas, la firma del artista. Por encima del hombre, de los demonios, de los Guardianes y constructores de Túneles, hay una inteligencia que precede al universo.
El círculo se ha cerrado.
Eleanor encontró, por fin, lo que buscaba.

CARL SAGAN, *Contact* (1985)

[Traducción, Raquel Albornoz]

Foto de Portada y Contraportada:
"FIRST VIEW AS ROSETTA APPROACHES HOME". Image of the Earth acquired with the OSIRIS narrow-angle camera from a distance of 633000 km on 12 November 2009 at 13:28 CET. Copyright: ESA ©2009 MPS for OSIRIS Team MPS/UPD/LAM/IAA/RSSD/INTA/UPM/DASP/IDA.

Agradecimientos - Acknowledgements

La presente Tesis Doctoral culmina el trabajo que durante varios años he realizado dentro del campo de la geología, geofísica y geodinámica, con el fin de avanzar en el conocimiento y comprensión de la dinámica y evolución interna de la Tierra y de los planetas de tipo terrestre. Pero también culmina el sueño de un niño que dibujaba volcanes y "dinosaurios", de un chaval al que le apasionaba la ciencia en general, desde la Tectónica de Placas hasta el Horizonte de Sucesos, y de un adulto que ha convertido su pasión por las Ciencias de la Tierra y Planetarias en su modo de vida. Como ocurre en cualquier proyecto de investigación, el desarrollo de la que aquí se presenta ha requerido la ayuda y el apoyo de numerosas personas.

En primer lugar, mi más profundo agradecimiento es para mis directores de Tesis, el Dr. Javier Ruiz, la Dra. Rosa Tejero y el Dr. Ramón Capote. Muchas gracias por darme la oportunidad y confiar en mí para llevar a cabo esta investigación, por la formación y experiencia adquirida estos años, por vuestro tiempo, por vuestros consejos y por apoyarme sin reservas.

Muchas gracias Ramón por cada día de trabajo de campo que hemos compartido estos años, desde Calzadilla hasta San Miguel, porque es difícil aprender y disfrutar más, y que han hecho mucho más llevaderos los largos días frente al ordenador. Muchas gracias por tu apoyo en los momentos difíciles, especialmente los previos a conseguir la beca predoctoral, y por nuestras charlas sobre "el ahora" y sobre "el mañana". Muchas gracias por todo.

Muchas gracias Rosa porque si alguien me ha visto crecer como geólogo, como investigador y como persona, esa eres tú. Desde que comencé a trabajar contigo con una beca de iniciación a la investigación durante el último año de carrera, hasta escribir estas líneas, hemos compartido muchos días de campo, prácticas, congresos, artículos, fracasos y éxitos. Muchas gracias por tu apoyo incondicional, tanto profesional como personal, y por estar siempre pendiente de mi carrera y mi futuro. Pero sobre todo, muchas gracias por ser más que una directora de Tesis, y ser también mi amiga. Muchas gracias por todo.

Muchas gracias Javi por todos y cada uno de tus consejos, por tu paciencia, sinceridad, honestidad y sacrificio, por hacerme partícipe de tus inquietudes y compartir conmigo proyectos apasionantes, por enseñarme la importancia de "los primeros principios" y de poner en "su contexto" cada resultado, y por enseñarme "el oficio". Muchas gracias por tu apoyo incondicional, tanto profesional como personal, y por estar siempre pendiente de mi carrera y mi futuro. Pero sobre todo, muchas gracias Javi por ser mi amigo siempre, y mi director de Tesis cuando debías. Esta Tesis no habría sido posible sin ti. Muchas gracias por todo.

Durante el desarrollo del trabajo de investigación he tenido el privilegio de contar con el apoyo del Dr. Carlos Villaseca, la Dra. Marta Pérez Gussinyé, el Dr. Jon F. Kirby, el Dr. José A. Álvarez Gómez y el Dr. Ignacio Romeo. A todos, muchas gracias por formar parte de esta Tesis.

Al Dr. Carlos Villaseca quiero agradecerle su ayuda en la caracterización de la litosfera en el centro de la península ibérica, y nuestras fructíferas charlas sobre la naturaleza de la corteza. Pero sobre todo, muchas gracias Carlos por tu apoyo e interés en la evolución de mi trabajo.

Quiero agradecer a la Dra. Marta Pérez Gussinyé su confianza en mí y por haber sido, en gran medida, la causa de que me haya apasionado por los métodos espectrales como herramienta para el estudio de las propiedades mecánicas de la litosfera. Muchas gracias Marta por acogerme durante dos semanas en Royal Holloway, University of London, por las decenas de charlas vía Skype, por los cientos de correos electrónicos intercambiados sobre aspectos técnicos, metodológicos y científicos, pero sobre todo, por toda tu ayuda y generosidad.

I would like to express my most sincere gratitude to Dr. Jon F. Kirby. This Thesis would not have been possible without his help, encouragement and constant support. One more time, thank you so much for all Jon. I continue learning from you.

Al Dr. José A. Álvarez Gómez quiero agradecerle todo el conocimiento sobre la geodinámica de Centroamérica que ha compartido conmigo, y su impagable ayuda en multitud de ocasiones durante la realización de esta Tesis. Muchas gracias José por todas esas referencias imprescindibles, por nuestras charlas sobre la sismotectónica y la anisotropía mecánica, y sobre otras muchas cuestiones científicas abordadas en esta investigación. Pero más importante aún, muchas gracias por todo tu apoyo, por tu interés en mi trabajo y por tu amistad.

Al Dr. Ignacio Romeo quiero agradecerle todo el conocimiento sobre Venus que ha compartido conmigo y, en especial, su ayuda para el tratamiento estadístico de los cráteres, coronas y volcanes. Muchas gracias Ignacio por contagiarme tu entusiasmo por este fascinante planeta, por tu apoyo y por tu amistad.

I would like to thank Randell Stephenson, Yanick Ricard, Oded Aharonson, Pascal Audet, James Dohm and anonymous reviewers for their revisions of the manuscripts included in this Thesis. I especially thank Giorgio Ranalli and Pascal Audet for their encouragements, useful comments and suggestions.

También agradezco enormemente a la Dra. Ana Negredo y al Dr. David Gómez Ortiz, la revisión formal de esta Memoria, su labor y sus comentarios.

Quiero dar las gracias a todas las personas que generosamente ponen sus códigos a disposición de la comunidad científica. Los programas y códigos de libre difusión FA2BOUG (Fullea et al., 2008), Generic Mapping Tools, GMT (Wessel et al., 2013), y SHTOOLS (Wieczorek y Meschede, 2015) han sido herramientas fundamentales para la realización de esta Tesis Doctoral. Mi reconocimiento y gratitud a todos ellos. Y en este punto, José A. Álvarez Gómez y Jorge Alonso Henar merecen una mención especial. Muchas gracias por toda vuestra ayuda, imprescindible para muchas de las figuras y análisis presentes en esta investigación, y por cambiar mi forma de abordar cualquier reto científico.

Agradezco al Departamento de Geodinámica de la Universidad Complutense de Madrid, y al Departamento de Dinámica Terrestre y Observación de la Tierra del Instituto de Geociencias (CSIC-UCM), los medios prestados para la realización de la presente investigación. De forma especial, quiero darles las gracias a Estefanía y a Jesús por su ayuda en distintos momentos. Gracias también al personal de la Biblioteca de la Facultad de Ciencias Geológicas, y en especial a Laura Donadeo, de la Biblioteca del Instituto de Geociencias.

Quiero tener un recuerdo especial para Valle López. Muchas gracias Valle por toda tu ayuda con la gestión y tratamiento de los datos de Venus y Marte, y por todas las dudas resueltas de ArcGIS. Pero sobre todo, muchísimas gracias por tu apoyo incondicional, por tu preocupación e implicación en mi trabajo, por tus consejos, por tu ánimo..., en definitiva, por ser mi amiga.

Quiero agradecer a mis compañeros y amigos del grupo de Tectónica Activa, Paleosismicidad y Riesgos Asociados, que a través de los años se han convertido para mí en una gran familia, su apoyo en todo momento. A José J. Martínez Díaz, Meaza Tsige, Juan Miguel Insua Arévalo, Martín J. Rodríguez Peces, Pilar Villamor, Julián García Mayordomo, Jorge Giner Robles, Marta Bejar, Miguel Ángel Rodríguez Pascua, Alejandra Staller, Eulalia Masana, Emilio Rodríguez Escudero, Carolina Canora y Raquel Martín Banda. Muchísimas gracias a todos por tantos y tan buenos momentos.

De forma especial, quiero dar las gracias a Raúl Pérez López y Fidel Martín González por todo su apoyo y por todos sus consejos durante la realización de esta investigación, tanto en lo profesional como en lo personal. Muchas gracias Raúl por "tu cheque en blanco", y por tu implicación en la etapa final de esta Tesis.

Quiero dar las gracias a todos los profesores y compañeros del Departamento de Geodinámica su apoyo durante estos años. En particular, la Dra. Pilar Llanes, la Dra. Loreto Antón, el Dr. José Luís Granja, el Dr. Alfonso Muñoz y el Dr. Ramón Vegas siempre se han interesado especialmente por la evolución de esta Tesis Doctoral. Muchas gracias Pilar y José por todos vuestros consejos.

Y también quiero tener un recuerdo especial para Sol López, José López, Lorena Ortega, Fernando Gervilla, Ricardo Arenas, Sonia Sánchez, Rubén Díez, María José Huertas, Isabel Egea y Gabriel Castilla, porque siempre se han interesado especialmente por la evolución de mi trabajo, y me han apoyado y animado para que siguiese investigado.

Quiero agradecer a Pilar Sánchez, al Dr. Javier Fullea y a la Dra. Ana Negredo, nuestras más que fructíferas charlas sobre la estimación del espesor elástico efectivo de la litosfera, y sobre las implicaciones de las cargas superficiales e internas. Muchas gracias Javier por tu interés en la evolución de mi trabajo, y por tu ánimo para que siga investigado. Y muchas gracias Ana por todo tu apoyo, por tu entusiasmo, por tu interés en mi trabajo, y por tu implicación en la etapa final de esta Tesis.

Una mención especial merecen mis compañeros y amigos del Departamento con quienes he compartido, y sigo compartiendo, el día a día dentro y fuera de la Facultad, por su apoyo, su ánimo y su amistad. A Jorge Alonso Henar, Ignacio García Flórez, Antonio J. Olaiz, Laura M. Parro, Álvaro

Martín Herrero, María Druet, Javier Fernández Lozano, Raquel De Vicente y Juan Martín de Blas. Jorge y Nacho, que deciros…, muchas gracias por nuestras "mil y una historias clandestinas, increíbles, salvadoreñas, cachimbonas, apasionadas, apasionantes…", por formar parte, de una u otra manera, de esta Tesis, y por ser mis amigos. Antonio, muchas gracias por todo tu apoyo, ánimo y aliento, por todos estos años de amistad, y porque sé que serás una de las personas que con más alegría leerá estas líneas. Laura, muchas gracias por compartir conmigo retos y proyectos de futuro sobre otro mundo, y por ser mi amiga en éste. Álvaro, muchas gracias por todo tu apoyo y ánimo, y por todos estos años de amistad.

Quiero dar las gracias a mis compañeros y amigos de la Licenciatura, Máster y Doctorado, y del día a día en la Facultad y fuera de ésta. A Emilio Segovia, Emma Losantos, Jorge Colmenar, Víctor Hernando, Pilar Herrera, Cristina García, Carlos Pimentel, Juan Morales, Roselis Salazar, Emma Quijada, Pablo Suárez, Belén Galán, Sonia Campos, Mario Morellón, Laura González, Baba Ahmed, Violeta Borruel, Enrique Merino, Eva Chicharro, Maialen López y tantos otros... Muchísimas gracias a todos por estar ahí de una forma u otra en diferentes momentos, por todo vuestro apoyo y ánimo, y por vuestro cariño y amistad.

De forma especial, quiero dar las gracias a Carlos Pimentel. Muchas gracias Pimen por tu sentido del humor, por todas nuestras charlas y cafés, por todo tu apoyo y ánimo, y por todos estos años de amistad.

Y a Emilio Segovia. Que decirte Emilio... Juntos hemos vivido muchas de las experiencias que me han llevado a escribir estas líneas. Juntos hemos creciendo como geólogos, pero sobre todo, como personas. Muchas gracias por ser mi compañero, muchas gracias por ser mi amigo.

A Francisco Coruña, por todo tu apoyo y ánimo, por todas nuestras charlas, por esos descansos imprescindibles, pero sobre todo, muchas gracias Paco por tu amistad incondicional.

A Arantxa Cruz, por tu paciencia todas esas noches llenas de geología y doctorados, por todo tu apoyo y ánimo, por tu sentido del humor, por tu cariño y por ser mi amiga..., en definitiva, muchas gracias Aran por ser nuestro "negativo #25".

A Juncal Cruz, por tu apoyo, ánimo y aliento en todo momento, por tu preocupación, por tus consejos, por tu confianza en mí, y por tu cariño. Pero sobre todo, muchas gracias Jun por estar siempre a mi lado, y por ser mi amiga.

A Ismael Coronado, por hacerme partícipe de tu manera de entender la ciencia y la vida, por contagiarme tu curiosidad e ilusión por la investigación, imprescindibles para llegar hasta aquí, por todas y cada una de nuestras charlas, por todos tus consejos, y por tu ánimo y aliento en todo momento, especialmente en los más duros. Pero sobre todo, muchas gracias por estar siempre a mi lado, y por ser el mejor de los amigos.

A mi familia.

A Esther y Antonio, por vuestro cariño y amistad, por creer siempre en mí, y por vuestro apoyo incondicional. Muchas gracias Esther por estar siempre a mi lado, muchas gracias por ser la mejor de las amigas, muchas gracias por ser mi mejor amiga. Y también quiero tener un recuerdo especial para Inés e Isidro, y para Cristina y Juan Antonio. Muchas por vuestro apoyo y cariño, y por celebrar mis éxitos como propios.

A Flory y Alfonso, por todo vuestro apoyo y cariño, por vuestra confianza en mí, y sobre todo, por sufrir, entender, respetar y aceptar las circunstancias, no siempre fáciles, derivadas de estas páginas.

A mis padres, Ufe y María; a mis hermanos, Alicia y Fran, Manuel y Alejandro; a mi sobrina, Patricia; y a mis abuelos, porque sois parte de quien soy. Muchas gracias por quererme, por vuestra confianza en mí y por vuestro apoyo incondicional, por vuestro ánimo y aliento, por sentiros orgullosos de mí, por vuestra preocupación en los momento difíciles, y por vuestra alegría con cada reto superado. Pero sobre todo, muchísimas gracias por sufrir, comprender, respetar y aceptar mis decisiones, mi pasión por la investigación, y mi modo de vida.

Y a María José, mi compañera en el día a día, y mi motivación para llegar hasta aquí, y para continuar. Muchas gracias por tu apoyo incondicional, por creer siempre en mí, y por estar siempre a mi lado. No lo hubiera conseguido sin ti. Muchas gracias por todo.

En definitiva, quiero dar las gracias a todas las personas que, en una forma u otra, han contribuido a la realización de esta Tesis Doctoral.

Índice general

Agradecimientos **III**

Indice general **IX**

Indice de figuras **XIII**

Indice de tablas **XIX**

Abstract **1**

1 Introducción y objetivos **5**

1.1. Presentación 7
1.2. Planteamiento y objetivos de la investigación 7
1.3. Estructura de la memoria y contribuciones originales 10
1.4. Enfoque integrado del estado térmico y mecánico de la litosfera 13

2 Análisis de la estructura térmica y mecánica de la litosfera continental: Estado térmico y resistencia de la litosfera en el centro de la península ibérica **15**

2.1. Introducción 17
2.2. The thermal state and strength of the lithosphere in the Spanish Central System and Tajo Basin from crustal heat production and thermal isostasy 19
2.2.1. Introduction 19
2.2.2. Temperature profiles 21
2.2.3. Crustal heat production 23
2.2.4. Strength of the lithosphere 26
2.2.5. Results 27
2.2.5.1. Thermal modeling 27
2.2.5.2. Mechanical structure and strength envelopes 29
2.2.6. Discussion and Conclusions 32

3 Estimación del espesor elástico efectivo de la litosfera mediante métodos espectrales: Resistencia de la litosfera en Centroamérica y las regiones circundantes **41**

3.1. Introducción 43

3.2. Spatial variations of effective elastic thickness of the lithosphere in Central America and surrounding regions . . . 45
3.2.1. Introduction . . . 45
3.2.2. T_e estimation by spectral methods . . . 47
3.2.2.1. Multitaper method . . . 48
3.2.2.2. Wavelet method . . . 49
3.2.2.3. Regional topography, gravity and crustal structure . . . 49
3.2.3. Results . . . 51
3.2.3.1. Spatial variations of T_e . . . 51
3.2.3.2. Comparison with previous T_e estimates . . . 54
3.2.4. Discussion . . . 55
3.2.4.1. T_e, surface heat flow and thermal age . . . 55
3.2.4.2. Loading of the lithosphere . . . 57
3.2.4.3. The Middle American and Lesser Antilles subduction zones . . . 60
3.2.4.4. T_e and seismicity . . . 61
3.2.5. Conclusions . . . 62
3.3. Supplementary Material . . . 69
3.3.1. Bouguer coherence . . . 69
3.3.2. Multitaper method . . . 73
3.3.3. Wavelet method . . . 77
3.3.4. Bias in T_e estimation . . . 82

4 Análisis integrado de la topografía y gravedad en el estudio de la estructura cortical y litosférica de los planetas terrestres: Estructura de la litosfera de Venus **87**
4.1. Introducción . . . 89
4.2. Lithospheric structure of Venus from gravity and topography . . . 91
4.2.1. Introduction . . . 91
4.2.2. Global gravity and topography of Venus . . . 93
4.2.3. Crustal thickness modelling . . . 95
4.2.4. Estimating the effective elastic thickness of the lithosphere . . . 98
4.2.5. Results of effective elastic thickness mapping . . . 99
4.2.6. Discussion . . . 102
4.2.7. Conclusions . . . 105

5 La (reconstrucción de la) historia térmica de los planetas terrestres: Estructura y evolución de la litosfera de Marte **115**
5.1. Introducción . . . 117
5.2. The thermal evolution of Mars as constrained by paleo-heat flows . . . 119
5.2.1. Introduction . . . 119
5.2.2. Strength of the lithosphere . . . 121

5.2.3. Temperature profiles . . . 125
5.2.4. Results . . . 128
5.2.5. Discussion . . . 131
5.2.6. Conclusions . . . 133

6 Discusión y conclusiones **141**
6.1. Marco conceptual integrador . . . 143
6.2. Sobre la anisotropía mecánica de la litosfera . . . 145
6.2.1. T_e, anisotropía de T_e y deformación litosférica . . . 149
6.2.2. Prospectiva . . . 150
6.3. Sobre la evolución interna (y climática) de Marte . . . 153
6.3.1. Espesor de corteza (T_c) . . . 153
6.3.2. Prospectiva . . . 156
6.4. Sobre la estimación del espesor elástico efectivo de la litosfera (T_e) mediante métodos espectrales . . . 158
6.5. Conclusiones . . . 161
6.6. Reflexión final . . . 163

Bibliografía **165**

Anexo I. Jiménez-Díaz, A., Ruiz, J., Villaseca, C., Tejero, R., Capote, R. The thermal state and strength of the lithosphere in the Spanish Central System and Tajo Basin from crustal heat production and thermal isostasy. Journal of Geodynamics 58, 29-37, 2012. **173**

Anexo II. Jiménez-Díaz, A., Ruiz, J., Pérez-Gussinyé, M., Kirby, J.F., Álvarez-Gómez, J.A., Tejero, R., Capote, R. Spatial variations of effective elastic thickness of the lithosphere in Central America and surrounding regions. Earth and Planetary Science Letters 391, 55-66, 2014. **185**

Anexo III. Ruiz, J., McGovern, P.J., Jiménez-Díaz, A., López, V., Williams, J.P., Hahn, B.C., Tejero, R. The thermal evolution of Mars as constrained by paleo-heat flows. Icarus 215, 508-517, 2011. **199**

Índice de figuras

2.1. Geographical and geological settings of the study area showing the two mountains ranges (Spanish Central System and Toledo Mountains) separated by the Tajo Basin. Map background is from the Neotectonic Map of Spain (IGME and ENRESA, 1998). 21

2.2. Estimates of heat production rates of rocks from the Spanish Central System upper crust, Toledo Mountains upper crust and Spanish Central System lower crustal granulite xenoliths. 25

2.3. Geotherm constructed for the Spanish Central System and the Tajo Basin. Variables used in estimations are provided in Table 2.1. See text for details. 28

2.4. Results of thermal models and strength envelopes, calculated for a strain rate of 10^{-15} s^{-1}, plotted along a NW-SE transverse section of the area. Outer black line binds differential stress estimated for dry rock composition. Inner dashed line denotes differential stress for wet rock composition of the upper crust (quartzite or granite) and lithospheric mantle (peridotite). F_s: Surface heat flow. T_e: Effective elastic thickness for wet/dry rheology. *Smax*: Maximum total lithospheric strength. *Moho*: crust-mantle boundary. *LAB*: lithosphere-asthenosphere boundary. 30

2.5. Total lithospheric strength values for dry and wet rocks in compression and tension plotted for the different tectonic units. Higher strength values were obtained for dry rheology and compressive differential stress. Minimum strength values correspond to wet rheology and tensional differential stress. 31

2.6. Compilation of effective elastic thickness values obtained for the study area. 32

2.7. Effective elastic thickness, in terms of strain rate, in the Spanish Central System and Tajo Basin (North). Dry and wet rheologies for the crust and mantle are used in the calculation. 34

3.1. Geotectonic setting of Central America and surrounding regions. Shaded relief image of bathymetry and topography is from ETOPO1 digital data (Amante and Eakins, 2009), and boundaries of lithospheric plates are based on the PB2002 model (Bird, 2003). Yellow arrows denote vectors of the plate motion from the MORVEL model (DeMets et al., 2010) with respect to the NNR reference frame as calculated at the given position with the Plate Motion Calculator. Triangles show the position of Holocene volcanoes (Siebert and Simkin, 2002). Abbreviations: CAR, Carnegie Ridge; CB, Colombian Basin; CHB, Chortis Block; CHCB, Chocó Block; CHTB, Chorotega Block; CR, Cocos Ridge; EPR, East Pacific Rise; GHS, Galápagos Hotspot; HE, Hess Escarpment; LAT, Lesser Antilles Trench; MAT, Middle America Trench; MB, Maya Block; MCR, Mid-Cayman Rise; MT, Muertos Trough; ND, Nicaraguan Depression; OTF, Oriente Transform Fault; PFZ, Panamá Fracture Zone; PMFS, Polochic-Motagua Fault System; PRT, Puerto Rico Trench; SITF, Swan Island Transform Fault; TR, Tehuantepec Ridge; VB, Venezuelan Basin. . . 47

3.2. Bouguer gravity anomaly used for the analysis. Topography shaded relief superimposed. 51

3.3. Effective elastic thickness, T_e, over Central America and surrounding regions from: (a) multitaper method, and (b) wavelet method. In both images, topography shaded relief is superimposed. Fig. 3.3a shows final T_e after merging the results from the three different window sizes (see Section 3.2.2 and Supp. Fig. 1). The final T_e structure retains the primary characteristics of the largest window, but it better resolves the sharp gradient between low and high T_e areas and the short wavelength variations in T_e. Fig. 3.3b shows T_e estimated from the wavelet method with $|\mathbf{k}_0| = 2.668$. 53

3.4. (a) Regional surface heat flow from the updated global heat flow database of the International Heat Flow Commission (Hasterok, 2010). Black circles indicate measurement sites. White triangles show the position of Holocene volcanoes (Siebert and Simkin, 2002). (b) Age-area distribution of ocean floor from Müller et al. (2008). (c) Effective elastic thickness, T_e, from the multitaper method versus age of the oceanic crust (Müller et al., 2008). 56

3.5. (a) Loading ratio (F) corresponding to the T_e obtained from the wavelet method (Fig. 3.3b). (b) Sediment thickness (meters) on the seafloor in the study area from the 5 arcminute digital total-sediment-thickness database for the world's oceans and marginal seas (Divins, 2003; Whittaker et al., 2013). 59

3.6. (a) Correlation between distribution of the shallow seismicity (depth <50 km) from the Global CMT seismic catalog (Ekström et al., 2012) with T_e derived from the wavelet method. (b) Histogram shows shallow earthquake events versus T_e. 61

4.1. (a) Topography and (b) Bouguer gravity anomaly of Venus derived from the spherical harmonic models SHTJV360u (Rappaport et al., 1999) and SHGJ180u (Konopliv et al., 1999), respectively, to degree and order 180. The map projection is Robinson with east-positive longitude convention and centered on 180º longitude. Black contour in (b) is the zero topography contour. 94
4.2. Crustal thickness model for Venus assuming a mean crustal thickness of 25 km, and crust and mantle densities of, respectively, 2900 and 3300 kg m^{-3}. 96
4.3. (a) Histogram of crustal thickness. (b) Crustal thickness model in an orthographic projection centered on 120° longitude and 40º latitude. The red lines correspond to the crustal structure profiles shown in (c). (c) Pole-to-pole longitudinal transects of the crustal structure, as well as an equatorial transect, where light blue corresponds to crust and gray corresponds to mantle. 97
4.4. Results of the inversion of the squared-real Bouguer coherency ($|\mathbf{k}_0| = 5.336$). (a) Effective elastic thickness, T_e. (b) Loading ratio, F, corresponding to the T_e results in (a). (c) Histograms of T_e and F. (d) Plot of T_e against F. 100
4.5. Equatorial transect of our crustal thickness model (figure format is the same as Fig. 4.3c). The red line corresponds to the variation of the effective elastic thickness (right axis) along the same profile. 102
4.6. Plot of crater density obtained with sampling windows of 10^6 km^2 against the mean value of T_e in each window (points); and crater density calculated counting the number of craters for T_e intervals of 10 km (white squares and black line). 103
4.7. Density of (a) volcanoes (Schaber et al., 1998) and (b) coronae (Stofan et al., 2001) against T_e and F corresponding to the results in Fig. 4.4. Figure format is the same as Fig. 4.6. 104
4.8. Gravity misfit derived from the crustal thickness modelling at spherical harmonic degree and order 180, corresponding to the results in Fig. 4.2 and Fig. 4.3. 107
4.9. T_e error corresponding to the results in Fig. 4.4. 107

5.1. MOLA topography map showing the analyzed regions. 121
5.2. Upper (red) and lower (blue) limits for the surface heat flows for several regions and times of Mars. For several regions only upper or lower limits are obtained, since lower or upper limits on effective elastic thickness are not available. Curves and horizontal lines indicate uncertainty related to surface age (and hence also to radioactive heating in the lithosphere), not to temporal evolution. The black curves show surface heat flows for three values of the Urey number (the ratio of the internal heat production to the total surface heat loss in a planet), calculated according to the composition model of Wänke and Dreibus (1988). Thus, the curve labeled ‘‘Radioactive ($Ur = 1$)’’ corresponds to the average surface heat flow which is equivalent to the total radioactive heat production of Mars. 129

5.3. Heat flows as a function of age and Urey number compared with the predictions of a thermal history model of Mars (calculated according to Williams and Nimmo (2004)), which obtain results similar to those of other thermal history models for Mars (e.g., Hauck and Phillips, 2002; Grott and Breuer, 2010). The Urey number is between 0.75 and 0.6 through the entire history of Mars. 129

5.4. Upper limits for the surface heat flows for several regions and times of Mars. Several categories of geological features are also indicated. Coracis Fossae, a rift zone with associated magmatism is not represented due to scale considerations (see Fig. 5.3). Curves indicate uncertainty related to surface age (and hence to radioactive heating in the lithosphere), not to temporal evolution. The black curve is the average heat flow equivalent to the total radioactive heat production of Mars according to the composition model of Wänke and Dreibus (1988). 130

5.5. Regional distribution of upper limits for the surface heat flow shown on MOLA topography. Most estimates correspond to the Tharsis region of Mars, where geological activity is concentrated. 131

5.6. Upper limits for the sublithospheric heat flow for several regions and times of Mars, calculating by imposing the condition of zero lithospheric heat sources. Coracis Fossae is not represented due to scale considerations (the sublithospheric heat flow upper limit is 68 mW m^{-2} for this feature). Several categories of geological features are also indicated. Black curve as in Fig. 5.4. 132

6.1. Marco conceptual de la investigación. 144

6.2. (a) Anisotropía de T_e (p_a) en Centroamérica y las regiones circundantes, obtenida a partir del análisis anisotrópico con el método *Wavelet* ($|\mathbf{k}_0|$ = 2.668). (b) Variación espacial de T_e a partir del análisis isotrópico realizado con el mismo método, correspondiente a los resultados presentados en el Capítulo 3 (véase la Figura 3.3 y la Figura Suplementaria 4). 147

6.3. La dirección débil de la anisotropía mecánica (β_w), representada como barras cuya longitud es proporcional a la magnitud de anisotropía de T_e, superpuestas a la variación espacial de T_e para dos regiones dentro del área de estudio. 148

6.4. Correlación entre la distribución de la sismicidad superficial (profundidad $<$ 50 km; Global CMT catalog, Ekström et al., 2012) con T_e (a) y con la magnitud de anisotropía de T_e (b). Los histogramas muestran los terremotos superficiales frente a T_e (c) y frente a la magnitud de anisotropía de T_e (d). 149

6.5. Resultados preliminares de la variación espacial de T_e en la península ibérica (a), y de la dirección débil de la anisotropía mecánica (β_w), superpuesta a la variación espacial de T_e (b), obtenidos con el método *Wavelet* ($|\mathbf{k}_0|$ = 2.668). 152

6.6. Modelo de espesor de corteza para Marte asumiendo un espesor cortical medio de 50 km, y unas densidades para la corteza y el manto litosférico de, respectivamente, 2900 y 3500 kg m^{-3}. La linea negra corresponde al contorno de cota 0 del modelo de forma de Marte *MarsTopo719* (Wieczorek, 2007). 154
6.7. (a) Histograma del espesor cortical. (b) Modelo de espesor de corteza para Marte en proyección ortográfica centrado en 120º de longitud y 40º de latitud. Las lineas rojas corresponden a los perfiles corticales mostrados en (c). (c) Cortes polo a polo de la estructura cortical, así como un corte ecuatorial, donde la corteza está representada en azul, y el manto en gris. 155

Índice de tablas

2.1. Parameters used to construct the geotherms and strength envelopes. Crustal structure and composition derived from seismic data (Banda et al., 1981; ILIHA DSS Group, 1993; Suriñach and Vegas, 1988), crustal density derived from gravity data analysis (Gómez-Ortiz et al., 2005b) and rheological parameters from Ranalli (1997). 23
2.2. Estimates of heat production of rocks from the Spanish Central System and Toledo Mountains. 24
2.3. Summary of values obtained from thermal modeling. 28

3.1. Symbols and values of constants. 50

4.1. Symbols and values of constants. 99

5.1. Values used for the calculation of heat flows from the effective elastic thickness (T_e) of the lithosphere. 123
5.2. Values used for the calculation of heat flows from the brittle–ductile transition (BDT) depth. 125
5.3. Heat-producing element abundances. 126

Abstract

"THERMAL AND MECHANICAL ASPECTS OF THE GEODYNAMICS OF THE LITHOSPHERE"

Recent progress in geophysical and geochemical studies has brought us far in the understanding of the structure, origin, and evolution of the lithosphere. This intense research activity has allowed to the development of techniques to estimate temperature profiles or the strength of rocks in terms of depth (known as strength envelopes or rheological profiles), and of concepts such as the total strength of the lithosphere or the effective elastic thickness; to the joint analysis of the gravity and topography data to constrain fundamental aspects of the structure and long-term mechanical behavior of the lithosphere; or to the use of mechanical indicators of the lithosphere to estimate its corresponding thermal properties, in order to constrain the thermal structure and evolution of a planetary body. Several of these concepts and techniques have also been used in research on other planetary bodies, reaching a significant level of refinement in the geodynamic analysis of their lithospheres. In this sense, the lithosphere of each planetary body has its own characteristics; however, the study methods are the same, although their application must be adapted to each case due to the quantity, nature and resolution of the available data. The terrestrial planets have a similar structure and composition than that of the Earth, and so it is not surprising that the same methods serve to study their lithospheres. In fact, the concepts applied to study, for example, Mercury, Venus, Mars or the Moon are the same as those used for the investigation of our own planet. In addition, a better understanding of these planetary bodies and their evolution leads to a better understanding of our own planet, since brings other models with which compare the Earth's dynamics and evolution, while providing a framework to test the general validity of certain concepts or methods, and thus, can be the inspiration source for tackle some problems of terrestrial dynamics. The comparison of the results obtained for other planetary bodies with the current knowledge of the evolution of the Earth provides an overview of the terrestrial planets, and an improved knowledge of how variations in the specific conditions (such as composition, mass or capacity to retain and recycle volatile elements) correspond to different evolutionary paths, and hence to different expressions of their global dynamics, such as the existence or absence of plate tectonics, and the intensity of internal cooling or heating. In a similar way, the results of these investigations allow us to advance in our understanding of the interrelationship between the functioning of the internal geodynamics of each planet and the evolution of its environmental and climatic conditions.

In this context, the main aim of this Ph.D. Thesis is the analysis of the thermal structure and long-term mechanical behaviour of the lithosphere, in order to improve our knowledge and understanding of the dynamics and internal evolution of the Earth and other terrestrial planets. The methodological nature of the research presented here allows the study of different geodynamic contexts of the Earth and other terrestrial planets (exemplified in this thesis by Venus and Mars), encouraging the learning and development of specific methods of analysis for determining the thermal state and strength of

the lithosphere in different contexts, and therefore providing a much broader view of the concept of lithosphere.

Thus, this study includes the following more specific objectives:

(i) Performing a detailed study of the thermal structure of the lithosphere, and its relation to the mechanical structure, in the Central Iberian Peninsula (Chapter 2).

(ii) To study the structure and long-term mechanical behaviour of the lithosphere by using the joint analysis of gravity and topography data, first for an area of the Earth, Central America and surrounding regions (Chapter 3), and then for Venus as a whole (Chapter 4).

(iii) To use the mechanical properties of the lithosphere to estimate their corresponding thermal properties, in order to constrain the thermal evolution of Mars (Chapter 5).

Chapter 2: The thermal state and strength of the lithosphere in the Spanish Central System and Tajo Basin from crustal heat production and thermal isostasy

Here it has been modelled the thermal structure of the lithosphere of the Spanish Central System and the Tajo Basin, and their implications for lithospheric strength. For this, refined heat-producing elements (HPE) values have been used to obtain new estimates of heat production rates in the Spanish Central System and Tajo Basin areas, which have been used joined to the relation between topography and thermal structure of the lithosphere to calculate the best-fit surface heat flows in the study area. Moreover, a temperature-dependent thermal conductivity (appropriate for olivine) for the lithospheric mantle has been implemented to improve the calculations of temperature profiles in the mantle. The geotherms so obtained, together with the implementation of a new rheological law for the upper lithospheric mantle, have been used to calculate refined estimations of the strength and effective elastic thickness of the lithosphere. It has been obtained surface heat flow values of 84 mW m^{-2} and 82 mW m^{-2} for the Spanish Central System and the Tajo Basin, respectively. The thermal state of the lithosphere affects mantle temperatures, and hence may be playing an important role in the uplift and maintenance of the Spanish Central System.

Chapter 3: Spatial variations of effective elastic thickness of the lithosphere in Central America and surrounding regions

As a proxy for long-term lithospheric strength, the effective elastic thickness (T_e) can be used to understand the relationship between lithospheric rheology and geodynamic evolution of complex tectonic settings. Here it has been presented, for the first time, high-resolution maps of spatial variations of T_e in Central America and surrounding regions from the analysis of the coherence between topography and Bouguer gravity anomaly using multitaper and wavelet methods. Regardless of the technical differences between the two methods, there is a good overall agreement in the spatial variations of T_e recovered from both methods. Although absolute T_e values can vary in both maps, the qualitative T_e structure and location of the main T_e gradients are very similar. The pattern of the T_e

variations in Central America and surrounding regions agrees well with the tectonic provinces in the region, and it is closely related to major tectonic boundaries, where the Middle American and Lesser Antilles subduction zones are characterized by a band of high T_e on the downgoing slab seaward of the trenches. These high T_e values are related to internal loads (and in the case of the southernmost tip of the Lesser Antilles subduction zone also associated with a large amount of sediments) and should be interpreted with caution. Finally, there is a relatively good correlation, despite some uncertainties, between surface heat flow and our T_e results for the study area. These results suggest that although this area is geologically complex, the thermal state of the lithosphere has profound influence on its strength, such that T_e is strongly governed by thermal structure.

Chapter 4: Lithospheric structure of Venus from gravity and topography

There are many fundamental and unanswered questions on the structure and evolution of the Venusian lithosphere, which are key issues for understanding Venus in the context of the terrestrial planets. Here the lithospheric structure of Venus has been investigated by calculating its crustal and effective elastic thicknesses (T_c and T_e, respectively) from an analysis of gravity and topography, in order to improve our knowledge of the large scale and long-term mechanical behaviour of its lithosphere. We found that the Venusian crust is usually 20-25 km thick with thicker crust under the highlands. Our effective elastic thickness values range between 14 km (corresponding to the minimum resolvable T_e value) and 94 km, but are dominated by low to moderate values. T_e variations deduced from our model could represent regional variations in the cooling history of the lithosphere and/or mantle processes with limited surface manifestation. The crustal plateaus are near-isostatically compensated, consistent with a thin elastic lithosphere, showing a thickened crust beneath them, whereas the lowlands exhibit higher T_e values, maybe indicating a cooler lithosphere than that when the Venusian highlands were emplaced. Meanwhile, the large volcanic rises show a complex signature, with a broad range of T_e and subsurface-to-surface load ratio (F) values. Finally, our results also reveal a significant contribution of the upper mantle to the strength of the lithosphere in many regions.

Chapter 5: The thermal evolution of Mars as constrained by paleo-heat flows

Lithospheric strength can be used to estimate the heat flow at the time when a given region was deformed, allowing us to constrain the thermal evolution of a planetary body. In this sense, the high ($>$300 km) effective elastic thickness of the lithosphere deduced from the very limited deflection caused by the north polar cap of Mars indicates a low surface heat flow for this region at the present time, a finding difficult to reconcile with thermal history models. This has started a debate on the current heat flow of Mars and the implications for the thermal evolution of the planet. Here it has been performed refined estimates of paleo-heat flow for 22 martian regions of different periods and geological context, derived from the effective elastic thickness of the lithosphere or from faulting depth beneath large thrust faults, by considering regional radioactive element abundances and realistic thermal conductivities for the crust and mantle lithosphere. For the calculations based on the effective

elastic thickness of the lithosphere we also consider the respective contributions of crust and mantle lithosphere to the total lithospheric strength. The obtained surface heat flows are in general lower than the equivalent radioactive heat production of Mars at the corresponding times, suggesting a limited contribution from secular cooling to the heat flow during the majority of the history of Mars. This is contrary to the predictions from the majority of thermal history models, but is consistent with evidence suggesting a currently fluid core, limited secular contraction for Mars, and recent extensive volcanism. Moreover, the interior of Mars could even have been heating up during part of the thermal history of the planet.

Concluding remarks

This research shows, through the study of individual cases and by using of different methodologies, the close interrelation between the mechanical structure of the lithosphere and its thermal state, and how every increase in the knowledge of one of these aspects can be used to improve our knowledge of the other, such that it is not possible a correct understanding of the first without an adequate knowledge of the second and vice versa.

Taken together, the papers included in this research show the universality of the methods used to study the thermal and mechanical structure of the lithosphere, strengthen the confidence in the application of these methodologies to the study of the lithosphere for different geodynamic contexts, as well as for different planetary bodies, and provide a much broader view of the concept of lithosphere.

As usual in any research, this Ph.D. Thesis is no more than a first step in the study of the thermal and mechanical structure of the lithosphere, in the understanding of the dynamics of the Earth and other terrestrial planets, and in how it has developed its internal evolution. Each of the papers collected here raises questions that represent a great opportunity, as well as a great challenge, for future work.

Capítulo 1

Introducción y objetivos

1. Introducción y objetivos

1.1. Presentación

La presente Tesis Doctoral ha sido realizada en el Departamento de Geodinámica de la Universidad Complutense de Madrid, y en el Departamento de Dinámica Terrestre y Observación de la Tierra del Instituto de Geociencias (CSIC-UCM), bajo la dirección del Dr. Javier Ruiz, la Dra. Rosa Tejero y el Dr. Ramón Capote, formando parte de las actividades de investigación y formación desarrolladas por el Grupo Consolidado de Investigación "Tectónica Activa, Paleosismicidad y Riesgos Asociados" (UCM-910368). Esta Tesis Doctoral se ha desarrollado dentro del Programa de Doctorado "Geología e Ingeniería Geológica" de la Facultad de Ciencias Geológicas de la Universidad Complutense de Madrid. La Universidad Complutense de Madrid ha financiado los estudios de este doctorado por medio de una beca predoctoral de cuatro años de Formación de Personal Investigador (Convocatoria 2010), disfrutada entre abril de 2011 y marzo de 2015. Además, esta investigación ha contado con los medios del departamento, y con el respaldo de los proyectos de investigación CGL2008-03463, CGL2009-14405-C02-02 y CGL2011-23857.

1.2. Planteamiento y objetivos de la investigación

La Tierra es un planeta dinámico. Este dinamismo es un reflejo del hecho de que la Tierra es un planeta denso y caliente en un universo frío y vacío (Sandiford, 1994). Su comportamiento se rige por procesos fundamentales de la naturaleza, como la transferencia de calor y la gravedad, que en combinación con las restricciones impuestas por los materiales que componen nuestro planeta, son responsables a todas las escalas de su intrincada estructura. El carácter e intensidad de estos procesos controla las características de la capa más externa de la Tierra, la litosfera, y su comportamiento mecánico. Hay varias definiciones posibles de litosfera. Por ejemplo, puede definirse como la capa que limita con la superficie terrestre dentro de la cual el calor se transfiere principalmente por conducción térmica, o como la capa de alta velocidad sísmica suprayacente a una zona de baja velocidad del manto, o también como la capa que forman las placas litosféricas en la que se divide la superficie terrestre.

No obstante, la definición más útil de litosfera sigue siendo aquella que fue acuñada en los inicios de la Tectónica de Placas: la litosfera es la parte de la corteza y el manto terrestre mecánicamente más resistente que no sufre una relajación viscosa significativa con el tiempo, y que se deforma elásticamente antes de llegar a su límite de rotura (para una revisión véase p.ej. Burov, 2011). Una manifestación de su comportamiento rígido es su respuesta flexural a la aplicación de cargas, tales como las asociadas al emplazamiento de, por ejemplo, volcanes o cuencas sedimentarias (p.ej., Watts, 2001). Comparando la flexión observada en regiones con cargas aplicadas con modelos reológicos elásticos, plásticos y viscosos se puede determinar la rigidez flexural de la litosfera y sus variaciones

espaciales. Tanto la litosfera oceánica como la continental se modifican por flexión, pero ambas tienen una evolución física y química diferente, respondiendo a las cargas aplicadas de distinta manera. La litosfera oceánica es relativamente joven y su rigidez flexural, expresada mediante el espesor elástico, depende de su edad térmica (Watts, 2001). La litosfera continental, por el contrario, es relativamente antigua, suele estar formada por capas de distinto comportamiento reológico y su rigidez flexural no depende de un único parámetro como la edad térmica, sino que está controlada por factores más locales como la estructura y composición de la corteza (p.ej., Watts y Burov, 2003; Afonso y Ranalli, 2004; Burov y Watts, 2006).

La litosfera terrestre responde a las fuerzas derivadas de la subducción, la orogénesis, la ruptura continental o la formación de cuencas sedimentarias, deformándose en función de sus propiedades mecánicas y los factores mencionados (p.ej., Watts et al., 2013). Las observaciones geológicas y geofísicas permiten describir y estudiar esta deformación en los estilos estructurales en orógenos, la ”arquitectura” estratigráfica de las cuencas sedimentarias, o la geometría a gran escala de la corteza y el manto superior. La naturaleza de la deformación, y en particular su escala espacial y temporal, limita las propiedades físicas de la litosfera que, a su vez, repercuten en las cuencas sedimentarias, el cambio del nivel del mar, o la topografía dinámica. Estos procesos son responsables de la gran diversidad y belleza de nuestro planeta, y proporciona la motivación básica en Ciencias de la Tierra.

Los estudios geofísicos y geoquímicos de la litosfera terrestre han alcanzado estos últimos años un grado notable de sofisticación, y han llegado lejos en la comprensión de su estructura, origen y evolución (para una revisión véase p.ej. Artemieva, 2011). Esta intensa actividad investigadora ha impulsado el desarrollo de técnicas que permiten calcular perfiles de temperatura o de resistencia a la deformación de las rocas (conocidos como perfiles reológicos o envolventes de resistencia) en relación con la profundidad, de conceptos como resistencia total de la litosfera o espesor elástico efectivo, el análisis integrado de los datos de topografía y gravedad como herramienta para constreñir aspectos fundamentales de la estructura y el comportamiento a largo plazo de la litosfera, o el uso de indicadores mecánicos de la litosfera para deducir sus correspondientes propiedades térmicas, con el fin de reconstruir la historia térmica de una región.

Algunos de estos conceptos y técnicas han sido usados también en la investigación de otros cuerpos planetarios, alcanzándose en los últimos años un nivel importante de refinamiento en el análisis geodinámico de sus litosferas. La exploración de otros planetas por medio de sondas espaciales tiene en la actualidad una gran repercusión, tanto pública como en el mundo académico. Este gran esfuerzo de investigación ha ampliado por tanto de una forma espectacular el área de acción de las ciencias de la Tierra, hasta abarcar al resto de cuerpos planetarios de nuestro entorno espacial, hasta el punto de que en los países anglosajones es muy frecuente hablar de “Ciencias de la Tierra y Planetarias” como un único campo de estudio.

Cada planeta y gran satélite del Sistema Solar es un mundo por derecho propio. La geología que caracteriza cada cuerpo planetario es consecuencia de fuerzas y procesos que actúan en unas condiciones particulares, una combinación única de intensidades, y sobre materiales que pueden cambiar drásticamente en composición. Pero además, es también consecuencia de una historia evolutiva única

en cada caso. De esta manera, la litosfera de cada cuerpo planetario posee características propias. Sin embargo, los métodos de estudio son los mismos, aunque su aplicación debe adaptarse a cada caso debido a la cantidad, naturaleza y resolución de los datos disponibles. Los planetas de tipo terrestre (o planetas terrestres) presentan una semejanza composicional, e incluso estructural, con la Tierra, por lo que no es sorprendente que los mismos métodos, dada su universalidad, sirvan para el estudio de sus litosferas. De hecho, los conceptos que se aplican para el estudio de por ejemplo Mercurio, Venus, Marte o la Luna son los mismos que se usan para la investigación de nuestro propio planeta, si bien las técnicas concretas que se pueden emplear dependen de la lejanía de cada cuerpo (lo que requiere de grandes presupuestos y recursos para enviar sondas espaciales) y de que, a excepción de la Luna, por el momento no resultan accesibles de forma directa para los seres humanos. Además, una mejor comprensión de éstos y de su evolución redunda en un mejor conocimiento de nuestro propio planeta, dado que aporta otros modelos con el que comparar la Tierra, su dinámica y su evolución, al tiempo que proporciona un marco para poner a prueba la validez general de ciertos conceptos o métodos considerados como "puramente terrestres", y puede ser por tanto fuente de inspiración para abordar algunos problemas de la dinámica terrestre (Ruiz, 2006). Así, el estudio de estos cuerpos resulta de un innegable interés, lo que justifica los esfuerzos que al mismo han dedicado la agencia espacial de Estados Unidos (NASA), la Agencia Espacial Europea (ESA), o las agencias de Rusia (FKA), Japón (JAXA), China (CNSA) y de la India (ISRO), entre otras.

La comparación de los resultados obtenidos para el resto de cuerpos planetarios con los conocimientos actuales de la evolución de la Tierra proporcionan una visión global de los planetas terrestres, y un conocimiento mejorado de como las variaciones en las condiciones específicas (como composición, masa o capacidad de retener y reciclar elementos volátiles) se corresponden con trayectorias evolutivas diferentes, y diferentes expresiones de su dinámica global, como por ejemplo la existencia o ausencia de tectónica de placas, y la intensidad del enfriamiento (o incluso calentamiento) de su interior. Así mismo, los resultados de estas investigaciones nos permiten avanzar en el conocimiento de la interrelación entre el funcionamiento de la geodinámica interna de cada planeta y la evolución de sus condiciones ambientales y climáticas. En este sentido, al tener implicaciones sobre la evolución de las condiciones ambientales, tienen también implicaciones para nuestro conocimiento de factores que influyen en el cambio climático, y para la astrobiología, rama de la ciencia muy influyente en la actualidad en relación con la exploración del Sistema Solar.

El estudio de la estructura térmica y mecánica de la litosfera aporta información sobre el modo en que las capas externas y relativamente rígidas de los planetas, responden a las fuerzas a las que se encuentran sometidas. También proporciona información sobre la evolución térmica, y sobre los cambios en la dinámica global experimentados a lo largo de su evolución. Por otro lado, el estudio de las deformaciones registradas en sus superficies permite conocer como son los procesos de geodinámica interna y cuál ha sido su evolución a lo largo de su historia geológica (los campos de esfuerzos que dan lugar a las deformaciones tectónicas tienen su origen en los procesos geodinámicos internos, es decir, están generados en última instancia por los procesos que gobiernan la pérdida de calor interno). En este contexto, el objetivo principal de esta Tesis Doctoral es el estudio de diferentes aspectos de la

estructura térmica y mecánica de la litosfera, con el fin de avanzar en el conocimiento y comprensión de la dinámica y evolución interna de la Tierra y de los planetas de tipo terrestre.

Este estudio se ha llevado a cabo para múltiples ambientes geodinámicos, desde unidades tectónicas intraplaca como el Sistema Central y la Cuenca del Tajo en el centro de la península ibérica, a áreas que engloban distintas placas litosféricas y litosferas de diferente naturaleza (continental u oceánica), como es Centroamérica; y para diferentes planetas de tipo terrestre, ejemplificados en esta Tesis Doctoral por Venus y Marte. Esta diversidad de contextos ha potenciado el aprendizaje y desarrollo de métodos de análisis específicos en función de los datos disponibles y de las características de las litosferas estudiadas, abriendo nuevas posibilidades en técnicas ya existentes. Estas aportaciones han permitido mejorar la caracterización el estado térmico y resistencia de la litosfera en diferentes ambientes tectónicos de la Tierra y en las litosferas de Venus y Marte, proporcionando una visión más amplia del concepto de litosfera.

El objetivo principal incluye los siguientes objetivos específicos:

(i) Estudiar la estructura térmica de la litosfera y su relación con la estructura mecánica de la misma en un dominio intraplaca como es el centro de la península ibérica.

(ii) Estudiar la estructura y el comportamiento mecánico a largo plazo de la litosfera usando como herramienta el análisis integrado de topografía y gravedad, primero en una región de la Tierra, Centroamérica y las regiones circundantes, y después de forma global en Venus.

(iii) Integrar los métodos desarrollados usando las propiedades mecánicas de la litosfera para deducir las correspondientes propiedades térmicas, con el fin de reconstruir la historia térmica de una región o un planeta, en este caso, de Marte.

1.3. Estructura de la memoria y contribuciones originales

La presente Tesis Doctoral se presenta como un compendio de publicaciones. El cuerpo principal de esta memoria está compuesto por cuatro artículos que abordan los objetivos planteados, organizados en cuatro capítulos temáticos, de acuerdo al Art. 10.3 que recoge las directrices para Tesis Doctorales presentadas en "formato de publicaciones" de la normativa de desarrollo del R.D. 99/2011 de 28 de enero (BOE 10/02/2011) que regula los estudios universitarios oficiales de postgrado en la Universidad Complutense de Madrid (BOUC nº14 del 21 de diciembre de 2012), y cumpliendo los requisitos para la presentación de Tesis Doctorales en "formato publicaciones" del Programa de Doctorado de Geología e Ingeniería Geológica.

Siguiendo estas directrices, tres de estos artículos se encuentran ya publicados en revistas internacionales incluidas en el *Scientific Citation Index* (SCI), y el cuarto se encuentra en fase de revisión, siendo el autor de esta memoria de Tesis Doctoral el primer firmante en tres de ellos.

Cada uno de los capítulos incluye una introducción en la que se hace una breve revisión del marco científico en el que se inscribe la investigación realizada, una síntesis de la motivación y objetivos,

así como los principales resultados de la investigación. En este punto son pertinentes algunos comentarios previos. Cada uno de los artículos presentados describe los conceptos metodológicos básicos necesarios para la comprensión de la investigación presentada. Además, la disponibilidad de excelentes obras que revisan el estado de conocimientos sobre la dinámica de la litosfera, tanto en inglés (p.ej., Watts, 2001; Stüwe, 2007; Watts, 2007; Artemieva, 2011; Turcotte y Schubert, 2014; Schubert, 2015) como en castellano (p.ej., Martín-Velázquez y De Vicente, 2011), hace totalmente innecesario repetir aquí esa labor de forma detallada. Por otra parte, existen obras generales de gran calidad, tanto en inglés (p.ej., Spohn et al., 2014) como en castellano (p.ej., Anguita y Castilla, 2010), que proporcionan una inmejorable base para la iniciación en el conocimiento de los planetas y satélites del Sistema Solar.

Los resultados obtenidos en la investigación se analizan de una forma global en el capítulo "Discusión y conclusiones". Las referencias citadas en los capítulos de Introducción y objetivos, Discusión y conclusiones, y en las introducciones de los diferentes capítulos temáticos, se han reunido en una lista de bibliografía presentada al final de la memoria.

A continuación se describe brevemente el contenido de cada uno de los capítulos. Como se ha comentado anteriormente, la descripción de la investigación planteada para cada caso concreto se realizará más detalladamente en las correspondientes secciones introductorias de los diferentes capítulos que presentan el trabajo realizado.

En el Capítulo 2 se presenta un estudio que caracteriza el estado térmico y la resistencia de la litosfera en el centro de la península ibérica, abordándose el primero de los objetivos específicos perseguidos en la realización de esta Tesis Doctoral:

> **Jiménez-Díaz, A.**, Ruiz, J., Villaseca, C., Tejero, R., Capote, R. The thermal state and strength of the lithosphere in the Spanish Central System and Tajo Basin from crustal heat production and thermal isostasy. *Journal of Geodynamics* 58, 29-37, 2012.

Uno de los hitos importantes de este trabajo es caracterizar la estructura térmica de la litosfera continental mediante la construcción de geotermas detalladas, explorando los parámetros térmicos implicados y su influencia en los resultados, y la relación entre altitud y estado térmico de la litosfera, conocida como isostasia térmica. Las geotermas detalladas elaboradas son de gran utilidad en el estudio de la reología y estructura mecánica de la litosfera mediante la construcción de perfiles reológicos, que son una manera de evaluar la resistencia de la litosfera en función de la profundidad. De esta manera se consigue una buena aproximación del comportamiento mecánico de la litosfera y de cómo varía verticalmente. También pretende poner de relieve la importancia del conocimiento de la estructura térmica local para deducir las correspondientes propiedades mecánicas y reducir las incertidumbres en las estimaciones de la resistencia de la litosfera, así como analizar las consecuencias que para dichas estimaciones tendría la variación de ciertos parámetros como, por ejemplo, la presión de fluidos en los poros o la tasa de deformación.

El segundo de los objetivos específicos se aborda en los Capítulos 3 y 4, donde se presentan dos artículos que en conjunto suponen una aproximación a la estructura y el comportamiento mecánico

a largo plazo de la litosfera. Un indicador de la resistencia de la litosfera a largo plazo es el espesor elástico efectivo (T_e). El concepto de espesor elástico efectivo, de una enorme utilización en los últimos años, no hace referencia al espesor de una capa real. Por el contrario, se refiere al espesor teórico de una capa elástica de propiedades homogéneas que integra contribuciones de todas las capas de la litosfera (p.ej., Watts y Burov, 2003). Este concepto se relaciona con otras formas de cuantificar las propiedades elásticas de la litosfera considerada como un todo, como puede ser la rigidez flexural, pero se ha impuesto dado que resulta muy intuitivo y fácil de visualizar.

En el Capítulo 3 se presenta un estudio donde se analiza la variación espacial de espesor elástico efectivo en Centroamérica y áreas vecinas:

> **Jiménez-Díaz, A.**, Ruiz, J., Pérez-Gussinyé, M., Kirby, J.F., Álvarez-Gómez, J.A., Tejero, R., Capote, R. Spatial variations of effective elastic thickness of the lithosphere in Central America and surrounding regions. *Earth and Planetary Science Letters* 391, 55-66, 2014.

El objetivo de este trabajo es calcular T_e mediante distintos métodos espectrales a partir de los datos de topografía y gravedad, explorando la elección de los diferentes parámetros que intervienen en cada método y su influencia en los resultados, así como los sesgos y limitaciones de cada uno de los métodos empleados. Además, esta zona representa un gran laboratorio natural para probar la respuesta de los métodos espectrales bajo diferentes factores y condiciones geodinámicas, y examinar las relaciones entre la deformación superficial, la estructura litosférica y la dinámica del manto. Cabe destacar que este estudio constituye el primer y único trabajo de estas características realizado hasta la fecha para esta región.

Por otra parte, el análisis integrado de los datos de topografía y gravedad es una potente herramienta para constreñir aspectos fundamentales sobre la geodinámica de los planetas terrestres, lo que permite "sondear" la estructura y el comportamiento mecánico de sus litosferas, por ejemplo, cómo responden ante cargas y descargas (Wieczorek, 2007; Watts et al., 2013). En particular, un parámetro muy útil que describe este comportamiento es el espesor elástico efectivo de la litosfera, el cual, a su vez, puede ser usado para constreñir la estructura y evolución térmica de un cuerpo planetario (p.ej., Zuber et al., 2000; McGovern et al., 2002; Ruiz et al., 2011).

Siguiendo esta línea de investigación, en el Capítulo 4 se presenta un estudio que aborda el análisis de la estructura litosférica de Venus mediante el cálculo del espesor cortical y el espesor elástico efectivo a partir del análisis de la topografía y la gravedad, con el objetivo de reevaluar la variación regional en la estructura y el comportamiento mecánico de su litosfera:

> **Jiménez-Díaz, A.**, Ruiz, J., Kirby, J.F., Romeo, I., Tejero, R., Capote, R. Lithospheric structure of Venus from gravity and topography. Enviado a *Icarus*, 2014.

Este estudio está concebido desde un punto de vista metodológico como una continuación del anterior, y pretende obtener una visión mucho más amplia del concepto de litosfera, aplicable a cualquier cuerpo planetario.

En el Capítulo 5 se aborda el tercer y último de los objetivos específicos de esta investigación: la reconstrucción de la historia térmica de los planetas terrestres. Uno de los grandes objetivos de las ciencias planetarias es comprender la evolución interna de los planetas y satélites mayores del Sistema Solar, y como ha afectado a las condiciones geológicas en su superficie, a su estructura y grado de diferenciación internos, o al grado y estilo de la actividad volcánica y tectónica. En este contexto, Marte es el objeto del Sistema Solar, aparte de la Tierra, cuyo estudio despierta más interés, dado que es el que presenta (o presentó en el pasado) condiciones ambientales más parecidas a las de nuestro propio planeta, aunque el conocimiento de su historia evolutiva es todavía muy incompleto.

En este capítulo se explorará de nuevo la relación entre la estructura térmica y mecánica de la litosfera, aunque procediendo en orden inverso a lo que se hace en el Capítulo 2: se usarán las propiedades mecánicas de la litosfera para deducir las correspondientes propiedades térmicas, así como ciertos atributos de la corteza. La relación entre temperatura y comportamiento mecánico de las rocas permite calcular el flujo térmico de los cuerpos planetarios a partir de indicadores geológicos de temperatura en profundidad, como el espesor elástico efectivo de la litosfera (McNutt, 1984; Watts y Burov, 2003), o la profundidad de grandes fallas (Schultz y Watters, 2001; Ruiz et al., 2008). Los resultados así obtenidos corresponden a la época en que se formaron las estructuras geológicas usadas como indicador, y por tanto esta aproximación puede potencialmente dar información sobre la evolución térmica de un planeta al ayudar a la caracterización del flujo térmico en distintas épocas (Zuber et al., 2000; McGovern et al., 2002), lo que resulta muy útil en ausencia de medidas directas de flujo térmico. Así, en el artículo que se presenta en este capítulo se calculan, de una manera matemáticamente consistente, paleo flujos térmicos para veintidós regiones de Marte de diferente época y contexto geológico, con el objetivo de constreñir la historia térmica del planeta rojo:

> Ruiz, J., McGovern, P.J., **Jiménez-Díaz, A.**, López, V., Williams, J.P., Hahn, B.C., Tejero, R. The thermal evolution of Mars as constrained by paleo-heat flows. *Icarus* 215, 508-517, 2011.

Finalmente, en el Capítulo 6 se presentan las principales conclusiones obtenidas en esta investigación, discutiendo los resultados de una forma integrada, y se exponen algunas lineas de trabajo futuras.

1.4. Enfoque integrado del estado térmico y mecánico de la litosfera

La investigación que se presenta en los siguientes capítulos pondrá de manifiesto, mediante el estudio de casos concretos, la profunda interrelación que existe entre el estado térmico de la litosfera y la estructura mecánica de la misma, y cómo cada aumento en el conocimiento de uno de estos aspectos puede ser utilizado para mejorar nuestro conocimiento del otro. Cada uno de los trabajos individuales que configuran esta Tesis Doctoral aborda cuestiones y problemas científicos de un gran interés en si mismo, constituyendo por tanto unidades autónomas de investigación que pueden ser analizadas, comprendidas y valoradas independientemente. No obstante, aunque los artículos presen-

tados se ocupan de dominios geodinámicos y problemáticas concretas y diferentes, todos ellos siguen un hilo conductor común, de modo que los resultados obtenidos en los artículos, cuando son tomados conjuntamente, ofrecen una visión más amplia del concepto de litosfera que la que puede encontrarse en cada uno de los artículos individuales, y permite una valoración más global de las aportaciones derivadas del trabajo realizado en esta investigación.

Capítulo 2

Análisis de la estructura térmica y mecánica de la litosfera continental: Estado térmico y resistencia de la litosfera en el centro de la península ibérica

2. Análisis de la estructura térmica y mecánica de la litosfera continental: Estado térmico y resistencia de la litosfera en el centro de la península ibérica

2.1. Introducción

El estado térmico y el comportamiento reológico de la litosfera continental dependen de muchos factores (p.ej., Ranalli y Murphy, 1987; Chapman y Furlong, 1992; Kohlstedt et al., 1995; Ranalli, 1997). Debido a la relación entre estructura térmica y mecánica, es necesario tener un conocimiento adecuado de los parámetros térmicos implicados, del flujo térmico superficial, y de la estructura térmica local para una mejor compresión de la resistencia de la litosfera. Por ejemplo, la cantidad y distribución de fuentes radiogénicas de calor, y el valor de las conductividades térmicas de la corteza y el manto litosférico afectan a estas estimaciones sustancialmente. Por tanto, el comportamiento mecánico y la estratificación reológica de la litosfera en áreas continentales es consecuencia, fundamentalmente, de las condiciones locales (p.ej., Watts y Burov, 2003; Afonso y Ranalli, 2004; Ruiz et al., 2006). Por otro lado, los experimentos de laboratorio más recientes sobre la resistencia de los minerales y rocas característicos de la corteza y el manto muestran un efecto significativo de parámetros como la composición, el tamaño de grano, la anisotropía cristalográfica, la temperatura, la presencia de fluidos, los esfuerzos, la tasa de deformación o la presión sobre sus propiedades reológicas (Bürgmann y Dresen, 2008), y han conducido a la obtención de nuevas leyes que describen el comportamiento mecánico de primer orden de los materiales litosféricos (p.ej., Katayama y Karato, 2008; Mei et al., 2010; Keefner et al., 2011).

El artículo que se presenta en este capítulo se diseñó con una doble finalidad. Por una parte, caracterizar la estructura térmica de la litosfera continental mediante la construcción de geotermas detalladas, explorando los parámetros térmicos implicados y su influencia en los resultados, y la relación entre altitud y estado térmico de la litosfera, conocida como isostasia térmica. También pretende poner de relieve la importancia del conocimiento de la estructura térmica local para deducir las correspondientes propiedades mecánicas y reducir las incertidumbres en las estimaciones de la resistencia de la litosfera, así como analizar las consecuencias que para dichas estimaciones tendría la variación de parámetros como, por ejemplo, la presión de fluidos en los poros o la tasa de deformación. Por otra parte, dentro de este contexto de análisis, pretende caracterizar el estado térmico y la resistencia de la litosfera en el centro de la península ibérica.

Para ello, se han utilizado valores refinados de las tasas de producción radiogénica de calor a partir de la abundancia de Uranio, Torio y Potasio (denominados HPE por sus siglas en inglés: *heat-*

producing elements) en los diferentes materiales de la zona de estudio (incluyendo xenolitos representativos de la corteza inferior; Villaseca et al., 1998, 1999, 2005; este estudio) que, junto con el uso de modelos de isostasia térmica, han permitido obtener geotermas detalladas y valores de flujo térmico superficial en el área de estudio. Además, se ha implementado una conductividad térmica dependiente de la temperatura (apropiada para el olivino; McKenzie et al., 2005) para el manto litosférico con el objetivo de constreñir el perfil de temperatura en esas condiciones. Por otra parte, gracias a la relación entre reología de la litosfera y flujo térmico, y junto con la implementación de una nueva ley reológica para la parte superior del manto litosférico (Mei et al., 2010), se han obtenido estimaciones refinadas de la resistencia y del espesor elástico efectivo (T_e) de la litosfera (derivadas de los perfiles de resistencia en función de la profundidad obtenidos), teniendo en cuenta la contribución de la corteza y el manto litosférico, y reologías tanto secas como húmedas. Finalmente, se comparan los resultados con los obtenidos por trabajos previos, y también se examina el posible efecto de la variación de la presión de fluidos en los poros o la tasa de deformación en las estimaciones de resistencia litosférica.

Respecto al estado térmico de la litosfera en el centro de la península ibérica, se han obtenido valores de flujo térmico superficial de 84 mW m^{-2} y 82 mW m^{-2} para el Sistema Central y Cuenca del Tajo, respectivamente. Además, se han obtenido temperaturas de 700 ºC y 630-650 ºC en el límite corteza-manto (Moho), así como flujos térmicos mantélicos de 24 mW m^{-2} y 26 mW m^{-2}, bajo el Sistema Central y Cuenca del Tajo, respectivamente. Las estimaciones de resistencia litosférica varían dentro de la zona de estudio, obteniéndose los valores máximos en el norte de la Cuenca del Tajo, y los valores mínimos asociados al Sistema Central, claro reflejo de que la litosfera en esta región está algo más caliente. Los perfiles de resistencia muestran variaciones en la profundidad de la transición frágil-dúctil en función de las reologías y del régimen de esfuerzos considerado, y para todos los casos, el Moho representa una importante discontinuidad mecánica entre la corteza inferior y la parte superior del manto litosférico. Por último, se han obtenido valores de espesor elástico efectivo de 16-28 km en el Sistema Central, y de 20-34 km y 17-30 km, respectivamente, en el norte y sur de la Cuenca del Tajo, en función de las reologías secas y húmedas, consistentes con el rango de valores obtenidos en estudios previos.

2.2. The thermal state and strength of the lithosphere in the Spanish Central System and Tajo Basin from crustal heat production and thermal isostasy

Alberto Jiménez-Díaz [a,b], Javier Ruiz [a], Carlos Villaseca [b,c], Rosa Tejero [a,b], Ramón Capote [a]

[a] *Departamento de Geodinámica, Facultad de Ciencias Geológicas, Universidad Complutense de Madrid. 28040 Madrid, Spain*

[b] *Instituto de Geociencias, IGEO (CSIC, UCM). 28040 Madrid, Spain*

[c] *Departamento de Petrología y Geoquímica, Facultad de Ciencias Geológicas, Universidad Complutense de Madrid. 28040 Madrid, Spain*

Journal of Geodynamics 58, 29-37, 2012.

Abstract

Here we have modeled the thermal structure of the lithosphere of the Spanish Central System and the Tajo Basin, and their implications for lithospheric strength. For this, we have used refined heat-producing elements (HPE) values to obtain new estimates of heat production rates in the Spanish Central System and Tajo Basin areas, which have been used joined to the relation between topography and thermal structure of the lithosphere to calculate the best-fit surface heat flows in the study area. Moreover, we have implemented a temperature-dependent thermal conductivity (appropriate for olivine) for the lithospheric mantle to improve the calculations of temperature profiles in the mantle. The geotherms so obtained, together with the implementation of a new rheological law for the upper lithospheric mantle, have been used to calculate refined estimations of the strength and effective elastic thickness of the lithosphere. We have obtained surface heat flow values of 84 mW m^{-2} and ~82 mW m^{-2} for the Spanish Central System and the Tajo Basin, respectively. The thermal state of the lithosphere affects mantle temperatures, and hence may be playing an important role in the uplift and maintenance of the Spanish Central System.

2.2.1. Introduction

The thermal state and the rheological behavior of the continental lithosphere depend on many factors (e.g., Afonso and Ranalli, 2004; Chapman and Furlong, 1992; Kohlstedt et al., 1995; Ranalli, 1997; Ranalli and Murphy, 1987). Due to the relationship between thermal and mechanical structure of the lithosphere, it is necessary to have an adequate knowledge of the thermal parameters, local heat flow and thermal structure, to reduce the uncertainty in strength estimates. For example, the amount and distribution of lithospheric heat-producing elements (HPE) and the values of the thermal conductivities of crust and mantle may affect the results substantially. Thus, the mechanical behavior and rheological stratification of the lithosphere in continental areas are largely a consequence of local

conditions (e.g., Afonso and Ranalli, 2004; Furlong and Chapman, 1987; Ruiz et al., 2006; Watts and Burov, 2003). On the other hand, recent laboratory experiments conducted under controlled microstructural and chemical conditions have shown a significant effect of important parameters on the rheological properties of major silicate rocks (Bürgmann and Dresen, 2008), and have yielded new rheological laws describing the first-order mechanical behavior of the lithospheric materials (e.g., Katayama and Karato, 2008; Keefner et al., 2011; Mei et al., 2010).

The aim of this work is to model the thermal structure and their implications for lithospheric strength of the Spanish Central System (SCS) and the Tajo Basin (TB). The SCS constitutes the most prominent topographic elevation in the interior of the Iberian Peninsula separating the Duero and Tajo watersheds. It is flanked by two Cenozoic intracontinental sedimentary basins, the Duero Basin to the north and the TB to the south (Fig. 2.1). The SCS is a thick-skinned double-vergence (pop-up) intraplate range built as a result of polyphase Alpine tectonic evolution (De Vicente and Vegas, 2009; De Vicente et al., 2004, 2007, 2009; Fernández-Lozano et al., 2011; Martín-Velázquez et al., 2009), in which the deformation partitioning of the basement in the intraplate convergence setting of Iberia has had a profound influence on the development of topography.

The surface heat flow map of the Iberian Peninsula performed by Fernández et al. (1998) provides some values at the SCS-TB boundary and the north and south of the TB. In contrast, the SCS is not well characterized due to the unavailability of heat flow measurement, and it is necessary to approach the study of the thermal state of the range through other methodologies. In this sense, Tejero and Ruiz (2002) modeled the thermal structure of the lithosphere of this area by using thermal isostasy to improve the calculated geotherms, considering surface heat flow values of 70 and 65-70 mW m^{-2} for the SCS and the TB, respectively.

On the other hand, several works have focused on characterizing the lithospheric strength from estimating the effective elastic thickness of the lithosphere through flexure modeling (Van Wees et al., 1996), the coherence between topography and Bouguer anomaly (Gómez-Ortiz et al., 2005a; Pérez-Gussinyé and Watts, 2005) or from rheological models (Martín-Velázquez et al., 2008; Ruiz et al., 2006; Tejero and Ruiz, 2002; Tesauro et al., 2007, 2009).

In the present work, we have used the relation between topography and thermal structure to calculate the best-fit surface heat flows. We included a temperature-dependent thermal conductivity (appropriate for olivine) for the lithospheric mantle to improve the calculations. Moreover, we have used refined HPE values based on bulk rock composition of main lithological formations of the SCS and the Toledo Mountains (e.g. Villaseca et al., 1998, 1999, 2005; this study), and these values have been used to obtain estimates of heat production rates. Finally, we have used our result for the thermal structure in order to analyze the strength of the lithosphere in the study area. To make this, we have implemented a new rheological law for the upper lithospheric mantle, largely controlled by low-temperature plasticity of olivine-rich rocks (Mei et al., 2010). All of this provides an opportunity to refine existing thermal and rheological models and lithospheric strength determinations of the study area.

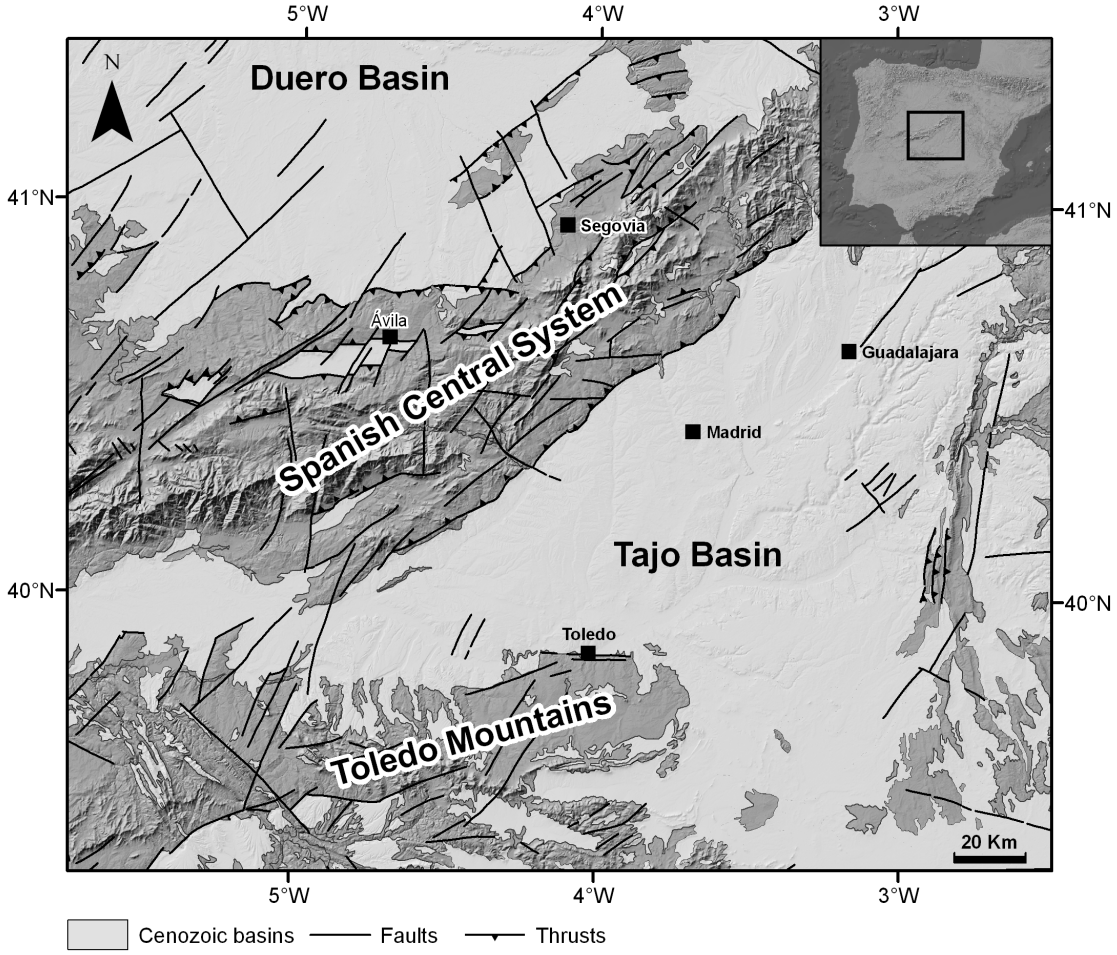

Figure 2.1: Geographical and geological settings of the study area showing the two mountains ranges (Spanish Central System and Toledo Mountains) separated by the Tajo Basin. Map background is from the Neotectonic Map of Spain (IGME and ENRESA, 1998).

2.2.2. Temperature profiles

The thermal structure of the lithosphere depends on heat flow, heat sources distribution and thermal conductivity of lithospheric rocks. The temperature profile within the lithosphere has been calculated assuming steady-state conditions and radioactive heat sources homogeneously distributed in three crustal layers and in the lithospheric mantle. The temperature at depth z in each crust layer is

$$T_z = T_s + \frac{F_s z}{k} - \frac{H z^2}{2k}, \tag{2.1}$$

where T_s and F_s are the temperature and heat flow at the layer top, k is the thermal conductivity, and H is the volumetric heat production rate. The calculations assume k = 2.5, 2.5 and 2.1 W m^{-1} K^{-1} for upper, middle and lower crust, respectively, and the surface temperature was taken as 288 K.

The thermal conductivity of olivine (the main mineral in the mantle) is strongly temperature-dependent; therefore temperature profiles in the mantle lithosphere are calculated from (see Ruiz et

al., 2011)

$$\frac{dT}{dz} = \frac{F_{cb} - \rho_m H_m (z - b_c)}{k_m(T)}, \tag{2.2}$$

where $F_{cb} = F - \rho_c H_c b_c$ is the heat flow at the base of the crust, ρ_m and H_m are, respectively, the density and heat production rate per mass unity of the mantle lithosphere, b_c is the base of the crust, and k_m is the thermal conductivity of the mantle lithosphere. For k_m we use the thermal conductivity of olivine, which is a function of temperature according to the expression (McKenzie et al., 2005)

$$k_m = \frac{a}{1 + c(T - 273)} + \sum_{i=0}^{3} d_i T^i, \tag{2.3}$$

where a = 5.3, c = 0.0015, d_0 = 1.753 x 10^{-2}, d_1 = -1.0364 x 10^{-4}, d_2 = 2.2451 x 10^{-7} and d_3 = -3.4071 x 10^{-11}. Results obtained from Equation (2.3) are similar to those of Hofmeister (1999) for forsterite olivine. For solving equations (2.2) and (2.3), we used the Newton iterative method.

Moreover, the use of concept of thermal isostasy is useful in order to constrain continental temperature profiles (e.g., Fernández et al., 1998; Hasterok and Chapman, 2007, 2011; Lachenbruch and Morgan, 1990; Tejero and Ruiz, 2002), by providing a link between the thermal structure of the lithosphere and the elevation of the surface. Elevation above sea level (e) can be expressed by

$$e = h_c + h_m - h_o, \tag{2.4}$$

where h_c and h_m are the individual contributions of crust and mantle components to the buoyancy of the lithosphere. h_o is the buoyant height of sea level above the free asthenosphere surface ($h_o \approx 2.4$ km; Lachenbruch and Morgan, 1990). Crust contribution is estimated from

$$h_c = \frac{1}{\rho_a}(\rho_a - \rho_c) b_c, \tag{2.5}$$

where b_c is crust thickness, ρ_c is mean crust density and ρ_a is asthenosphere density (3200 kg m^{-3}). Mantle contribution is related to the thermal state of the lithosphere mantle by

$$h_m = \alpha(\bar{T}_m - T_a) b_m, \tag{2.6}$$

where α is the thermal volumetric expansion coefficient (3.5 x 10^{-5} K^{-1}), b_m is the thickness of the lithospheric mantle until the asthenosphere temperature T_a, assumed to be the isotherm of 1350 ºC, and $\bar{T}_m$ is the mean lithosphere mantle temperature given by

$$\bar{T}_m = \frac{1}{b_m} \int_0^{b_m} T(z) dz, \tag{2.7}$$

which we use here in order to determine the depth of the lithospere-asthenosphere boundary (*LAB*). Here we use crustal structure and composition derived from seismic data (Banda et al., 1981; ILIHA DSS Group, 1993; Suriñach and Vegas, 1988), and crustal density derived from gravity data analysis (Gómez-Ortiz et al., 2005b). Mantle heat flow was estimated by subtracting crustal contribution from surface heat flow. We applied the thermal isostasy model by iterative calculation to fit the calculated elevation to the observed mean elevation ($\sim$1250 m and $\sim$650 m for SCS and TB, respectively). Table 2.1 summarizes the parameters used in the calculations.

	Thickness (km)	Thermal conductivity (W m^{-1} K^{-1})	Heat production (μW m^{-3})	Density (kg m^{-3})	A (MPa^{-n} s^{-1})	Q (kJ mol^{-1})	n
Spanish Central System							
Upper crust (dry granite)	11	2.5	2.45	2670	1.8×10^{-9}	123	3.2
Upper crust (wet granite)					2.0×10^{-4}	137	1.9
Middle crust (quarzdiorite)	14	2.5	1.75	2800	1.3×10^{-3}	219	2.4
Lower crust (felsic granulite)	9	2.1	0.96	2900	8.0×10^{-3}	243	3.1
Tajo Basin							
Sediments layer	2/1[a]	2.5	2.40	2400	6.7×10^{-6}	156	2.4
Upper crust (dry quarzite)	12/13[a]	2.5	2.36	2780	6.7×10^{-6}	156	2.4
Upper crust (wet quarzite)					3.2×10^{-4}	154	2.3
Middle crust (quarzdiorite)	9	2.5	1.65	2800	1.3×10^{-3}	219	2.4
Lower crust (felsic granulite)	8	2.1	0.96	2900	8.0×10^{-3}	243	3.1

[a] Thickness for north/south Tajo Basin, respectively.

Table 2.1: Parameters used to construct the geotherms and strength envelopes. Crustal structure and composition derived from seismic data (Banda et al., 1981; ILIHA DSS Group, 1993; Suriñach and Vegas, 1988), crustal density derived from gravity data analysis (Gómez-Ortiz et al., 2005b) and rheological parameters from Ranalli (1997).

2.2.3. Crustal heat production

Uranium, Thorium and Potassium (collectively termed as heat-producing elements, HPE) abundance determines heat production rates of crustal rocks. Thus, heat production is calculated from HPE abundance by the addition of the contribution of each element as follows (Rybach, 1988)

$$H(\mu W m^{-3}) = 10^{-5}\rho(9.52C_U + 2.56C_{Th} + 3.48C_K), \tag{2.8}$$

where C_U and C_{Th} are in ppm and C_K in percent, and ρ is the density (in kg m^{-3}). This method has been used to estimate heat production rates of the crust of Central Iberia (Spain), where 196 samples of metamorphic and igneous rocks of Variscan basement were collected and their content on HPE determined. They represent main outcropping lithologies mostly orthogeneiss and granites. Furthermore, granulite xenoliths carried by Upper Permian alkaline lamprophyres have been interpreted as samples of the lower crust below the SCS (Villaseca et al., 1999). Table 2.2 summarizes HPE abundances collected from 196 sites covering the Spanish Central System and the Toledo Mountains.

HPE abundances and heat production values for the SCS complex comprises outcropping metamorphic rocks mostly of two types: metasedimentary sequences and felsic orthogneissic rocks. These Cambrian-Lower Ordovician metaigneous rocks are the dominant country rocks, and they show higher heat production rates than metasedimentary types because they are enriched in U and K (Table 2.2). Metabasic rocks have been also described in the SCS, but defining a very minor surface; regional geologic maps suggest that felsic orthogneisses constitute approximately the 80% of the metamorphic rock exposures at least in his eastern half sector. Otherwise, most of the SCS is occupied by a huge granitic batolith. Proportions determined by mapped lithologies suggest that granites might be 75% of the SCS. The SCS Variscan granites are characterized by an averaged heat production of 2.49 μW

	Area (%)	Numbers of samples	U (ppm)	Th (ppm)	K (%)	H (μW m^{-3})
Spanish Central System						
Metamorphic rocks						
Metabasites	<0.1	6	1.37	5.70	0.54	0.86
Metapelites	20	8	2.65	14.82	2.76	2.00
Metagranites	80	41	4.61	12.25	3.69	2.42
Granitic rocks						
Monzogranites	85	25	3.07	15.63	3.72	2.22
Leucogranites	15	31	8.61	21.23	3.83	4.04
LC Granulite Xenoliths						
Charnockites	<1	4	1.18	2.61	1.87	0.69
Pelites	5	6	0.78	9.14	2.32	1.21
Metaigneous	95	17	0.70	6.54	2.55	0.95
Toledo Mountains						
Metasediments	55	5	3.66	10.97	2.63	1.98
Granites	35	42	6.38	14.76	3.55	2.99
ACT Migmatites	10	11	3.39	12.88	4.97	2.27

Table 2.2: Estimates of heat production of rocks from the Spanish Central System and Toledo Mountains.

m^{-3} (pondered by granite type and area, Table 2.2), higher values than those of orthogneissic wall-rocks. This approach yields an averaged heat production value of 2.45 μW m^{-3} for the outcropping SCS rocks (Figure 2.2).

In the south, Toledo Mountains is also comprised by metamorphic rocks intruded by Variscan granite plutons. Country rocks are dominated by Neoproterozoic-Low Palaeozoic metasedimentary sequences (the Schist-Greywacke Complex), most of low-grade metamorphism (San José et al., 1990). The estimated average heat production rate of 2.36 μW m^{-3} (Table 2.2 and Fig. 2.2) for the whole Toledo Mountains area is lower than that obtained for the whole granite-high-grade metamorphic complex of the SCS, mostly due to the lower abundance of granites in the Toledo Mountains area (Table 2.2). HPE abundances for Tajo sedimentary rocks are not available, although representative heat production rates can be estimated from the surrounding orogenic areas as their sedimentary source regions (averaged heat production of 2.40 μW m^{-3}; Table 2.1).

The averaged heat production rate of the lower crust is estimated to be 0.96 μW m^{-3}; value slightly lower than preliminary estimates (Villaseca et al., 2005), but clearly higher than values usually considered for the lower crust (Furlong and Chapman, 1987; Hasterok and Chapman, 2011; Rudnick and Gao, 2003; Vilá et al., 2010). This is a consequence of the markedly felsic composition of the SCS lower crust, dominated by felsic meta-igneous (95 vol%) and pelitic (5 vol%) granulites (Villaseca et al., 1999). The felsic nature of the SCS lower crust is best shown in comparison with other lower-crustal xenoliths suites which, on average, are more mafic than granulite terranes (Villaseca et al., 1999 and references therein).

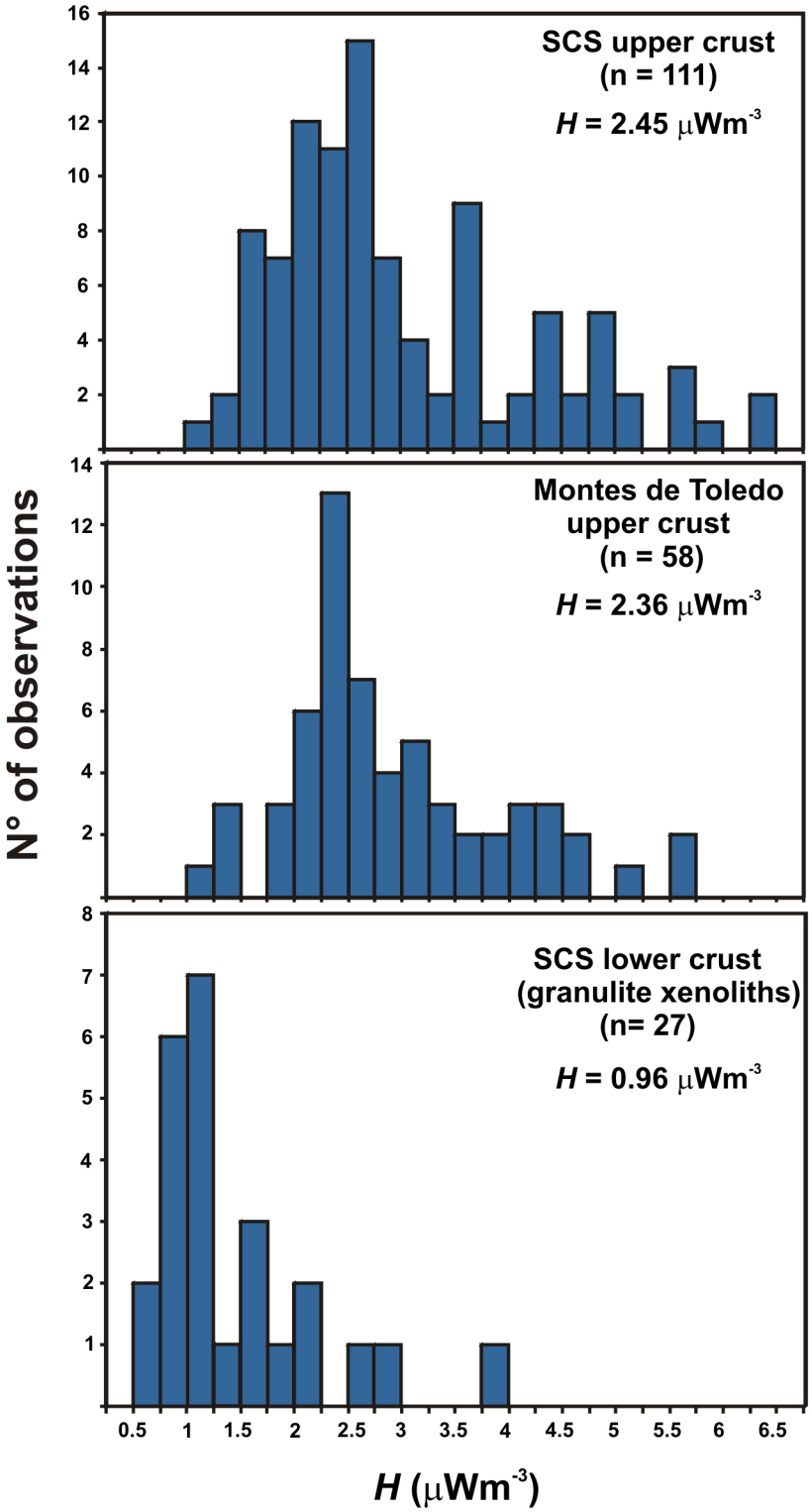

Figure 2.2: Estimates of heat production rates of rocks from the Spanish Central System upper crust, Toledo Mountains upper crust and Spanish Central System lower crustal granulite xenoliths.

Heat production of the middle crust is not well characterized due to the unavailability of direct measurement, and thus, there is considerable uncertainty with regard to this parameter. The mid-crustal layer is not pervasive globally, and where it exists, tends to have radiogenic heat generation more similar to lower rather than to upper crust (Hasterok and Chapman, 2011 and references therein). On the other hand, the middle crust of the area is made of intrusive felsic materials (Villaseca et al., 1999) similar to those forming the upper crust in many continental areas, and seismic velocities findings point to a granodioritic composition of the middle crust (Banda et al., 1981). Unknown of the depth distribution of rocks compelled us to consider layer homogeneity, and we have assumed an intermediate (density weighted) heat production rate between upper and lower crust. Finally, for the lithospheric mantle we use a standard heat production rate of 0.02 μW m^{-3} (e.g., Chapman and Furlong, 1992; Hasterok and Chapman, 2011).

2.2.4. Strength of the lithosphere

The concept of strength envelopes is useful to illustrate a first-order approximation of the rheological properties of lithosphere (e.g., Brace and Kohlstedt, 1980; Kohlstedt et al., 1995; Ranalli, 1997; Ranalli and Murphy, 1987). Thus, the strength of the lithosphere at any depth is the minimum between the strengths for brittle and ductile deformation. Assuming a prefractured medium with fractures ideally oriented, the brittle strength, $(\sigma_1 - \sigma_3)_b$, is calculated according to the expression (e.g., Ranalli, 1997; Ranalli and Murphy, 1987)

$$(\sigma_1 - \sigma_3)_b = \beta \rho g (1 - \lambda) z, \tag{2.9}$$

where β is a coefficient depending on the stress regime (0.75 for tension and 3 for compression), ρ is the density, g is the acceleration due to the gravity (9.8 m s^{-2}), λ is the pore fluid factor defined as the ratio of pore fluid pressure to lithostatic pressure (Sibson, 1974), and z the depth. The density of the brittle crust, adequate for rocks in the upper crust, is taken as 2670 kg m^{-3} for the SCS and 2780 kg m^{-3} for the TB (Gómez-Ortiz et al., 2005b). In addition, a sedimentary layer is considered in the TB (Table 2.1). We use the same hydrostatic pore fluid factor (λ = 0.37) for the whole lithosphere.

The ductile strength, $(\sigma_1 - \sigma_3)_d$, does not depend on the stress regime but it is strongly strain rate- and temperature-dependent (Burov and Diament, 1995; Ranalli and Murphy, 1987; Stüwe, 2002), and can be described by a thermally activated power law,

$$(\sigma_1 - \sigma_3)_d = \left(\frac{\dot{e}}{A}\right)^{1/n} exp\left(\frac{Q}{nRT}\right), \tag{2.10}$$

where $\dot{e}$ is the strain rate, A, Q, and n are laboratory-determined constants, R is the gas constant (8.31447 J mol^{-1} K^{-1}), and T is the absolute temperature. Strength envelopes are calculated for a strain rate of 10^{-15} s^{-1}.

The ductile strength of the upper crust is calculated using flow laws for wet/dry granite and wet/dry quartzite for the SCS and TB, respectively. The lower crust of the central Iberian Peninsula is of a

felsic granulite nature (Villaseca et al., 1999), and bearing in mind its flow law it should not appreciably contribute to the strength of the lithosphere. It is therefore not taken into account in the present work (see Tejero and Ruiz, 2002; Ruiz et al., 2006). In turn, the middle crust of the area is made of intrusive felsic materials (Villaseca et al., 1999) similar to those forming the upper crust in many continental areas; its mechanical behavior is therefore likely to be similar (Ruiz et al., 2006).

For the estimation of the strength of the lithospheric mantle we use dry and wet olivine rheologies, which give upper and lower limits, respectively. The behavior of the upper lithospheric mantle is in turn largely controlled by low-temperature plasticity of olivine-rich rocks (Mei et al., 2010), resulting in a rheology significantly weaker than that usually used for the lithosphere mantle. Under anhydrous conditions, Mei et al. (2010) define a flow law for a quasi steady state deformation of olivine under low-temperature and high-stress, which can be written in terms of differential stress as

$$(\sigma_1 - \sigma_3) = \left(\frac{\dot{e}}{A_p}\right)^{1/2} exp\left[\frac{E_k(0)}{2RT}\left(1 - \sqrt{\frac{(\sigma_1 - \sigma_3)}{\sigma_p}}\right)\right], \tag{2.11}$$

where A_p = 1.4 x 10^{-7} s^{-1} MPa^{-2}, $E_k(0)$ is the zero-stress activation energy (320 ± 50 kJ mol^{-1}), and σ_p is Peierls stress (5.9 ± 0.2 GPa). Thus, for dry olivine we use the minimum strength obtained from equation (2.11) and from the high temperature flow law obtained for artificially dried dunites: A = 28840 MPa^{-n} s^{-1}, n = 3.6 and Q = 535 kJ mol^{-1} (Chopra and Paterson, 1984). For wet olivine, we use the flow law of the Anita Bay dunite: A = 9550 MPa^{-n} s^{-1}, n = 3.35 and Q = 444 kJ mol^{-1} (Chopra and Paterson, 1984). This flow law places a lower limit on the strength of wet olivine due to its relative weakness (compared with other wet dunites, such as Aheim dunite).

Finally, the total lithospheric strength (Ranalli, 1997) can be defined as

$$S = \int_0^{b_L} (\sigma_1 - \sigma_3)(z)dz, \tag{2.12}$$

where $(\sigma_1 - \sigma_3)$ is the minor, at z depth, between the brittle and ductile strength, and b_L is the mechanical thickness of the lithosphere. The base of the mechanical lithosphere is here defined as the depth at which the ductile strength reaches a low value of 10 MPa (McNutt, 1984; Ranalli, 1994), and below which there are no further significant increases in strength, although the exact value selected does not produce significant changes in the calculations due to the exponential dependence of ductile strength on temperature. Table 2.1 summarizes the rheological model parameters.

2.2.5. Results

2.2.5.1. Thermal modeling

Figure 2.3 shows the geotherms obtained by our thermal model. For the SCS, we have obtained a value of F_s = 84 mW m^{-2}, with elevation adjustment of ± 1 m (Table 2.3 and Fig. 2.3). For the north and south TB, we have obtained values of F_s = 81 mW m^{-2} and F_s = 83 mW m^{-2} respectively, with elevation adjustment of ± 2 m in both cases (Table 2.3 and Fig. 2.3). We have calculated the

surface heat flow from the thermal isostasy model obtaining through iterative calculation the surface heat flow best-fitting the observed mean elevation. In this sense, a heat flow uncertainty of $\pm$ 0.1 mW m^{-2} and $\pm$ 0.01 mW m^{-2} results in an elevation uncertainty of $\pm$ 10 m and $\pm$ 2 m, respectively.

At the crust-mantle boundary (*Moho*) under the SCS, we have obtained a temperature of 700°C and a mantle heat flow of 24 mW m^{-2}. For the north and south TB, at Moho depth, the temperature decreases to 630°C and to 650°C, and the mantle heat flow increases to 25 mW m^{-2} and to 27 mW m^{-2}, respectively. The lithosphere–asthenosphere boundary (*LAB*) is located at 99 km in the SCS and at 100 km and 95 km in the north and south TB, respectively.

The differences between the coldest geotherm (North TB) and the hottest geotherm (SCS) remain almost constant, and even show a certain convergence of the curves in depth, indicating an effective lateral homogenization of the temperature in the sublithospheric mantle. Table 2.3 summarizes the values of the thermal models obtained in this study.

	Surface heat flow (mW m^{-2})	Mantle heat flow (mW m^{-2})	*Moho* temperature (ºC)	Thermal lithospheric thickness (km)
Spanish Central System	84	24	700	98
Tajo Basin (North)	81	25	630	100
Tajo Basin (South)	83	27	650	95

Table 2.3: Summary of values obtained from thermal modeling.

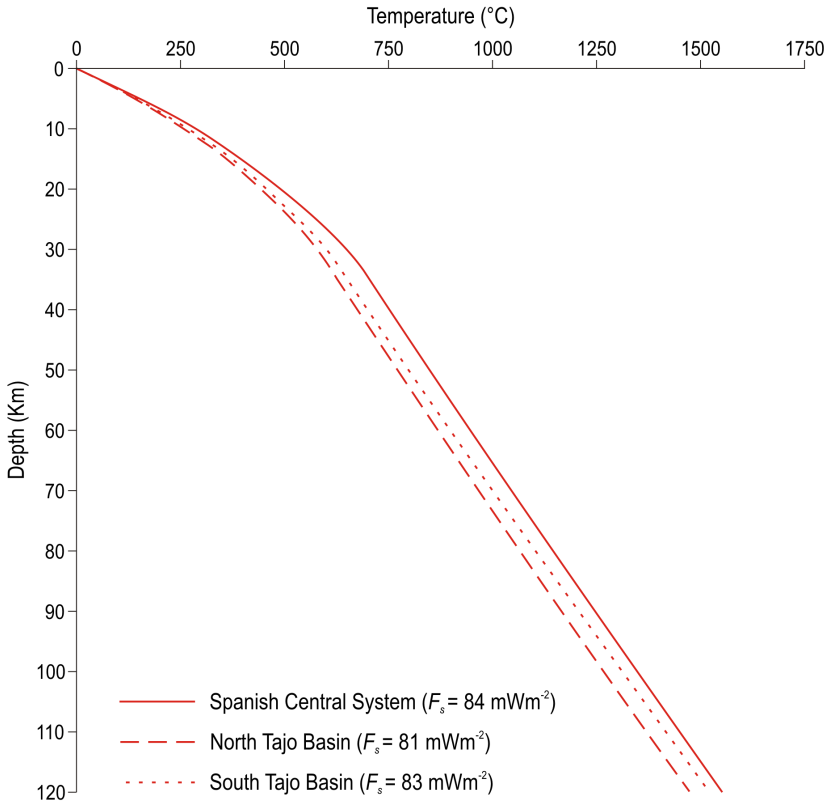

Figure 2.3: Geotherm constructed for the Spanish Central System and the Tajo Basin. Variables used in estimations are provided in Table 2.1. See text for details.

2.2.5.2. Mechanical structure and strength envelopes

Strength envelopes for the study area have been constructed using the geotherms presented in the previous section. For the SCS, two crustal brittle-ductile transitions (BDT) appear under tensional stress (Fig. 2.4), the upper BDT within the upper crust at a depth between 6 and 7 km, depending on rheology, while the lower BDT is found in the middle crust at depth of 13 km. On the other hand, under compression stress, the upper BDT depth is between 5 and 6 km, but there is no BDT in the middle crust. In the case of the TB, a BDT appears within the upper crust but there is no BDT in the middle crust (Fig. 2.4). Under tensional stress, BDT is located at a depth between 6 and 10 km, depending on rheology. Under compression stress, BDT depth is between 5 and 8 km, depending on rheology. The lithospheric mantle remained in the ductile field for a wet peridotite rheology for the whole area (Fig. 2.4). For dry peridotite and tensional stresses, only the north TB presents a brittle portion in the lithospheric mantle with a BDT depth of $\sim$32 km. Under compression conditions, the entire lithospheric mantle presents ductile behavior. Finally, all the strength envelopes show that the Moho always represents a strong mechanical discontinuity between the lower crust and the uppermost lithospheric mantle (Fig. 2.4).

Figure 2.5 shows total lithospheric strength for compressional and tensional stresses and, in each case, for dry and wet rheologies. Total strength ranges from $\sim$8.2 x 10^{12} to $\sim$1.2 x 10^{12} N m^{-1}. In general, higher total lithospheric strengths are associated with the north TB, while minimum values corresponded to the SCS. These values are consistent with mean integrated strength values estimated under compressional conditions by Tesauro et al. (2009) for the continental lithosphere in Iberia. In the same way, the contribution of the lithospheric mantle to the total lithospheric strength ranges from $\sim$7 x 10^{12} to $\sim$2 x 10^{11} N m^{-1}. These values are consistent with the wavelengths ($<$250 km) of the lithospheric folds, which suggests low mean mantle strength values ($<10^{13}$ N m^{-1}; Sokoutis et al., 2005), proposed by Muñoz-Martín et al. (2010) from the spectral analysis of the gravity and elevation for continental lithosphere at the Africa–Eurasia boundary.

Our results can also be interpreted in terms of the effective elastic thickness of the lithosphere (T_e), a measure of the total strength of the lithosphere which integrates the contributions from brittle and ductile layers and from elastic cores of the lithosphere (for a review see Watts and Burov, 2003). We have calculated T_e from the strength envelopes constructed for the SCS and the TB. Following Burov and Diament (1995), the total effective elastic thickness of an unflexed plate constituted by n detached layers is

$$T_e = \left(\sum_{i=1}^{n} t_{ei}^3 \right)^{1/3}, \tag{2.13}$$

where t_{ei} is the mechanical thickness of the layer i. We take the base of each mechanical layer as the depth in which the strength goes down to a value of 10 MPa (see above). If strength levels at the base layer are higher than 10 MPa, the layer is considered welded to the layer below. The calculations were performed for both wet and dry rheology. For the SCS, the results are 16 km for wet rheology and 28 km for dry rheology. For the north and south TB, the obtained values are 17-20 and 30-34 km

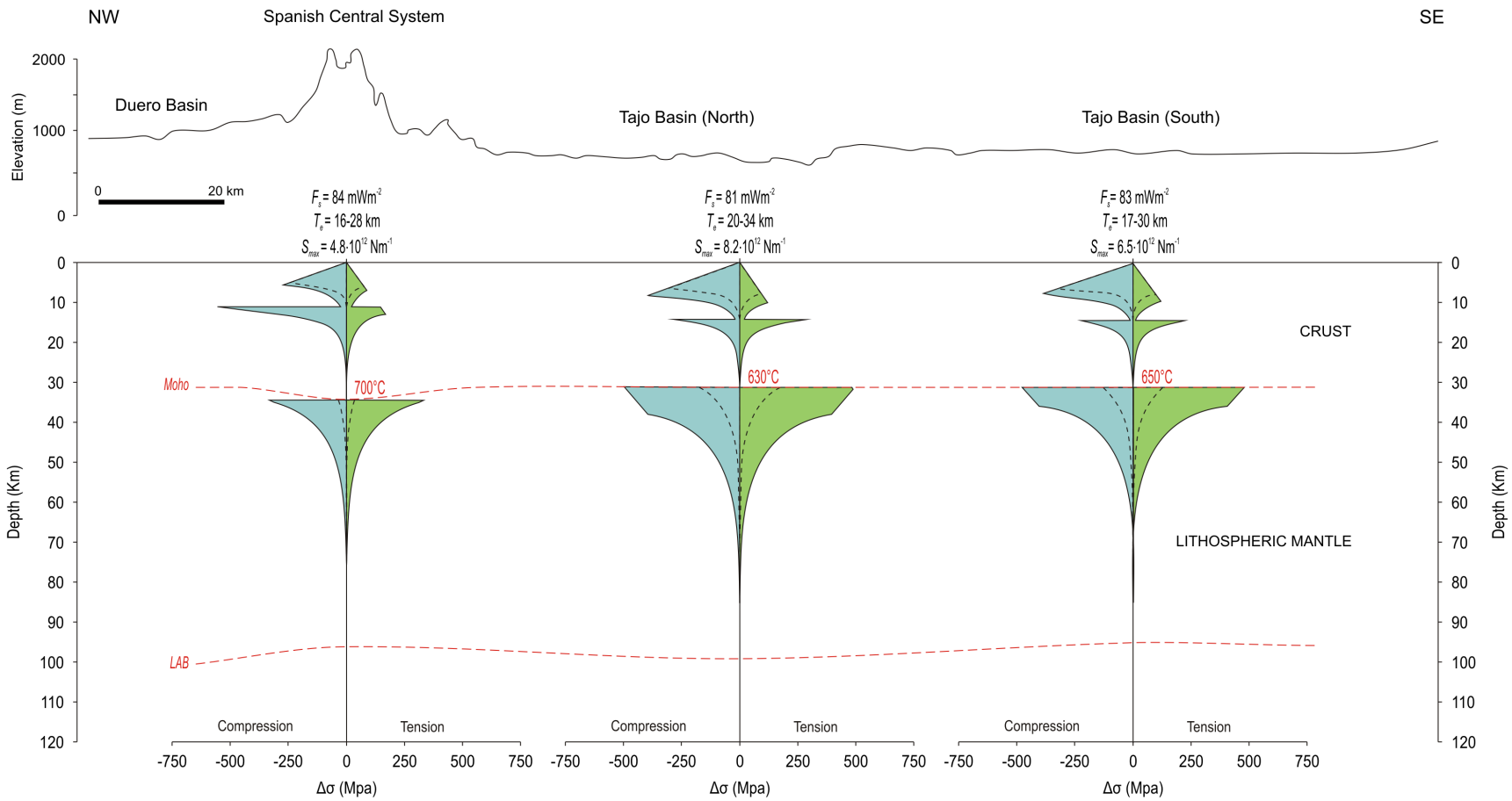

Figure 2.4: Results of thermal models and strength envelopes, calculated for a strain rate of 10^{-15} s^{-1}, plotted along a NW-SE transverse section of the area. Outer black line binds differential stress estimated for dry rock composition. Inner dashed line denotes differential stress for wet rock composition of the upper crust (quartzite or granite) and lithospheric mantle (peridotite). F_s: Surface heat flow. T_e: Effective elastic thickness for wet/dry rheology. *Smax*: Maximum total lithospheric strength. *Moho*: crust-mantle boundary. *LAB*: lithosphere-asthenosphere boundary.

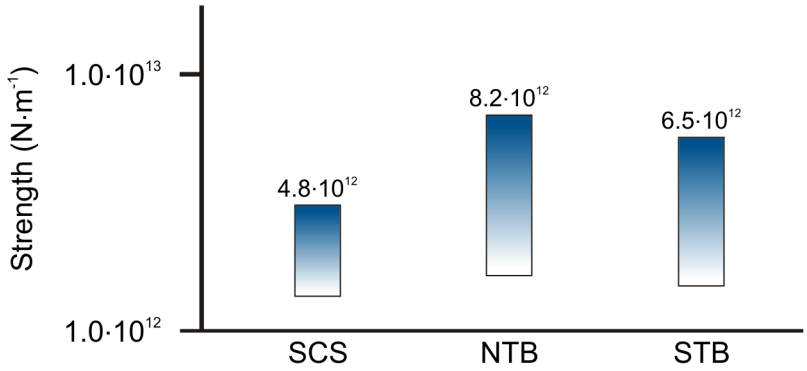

Figure 2.5: Total lithospheric strength values for dry and wet rocks in compression and tension plotted for the different tectonic units. Higher strength values were obtained for dry rheology and compressive differential stress. Minimum strength values correspond to wet rheology and tensional differential stress.

for wet and dry rheology, respectively. The lower values for the SCS are greatly resulting from the weaker upper mantle in this zone, which has a more limited contribution to the total strength of the lithosphere.

The effective elastic thickness depends on the thermal state of the lithosphere, which determines the thickness and contribution of mechanically competent layers, and on the local curvature of the plate (which in turn depends on the rheological structure and distribution of the external loads applied to the plate; e.g., Burov and Watts, 2006; Watts and Burov, 2003). Since curvature reduces the bending moment of the lithosphere, assuming an unflexed lithosphere our values of T_e (obtained for dry rheology, which represent the maximum strength) can be considered upper limits.

Several works have focused on characterizing the lithospheric strength in the study area from estimating the effective elastic thickness of the lithosphere following different procedures (Fig. 2.6). Van Wees et al. (1996) calculated a value of T_e of 7 km for the TB through flexure modeling, Gómez-Ortiz et al. (2005a) obtained values of 14–21 km for the central Iberian Peninsula from the coherence between topography and Bouguer anomaly, and Pérez-Gussinyé and Watts (2005) obtained best-fits of 15-30 km for the Iberian peninsula also from Bouguer coherence (but with the method of the free-air admittance these authors obtained higher T_e values). Ruiz et al. (2006) used the relationship between rheology of the lithosphere and heat flow to calculate theoretical T_e values of 18-20 km for the TB and 15-18 km for the SCS. The map of effective elastic thickness of the European lithosphere performed by Tesauro et al. (2007) shows an increase from 5-10 km in the SCS to 35 km within the basin. Tesauro et al. (2007) assumed an unflexed lithosphere, so their values of T_e actually are upper limits as our results. For the TB, there is good correspondence between the values obtained by these authors and our results. Although for the case of SCS we obtain higher T_e values. Finally, Martín-Velázquez et al. (2008), by means of a finite elements model, obtained an elastic thickness of 24 km for the SCS and 23-25 km for the TB.

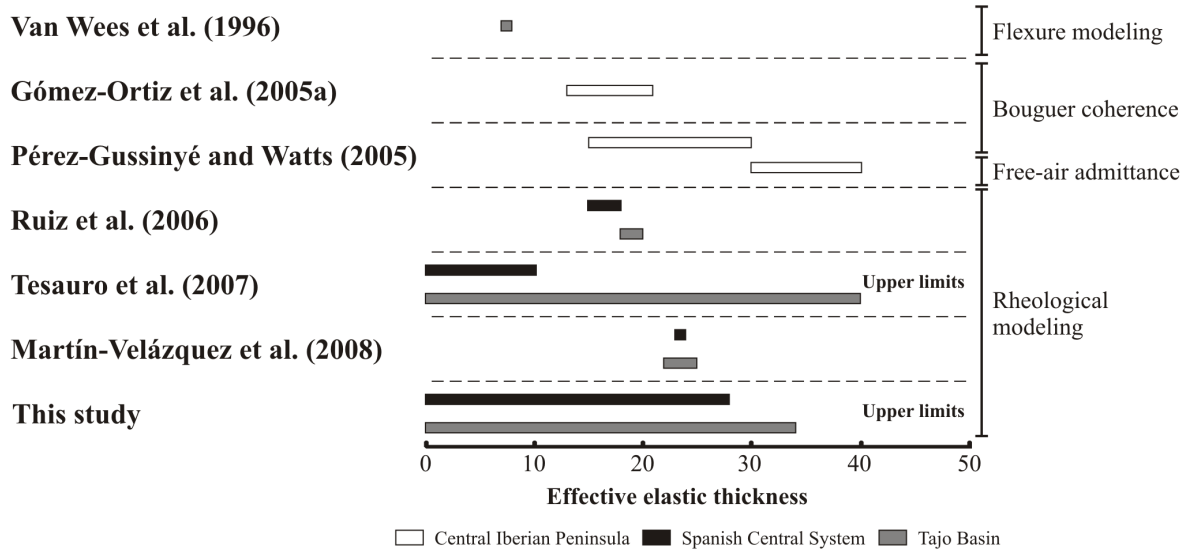

Figure 2.6: Compilation of effective elastic thickness values obtained for the study area.

2.2.6. Discussion and Conclusions

In the present work we have used refined HPE values to obtain new estimates of heat production rates in the SCS and TB areas, which have been used joined to the relation between topography and thermal structure of the lithosphere to calculate the best-fit surface heat flows in the study area (see section 2.2.2 and 2.2.3). Moreover, we have implemented a temperature-dependent thermal conductivity (appropriate for olivine) for the lithospheric mantle to improve the calculations of temperature profiles in the mantle. The main influence of these procedures is that higher surface heat flows are needed to achieve similar temperatures at Moho depth, and small variations in surface heat flow have great influence on the temperature distribution within the lithosphere. The geotherms so obtained, together with the implementation of a new rheological law for the upper lithospheric mantle (see section 2.2.4), have been used to calculate refined estimations of the strength and effective elastic thickness of the lithosphere. Thus, our results refine the thermo-mechanical models and lithospheric strength determinations for the study area.

Surface heat flow obtained for the north TB show good agreement with measurements of Fernández et al. (1998), which fall within the range between 62 and 94 mW m^{-2} with a mean value of 77 $\pm$ 5 mW m^{-2} (n = 6). In contrast, the south TB presents values of surface heat flow clearly higher than the observed range of values in that region (with a mean value of 48 $\pm$ 7 mW m^{-2} for n = 6, Fernández et al., 1998). This difference may be due to local effects. Surface heat flow determinations for the south TB were carried out on water, geothermal and mining explorations wells (Fernández et al., 1998). These wells can be affected by thermal disturbances due to water circulation (Marzán et al., 1996). In the south TB, geothermal gradient values observed are scattered, and the thermal regime may be affected by surface water flow in porous levels and hydraulic connection between aquifers through the well (Marzán et al., 1996). Moreover, an average of 48 mW m^{-2} leads to an increase of the total lithospheric strength ($S \approx 1$ x 10^{15} N m^{-1}), and effective elastic thickness ($T_e \approx$ 150 km), much higher

than any previous estimates for the Central Iberian Peninsula (see Section 2.2.5.2).

Some authors use the mean value (and sometimes the median value) for the heat production rate in their models (e.g., Hasterok and Chapman, 2011). A heat production rate weighted by the areal distribution characterizes better our crust model that a purely statistical value, where less abundant rocks, but with higher sampling, would have greater weight in the calculations (see Table 2.2). We also consider a heat production rate weighted by the areal distribution more correct, therefore considering a radioactive heat sources homogeneously distributed. To check the influence on the results of our models, we have considered the effect of using mode values without taking into account the areal distribution of samples in order to study the model response. These slightly higher estimates of heat production rates (2.6 μW m^{-3} for the upper crust, and 1.1 μW m^{-3} for the lower crust), leads to an average increase of 4 mW m^{-2} in the surface heat flow, 20ºC of the temperature at the crust-mantle boundary (*Moho*), and enlarge 1 km in the thermal lithospheric thickness. In turn, the mantle heat flow is reduced by 1 mW m^{-2}. This change in the thermal state, results in a decrease in 1 km of the T_e, and a reduction over 10-20% of the total lithospheric strength, depending on the stress regime. Thus, we consider our results robust.

In the case of the SCS, the crustal thickening (especially of the lower crust, which has a relatively high content of HPE; see section 2.2.3), may be an important factor in its thermal structure. This thickening can be translated into a lithospheric mantle with a minor contribution in the calculation of surface heat flow, but proportionally hotter. So, the HPE-enriched and hot lower crust could reduce the heat loss from the lithospheric mantle. Recently, Boschi et al. (2010) and Faccenna and Becker (2010) have proposed the existence of a vigorous mantle upwelling in the western Mediterranean (from southern Iberia to the French Massif Central), based on interpreting residual topography (after correcting by isostasy) as dynamical topography due to mantle flow. In their models, the mantle upwelling would be driven by density variations caused by temperature differences derived from seismic tomography. However, thermal insulation of the upper mantle due to an HPE-enriched lower crust might be an important factor by contributing to mantle high temperatures. This state, together with an important contribution from crustal shortening and thickening, erosion during the endorheic–exorheic drainage transition, and lithospheric folding process (Casas-Sainz and De Vicente, 2009; De Vicente and Vegas, 2009; De Vicente et al., 2007, 2011; Fernández-Lozano et al., 2011) may be playing an important role in the uplift and maintenance of the SCS.

Moreover, the implementation of a new rheological law related to behavior of dry olivine in lithospheric conditions (see Section 2.2.4) results in a lithospheric mantle significantly weaker, with a consequent reduction of its contribution to the total effective strength. In the TB, the lithospheric mantle has a large contribution to the strength and the effective elastic thickness of the lithosphere. Consequently the strength of the mantle top would be in clear contrast with that of the weaker lower crust. Otherwise, the lithospheric mantle under the SCS is significantly weaker, clear reflection of its thermal state.

One non-well determined factor is the pore pressure. For crustal rocks, a hydrostatic pore fluid factor (equal to a column of water of height z) is usually assumed. In the absence of information per-

taining to high temperature regimes and greater depths, the pore fluid factor is usually taken uniform for the whole lithosphere (e.g., Afonso and Ranalli, 2004; Mahatsente et al., 2012; Tesauro et al., 2009). In this study, the pore pressure is assumed as 0.37 (see section 2.2.4). Previous works have assumed a hydrostatic pore fluid factor for the study area, ranging from 0.36 to 0.4 (Ruiz et al., 2006; Tejero and Ruiz, 2002; Tesauro et al., 2009). This range leads to a variation of the total lithospheric strength over 1-4% depending on stress regimen. In addition, if an increase of the pore fluid factor to values of 0.6 and 0.8 is considered in order to simulate the presence of super-hydrostatic pressures, leads to a decrease of the total lithospheric strength over 15-25% and 40-50% depending on stress regimen, respectively. This pattern is similar to that observed by Tesauro et al. (2009). It must be noted that pore fluid pressure reduces brittle strength, and hence increases temperature at the BDT depth (Ruiz et al., 2011).

On the other hand, the ductile strength is largely strain rate dependent. As in previous works (e.g., Martín-Velázquez et al., 2008; Ruiz et al., 2006; Tejero and Ruiz, 2002), our strength envelopes are here calculated for a strain rate of 10^{-15} s^{-1}, but other authors consider a value of 10^{-16} s^{-1} as a characteristic strain rate value for intraplate Europe (Tesauro et al., 2007). Figure 2.7 shows the effective elastic thickness calculated for the SCS and TB in terms of strain rate. If we considered a strain rate of 10^{-16} s^{-1}, the results are 12-22 km and 14-28 km respectively for the SCS and the TB (depending on wet or dry rheology). Other of the main uncertainties could be due to not considering the effect of the horizontal regional stresses, which could have a strong effect on the T_e (Cloetingh and Burov, 1996).

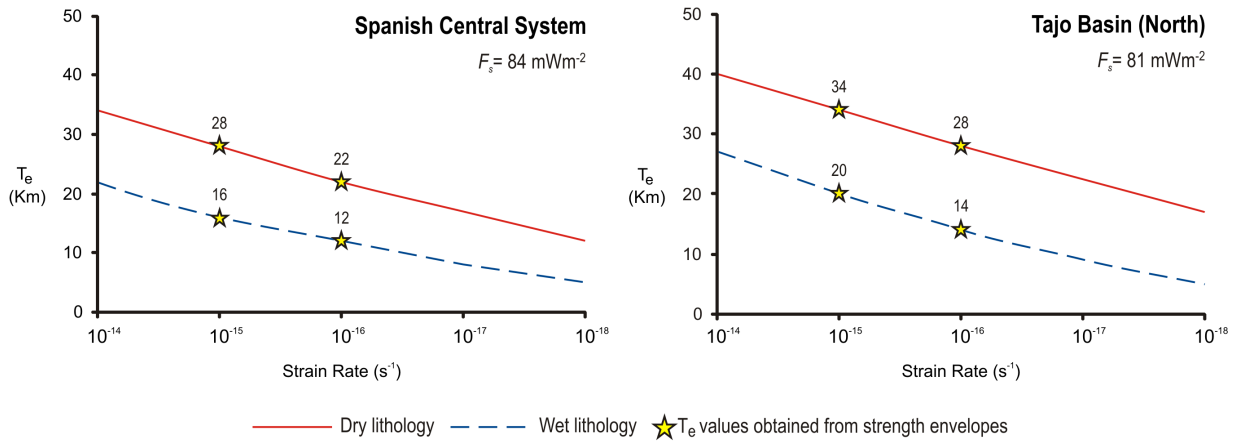

Figure 2.7: Effective elastic thickness, in terms of strain rate, in the Spanish Central System and Tajo Basin (North). Dry and wet rheologies for the crust and mantle are used in the calculation.

Finally, future investigations should also consider other important influences on the rheological properties of major silicate rocks. For example, oxygen fugacity under anhydrous conditions (Keefner et al., 2011) or water fugacity under water-saturated conditions (Katayama and Karato, 2008) could significantly affect upper mantle rheology. This kind of consideration further will constrain the mechanical behavior of lithospheric materials, and their implications for the thermal and mechanical state of the lithosphere.

Acknowledgments

The authors would like to thank the Editor Randell Stephenson and two anonymous reviewers for their comprehensive revision and comments, which were of great help in the preparation of the final version of this paper. We also thank Giorgio Ranalli and Alfonso Muñoz Martín for their useful comments and suggestions that helped to improve the manuscript and Viazmelya Monroy for her assistance with the English language of this article. AJ-D was supported by a grant of the Complutense University of Madrid (Spain). JR was supported by a contract Ramón y Cajal cofinanced from the Ministerio de Ciencia e Innovación of Spain and the Fondo Social Europeo (ESF). This work was carried out in the projects CGL2008-03463, CGL2008-05952 and CGL2009-14405-C02-02 of the Ministerio de Ciencia e Innovación of Spain and the GR35/10-A-910492-UCM.

References

Afonso, J.C., Ranalli, G., 2004. Crustal and mantle strengths in continental lithosphere: is the jelly sandwich model obsolete? Tectonophysics 394, 221–232.

Banda, E., Suriñach, E., Aparicio, A., Sierra, J., Ruiz de la Parte, E., 1981. Crust and upper mantle structure of the central Iberian Meseta (Spain). Geophys. J. Int. 67, 779–789.

Boschi, L., Faccenna, C., Becker, T.W., 2010. Mantle structure and dynamic topography in the Mediterranean Basin. Geophys. Res. Lett. 37, L20303.

Brace, W.F., Kohlstedt, D.L., 1980. Limits on lithospheric stress imposed by laboratory experiments. J. Geophys. Res. 94, 3967–3990.

Bürgmann, R., Dresen, G., 2008. Rheology of the lower crust and upper mantle: evidence from rock mechanics, geodesy, and filed observations. Annu. Rev. Earth Planet. Sci. 36, 531–567.

Burov, E.B., Diament, M., 1995. The effective elastic thickness of (Te) continental lithosphere. What does it really means? J. Geophys. Res. 100 (B3), 3905–3927.

Burov, E.B., Watts, A.B., 2006. The long-term strength of continental lithosphere: jelly sandwich or crème brûlée? GSA Today 16 (1), 4–10.

Casas-Sainz, A.M., De Vicente, G., 2009. On the tectonic origin of Iberian topography. Tectonophysics 474, 214–235.

Chapman, D.S., Furlong, K.P., 1992. Thermal state of continental lower crust. In: Fountain, D.M., Arculus, R., Kay, R.W. (Eds.), Continental Lower Crust. Elsevier Science, Amsterdam, pp. 179–199.

Chopra, P.N., Paterson, M.S., 1984. The role of water in the deformation of dunite. J. Geophys. Res. 89, 7861–7876.

Cloetingh, S.E.B., Burov, E.B., 1996. Thermomechanical structure of European continental lithosphere: constraints from rheological profiles and EET estimates. Geophys. J. Int. 124, 695–723.

De Vicente, G., Cloetingh, S., Van Wees, J.-D., Cunha, P.P., 2011. Tectonic classification of Cenozoic Iberian foreland basins. Tectonophysics 502, 38–61.

De Vicente, G., Vegas, R., Munoz-Martín, A., Van Wees, J.D., Casas-Sáinz, A., Sopena, A., Sánchez-Moya, Y., Arche, A., López-Gómez, J., Olaiz, A., Fernández-Lozano, J., 2009. Oblique strain partitioning and transpression on an inverted rift The Castilian Branch of the Iberian Chain. Tectonophysics 470, 224–242.

De Vicente, G., Vegas, R., 2009. Large-scale distributed deformation controlled topography along the western Africa–Eurasia limit: tectonic constrains. Tectonophysics 474, 124–143.

De Vicente, G., Vegas, R., Munoz Martín, A., González-Casado, J.M., Carbó, A., Álvarez, J., Cloetingh, S., Andriessen, P., Elorza, F.J., Olaiz, A., 2004. Estructura alpina del Antepaís Ibérico. Cadenas sin cobertera. El Sistema Central. In: Vera, J.A. (Ed.), Geología de Espana. SGE-IGME, Madrid, pp. 621–626.

De Vicente, G., Vegas, R., Munoz Martín, A., Silva, P.G., Andriessen, P., Cloetingh, S., González Casado, J.M., Van Wees, J.D., Álvarez, J., Carbó, A., Olaiz, A., 2007. Cenozoic thick-skinned deformation and topography evolution of the Spanish Central System. Global Planet. Change 58, 335–338.

Faccenna, C., Becker, T.W., 2010. Shaping mobile belts by smallscale convection. Nature 465, 602–605.

Fernàndez, M., Marzám, I., Correia, A., Ramalho, E., 1998. Heat flow, heat production, and lithospheric thermal regime in the Iberian Peninsula. Tectonophysics 291, 29–53.

Fernández-Lozano, J., Sokoutis, D., Willingshofer, E., Cloetingh, S., De Vicente, G., 2011. Cenozoic deformation of Iberia: a model for intraplate mountain build- ing and basin development based on analogue modeling. Tectonics 30, TC1001.

Furlong, K.P., Chapman, D.S., 1987. Crustal heterogeneities and the thermal structure of the continental crust. Geophys. Res. Lett. 14, 314–317.

Gómez-Ortiz, D., Tejero, R., Ruiz, J., Babín-Vich, R., González-Casado, J.M., 2005a. Estimating the effective elastic thickness of the Iberian Peninsula's lithosphere based on multitaper spectral analysis. Geophys. J. Int. 160, 729–735.

Gómez-Ortiz, D., Tejero-López, R., Babín-Vich, R., Rivas-Ponce, A., 2005b. Crustal density structure in the Spanish Central System derived from gravity data analysis (central Spain). Tectonophysics 403, 131–149.

Hasterok, D., Chapman, D., 2007. Continental thermal isostasy. I: methods and sensitivity. J. Geophys. Res. 11, 2, doi:10.1029/2006JB004663.

Hasterok, D., Chapman, D., 2011. Heat production and geotherms for the continental lithosphere. Earth Planet. Sci. Lett., doi:10.1016/j.epsl.2011.04.034.

Hofmeister, A.M., 1999. Mantle values of thermal conductivity and the geotherm from phonon lifetimes. Science 283, 1699–1706.

IGME-ENRESA, 1998. Neotectonic Map of Spain Sc: 1/1.000.000 (J. Baena, Coord.). Madrid, Spain.

ILIHA DSS Group, 1993. A deep seismic sounding investigation of the lithospheric heterogeneity and anisotropy beneath the Iberian Peninsula. Tectonophysics 221, 35–51.

Katayama, I., Karato, S.-I., 2008. Low-temperature, high-stress deformation of olivine under water-saturated conditions. Phys. Earth Planet. Inter. 168, 125–133.

Keefner, J.W., Mackwell, S.J., Kohlstedt, D.L., Heidelbach, F., 2011. Dependence of dislocation creep of dunite on oxygen fugacity: implications for viscosity variations in Earth's mantle. J. Geophys. Res. 116, B05201.

Kohlstedt, D.L., Evans, B., Mackwell, S.J., 1995. Strength of the lithosphere: constraints imposed by laboratory experiments. J. Geophys. Res. 100, 17587–17602.

Lachenbruch, A.H., Morgan, P., 1990. Continental extension, magmatism and elevation; formal relations and rules of thumb. Tectonophysics 174, 39–62.

Mahatsente, R., Ranalli, G., Bolte, D., Götze, H.-J., 2012. On the relation between lithospheric strength and ridge push transmission in the Nazca plate. J. Geodyn. 53, 18–26.

Martín-Velázquez, S., De Vicente, G., Elorza, F.J., 2008. Resistencia, espesor elástico efectivo y deformación de la litosfera Ibérica (Sistema Central y cuencas del Duero y Tajo). Geo-Temas 10, 1523–1526.

Martín-Velázquez, S., De Vicente, G., Elorza, F.J., 2009. Intraplate stress state from finite element modelling: the southern border of the Spanish Central System. Tectonophysics 473, 417–427.

Marzán, I., Fernández, M., Cabal, J., 1996. Estudio geotérmico en la mitad Occidental de Espana. Geogaceta 20, 745–748.

McKenzie, D., Jackson, J., Priestley, K., 2005. Thermal structure of oceanic and continental lithosphere. Earth Planet. Sci. Lett. 233, 337–349.

McNutt, M.K., 1984. Lithospheric flexure and thermal anomalies. J. Geophys. Res. 89, 11180–11194.

Mei, S., Suzuki, A.M., Kohlstedt, D.L., Dixon, N.A., Durham, W.B., 2010. Experimental constraints on the strength of the lithospheric mantle. J. Geophys. Res. 115, B08204.

Munoz-Martín, A., De Vicente, G., Fernandez-Lozano, J., Cloetingh, S., Willingshofer, E., Sokoutis, D., Beekman, F., 2010. Spectral analysis of the gravity and elevation along the western Africa–Eurasia plate tectonic limit: continental versus oceanic lithospheric folding signals. Tectonophysics 495, 298–314.

Pérez-Gussinyé, M., Watts, A.B., 2005. The long-term strength of Europe and its implications for plate-forming processes. Nature 436, doi:10.1038/nature03854.

Ranalli, G., 1994. Nonlinear flexure and equivalent mechanical thickness of the lithosphere. Tectonophysics 240, 107–114.

Ranalli, G., 1997. Rheology of the lithosphere in space and time. Geol. Soc. Spec. Pub. 121, 19–37.

Ranalli, G., Murphy, D.C., 1987. Rheological stratification of the lithosphere. Tectonophysics 132, 281–295.

Rudnick, R.L., Gao, S., 2003. Composition of the continental crust. In: Rudnick, R.L. (Ed.), The Crust (In: Holland, H.D., Turekian, K.K.(Eds.), Vol. 3 Treatise of Geochemistry. Elsevier-Pergamon, Oxford, pp. 1–64.

Ruiz, J., Gómez-Ortiz, D., Tejero, R., 2006. Effective elastic thicknesses of the lithosphere in the Central Iberian Peninsula from heat flow: implications for the rheology of the continental lithospheric mantle. J. Geodyn. 41, 500–509.

Ruiz, J., McGovern, P.J., Jiménez-Díaz, A., López, V., Williams, J.-P., Hahn, B.C., Tejero, R., 2011. The thermal evolution of Mars as constrained by paleo-heat flows. Icarus 215, 508–517.

Rybach, L., 1988. Determination of heat production rate. In: Haenel, R., Rybach, L., Stegena, L. (Eds.), Handbook of Terrestrian Heat-flow Density Determination. Kluwer, pp. 125–142.

San José, M.A., Pieren, A., García-Hidalgo, J.F., Vilas, L., Herranz, P., Peláez, J.R., Perejón, A., 1990. Ante-Ordovician Stratigraphy. Authocthonous sequences of Central-Iberian Zone. In: Dallmayer, R.D., Martínez-García, E. (Eds.), Pre-Mesozoic Geology of Iberia. Springer-Verlag, Berlín, pp. 145–159.

Sibson, R.H., 1974. Frictional constraints on thrust, wrench and normal faults. Nature 249, 542–544.

Sokoutis, D., Burg, J.P., Bonini, M., Corti, G., Cloetingh, S., 2005. Lithospheric-scale structures from the perspective of analogue continental collision. Tectonophysics 406, 1–15.

Stüwe, K., 2002. Geodynamics of the Lithosphere. An Introduction. Springer-Verlag, Berlin, p. 449.

Surinach, E., Vegas, R., 1988. Lateral inhomogeneities of the Hercyninan crust in central Spain. Phys. Earth Planet. Inter. 51, 226–234.

Tejero, R., Ruiz, J., 2002. Thermal and mechanical structure of the central Iberian Peninsula lithosphere. Tectonophysics 350, 49–62.

Tesauro, M., Kaban, M.K., Cloetingh, S., 2009. A new thermal and rheological model of the European lithosphere. Tectonophysics 476, 478–495.

Tesauro, M., Kaban, M.K., Cloetingh, S., Hardebol, N.J., Beekman, F., 2007. 3D strength and gravity anomalies of the European lithosphere. Earth Planet. Sci. Lett. 263, 56–73.

Van Wees, J.D., Cloetingh, S., de Vicente, G., 1996. The role of pre-existing faults in basin evolution: constraints from 2D finite element and 3D flexure models. Geol. Soc. Spec. Pub. 99, 297–320.

Vilà, M., Fernández, M., Jiménez-Munt, I., 2010. Radiogenic heat production variability of some common lithological groups and its significance to lithospheric thermal modeling. Tectonophysics 490, 152–164.

Villaseca, C., Barbero, L., Rogers, G., 1998. Crustal origin of Hercynian peraluminous granitic batholiths of Central Spain: petrological, geochemical and isotopic (Sr, Nd) constraints. Lithos 43, 55–79.

Villaseca, C., Downes, H., Pin, C., Barbero, L., 1999. Nature and composition of the lower continental crust in central Spain and the granulite–granite linkage: inferences from granulitic xenoliths. J. Petrol. 40, 1465–1496.

Villaseca, C., Orejana, D., Pérez-Soba, C., Reyes, J., 2005. Estimación del régimen térmico y producción de calor de los niveles litosféricos del Sistema Central Espanol. Geogaceta 38, 215–218.

Watts, A.B., Burov, E.B., 2003. Lithospheric strength and its relation to the elastic and seismogenetic layer thickness. Earth Planet. Sci. Lett. 213, 113–131.

Capítulo 3

Estimación del espesor elástico efectivo de la litosfera mediante métodos espectrales: Resistencia de la litosfera en Centroamérica y las regiones circundantes

3. Estimación del espesor elástico efectivo de la litosfera mediante métodos espectrales: Resistencia de la litosfera en Centroamérica y las regiones circundantes

3.1. Introducción

Conocer la variación lateral de la resistencia de la litosfera puede ayudar a comprender cómo la deformación superficial está relacionada con los procesos geodinámicos profundos. Como indicador de la resistencia de la litosfera a largo plazo, el espesor elástico efectivo (T_e) se puede utilizar para entender la relación entre la reología de la litosfera y la evolución geodinámica de ambientes tectónicos complejos (p.ej., Burov y Diament, 1995; Watts, 2001).

El artículo que se presenta en este capítulo aborda el cálculo de T_e mediante distintos métodos espectrales, explorando la elección de los diferentes parámetros que intervienen en cada método y su influencia en los resultados, así como los sesgos y limitaciones de cada uno de los métodos empleados (análisis ampliamente recogido en el material suplementario asociado a este artículo). Para este análisis se ha elegido Centroamérica y las regiones circundantes como área de estudio.

La región de Centroamérica-Caribe se caracteriza por la interacción de seis placas litosféricas. La placa de Caribe deriva hacia el Este en relación a sus dos placas vecinas, las placas de Norte y Suramérica (DeMets et al., 2010), y su perímetro se caracteriza por una alta complejidad y variabilidad de procesos tectónicos y geodinámicos (p.ej., Sykes et al., 1982; Ross y Scotese, 1988). Por lo tanto, esta zona representa un gran laboratorio natural para estudiar las variaciones espaciales de T_e, probar la respuesta de los métodos espectrales bajo diferentes factores y condiciones geodinámicas, y examinar las relaciones entre la deformación superficial, la estructura litosférica y la dinámica del manto.

En este artículo se presentan, por primera vez, mapas de alta resolución de las variaciones espaciales de T_e en Centroamérica y regiones circundantes, obtenidos a partir del análisis de la coherencia entre la topografía y la gravedad (anomalía de Bouguer) por medio de dos métodos espectrales (conocidos por sus nombres en inglés como los métodos *Multitaper* y *Wavelet*, respectivamente). También se examinan las relaciones entre T_e y otros observables de la estructura litosférica y sub-litosférica, con el objetivo de mejorar nuestro conocimiento de la reología y el comportamiento mecánico de la litosfera a largo plazo en la zona de estudio. Finalmente, se discute cómo la estructura litosférica derivada del análisis de T_e se relaciona con la deformación superficial observada.

Los resultados muestran que, independientemente de las diferencias técnicas entre los dos métodos, hay una gran correspondencia en la variación espacial de T_e recuperada por ambos. Aunque los valores absolutos de T_e pueden variar en los mapas obtenidos por ambos procedimientos, la estructura cualitativa y la ubicación de sus principales gradientes son muy similares, de modo que la estimación de T_e es relativamente insensible a la elección del método espectral usado. El patrón de las variaciones de T_e en Centroamérica y regiones circundantes concuerda bien con las provincias tectónicas de la región, y está estrechamente relacionada con los principales límites tectónicos. Las zonas de subducción Mesoamericana y de las Antillas Menores se caracterizan por una banda de altos valores de T_e en la placa subducente previos a la fosa. Estos altos valores de T_e están relacionados con el dominio de cargas internas (y en el caso del extremo meridional de la zona de subducción de las Antillas Menores, también se asocian con la presencia de una gran cantidad de sedimentos), y deben ser interpretados con cautela. Por otra parte, hay una buena correlación, a pesar de algunas incertidumbres, entre el flujo térmico superficial y los resultados de T_e en el área de estudio. Estos resultados sugieren que aunque esta región es geológicamente muy compleja, el estado térmico de la litosfera tiene una profunda influencia en su comportamiento mecánico, de manera que el espesor elástico efectivo de la misma está fuertemente controlado por la estructura térmica.

3.2. Spatial variations of effective elastic thickness of the lithosphere in Central America and surrounding regions

Alberto Jiménez-Díaz [a,b], Javier Ruiz [a], Marta Pérez-Gussinyé [c], Jon F. Kirby [d],

José A. Álvarez-Gómez [a], Rosa Tejero [a,b], Ramón Capote [a]

[a] *Departamento de Geodinámica, Facultad de Ciencias Geológicas, Universidad Complutense de Madrid. 28040 Madrid, Spain*

[b] *Instituto de Geociencias, IGEO (CSIC, UCM). 28040 Madrid, Spain*

[c] *Department of Earth Sciences, Royal Holloway, University of London, Egham Hill, TW20 0EX Egham, United Kingdom*

[d] *Department of Spatial Sciences, Curtin University, GPO Box U1987, Perth WA 6845, Australia*

Earth and Planetary Science Letters 391, 55-66, 2014.

Abstract

As a proxy for long-term lithospheric strength, the effective elastic thickness (T_e) can be used to understand the relationship between lithospheric rheology and geodynamic evolution of complex tectonic settings. Here we present, for the first time, high-resolution maps of spatial variations of T_e in Central America and surrounding regions from the analysis of the coherence between topography and Bouguer gravity anomaly using multitaper and wavelet methods. Regardless of the technical differences between the two methods, there is a good overall agreement in the spatial variations of T_e recovered from both methods. Although absolute T_e values can vary in both maps, the qualitative T_e structure and location of the main T_e gradients are very similar. The pattern of the T_e variations in Central America and surrounding regions agrees well with the tectonic provinces in the region, and it is closely related to major tectonic boundaries, where the Middle American and Lesser Antilles subduction zones are characterized by a band of high T_e on the downgoing slab seaward of the trenches. These high T_e values are related to internal loads (and in the case of the southernmost tip of the Lesser Antilles subduction zone also associated with a large amount of sediments) and should be interpreted with caution. Finally, there is a relatively good correlation, despite some uncertainties, between surface heat flow and our T_e results for the study area. These results suggest that although this area is geologically complex, the thermal state of the lithosphere has profound influence on its strength, such that T_e is strongly governed by thermal structure.

3.2.1. Introduction

The knowledge of lateral variations in lithosphere strength can aid in understanding how surface deformation relates to deep Earth processes. As a proxy for long-term lithospheric strength, the

effective elastic thickness of the lithosphere (T_e) corresponds to the thickness of an idealized elastic plate bending under the same applied loads (Watts, 2001), and is related to the integrated mechanical strength of the lithosphere (Burov and Diament, 1995). The knowledge of T_e in different places provides a measurement of the spatial variation of the lithospheric strength, which is strongly controlled by local and regional conditions. Although T_e does not represent an actual depth to the base of the mechanical lithosphere, its spatial variations reflect relative lateral variations in lithospheric mechanical thickness (see McNutt, 1984). Thus it can be used to understand the relationship between lithospheric rheology and geodynamic evolution of complex tectonic settings.

T_e primarily depends on the thickness and structure of the crust, the composition of the crust and the lithospheric mantle, the degree of their coupling, the thermal state of the lithosphere, the state of stress, plate curvature, and the presence of melts, fluids and faults (e.g., Lowry and Smith, 1995; Burov and Diament, 1995; Lowry et al., 2000; Watts, 2001; Artemieva, 2011). The oceanic lithosphere generally behaves like a single mechanical layer due to the thin crust, which is usually coupled to the lithospheric mantle, and T_e is to first order controlled by the thermal age of the lithosphere at the time of loading (Watts, 2001; Kalnins and Watts, 2009). By contrast, the thermal state and rheological behavior of the lithosphere in continental areas are largely a consequence of local conditions (e.g., Ranalli, 1997; Afonso and Ranalli, 2004; Bürgmann and Dresen, 2008; Hasterok and Chapman, 2011; Mareschal and Jaupart, 2013), such that there is a complex relationship between T_e and its controlling parameters (Watts and Burov, 2003; Burov and Watts, 2006; Burov, 2011).

In this study we present, for the first time, high-resolution maps of spatial variations of T_e in Central America and surrounding regions from the analysis of the Bouguer coherence using both multitaper and wavelet methods. The Central America-Caribbean region is characterized by the interaction of six lithospheric plates (Fig. 3.1). The Caribbean plate moves eastward relative to its two neighboring plates, North and South America plates (DeMets et al., 2010), and its perimeter is characterized by a high variability and complexity of geodynamic and tectonic processes (e.g., Sykes et al., 1982; Ross and Scotese, 1988). Therefore, this area represents a good natural laboratory to study the spatial variations of T_e, test the response of spectral methods to different factors and geodynamic conditions, and examine relationships between surface deformation, lithospheric structure and mantle dynamics.

In the following sections we first introduce the methodology and data employed for estimating T_e. We then present our results and compare them to previous estimates of T_e in the study area. Finally, we examine the relationships between T_e with other proxies for lithospheric and sub-lithospheric structure to improve our knowledge of the long-term rheology and mechanical behavior of the lithosphere in the study area. We also discuss how the lithospheric structure derived from our T_e analysis relates to surface deformation.

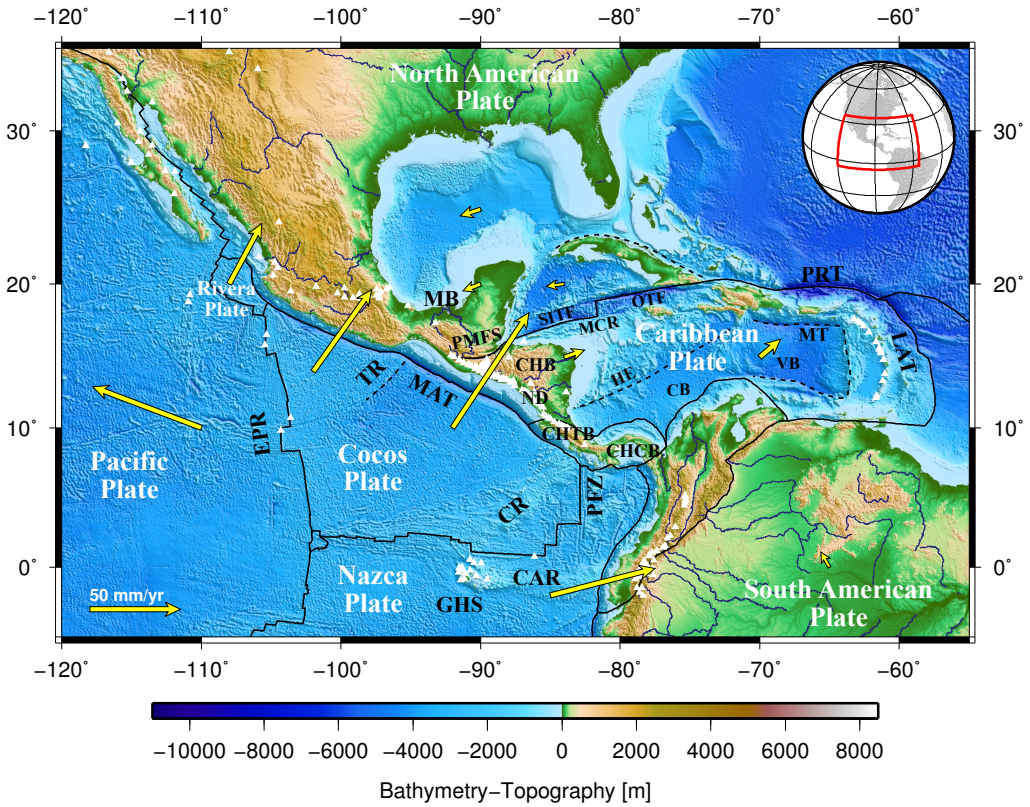

Figure 3.1: Geotectonic setting of Central America and surrounding regions. Shaded relief image of bathymetry and topography is from ETOPO1 digital data (Amante and Eakins, 2009), and boundaries of lithospheric plates are based on the PB2002 model (Bird, 2003). Yellow arrows denote vectors of the plate motion from the MORVEL model (DeMets et al., 2010) with respect to the NNR reference frame as calculated at the given position with the Plate Motion Calculator. Triangles show the position of Holocene volcanoes (Siebert and Simkin, 2002). Abbreviations: CAR, Carnegie Ridge; CB, Colombian Basin; CHB, Chortis Block; CHCB, Chocó Block; CHTB, Chorotega Block; CR, Cocos Ridge; EPR, East Pacific Rise; GHS, Galápagos Hotspot; HE, Hess Escarpment; LAT, Lesser Antilles Trench; MAT, Middle America Trench; MB, Maya Block; MCR, Mid-Cayman Rise; MT, Muertos Trough; ND, Nicaraguan Depression; OTF, Oriente Transform Fault; PFZ, Panamá Fracture Zone; PMFS, Polochic-Motagua Fault System; PRT, Puerto Rico Trench; SITF, Swan Island Transform Fault; TR, Tehuantepec Ridge; VB, Venezuelan Basin.

3.2.2. T_e estimation by spectral methods

To estimate the effective elastic thickness we calculate the coherence function relating the topography and Bouguer anomaly, commonly known as Bouguer coherence, using multitaper and wavelet methods. This function gives information on the wavelength band over which topography and Bouguer anomaly are correlated. In the coherence deconvolution method of Forsyth (1985), T_e is estimated by comparing the observed coherence curve with coherence functions predicted for a range of T_e values. For each given T_e, we calculate via deconvolution the initial surface and subsurface loads and compensating deflections that generate a predicted topography and gravity that best fit the observed topography and gravity anomaly, and a predicted coherence that best fits the observed coherence (Forsyth, 1985). The T_e value that minimizes the differences between the predicted and ob-

served quantities is the optimal one for the analysed area. The Bouguer coherence generally tends to zero at short wavelengths, where the topography is not compensated and loads are supported predominantly by the elastic strength of the lithosphere (Forsyth, 1985). At long wavelengths, the response to loading approaches the Airy limit and the coherence tends to one. The wavelengths at which the coherence rapidly increases from 0 to 1 depend on the effective elastic thickness of the lithosphere, such that when the lithosphere is weak and T_e is small, local compensation for loading occurs at relatively shorter wavelengths and vice versa.

In this Section we describe briefly the methodology and data employed to estimate T_e. For an extensive description of the methods, choice of parameters and biases in T_e estimation, see Supplementary Material associated with this article.

3.2.2.1. Multitaper method

To recover spatial variations in T_e we divide the analysis area into overlapping windows, such that in each window the coherence is calculated and inverted assuming a spatially constant T_e, moving the centre of each window 50 km for each new estimate. Calculation of the observed and predicted coherence involves transformation into the Fourier domain of the topography and Bouguer gravity anomaly to estimate their auto- and cross-power spectra. Because both data sets are non-periodic and finite, the Fourier transformation presents problems of frequency leakage (Thomson, 1982; Simons et al., 2000), resulting in estimated spectra that differ from the true spectra. To reduce leakage, the data are first multiplied by a set of orthogonal tapers in the space domain, the Fourier transform of the data-taper product taken for each taper, and the power spectrum determined at each taper. The final estimate of the signal's true power spectrum is then the weighted average of the individual power spectra over all tapers. The set of orthogonal tapers is defined by the bandwidth product NW that controls the wavelength resolution and spectral leakage (where N is the number of samples within the data window and W is the half bandwidth of the central lobe of the power spectral density of the first-order taper) and by the number of tapers K that governs the estimation variance (see Simons et al., 2000). The choice of bandwidth parameter NW in the multitaper technique is important. As the bandwidth increases, the resolution (i.e. the minimum separation in wave number between approximately uncorrelated spectral estimates) decreases (Walden et al., 1995). For a given bandwidth, W, there are up to $K = 2NW$-1 tapers with good leakage properties (Percival and Walden, 1993). The variance of the spectral estimates decreases with the number of tapers as $1/K$, so the bandwidth and resolution are chosen depending on the individual function under analysis (Percival and Walden, 1993). Here we apply the multitaper method using $NW = 3$ and $K = 3$, which are also used in several recent studies for T_e estimation (see e.g. Daly et al., 2004; Audet et al., 2007; Pérez-Gussinyé et al., 2009a; Kirby and Swain, 2011).

The effect of calculating T_e within a finite-size window is to limit the maximum wavelength of the gravity and topography that can be recovered. The choice of window size is critical in the multitaper estimation of T_e because it compromises the trade-off between resolution and variance of the estimates (Pérez-Gussinyé et al., 2004; Audet et al., 2007), such that large windows are better

able to retrieve high T_e but degrade the spatial resolution and potentially merge tectonic provinces, while small windows provide high spatial resolution and analyse perhaps just one province but cannot resolve long flexural wavelengths. As the resulting T_e estimate depends on window size, we use three different window sizes (400 x 400 km, 600 x 600 km and 800 x 800 km, respectively; see Suppl. Fig. 1) to obtain high spatial resolution and at the same time recover potentially high T_e. Finally, the T_e results estimated from three different window sizes are merged to obtain the final T_e map. This is done by calculating a weighted average of the T_e estimated from each of the three windows following the approach of Pérez-Gussinyé et al. (2009b). This approach combines the information content regarding abrupt T_e gradients recovered by small windows and the more reliable information on high T_e recovered by the larger windows.

3.2.2.2. Wavelet method

The wavelet method convolves a range of scaled wavelets with the whole data set to map and invert the coherence at each grid point, and achieves good wavenumber resolution over long length scales and good spatial resolution over short length scales. Here we employ a Morlet wavelet of high spatial resolution in the fan wavelet transform (Kirby and Swain, 2011). The value of the central wavenumber of the Morlet wavelet, denoted by $|\mathbf{k}_0|$, governs the resolution of the wavelet in the space and wavenumber domains. Larger values of $|\mathbf{k}_0|$ give better wavenumber resolution but poorer spatial resolution, and vice versa for smaller values (Addison, 2002).The choice of the value of $|\mathbf{k}_0|$, described in Kirby and Swain (2011), is governed by the amplitude of the first sidelobes of the simple wavelet. If this amplitude is a fraction $1/p$ ($p > 1$) of the amplitude of the central peak of the real part of the space-domain wavelet, then $|\mathbf{k}_0| = \pi\sqrt{2/\ln p}$. The $|\mathbf{k}_0|$ value used in this study is 2.668, which gives a space-domain wavelet whose first sidelobes is 1/16 of the magnitude of the central amplitude (Kirby and Swain, 2011).

To recover T_e, the Bouguer gravity anomaly and topography are mirrored about their edges prior to Fourier transformation, which, when used with the wavelet transform does not generally bias the results significantly, as it can with the periodogram method (Kirby and Swain, 2008). The wavelet transform is then applied to both datasets to calculate the auto and cross-spectra at different azimuths and scales. We follow Kirby and Swain (2009) and invert the square of the real part of the wavelet coherency (SRC), rather than the coherence, because it is less sensitive to correlations between the initial loads on the plate and to "gravitational noise", both of which can cause incorrect recovery of T_e (Kirby and Swain, 2009, 2011).

3.2.2.3. Regional topography, gravity and crustal structure

The elevation data used in our analysis are obtained from the ETOPO1 digital elevation model, a 1 arc-minute global relief model of Earth's surface that integrates land topography and ocean bathymetry (Amante and Eakins, 2009). Our area contains both continental and oceanic lithosphere, with the latter being subject to an additional water load. To treat mixed land and marine environments,

we adopt the approach of Stark et al. (2003) and Kirby and Swain (2008). This approach scales ocean bathymetry (h) to an equivalent topography $[h' = (\rho_c - \rho_w)h/\rho_c]$ prior to Fourier transformation, with subsequent application of the land loading deconvolution equations to the entire data set. Kirby and Swain (2008) showed that although this approach may bias T_e in ocean areas, the bias is small. Values of the densities are given in Table 3.1. The equivalent topography represents the bathymetry that would be expected if there were no water present (provided Airy isostasy operates). This allows the loading equations for a land environment to be used for the whole area, rather than performing two separate analyses and inversions on land and ocean areas (Perez-Gussinye et al., 2004).

Constant	Symbol	Value	Units
Young's modulus	E	100	GPa
Poisson's ratio	υ	0.25	
Newtonian gravitational constant	G	6.67259×10^{-11}	$m^3\ kg^{-1}\ s^{-2}$
Gravity acceleration	g	9.79	$m\ s^{-2}$
Seawater density	ρ_w	1030	$kg\ m^{-3}$
Crust density	ρ_c	2670	$kg\ m^{-3}$
Mantle density	ρ_m	3300	$kg\ m^{-3}$

Table 3.1: Symbols and values of constants.

The regional free-air gravity anomaly data are taken from the V18 Global Gravity Anomaly model of Sandwell and Smith (2009), on a 1´×1´ grid over both land and ocean. The Bouguer gravity anomaly has been calculated applying the complete Bouguer correction at regional scales to free-air data using the FA2BOUG code (Fullea et al., 2008). We calculated terrain corrections using the ETOPO1 digital elevation model (see above), with a reduction density of 2670 kg m^{-3}. The Bouguer gravity anomaly of the study area obtained following this procedure is shown in Fig. 3.2.

The deconvolution requires detailed information on the internal structure of the crust and uppermost mantle. To define the internal density profile and lateral variation of the different interfaces, we use the global crustal model CRUST2.0 (Laske and Masters, 1997; Bassin et al., 2000; Laske et al., 2000). CRUST2.0 includes three crustal and two sediment layers, whose 7th layer describes the Moho depth. Forsyth's (1985) original formulation of the predicted coherence assumes that all internal density variations and loading occurs at the Moho. In this study we assumed that internal loading occurs at the interface between upper and mid-crust. Since the observed coherence can be reproduced equally well by either low T_e and shallow loading or a larger T_e and deeper loading, there is a trade-off between T_e and assumed depth of loading. However, Pérez-Gussinyé and Watts (2005) tested the sensitivity of T_e to loading depth in Europe and found that changing the loading depth from the mid-crust to Moho changed T_e by $\sim$5 km, but the general patterns of variations remained the same (Pérez-Gussinyé and Watts, 2005; Pérez-Gussinyé et al., 2007). Other constants are given in Table 3.1.

We project all data sets to a Cartesian coordinate system using the Mercator projection to mitigate errors arising from the planar treatment of curvilinear coordinates. The data cover a much larger area than the study area to mitigate boundary effects.

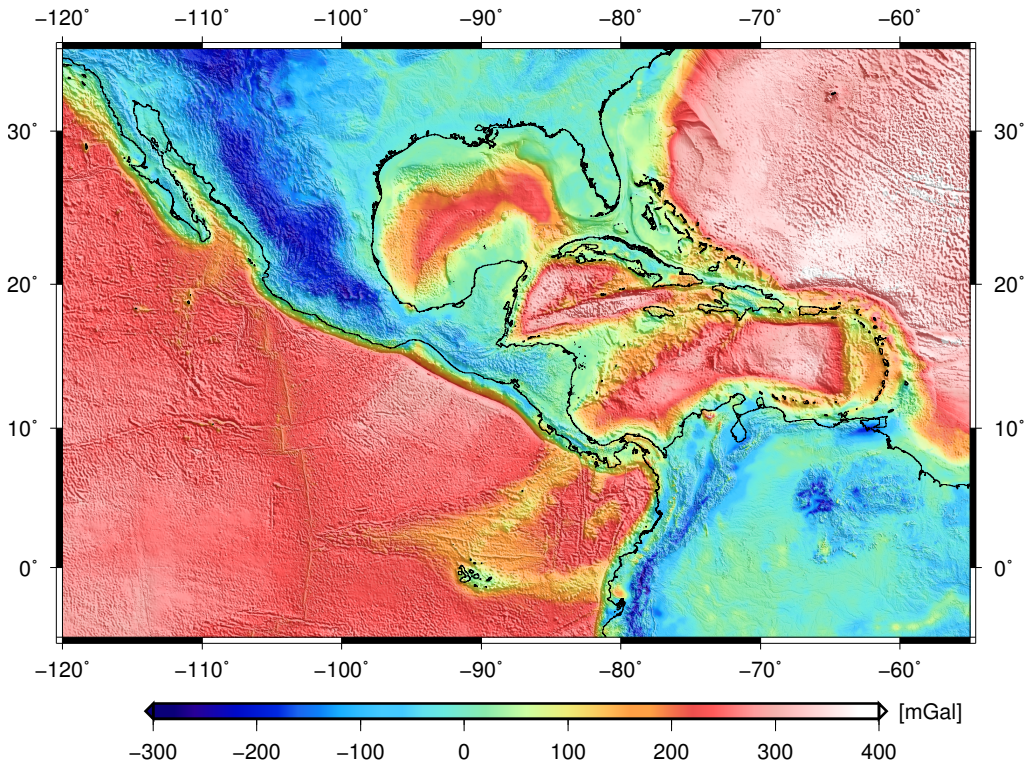

Figure 3.2: Bouguer gravity anomaly used for the analysis. Topography shaded relief superimposed.

3.2.3. Results

3.2.3.1. Spatial variations of T_e

The effective elastic thickness obtained from the multitaper and wavelet methods are shown in Fig. 3.3. Fig. 3.3a shows the final T_e from multitaper method after merging results from three different window sizes. Fig. 3.3b shows T_e estimated from the wavelet method with $|\mathbf{k}_0|$ = 2.668. In the following, we present our results and describe only those T_e variations present in the results obtained with both multitaper and wavelet methods.

The pattern of T_e variations in Central America and surrounding regions agrees well with the tectonic provinces in the area, and it is closely related to major tectonic boundaries (Fig. 3.3). The stable platforms of the North and South American plates have relatively high values. Otherwise, both methods give low values over the southern Cordillera and Baja California areas of North America. A steep T_e gradient separates this region from the southerly regions of the Interior Platform, which are characterized by intermediate to high T_e values (50-100 km). To the east, T_e decreases smoothly towards the Atlantic plain. Over northern South America, we also recover a high T_e within the stable platform. Both methods give very large values ($>$ 90 km) over the northern part of the Amazonia craton, where a linear SW-NE trending of much lower T_e values characterize the eastern part of the Guyana Shield within the rigid cratonic interior. Northward along the Northern Andes there is an

increase of T_e to intermediate values at the junction with the boundary between the South American and Caribbean plates.

The northern part of the Maya block shows a linear SW-NE trend of intermediate to high T_e values. The Trans-Mexican Volcanic Belt is characterized by very low T_e values, which are bounded to the south by a narrower band of relatively higher T_e. The Maya-Chortis and Chortis-Chorotega active boundaries (i.e., the Polochic-Motagua Fault System and Santa Elena shear zone, respectively) show steep gradients with lower T_e values than the surrounding regions, such that the interaction between these blocks has reduced the strength of the lithosphere near their boundaries. Our results also show a linear NW-SE trending zone of low T_e associated with the Central American volcanic arc, probably associated with high heat flow related to magma transport along the arc (see below). Within the Chortis block, which shows low T_e values, there are two areas of relatively high T_e that coincide with the Nicaraguan depression and the eastern passive margin of this block.

Low to intermediate T_e values characterize the Eastern Pacific Ocean, where both methods give extremely low values ($<$5 km) along region under intensive extension and volcanism, e.g., the East Pacific Rise, around the Galapagos hotspot, Cocos Ridge, Carnegie Ridge and the Cocos-Nazca spreading center, as well as the Cayman spreading center in the Caribbean Sea. The Eastern Pacific also shows contrasting patches of high and low T_e. The Middle American subduction zone is characterized by a narrower band of high T_e on the downgoing slab, greater than 30 km, over the outer rise seaward of the trench. These T_e values decrease sharply under the Middle American Trench (MAT) offshore of Central America. In this zone, the Tehuantepec Ridge (TR) represents a major limit which separates the oceanic lithosphere into two distinct tectonic regions with a maximum T_e offset of $\sim$30 km, such that seaward of the trench show higher T_e values in the northwest of the TR than to the southeast of the TR.

Over the Gulf of Mexico there is a linear SW-NE trend of intermediate to high T_e values (20-40 km) associated with old oceanic crust (seafloor ages of $\sim$160-120 Myr; Müller et al., 2008) which outcrops in this area. Moreover, most of the Caribbean oceanic domain seems to be uniformly weak. In addition, several patches of intermediate to high T_e are also visible in the Colombian and Venezuelan basins. Westward, the Cocos-Nazca slab window beneath southeastern Costa Rica and northwestern Panamá is characterized by extremely low T_e ($<$ 4 km). Finally, T_e increases to high values clearly delineated along the transform plate boundary between the South American and Caribbean plates and Lesser Antilles Trench, which connect northward with the high T_e values in the Puerto Rico Trench, western North Atlantic margin and the Bermuda Rise region.

Regardless of the technical differences between the two methods, there is a good overall agreement in the relative spatial variations of T_e recovered from both techniques. Although absolute T_e values can vary in both maps, the qualitative T_e structure and location of the main T_e gradients are very similar. The greater discrepancies between both methods are local spatial variations of T_e in the stable platforms of the North and South American plates. Other differences are observed in T_e values recovered along the plate boundary between the South American and Caribbean plates, northward of the Lesser Antilles Trench and Bermuda Rise region. Since this study focuses on spatial variations of

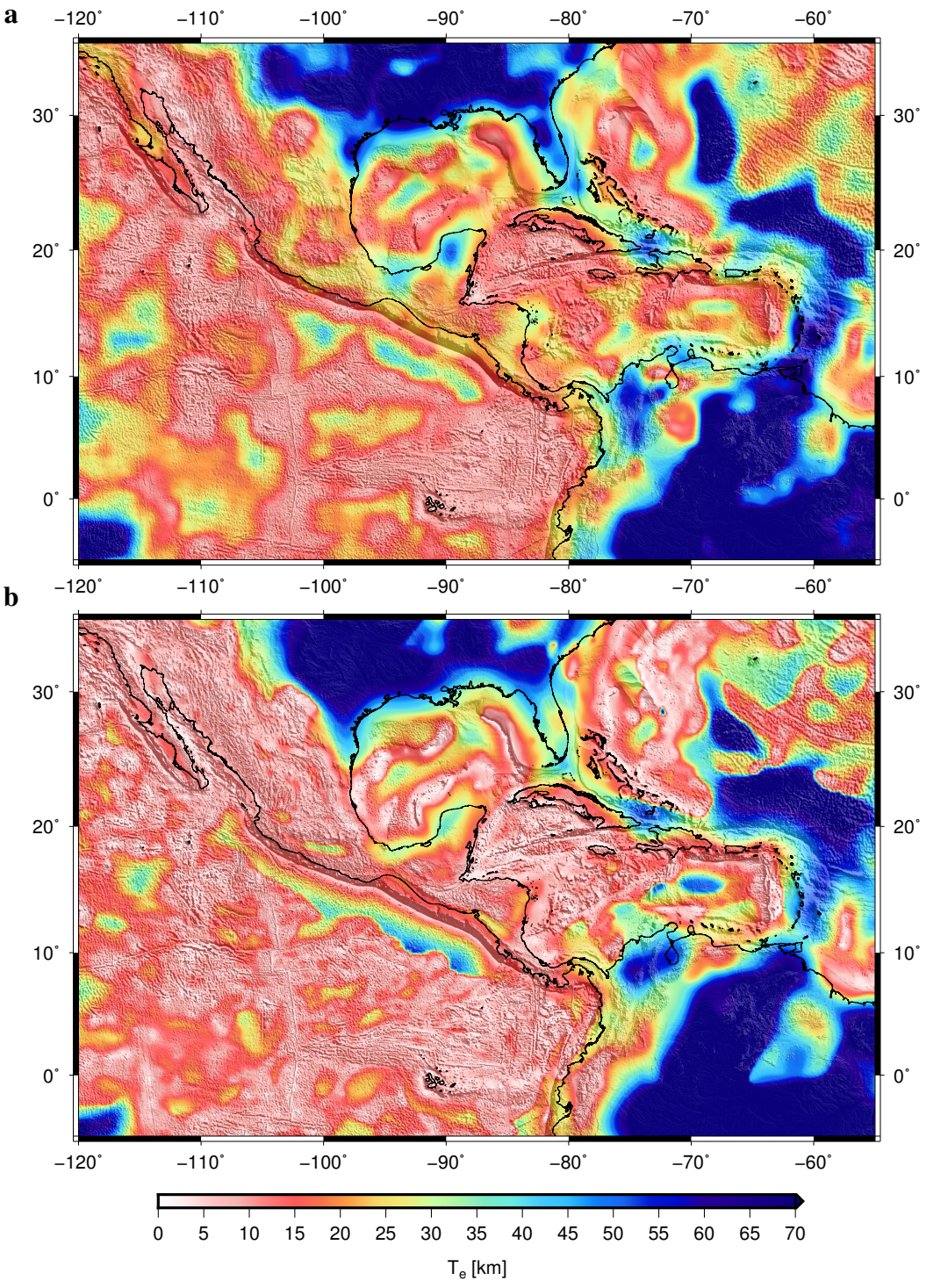

Figure 3.3: Effective elastic thickness, T_e, over Central America and surrounding regions from: (a) multitaper method, and (b) wavelet method. In both images, topography shaded relief is superimposed. Fig. 3.3a shows final T_e after merging the results from the three different window sizes (see Section 3.2.2 and Supp. Fig. 1). The final T_e structure retains the primary characteristics of the largest window, but it better resolves the sharp gradient between low and high T_e areas and the short wavelength variations in T_e. Fig. 3.3b shows T_e estimated from the wavelet method with $|\mathbf{k}_0| = 2.668$.

T_e and its geodynamic implications for Central America and surrounding regions, we do not discuss here the differences in absolute values between both maps produced by the methods, and the interested reader can find a more thorough comparison between the wavelet and multitaper methods in, for example, Daly et al. (2004), Audet et al. (2007), Pérez-Gussinyé et al. (2007, 2009a), and Kirby and Swain (2011).

As mentioned above, there are several 'key' parameters used in the analysis that lead to small (but perhaps significant) changes in resolution and accuracy of the results from both methods. Here we follow the approach of Pérez-Gussinyé et al. (2009b) and Kirby and Swain (2011) to obtain high spatial resolution and at the same time recover potentially high T_e from both methods. We have included an extensive description of the choice of parameters and its influence on the results, as well as the biases in T_e estimation, in the Supplementary Material. It should also be noted that "gravitational noise" (McKenzie and Fairhead, 1997; McKenzie, 2003; Kirby and Swain, 2009) does exist in the study area, which casts doubt upon T_e values in some regions, especially where we have recovered very high values; we will return to this issue in the Discussion.

3.2.3.2. Comparison with previous T_e estimates

Direct comparison of T_e values and its variations is possible between our results and the previous study of T_e from the multitaper method by Lowry and Pérez-Gussinyé (2011) for the western United States, and with T_e computed by Tassara et al. (2007) and Kirby and Swain (2011) for northern South America using $|\mathbf{k}_0|$ = 2.668 and $|\mathbf{k}_0|$ = 5.336 wavelets (Supp. Fig. 6 shows our results obtained from wavelet method with $|\mathbf{k}_0|$ = 5.336). Our results are consistent with these and other previous regional studies of North America (Kirby and Swain, 2009), and South America (Pérez-Gussinyé et al., 2007, 2008, 2009a). This consistency indicates the viability of our results over Central America and surrounding regions.

Regarding the Central America region, there are numerous studies of oceanic T_e performed for given places (for a compilation see Watts, 2001). For the Middle America Trench, Caldwell and Turcotte (1979) estimated a T_e of 18.6 ± 2.2 km for seafloor age of 32.5 ± 2.5 Myr. Meanwhile, McNutt (1984) obtained a T_e of 17.5 ± 2.5 km for 20 ± 5 Myr, McAdoo and Martin (1984) a T_e of 29.7 ± 2.2 km for 20 ± 5 Myr, and Levitt and Sandwell (1995) a T_e of 27.3 ± 10 km for 19.9 ± 8 Myr. Feighner and Richards (1994) studied the Galápagos region using a variety of compensation models, obtaining a T_e of 12 ± 2 km and 3 ± 3 km for 7.5 ± 1 Myr. McAdoo et al. (1985) obtained a T_e of 31.7 ± 5.2 km for 80 ± 5 Myr over the Puerto Rico Trench, and Levitt and Sandwell (1995) a T_e of 40.7 ± 5 km for 101.6 ± 12 Myr over the Antilles Trench. Furthermore, in their study Manea et al. (2005) estimated T_e of the oceanic lithosphere beneath Tehuantepec Ridge by means of an admittance analysis of a set of profiles across this structure. These authors obtained a T_e of ∼5-10 km in the NW area of the TR, while in the SE area T_e is of ∼10-15 km. As mentioned above, we recover a complex pattern of T_e associated with the TR, with a maximum offset of ∼30 km.

Finally, our results are in a good agreement with previous global studies as in e.g., Watts et al. (2006), who obtained T_e estimates from a wide range of submarine volcanic features in the East

Pacific Ocean. Recently, Kalnins (2011) produced a global map of elastic thickness in the world's oceans, and recovered T_e at major constructional volcanic features in our study area, as the Bermuda Rise (T_e of 15-21 km), Carnegie Ridge (3-4 km), Cocos Ridge (3-4 km), Galapagos Islands (3-4 km) or Nazca Ridge (4-5 km). Furthermore, our results are also in a good agreement with the worldwide T_e map obtained by Audet and Bürgmann (2011) from the Bouguer coherence using the continuous wavelet transform, and with T_e results of Tesauro et al. (2012) from a rheological approach based on the lithospheric strength distribution, although our results have higher resolution due to the regional nature of the present work.

3.2.4. Discussion

3.2.4.1. T_e, surface heat flow and thermal age

Due to the dependence of lithosphere strength on temperature, T_e should show an inverse correlation with heat flow (McNutt, 1984; Lowry and Smith, 1995): higher surface heat flow implies higher lithospheric temperatures and hence lower lithospheric strength. Several studies examining the dependence of the strength of the lithosphere on the temperature structure (e.g., Watts and Burov, 2003; Afonso and Ranalli, 2004; Burov and Watts, 2006), found that there is not a simple relation between T_e and surface heat flow for continental areas, due to local differences in crustal structure and composition (which implies differences in radioactive heat production and thermal and rheological properties of the rocks) and lithosphere flexure (which affects the vertical distribution of elastic stresses). Otherwise, the situation is relatively simpler for oceanic areas, because oceanic crust is thinner and comparatively devoid of radioactive elements, implying that the strength of the lithosphere is mostly controlled by the cooling history (i.e., thermal age) of the oceanic lithosphere, although flexural effects can be important.

Fig. 3.4a shows the regional surface heat flow in the study area from the updated global heat flow database of the International Heat Flow Commission (Hasterok, 2010). Despite some uncertainties, there is a relatively good (inverse) correlation between surface heat flow and T_e values in Central America and surrounding regions. Low T_e values observed in the southern Cordillera and Baja California are associated with relatively high heat flow. Similarly, high T_e values recovered for southern regions of the Interior Platform match the observed low heat flow (Fig. 3.3 and Fig. 3.4a). By contrast, there are extensive areas with no measurements, e.g., the northern South America. Pérez-Gussinyé et al. (2007, 2008) examined the relationship of T_e to heat flow in South America, concluding that both parameters correlate well. Our relatively high T_e values observed in the northern part of the Maya block and in the southern boundary of the Trans-Mexican Volcanic Belt are well correlated with the low surface heat flow of these areas. The Trans-Mexican Volcanic Belt is characterized by intermediate to high heat flow and low T_e values. The southern Maya block and northwestern Chortis block, including the northwestern Central American volcanic arc, are also characterized by high surface heat flow and low T_e values. By contrast, the southeastern part of the Central American volcanic arc and Chorotega block are characterized by low heat flow and low T_e values (Fig. 3.3 and Fig. 3.4a), such

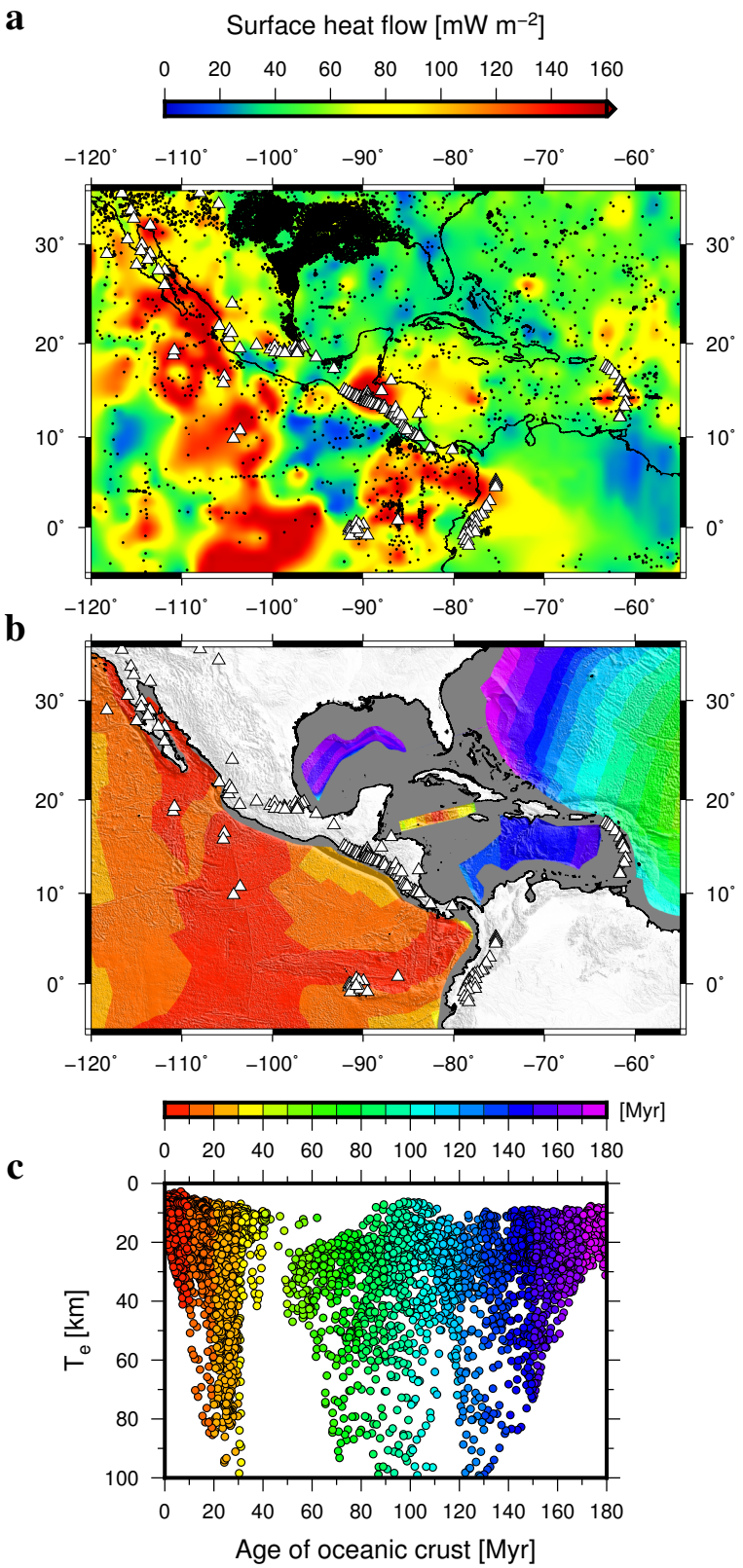

Figure 3.4: (a) Regional surface heat flow from the updated global heat flow database of the International Heat Flow Commission (Hasterok, 2010). Black circles indicate measurement sites. White triangles show the position of Holocene volcanoes (Siebert and Simkin, 2002). (b) Age-area distribution of ocean floor from Müller et al. (2008). (c) Effective elastic thickness, T_e, from the multitaper method versus age of the oceanic crust (Müller et al., 2008).

that it's possible that due to the narrow width of the Central American land bridge in this area, the T_e recovered over the continent is very influenced by the low T_e values of the surrounding oceanic regions.

As illustrated in Fig. 3.4a, high heat flow is observed in the Eastern Pacific Ocean in regions under intensive extension and volcanism, e.g. the East Pacific Rise, around the Galapagos hotspot, Cocos Ridge, Carnegie Ridge and the Cocos-Nazca spreading center, as well as over the Cayman spreading center in the Caribbean Sea. This first-order pattern of surface heat flow variation is in accord with our low T_e estimates for these areas (Fig. 3.3). However, a low heat flow is observed within the Cocos plate where there is not a clear correlation with the T_e signature associated to the Middle American subduction zone (see below). The western Caribbean region shows moderate surface heat flow, where the Cocos-Nazca slab window beneath Central America, characterized by extremely low T_e, does not show a high surface heat flow. Meanwhile the eastern Caribbean region is characterized by lower values, with several contrasting patches of high surface heat flow as in the central part of the Hess Escarpment or over the Aves Ridge associated with the Lesser Antilles.

It is commonly accepted that T_e reflects a fossil lithospheric equilibrium developed at the time of loading (for a review see Artemieva, 2011). If loading occurs when the lithosphere is weak and no mass redistribution occurs afterwards, there is no need for stress to re-equilibrate, and isostatic analyses might yield a low T_e estimate even after subsequent cooling and strengthening of the lithosphere, as is the case for oceanic lithosphere (Pérez-Gussinyé et al., 2009b). Fig.3.4b shows the age-area distribution of the ocean floor from Müller et al. (2008) in the study area. If we compare our T_e results with the age of the ocean crust in the study area (Fig. 3.4c), a direct relationship between them is not evident. This is consistent with the scatter observed in previous works on other oceanic regions (e.g., Tassara et al., 2007; Kalnins and Watts, 2009). Watts (2001) notes that the load age, which is not necessarily the same of the crust age, would explain much of this scatter. Other contributing sources could be uncertainties in load, infill and mantle densities, thermal perturbations due to hot and cold spots (e.g., Tassara et al., 2007), viscoelastic stress relaxation (Watts and Zhong, 2000), yielding in regions of large loads and high curvature (McNutt and Menard, 1982), or spatial variations in the controlling isotherms that determine T_e (Kalnins and Watts, 2009).

Otherwise, as stated above, the thermal state and rheological behavior of the lithosphere in continental areas are largely a consequence of local conditions, such that there is a complex relationship between T_e and the age of the continental lithosphere. Surface processes of erosion and deposition constantly redistribute continental surface mass loads. In any case, the high T_e values recovered here for the stable platforms of the North and South American plates (see Fig. 3.3) are consistent with previous studies for these regions (Tassara et al., 2007; Pérez-Gussinyé et al., 2007, 2009a; Kirby and Swain, 2009, 2011).

3.2.4.2. Loading of the lithosphere

A fundamental assumption of the load deconvolution method developed by Forsyth (1985) is that surface and subsurface loads are statistically uncorrelated. In many cases, however, surface and

subsurface loading are likely to be tectonically related processes and, therefore, spatially correlated (Forsyth, 1985). Subsurface loads include mafic intrusions, accreted lower crustal material, thermal anomalies and compositional variations, which cause lateral variations of density at depth and may have a strong influence on T_e estimates (Stark et al., 2003). Meanwhile, surface loading is caused by topography and large-scale variations in surface density (e.g., mountains and sedimentary basin). Macario et al. (1995) showed that when the degree of correlation of initial surface and subsurface loading increases, the T_e values estimated using Forsyth's (1985) deconvolution method can be biased downward. Furthermore, erosion and sedimentation may play an important role in modifying the relationship between surface topography and subsurface density anomalies (e.g., Forsyth, 1985; McKenzie and Fairhead, 1997). Both processes can reduce the landscape to a perfectly flat surface, removing the topographic expression of subsurface loads. The presence of topographically unexpressed internal loading, known as "noise" or "gravitational noise" (McKenzie and Fairhead, 1997; McKenzie, 2003; Kirby and Swain, 2009), biases the T_e upward. As pointed out by Kirby and Swain (2009), this problem can occur in regions of subdued topography, and predominantly affects areas where the coherence method indicates high T_e (see Suppl. Fig. 7).

The load deconvolution wavelet method can also estimate the ratio between the initial internal and surface load amplitudes (the loading ratio, f; Forsyth, 1985). We can display the loading ratio results in terms of the F parameter, the internal load fraction (McKenzie, 2003), where purely surface loading gives $F = 0$, purely internal loading gives $F = 1$, while equal surface and internal loading gives $F = 0.5$ (see Supplementary Material for an extended explanation). Fig. 3.5a shows best fitting F values corresponding to the T_e recovered from the wavelet method (Fig. 3.3b). For North America, our results are consistent with Kirby and Swain's (2009) F results, which show that subsurface loading has dominated continental tectonics, or at least been equal in magnitude to surface loading, in North America. Our results are also consistent with the pattern of the flexural loading ratio, f_F, obtained by Tassara et al. (2007) in northern South America, which suggest that below the north-eastern limit of the Amazonia craton there are strong lateral variations in density not compensated by surface topography. Subsurface loading dominates along the East Pacific Rise, around the Galapagos hotspot, Cocos Ridge, Carnegie Ridge and the Cocos-Nazca spreading center (Fig. 3.5a). In this zone, the Tehuantepec Ridge represents, again, a major limit which separates the oceanic lithosphere into two distinct load regions, such that the northwest TR is dominated by surface loading while the southeast TR is dominated by internal loads. The Caribbean region is characterized by all range of F values. Higher F values are observed over the eastern Cayman spreading center, the Caribbean Large Igneous Province, the Cocos-Nazca slab window beneath Central America, the Aves Ridge, and along the Lesser Antilles Trench and east North American margin.

Fig. 3.5b shows seafloor sediment thickness (Divins, 2003; Whittaker et al., 2013) in the study area. Large amount of sediments are located on the Gulf of Mexico basin, along of the western North Atlantic margin, the Colombian, Venezuelan and Grenada basins, and on the Barbados Accretionary Complex associated to the Lesser Antilles. In many cases sediment thickness exceeds 10 km. However, most of the Caribbean lithosphere, where both methods recovered low T_e values (see Fig.

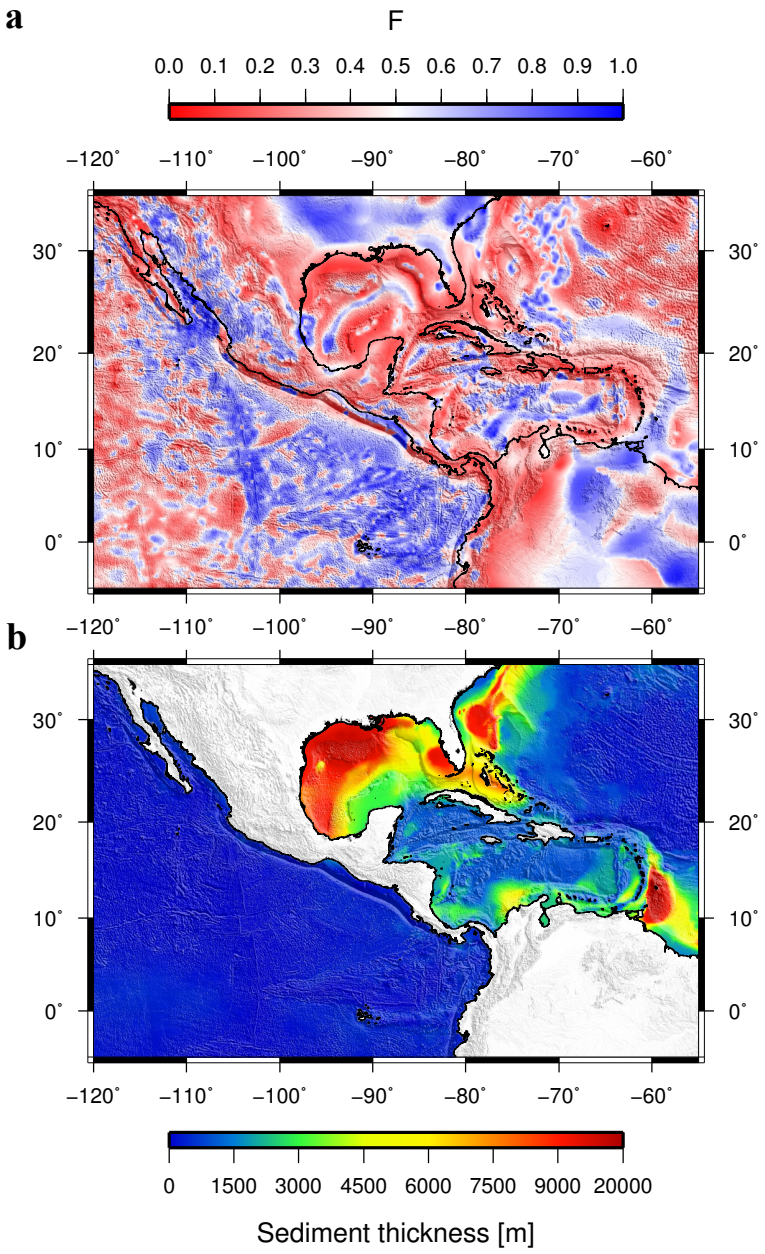

Figure 3.5: (a) Loading ratio (F) corresponding to the T_e obtained from the wavelet method (Fig. 3.3b). (b) Sediment thickness (meters) on the seafloor in the study area from the 5 arc-minute digital total-sediment-thickness database for the world's oceans and marginal seas (Divins, 2003; Whittaker et al., 2013).

3.3), seems to be uniformly weak, suggesting that the effect of the sediments on T_e estimates is very small. The continental shelf of the Gulf of Mexico, which shows a smooth surface, is characterized by moderate to high T_e values (between 40-50 km; see Fig. 3.3) and low F values, with surface loads dominating. Seaward, high T_e values are recovered for the Mississippi delta system (Fig. 3.3). Southwestward in the Gulf of Mexico, over the old oceanic crust which outcrops in this area, both methods recover a linear SW-NE trending of intermediate to high T_e values associated with a high F value. The Venezuelan basin also shows high T_e values associated with a subsurface loading domain,

possibly related to the oceanic basement underneath the Caribbean Large Igneous Province. Müller et al. (2008) found prominent negative residual basement depth anomalies (in a range between 750 and 1500 m) associated with the Gulf of Mexico, northeast of Venezuela, and off the east coast of North America, which may be related to subducted slab material descending in the mantle or to asthenospheric flow. In the case of the Colombian basin, the presence of sediments on the continental shelf may play a major role on the estimation of T_e ($\sim$40 km; Fig. 3.3 and Fig. 3.5b). Interestingly, the presently active Nicaraguan depression, which experienced significant extension in the Cenozoic, shows intermediate T_e values ($\sim$25 km) and a F value of 0.5, such that it is possible that in this case T_e values are overestimated due to the effect associated with its sediment fill (see Suppl. Fig. 7).

3.2.4.3. The Middle American and Lesser Antilles subduction zones

The results over the Middle American and Lesser Antilles subduction zones should be interpreted with caution. As exposed in the Results Section, the Middle American subduction zone is characterized by a narrower band of high T_e on the downgoing slab seaward of the trench (Fig. 3.3). These T_e values decrease sharply under the MAT offshore of Central America, indicating a substantial degree of weakening within the downgoing plate due to the flexure of the lithosphere (see McNutt and Menard, 1982; Judge and McNutt, 1991; Billen and Gurnis, 2005; Contreras-Reyes and Osses, 2010). In fact, the bathymetry of the MAT offshore of Central America shows a complex response of the crust to the subduction process, with widespread outer-rise normal faulting subparallel to the trench axis due to the plate bending, increasing in number and offset where the bending is more pronounced (Ranero et al., 2003, 2005; Harders et al. 2011; Manea et al., 2013). This high T_e signature is very evident (broader and even exceeding 50 km at the Lesser Antilles Trench; see Fig. 3.3), and can also be observed in other subduction zones, as e.g. along the Peru-Chile Trench (Tassara et al., 2007; Pérez-Gussinyé et al., 2009a; Kirby and Swain, 2011), or over the Japan, Izu-Bonin, and Mariana trenches and at the northernmost tip of the Tonga-Kermadec trench (Kalnins and Watts, 2009).

Subsurface loads, such as those due to a dense downgoing slab, should be taken into account when interpreting the results over subduction zones (Kalnins and Watts, 2009). We have found that the high T_e values over the Middle American and Lesser Antilles subduction zones are dominated by internal loads (and in the case of the southernmost tip of the LAT also associated with a large amount of sediments; see Fig. 3.5), where the corresponding noise levels are high (see Supp. Fig. 7) and thus, these results may be biased upward. If T_e over the Middle American subduction zone is actually low (at least relatively), it would be in accordance with they reflecting a "frozen in" signal which is not affected in this zone by subsequent cooling and strengthening of the oceanic lithosphere. Interestingly, this is not the case of the Lesser Antilles subduction zone, where the high T_e values are free of noise (excepting the southernmost tip of the LAT associated with a large amount of sediments; see Fig. 3.5b and Suppl. Fig. 7), and persist in all our results from different window sizes and $|\mathbf{k}_0|$ in both multitaper and wavelet methods, respectively (see Fig. 3.3 and Supp. Fig. 1 and 6). This is in accordance with the strength of the oceanic lithosphere is being in this case controlled by the thermal age of the lithosphere at the time of loading (Watts, 2001; Kalnins and Watts, 2009), such that T_e

values increase with cooling of the oceanic lithosphere away from the ridge. Furthermore, it should be noted that the results over the Middle American and Lesser Antilles subduction zones, especially in relation to the high gradient that limits these bands of higher T_e, are highly dependent on the choice of spectral parameters in both multitaper and wavelet methods (see Fig. 3.3 and Supp. Fig. 1 and 6).

3.2.4.4. T_e and seismicity

The magnitude and spatial variations of T_e could control the degree, style and localization of deformation in response to long-term tectonic loads, and potentially the distribution of seismic activity (e.g., Lowry and smith, 1995; Tassara et al., 2007; Audet and Bürgmann, 2011; Chen et al., 2013). The seismotectonics of the circum-Caribbean area is complex, and essentially related to plate boundaries, with intraplate activity being very scarce (Fig. 3.6a).

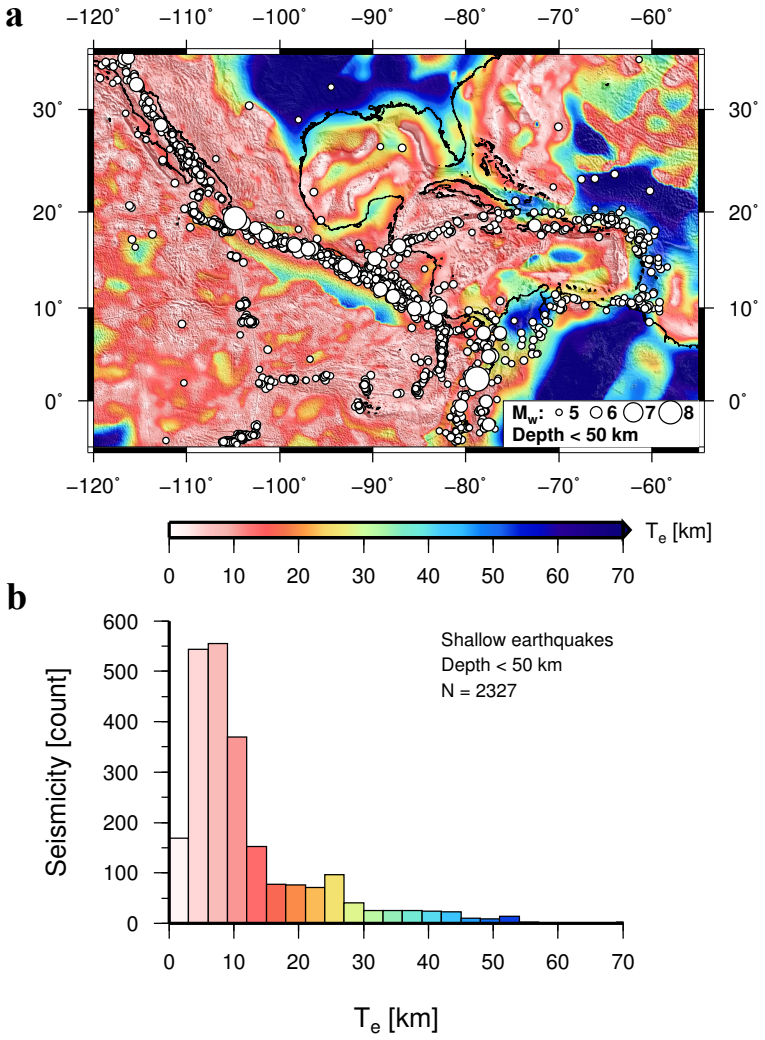

Figure 3.6: (a) Correlation between distribution of the shallow seismicity (depth <50 km) from the Global CMT seismic catalog (Ekström et al., 2012) with T_e derived from the wavelet method. (b) Histogram shows shallow earthquake events versus T_e.

Comparison of the spatial variation of T_e with the shallow (<50 km deep) earthquake distribution indicates that most of the seismic activity is located in regions with low T_e or steep T_e gradient, while the lack of seismicity in stable tectonic provinces characterized by high T_e values is evident (Fig. 3.6a). As illustrated in Fig. 3.6b, shallow earthquakes are very frequent in regions with low T_e (<20 km), and are relatively scarce in regions with higher values. This suggests that the stronger lithosphere resists deformation and transfers the stress effectively, while the weak lithosphere and areas with steep change of T_e are prone to accumulate and then release tectonic stresses causing earthquakes (Mao et al., 2012; Chen et al., 2013).

3.2.5. Conclusions

We have used two different spectral methods (multitaper and wavelet) to calculate the coherence between the Bouguer gravity anomaly and the topography in order to estimate the spatial variations in effective elastic thickness in Central America and surrounding regions. We have generated, for the first time, high-resolution maps of spatial variations of T_e for this region. Regardless of the technical differences between the two methods, there is a good overall agreement in the spatial variations of T_e recovered from both methods. Although absolute T_e values can vary in both maps, the qualitative T_e structure and location of the main T_e gradients are very similar, such that estimation of T_e is relatively insensitive to the choice of spectral estimator.

The pattern of the T_e variations in Central America and surrounding regions agrees well with the tectonic provinces in the region, and it is closely related to major tectonic boundaries. There is a relatively good correlation, despite some uncertainties, between surface heat flow and our T_e results. These results suggest that although this area is geologically complex, the thermal state of the lithosphere has profound influence on its strength, such that T_e is strongly governed by thermal structure. Otherwise, in general there is not a direct relationship between T_e and the age of the ocean crust in of our study area (contrary to that expected if T_e is exclusively controlled by the thermal structure of the oceanic lithosphere), which could be explained for other factors, maybe mainly differences in age loading.

The Middle American and Lesser Antilles subduction zones are characterized by a band of high T_e on the downgoing slab seaward of the trenches. These high T_e values are related to internal loads (and in the case of the southernmost tip of the LAT also associated with a large amount of sediments); showing high noise levels and they may be biased upward. Thus, the results over subduction zones should be interpreted with caution, and warrant further analysis.

Finally, future research should also evaluate the relationship between T_e, as well as its anisotropy, Moho structure and mantle structure within a geodynamical perspective, in order to improve our understanding on the evolution of the Caribbean plate.

Acknowledgements

We thank Pascal Audet, an anonymous reviewer, and Editor Yanick Ricard for their useful reviews that significantly improved this manuscript. We also thank Javier Fullea for providing the FA2BOUG code. AJ-D especially thanks Pilar Llanes and Yangfan Deng for fruitful discussion on various topics of the methodology. The figures have been produced with the GMT software (Wessel et al., 2013). AJ-D work was supported by a grant of the Universidad Complutense de Madrid. J.R. work was supported by a contract Ramón y Cajal co-financed from the Ministerio de Economía y Competitividad of Spain and the European Social Fund. This work was carried out in the projects CGL2008-03463 and CGL2009-14405-C02-02. This work is a contribution from the Active Tectonics, Paleoseismology and Associated Hazards research group (UCM-910368; http://tectact.wordpress.com/).

References

Addison, P.S., 2002. The Illustrated Wavelet Transform Handbook. Institute of Physics Publishing, Bristol, UK.

Afonso, J.C., Ranalli, G., 2004. Crustal and mantle strengths in continental lithosphere: is the jelly sandwich model obsolete?. Tectonophysics 394, 221–232.

Amante, C., Eakins, B.W., 2009. ETOPO1 1 arc-minute global relief model: procedures, data sources and analysis. NOAA Technical Memorandum NESDIS NGDC24. 19 pp.

Artemieva, I., 2011. The Lithosphere: An Interdisciplinary Approach, vol. 773. Cambridge University Press. 773 pp.

Audet, P., Bürgmann, R., 2011. Dominant role of tectonic inheritance in supercontinent cycles. Nat. Geosci. 4, 184–187.

Audet, P., Jellinek, A.M., Uno, H., 2007. Mechanical controls on the deformation of continents at convergent margins. Earth Planet. Sci. Lett. 264, 151–166.

Bassin, C., Laske, G., Masters, T.G., 2000. The current limits of resolution for surface wave tomography in North America. Eos Trans. AGU 81, F897.

Billen, M.I., Gurnis, M., 2005. Constraints on subducting plate strength within the Kermadec trench. J. Geophys. Res. 110, B05407.

Bird, P., 2003. An updated digital model of plate boundaries. Geochem. Geophys. Geosyst. 4 (3), 1027.

Bürgmann, R., Dresen, G., 2008. Rheology of the lower crust and upper mantle: evidence from rock mechanics, geodesy, and filed observations. Annu. Rev. Earth Planet. Sci. 36, 531–567.

Burov, E.B., 2011. Rheology and strength of the lithosphere. Mar. Pet. Geol. 28, 1402–1443.

Burov, E.B., Diament, M., 1995. The effective elastic thickness of (Te) continental lithosphere. What does it really means?. J. Geophys. Res. 100 (B3), 3905–3927.

Burov, E.B., Watts, A.B., 2006. The long-term strength of continental lithosphere: "jelly sandwich" or "crème brûlée"?. GSA Today 16 (1), 4–10.

Caldwell, J.G., Turcotte, D.L., 1979. Dependence of the elastic thickness of the oceanic lithosphere on age. J. Geophys. Res. 84, 7572–7576.

Chen, B., Chen, C., Kaban, M.K., Du, J., Liang, Q., Thomas, M., 2013. Variations of the effective elastic thickness over China and surroundings and their relation to the lithosphere dynamics. Earth Planet. Sci. Lett. 363, 61–72.

Contreras-Reyes, E., Osses, A., 2010. Lithospheric flexure modeling seaward of the Chile trench: implications for oceanic plate weakening in the Trench Outer Rise region. Geophys. J. Int. 182 (1), 97–112.

Daly, E., Brown, C., Stark, C.P., Ebinger, C.J., 2004. Wavelet and multitaper coherence methods for assessing the elastic thickness of the Irish Atlantic margin. Geophys. J. Int. 159, 445–459.

DeMets, C., Gordon, R.G., Argus, D.F., 2010. Geologically current plate motions. Geophys. J. Int. 181, 1–80. See also: Erratum. Geophys. J. Int. 187 (2011) 538.

Divins, D.L., 2003. Total Sediment Thickness of the World's Oceans & Marginal Seas. NOAA National Geophysical Data Center, Boulder, CO.

Ekström, G., Nettles, M., Dziewonski, A., 2012. The global CMT project 2004–2010: centroid-moment tensors for 13,017 earthquakes. Phys. Earth Planet. Inter. 200–201, 1–9.

Feighner, M.A., Richards, M.A., 1994. Lithospheric structure and compensation mechanism of the Galápagos Arc. J. Geophys. Res. 99, 6711–6729.

Forsyth, D.W., 1985. Subsurface loading estimates of the flexural rigidity of continental lithosphere. J. Geophys. Res. 90, 12,623–12,632.

Fullea, J., Fernàndez, M., Zeyen, H., 2008. FA2BOUG – A FORTRAN 90 code to compute Bouguer gravity anomalies from gridded free air anomalies: application to the Atlantic–Mediterranean transition zone. Comput. Geosci. 34, 1665–1681.

Harders, R., Ranero, C.R., Weinrebe, W., Behrmann, J.H., 2011. Submarine slope failures along the convergent continental margin of the Middle America Trench. Geochem. Geophys. Geosyst. 12, Q05S32.

Hasterok, D., 2010. Thermal state of the Oceanic and Continental lithosphere. Ph.D. Thesis. University of Utah.

Hasterok, D., Chapman, D.S., 2011. Heat production and geotherms for the continental lithosphere. Earth Planet. Sci. Lett. 307, 59–70.

Judge, A.V., McNutt, M.K., 1991. The relationship between plate curvature and elastic plate thickness: a study of the Peru–Chile trench. J. Geophys. Res. 96 (B10), 16625–16639.

Kalnins, L.M., 2011. Spatial variations in the effective elastic thickness of the lithosphere and their tectonic implications. Ph.D. Thesis. University of Oxford.

Kalnins, L.M., Watts, A.B., 2009. Spatial variations in effective elastic thickness in the Western Pacific Ocean and their implications for Mesozoic volcanism. Earth Planet. Sci. Lett. 286, 89–100.

Kirby, J.F., Swain, C.J., 2008. An accuracy assessment of the fanwavelet coherence method for elastic thickness estimation. Geochem. Geophys. Geosyst. 9 (3), Q03022. Correction: Geochem. Geophys. Geosyst. 9 (5) (2008) Q05021.

Kirby, J.F., Swain, C.J., 2009. A reassessment of spectral Te estimation in continental interiors: the case of North America. J. Geophys. Res. 114, B08401.

Kirby, J.F., Swain, C.J., 2011. Improving the spatial resolution of effective elastic thickness estimation with the fan wavelet transform. Comput. Geosci. 37, 1345–1354.

Laske, G., Masters, G., 1997. A global digital map of sediment thickness. Eos Trans. AGU 78, F483.

Laske, G., Masters, G., Reif, C., 2000. A new global crustal model at 2 × 2 degrees (CRUST2.0). http://igppweb.ucsd.edu˜gabi/rem.dir/crust/crust2.html.

Levitt, D.A., Sandwell, D.T., 1995. Lithospheric bending at subduction zones based on depth soundings and satellite gravity. J. Geophys. Res. 100, 379–400.

Lowry, A.R., Pérez-Gussinyé, M., 2011. The role of crustal quartz in controlling Cordilleran deformation. Nature 471 (7338), 353–357.

Lowry, A.R., Smith, R.B., 1995. Strength and rheology of the western U.S. Cordillera. J. Geophys. Res. 100, 17,947–17,963.

Lowry, A.R., Ribe, N.M., Smith, R.B., 2000. Dynamic elevation of the Cordillera, western United States. J. Geophys. Res. 105, 23,371–23,390.

Macario, A., Malinverno, A., Haxby, W.F., 1995. On the robustness of elastic thickness estimates obtained using the coherence method. J. Geophys. Res. 100 (D8), 15,163–15,172.

Manea, M., Manea, V.C., Kostoglodov, V., Guzman-Speziale, M., 2005. Elastic thickness of the lithosphere below the Tehuantepec Ridge. Geofis. Int. 44, 2157–2168.

Manea, V.C., Manea, M., Ferrari, L., 2013. A geodynamical perspective on the subduction of Cocos and Rivera plates beneath Mexico and Central America. Tectonophysics 609, 56–81.

Mao, X., Wang, Q., Liu, S., Xu, M., Wang, L., 2012. Effective elastic thickness and mechanical anisotropy of South China and surrounding regions. Tectonophysics 550–553, 47–56.

Mareschal, J.-C., Jaupart, C., 2013. Radiogenic heat production, thermal regime and evolution of Continental Crust. Tectonophysics 609, 524–534.

McAdoo, D.C., Martin, C.F., 1984. Seasat observation of geoid anomalies due to subducting slabs. J. Geophys. Res. 87, 8684–8692.

McAdoo, D.C., Martin, C.F., Poulose, S., 1985. Seasat observations of flexure: Evidence for a strong lithosphere. Tectonophysics 116, 209–222.

McKenzie, D., 2003. Estimating Te in the presence of internal loads. J. Geophys. Res. 108 (B9), 2438.

McKenzie, D.P., Fairhead, J.D., 1997. Estimates of the effective elastic thickness of the continental lithosphere from Bouguer and free air gravity anomalies. J. Geophys. Res. 102 (B12), 27523–27552.

McNutt, M.K., 1984. Lithospheric flexure and thermal anomalies. J. Geophys. Res. 89 (11), 11180–11194.

McNutt, M.K., Menard, H.W., 1982. Constraints on yield strength in the oceanic lithosphere derived from observations of flexure. Geophys. J. R. Astron. Soc. 71, 363–394.

Müller, R.D., Sdrolias, M., Gaina, C., Roest, W.R., 2008. Age, spreading rates, and spreading asymmetry of the world's ocean crust. Geochem. Geophys. Geosyst. 9, Q04006.

Percival, D.B., Walden, A.T., 1993. Spectral Analysis for Physical Applications, Multitaper and Conventional Univariate Techniques. Cambridge Univ. Press, New York, pp. 1–190.

Pérez-Gussinyé, M., Watts, A.B., 2005. The long-term strength of Europe and its implications for plate forming processes. Nature 436, 381–384.

Pérez-Gussinyé, M., Lowry, A.R., Watts, A.B., Velicogna, I., 2004. On the recovery of the effective elastic thickness using spectral methods: examples from synthetic data and from the Fennoscandian Shield. J. Geophys. Res. 109.

Pérez-Gussinyé, M., Lowry, A.R., Watts, A.B., 2007. Effective elastic thickness of South America and its implications for intracontinental deformation. Geochem. Geophys. Geosyst. 8 (5), Q05009.

Pérez-Gussinyé, M., Lowry, A.R., Phipps Morgan, J., Tassara, A., 2008. Effective elastic thickness variations along the Andean margin and their relationship to subduction geometry. Geochem. Geophys. Geosyst. 9, Q02003.

Pérez-Gussinyé, M., Swain, C.J., Kirby, J.F., Lowry, A.R., 2009a. Spatial variations of the effective elastic thickness, Te, using multitaper spectral estimation and wavelet methods: examples from synthetic data and application to South America. Geochem. Geophys. Geosyst. 10, Q04005.

Pérez-Gussinyé, M., Metois, M., Fernández, M., Vergés, J., Fullea, J., Lowry, A.R., 2009b. Effective elastic thickness of Africa and its relationship to other proxies for lithospheric structure and surface tectonics. Earth Planet. Sci. Lett. 287, 152–167.

Ranalli, G., 1997. Rheology of the lithosphere in space and time. Geol. Soc. (Lond.) Spec. Publ. 121, 19–37.

Ranero, C.R., Morgan, J.P., McIntosh, K., Reichert, C., 2003. Bending-related faulting and mantle serpentinization at the Middle America trench. Nature 425, 367–373.

Ranero, C.R., Villaseñor, A., Morgan, J.P., Weinrebe, W., 2005. Relationship between bend-faulting at trenches and intermediate-depth seismicity. Geochem. Geophys. Geosyst. 6, Q12002.

Ross, M.I., Scotese, C.R., 1988. A hierarchical tectonic model of the Gulf of Mexico and Caribbean region. Tectonophysics 155, 139–168.

Sandwell, D.T., Smith, W.H.F., 2009. Global marine gravity from retracked Geosat and ERS-1 altimetry: ridge segmentation versus spreading rate. J. Geophys. Res. 114, B01411.

Siebert, L., Simkin, T., 2002. Volcanoes of the world: an illustrated catalog of Holocene volcanoes and their eruptions. In: Smithsonian Institution, Global Volcanism Program Digital Information Series, GVP-3. http://www.volcano. si.edu/world/.

Simons, F.J., Zuber, M.T., Korenaga, J., 2000. Isostatic response of the Australian lithosphere: estimation of effective elastic thickness and anisotropy using multitaper spectral analysis. J. Geophys. Res. 105 (B8), 19,163–19,184.

Stark, C.P., Stewart, J., Ebinger, C.J., 2003. Wavelet transform mapping of effective elastic thickness and plate loading: validation using synthetic data and application to the study of southern African tectonics. J. Geophys. Res. 108 (B12), 2558.

Sykes, L.R., McCann, W.R., Kafka, A.L., 1982. Motion of Caribbean Plate during last 7 million years and implications for early Cenozoic movements. J. Geophys. Res. 87 (B13), 10656–10676.

Tassara, A., Swain, C.J., Hackney, R.I., Kirby, J.F., 2007. Elastic thickness structure of South America estimated using wavelets and satellite-derived gravity data. Earth Planet. Sci. Lett. 253, 17–36.

Tesauro, M., Kaban, M.K., Cloetingh, S.A.P.L., 2012. Global strength and elastic thickness of the lithosphere. Glob. Planet. Change 90–91, 51–57.

Thomson, D.J., 1982. Spectrum estimation and harmonic-analysis. Proc. IEEE 70 (9), 1055–1096.

Walden, A.T., McCoy, E.J., Percival, D.B., 1995. The effective bandwidth of a multitaper spectral estimator. Biometrika 82 (1), 201–214.

Watts, A.B., 2001. Isostasy and Flexure of the Lithosphere. Cambridge University Press. 472 pp.

Watts, A.B., Burov, E.B., 2003. Lithospheric strength and its relation to the elastic and seismogenetic layer thickness. Earth Planet. Sci. Lett. 213, 113–131.

Watts, A.B., Zhong, S., 2000. Observations of flexure and the rheology of oceanic lithosphere. Geophys. J. Int. 142 (3), 855–875.

Watts, A.B., Sandwell, D.T., Smith, W.H.F., Wessel, P., 2006. Global gravity, bathymetry, and the distribution of submarine volcanism through space and time. J. Geophys. Res. 111 (B8).

Wessel, P., Smith, W.H.F., Scharroo, R., Luis, J.F., Wobbe, F., 2013. Generic mapping tools: Improved version released. Eos Trans. AGU 94, 409–410.

Whittaker, J., Goncharov, A., Williams, S., Müller, R.D., Leitchenkov, G., 2013. Global sediment thickness dataset updated for the Australian–Antarctic Southern Ocean. Geochem. Geophys. Geosyst. 14 (8), 2547–3313.

3.3. Supplementary Material

"Spatial variations of effective elastic thickness of the lithosphere in Central America and surrounding regions"

Alberto Jiménez-Díaz, Javier Ruiz, Marta Pérez-Gussinyé, Jon F. Kirby,

José A. Álvarez-Gómez, Rosa Tejero and Ramón Capote

3.3.1. Bouguer coherence

To estimate the effective elastic thickness of the lithosphere (T_e) we calculate the coherence function relating the topography and Bouguer anomaly, commonly known as Bouguer coherence, using multitaper and wavelet methods. This function gives information on the wavelength band over which topography and Bouguer anomaly are correlated. In the coherence deconvolution method of Forsyth (1985), T_e is estimated by comparing the observed coherence curve with coherence functions predicted for a range of T_e values. For each given T_e, we calculate via deconvolution the initial surface and subsurface loads and compensating deflections that generate a predicted topography and gravity that best fit the observed topography and gravity anomaly, and a predicted coherence that best fits the observed coherence (Forsyth, 1985). The T_e value that minimizes the differences between the predicted and observed quantities is the optimal one for the analysed area.

The observed Bouguer coherence $\gamma^2_{obs}(k)$ in the Fourier domain is given by

$$\gamma^2_{obs}(k) = \frac{|\,\langle B(\mathbf{k})H^*(\mathbf{k})\rangle\,|^2}{\langle B(\mathbf{k})B^*(\mathbf{k})\rangle\,\langle H(\mathbf{k})H^*(\mathbf{k})\rangle}, \tag{3.1}$$

where B and H are the power spectrum of the Bouguer gravity anomaly and topography, respectively. Angle brackets denote averaging over wavenumber bands, the asterisk denotes complex conjugation, $\mathbf{k}$ is the two-dimensional wavenumber, and the modulus is $k = |\mathbf{k}| = \sqrt{k_x^2 + k_y^2}$. The Bouguer coherence generally tends to zero at short wavelengths, where the topography is not compensated and loads are supported predominantly by the elastic strength of the lithosphere (Forsyth, 1985). At long wavelengths, the response to loading approaches the Airy limit and the coherence tends to one. The wavelengths at which the coherence rapidly increases from 0 to 1 depend on the effective elastic thickness of the lithosphere, such that when the lithosphere is weak and T_e is small, local compensation for loading occurs at relatively shorter wavelengths and vice versa.

A fundamental assumption of the load deconvolution method developed by Forsyth (1985) is that surface loads (atop the lithosphere) and subsurface loads (within or below the lithosphere) are statistically uncorrelated. Consider two initial loads of geometric amplitude H_i and W_i applied at the surface and Moho (at depth z_m from sea level), respectively, of a thin elastic plate of known T_e. The initial surface load produces new surface topography H_T, and new Moho topography W_T. Similarly,

the initial internal load produces new surface topography H_B, and new Moho topography W_B. The relationships between the final surface/Moho topographies and the initial loads are

$$\begin{aligned} W_B &= v_B W_i \\ W_T &= v_T H_i \\ H_B &= \kappa_B W_i \\ H_T &= \kappa_T H_i, \end{aligned} \tag{3.2}$$

where the wavenumber-dependent deconvolution coefficients are obtained from the solution to the thin elastic plate equations (Forsyth, 1985)

$$\begin{aligned} v_B &= 1 - \frac{\Delta\rho_2}{\Phi} \\ v_T &= -\frac{\Delta\rho_1}{\Phi} \\ \kappa_B &= -\frac{\Delta\rho_2}{\Phi} \\ \kappa_T &= 1 - \frac{\Delta\rho_1}{\Phi}, \end{aligned} \tag{3.3}$$

where in turn $\triangle\rho_1 = \rho_c - \rho_f$, $\triangle\rho_2 = \rho_m - \rho_c$, ρ_c and ρ_m are respectively, crust and mantle densities, ρ_f is the density of the overlying fluid (i.e. either $\rho_f = 0$ on the continent or $\rho_f = \rho_w$ on the ocean), Φ is a function of D, $|\mathbf{k}|$ and g,

$$\Phi = \frac{D|\mathbf{k}|^4}{g} + \rho_m - \rho_f, \tag{3.4}$$

D is the flexural rigidity, $|\mathbf{k}|$ is the 1D wavenumber, and g is the gravitational acceleration (9.8 ms^{-2}). The flexural rigidity (D) is related to the elastic thickness (T_e) by

$$D = \frac{ET_e^3}{12(1-\upsilon^2)}, \tag{3.5}$$

where the elastic constants E and υ are respectively, Young's modulus (100 GPa) and Poisson's ratio (0.25) of the lithosphere.

The total resultant surface topography, H, and the net Moho topography, W, if both processes act together will be the sum of the components,

$$\begin{aligned} H &= H_T + H_B \\ W &= W_T + W_B. \end{aligned} \tag{3.6}$$

For combined surface and internal loading, the initial loads are related to the final, predicted Moho and surface topography after flexure (W and H, respectively) by a matrix equation

$$\begin{pmatrix} W \\ H \end{pmatrix} = \begin{pmatrix} v_B & v_T \\ \kappa_B & \kappa_T \end{pmatrix} \begin{pmatrix} W_i \\ H_i \end{pmatrix}. \tag{3.7}$$

In Forsyth (1985)'s original method, the observed Moho topography (W) is determined from the observed Bouguer gravity anomaly (B) using the relationship

$$W = \frac{Be^{|\mathbf{k}|z_m}}{2\pi G \triangle \rho_2}, \tag{3.8}$$

where G is the Newtonian gravitational constant.

Assuming that surface and subsurface loads are statistically uncorrelated, the predicted coherence $\gamma^2_{pre}(k)$ for an assumed T_e is then determined by substituting equations (3.6) and (3.8) into the coherence (equation 3.1) (Forsyth, 1985; Lowry and Smith, 1994), and can be written as

$$\gamma^2_{pre}(k) = \frac{|\left\langle W_T H_T^* + W_B H_B^* \right\rangle|^2}{\left\langle W_T W_T^* + W_B W_B^* \right\rangle \left\langle H_T H_T^* + H_B H_B^* \right\rangle}. \tag{3.9}$$

Alternatively, based on the gravity-deconvolution approach of Kirby and Swain (2011), we can compute the surface and internal loading components of the Bouguer anomaly, rather than Moho topography [as in Eq. (3.2)]. In this fashion, we have

$$\begin{aligned} B_B &= \mu_B W_i \\ B_T &= \mu_T H_i \\ H_B &= \kappa_B W_i \\ H_T &= \kappa_T H_i, \end{aligned} \tag{3.10}$$

where the wavenumber-dependent gravity deconvolution coefficients are

$$\begin{aligned} \mu_B &= 2\pi G \triangle \rho_2 e^{-|\mathbf{k}|z_m} v_B \\ \mu_T &= 2\pi G \triangle \rho_2 e^{-|\mathbf{k}|z_m} v_T, \end{aligned} \tag{3.11}$$

and the expressions for κ_B and κ_T in the Eq. (3.3) do not change. H and the net Bouguer anomaly, B, will be, if both processes act together, the sum of the components

$$\begin{aligned} H &= H_T + H_B \\ B &= B_T + B_B. \end{aligned} \tag{3.12}$$

For combined surface and internal loading, the initial loads are related to the final, predicted Bouguer anomaly and surface topography after flexure (B and H, respectively) by

$$\begin{pmatrix} B \\ H \end{pmatrix} = \begin{pmatrix} \mu_B & \mu_T \\ \kappa_B & \kappa_T \end{pmatrix} \begin{pmatrix} W_i \\ H_i \end{pmatrix}. \tag{3.13}$$

The predicted Bouguer coherence (Kirby and Swain, 2011) is then

$$\gamma^2_{pre}(k) = \frac{|\left\langle B_T H_T^* + B_B H_B^* \right\rangle|^2}{\left\langle B_T B_T^* + B_B B_B^* \right\rangle \left\langle H_T H_T^* + H_B H_B^* \right\rangle}. \tag{3.14}$$

We compare the observed coherence with curves predicted for a range of T_e values. The T_e value that minimizes the difference between predicted and observed coherence is the assigned T_e for the analysed area, such that this best fit T_e minimizes the weighted root-mean-square error:

$$\varepsilon = \sqrt{\frac{\sum_{i=1}^{N} \left[\gamma_{obs}^2(k_i) - \gamma_{pre}^2(k_i)\right]^2 / \sigma^2(k_i)}{\sum_{i=1}^{N} 1/\sigma^2(k_i)}}, \tag{3.15}$$

where N is the number of annular wavenumber bins, k_i is the i wavenumber (i =1, 2, ..., N), and $\sigma^2(k_i)$ is the jackknifed error estimated (Thomson and Chave, 1991) of the observed coherence and averaged within annular bins.

3.3.2. Multitaper method

To recover spatial variations in T_e we divide the analysis area into overlapping windows, such that in each window the coherence is calculated and inverted assuming a spatially constant T_e, moving the centre of each window 50 km for each new estimate. Calculation of the observed and predicted coherence involves transformation into the Fourier domain of the topography and Bouguer gravity anomaly to estimate their auto- and cross-power spectra. Because both data sets are non-periodic and finite, the Fourier transformation presents problems of frequency leakage (Thomson, 1982; Simons et al., 2000), resulting in estimated spectra that differ from the true spectra. To reduce leakage, the data are first multiplied by a set of orthogonal tapers in the space domain, the Fourier transform of the data-taper product taken for each taper, and the power spectrum determined at each taper. The final estimate of the signal's true power spectrum is then the weighted average of the individual power spectra over all tapers. The set of orthogonal tapers is defined by the bandwidth product NW that controls the wavelength resolution and spectral leakage (where N is the number of samples within the data window and W is the half bandwidth of the central lobe of the power spectral density of the first-order taper) and by the number of tapers K that governs the estimation variance (see Simons et al., 2000). The choice of bandwidth parameter NW in the multitaper technique is important. As the bandwidth increases, the resolution (i.e. the minimum separation in wave number between approximately uncorrelated spectral estimates) decreases (Walden et al., 1995). For a given bandwidth, W, there are up to $K = 2NW$-1 tapers with good leakage properties (Percival and Walden, 1993). The variance of the spectral estimates decreases with the number of tapers as $1/K$, so the bandwidth and resolution are chosen depending on the individual function under analysis (Percival and Walden, 1993). Here we apply the multitaper method using $NW = 3$ and $K = 3$, which are also used in several recent studies for T_e estimation (see e.g. Daly et al., 2004; Audet et al., 2007; Pérez-Gussinyé et al., 2009a; Kirby and Swain, 2011).

The effect of calculating T_e within a finite-size window is to limit the maximum wavelength of the gravity and topography that can be recovered. The choice of window size is critical in the multitaper estimation of T_e because it compromises the trade-off between resolution and variance of the estimates (Pérez-Gussinyé et al., 2004; Audet et al., 2007), such that large windows are better able to retrieve high T_e but degrade the spatial resolution and potentially merge tectonic provinces, while small windows provide high spatial resolution and analyse perhaps just one province but cannot resolve long flexural wavelengths. As the resulting T_e estimate depends on window size, we use three different window sizes (400 x 400 km, 600 x 600 km and 800 x 800 km, respectively; see Suppl. Fig. 1) to obtain high spatial resolution and at the same time recover potentially high T_e. Finally, the T_e results estimated from three different window sizes are merged to obtain the final T_e map. This is done by calculating a weighted average of the T_e estimated from each of the three windows following the approach of Pérez-Gussinyé et al. (2009b). This approach combines the information content regarding abrupt T_e gradients recovered by small windows and the more reliable information on high T_e recovered by the larger windows.

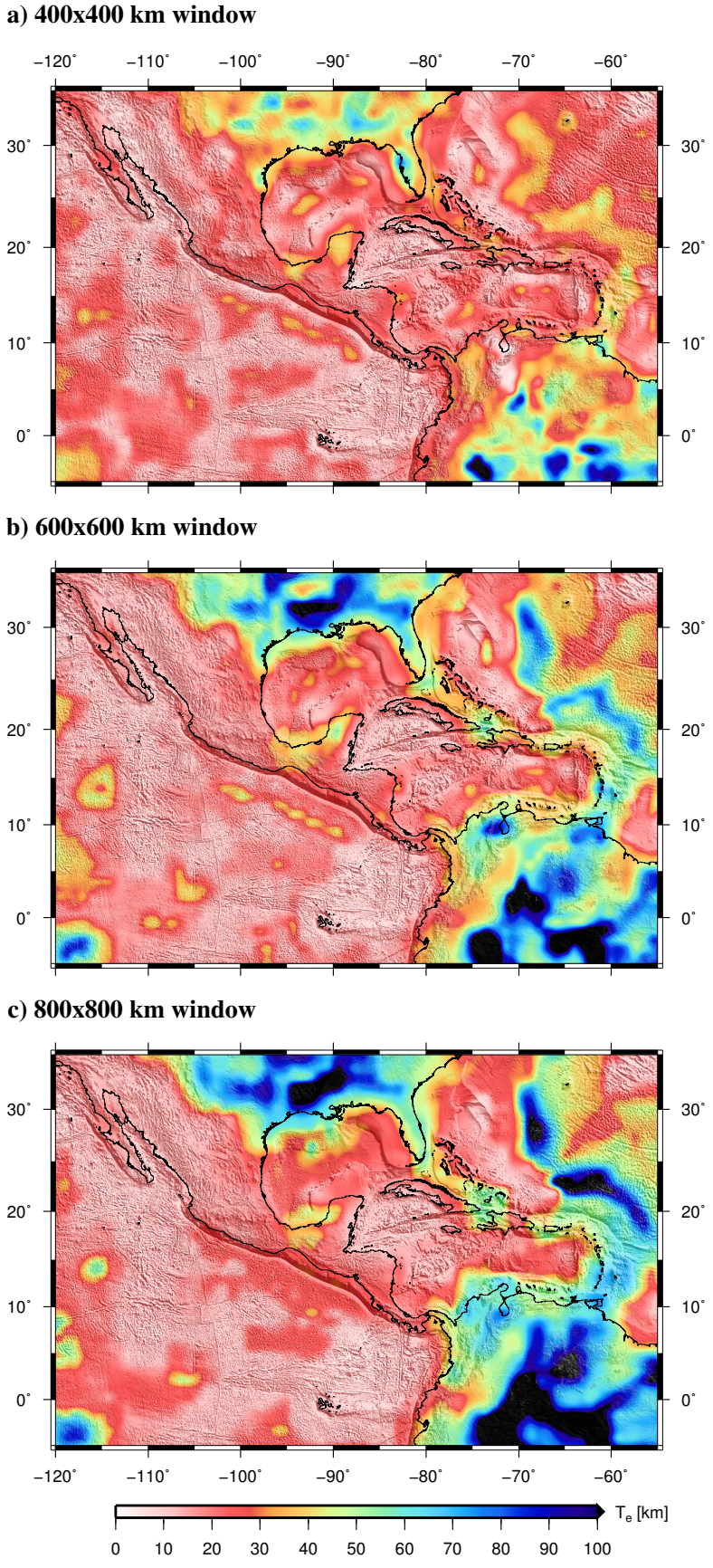

Supplementary Figure 1: Panels (a) to (c) show T_e of Central America and surrounding regions for three different window sizes using the multitaper method.

Suppl. Fig. 2 shows the weight scheme, which is designed so that estimates from small windows predominate when the recovered T_e^{rec} is low and large window estimates prevail when T_e^{rec} is high. The merged value, T_e^{merged}, is given by

$$T_e^{merged} = \left(\sum_{i=1}^{nwin} \omega_i\right) \left[\sum_{i=1}^{nwin} \omega_i f_i^{-1}(T_e^{rec})\right], \tag{3.16}$$

(Pérez-Gussinyé et al., 2009b), where ω_i are the weights assigned to each window. These weights are defined as Gaussian curves centred on T_e^{cen}, located midway between the maximum T_e recoverable within the given window and the maximum T_e recoverable within the next smaller window. We assume that the maximum recoverable T_e corresponds to that having the maximum transitional wavelength that fits within the window (e.g. 37, 63 and 93 km for 400 x 400 km, 600 x 600 km and 800 x 800 km windows, respectively; Pérez-Gussinyé et al., 2009b). The smallest and largest windows are given a weight of 1 for T_e lower and higher, respectively, than T_e^{cen}. The bandwidth of the Gaussian curve was chosen so the transition from one window to the next would be smooth. Pérez-Gussinyé et al. (2009b) tested a range of bandwidths and the difference in resulting merged maps is not appreciable.

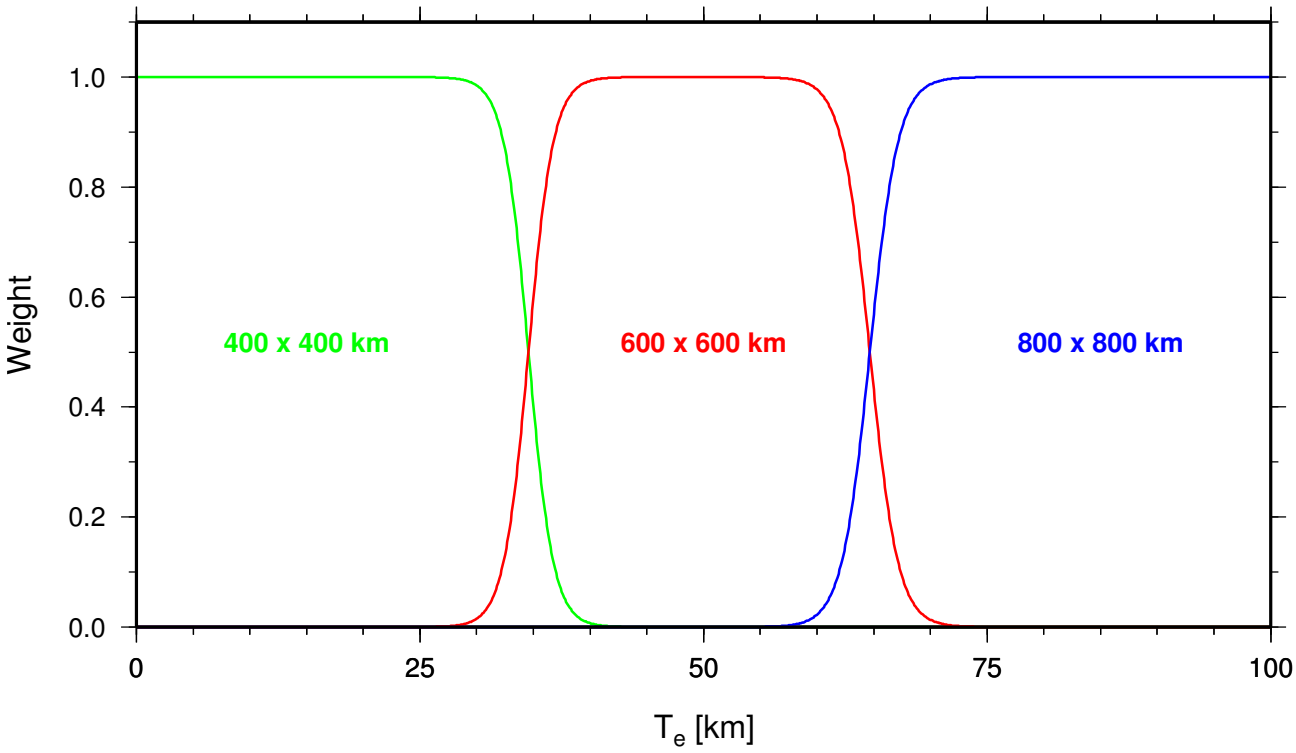

Supplementary Figure 2: Weights, w_i, applied to the results obtained with each window. The weights are Gaussian curves, centred on T_e^{cen} mid-way between the maximum T_e recoverable with a given window and the maximum T_e recoverable with the next smaller window. Three windows for analysis are used, 400×400 km: green line, 600×600 km windows: red line, and 800×800 km windows: blue line.

Suppl. Fig. 3 shows final T_e after merging the results from the three different window sizes (400, 600 and 800 km^2; see Supp. Fig. 1). The final T_e structure retains the primary characteristics of the largest window, but it better resolves the sharp gradient between low and high T_e areas and the short wavelength variations in T_e.

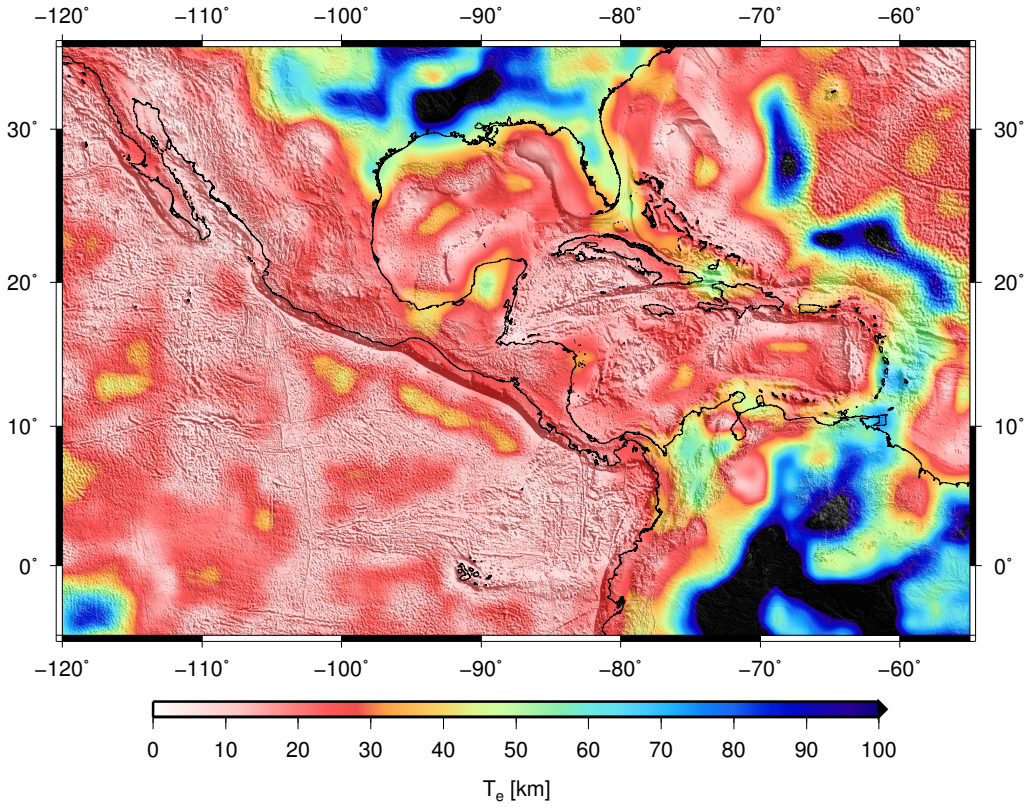

Supplementary Figure 3: T_e over Central America and surrounding regions from the multitaper method. Figure shows final T_e after merging the results from the three different window sizes (see Supp. Fig. 1).

The effect of window size and/or of the multitaper parameters on the coherence and the nature of bias at short/long wavelengths, as well as on T_e estimates, is discussed in more detail by McKenzie and Fairhead (1997), Simons et al. (2000), Daly et al. (2004), Pérez-Gussinyé et al. (2004, 2007, 2008, 2009a, 2009b), Audet et al. (2007), Kirby and Swain (2011, 2013) and Deng et al. (2013).

3.3.3. Wavelet method

The wavelet method convolves a range of scaled wavelets with the whole data set to map and invert the coherence at each grid point, and achieves good wavenumber resolution over long length scales and good spatial resolution over short length scales. Here we employ a Morlet wavelet of high spatial resolution in the fan wavelet transform (Kirby and Swain, 2011). The 2-D Morlet wavelet (Dallard and Spedding, 1993), can be defined in both space and wavenumber domains. Furthermore, it has two forms, the simple and complete wavelets.

The space-domain equation of the simple 2-D Morlet wavelet is

$$\psi(\mathbf{x}) = \mathrm{e}^{i\mathbf{k}_0\mathbf{x}} - \mathrm{e}^{-|\mathbf{x}|^2/2} \tag{3.17}$$

(Dallard and Spedding, 1993; Antoine et al., 2004), where $|\mathbf{k}_0|$ is the 'central wavenumber', and governs the resolution of the wavelet in the space and wavenumber domains. Larger values of $|\mathbf{k}_0|$ give better wavenumber resolution but poorer spatial resolution, and vice versa for smaller values (Addison, 2002). In the wavenumber domain the simple 2-D Morlet wavelet's equation is

$$\hat{\psi}(\mathbf{k}) = \mathrm{e}^{-|\mathbf{k}-\mathbf{k}_0|^2/2} \tag{3.18}$$

(Dallard and Spedding, 1993; Antoine et al., 2004). However, when $|\mathbf{k}_0|$ is small (generally taken to be $|\mathbf{k}_0| < 5$), the simple Morlet wavelet has a significant non-zero mean value, which results in it no longer being a true wavelet (Addison, 2002). Hence, a correction is made to restore zero mean, giving the complete Morlet wavelet. The space-domain equation of the complete 2-D Morlet wavelet is

$$\psi(\mathbf{x}) = (\mathrm{e}^{i\mathbf{k}_0\mathbf{x}} - \mathrm{e}^{-|\mathbf{k}_0|^2/2})\mathrm{e}^{-|\mathbf{x}|^2/2} \tag{3.19}$$

(Addison et al., 2002; Antoine et al., 2004), with Fourier transform

$$\hat{\psi}(\mathbf{k}) = \mathrm{e}^{-|\mathbf{k}-\mathbf{k}_0|^2/2} - \mathrm{e}^{-(|\mathbf{k}|^2+|\mathbf{k}_0|^2)/2} \tag{3.20}$$

(Addison et al., 2002; Antoine et al., 2004). The extra terms present in the complete wavelet's formulae make closed, analytic solutions of some of its properties impossible.

The choice of the value of $|\mathbf{k}_0|$, described in Kirby and Swain (2011), is governed by the amplitude of the first sidelobes of the simple wavelet. If this amplitude is a fraction $1/p$ ($p > 1$) of the amplitude of the central peak of the real part of the space-domain wavelet, then $|\mathbf{k}_0| = \pi\sqrt{2/\ln p}$. The values of $|\mathbf{k}_0|$ that we use in this study are 2.668, 3.081, 3.773 and 5.336 (see Suppl. Fig. 4-6), which give a space-domain wavelet whose first sidelobes are 1/16, 1/8, 1/4 and 1/2 of the magnitude of the central amplitude, respectively.

The peak wavenumber of the simple 2-D Morlet wavelet at a scale s is given by

$$\kappa = \frac{|\mathbf{k}_0|}{s} \tag{3.21}$$

(Kirby 2005). Kirby and Swain (2011) have given a method to compute the peak wavenumber for the complete version, which has no closed, analytic equation.

Kirby and Swain (2011) find that owing to the better **k**-resolution, values of $|\mathbf{k}_0| > 5$ give more accurate absolute T_e estimates if the tectonic province is large and contains a relatively uniform T_e; in such case, the low **x**-resolution of these wavelets is of less importance. If detailed T_e structure and/or accurate relative T_e differences are required, then values of $|\mathbf{k}_0| < 3.5$ are more likely to be useful, though the lower **k**-resolution of these wavelets could indicate grater uncertainty on the T_e estimates. Kirby and Swain (2013) also find that the bandwidth, as a proxy for uncertainty, varies linearly with wavenumber. That is, 2-D Morlet wavelets have better wavenumber resolution at low wavenumbers than at large ones. The bandwidth is also inversely proportional to $|\mathbf{k}_0|$, with high values of this parameter giving better wavenumber resolution (see Kirby and Swain, 2013 for an expanded discussion).

To recover T_e, the Bouguer gravity anomaly and topography are mirrored about their edges prior to Fourier transformation, which, when used with the wavelet transform does not generally bias the results significantly, as it can with the periodogram method (Kirby and Swain, 2008). The wavelet transform is then applied to both data sets to calculate the auto and cross-spectra at different azimuths and scales. We follow Kirby and Swain (2009) and invert the square of the real part of the wavelet coherency (SRC), rather than the coherence, because it is less sensitive to correlations between the initial loads on the plate and to "gravitational noise", both of which can cause incorrect recovery of T_e (Kirby and Swain, 2009, 2011). The observed Bouguer SRC (Kirby and Swain, 2009) is given by

$$\Gamma_R^2(|\mathbf{k}|) = \frac{(\mathrm{Re}\,\langle BH^*\rangle)^2}{\langle BB^*\rangle\,\langle HH^*\rangle}, \tag{3.22}$$

where B and H are now wavelet transforms of Bouguer anomaly and topography, respectively, and Re denotes that only the real part is used.

Equivalently, the predicted Bouguer SRC expression is then

$$\Gamma_{pre}(|\mathbf{k}|) = \frac{\langle B_T H_T^* + B_B H_B^*\rangle_{|\mathbf{k}|}}{\langle B_T B_T^* + B_B B_B^*\rangle_{|\mathbf{k}|}^{1/2}\,\langle H_T H_T^* + H_B H_B^*\rangle_{|\mathbf{k}|}^{1/2}}. \tag{3.23}$$

The fan wavelet method is based on a further development of Eq. (3.23) which greatly improves computation times (Kirby and Swain, 2011). If Eq. (3.10) is substituted into Eq. (3.23), we get

$$\Gamma_{pre}(|\mathbf{k}|) = \frac{\langle \mu_T \kappa_T |H_i|^2 + \mu_B \kappa_B |W_i|^2\rangle_{|\mathbf{k}|}}{\langle \mu_T^2 |H_i|^2 + \mu_B^2 |W_i|^2\rangle_{|\mathbf{k}|}^{1/2}\,\langle \kappa_T^2 |H_i|^2 + \kappa_B^2 |W_i|^2\rangle_{|\mathbf{k}|}^{1/2}}, \tag{3.24}$$

as the Fourier transform expression. On the other hand, as a consequence of load deconvolution procedure, the loading ratio can be estimated from the recreated initial loads (Forsyth, 1985). Based on the approach of Kirby and Swain (2011), we can use the loading ratio (f) introduced by Forsyth (1985), and get the predicted Bouguer SRC in terms of the wavelet transform through

$$\Gamma_{pre}^{(WT)}(s,\mathbf{x}) = \frac{\mu_T \kappa_T + \mu_B \kappa_B f^2 r^2}{\left[\mu_T^2 + \mu_B^2 f^2 r^2\right]^{1/2}\left[\kappa_T^2 + \kappa_B^2 f^2 r^2\right]^{1/2}}, \tag{3.25}$$

where $f^2(s,\mathbf{x}) = \frac{\langle|\tilde{W}_i|^2\rangle_\theta}{r^2\langle|\tilde{H}_i|^2\rangle_\theta}$, and $r = \Delta\rho_1/\Delta\rho_2$.

The minimum χ^2 misfit between observed and predicted SRC is found using Brent's method of minimisation (Press et al., 1992), with the inversion weighted using jackknife error estimates (Thomson and Chave, 1991) calculated through

$$\chi^2 = \sum \left(\frac{\Gamma^2_{B,o,R} - \Gamma^2_{B,p,R}}{\varepsilon_{\Gamma^2_{B,o,R}}} \right)^2, \tag{3.26}$$

where $\Gamma^2_{B,o,R}$ is the observed Bouguer SRC, $\Gamma^2_{B,p,R}$ is the predicted Bouguer SRC, and $\varepsilon_{\Gamma^2_{B,o,R}}$ is the error on the observed Bouguer SRC. The T_e values corresponding to the minimum χ^2 misfit is assigned to the grid nodes in the study area.

The load deconvolution wavelet method can also estimates the ratio between the initial internal and surface load amplitudes (the loading ratio, f ; Forsyth, 1985). We can display the loading ratio results in terms of the F parameter, the internal load fraction (McKenzie, 2003). The relationship between f and F is given by

$$F = \frac{f}{1+f}. \tag{3.27}$$

Thus, whereas f is the ratio of the initial internal load amplitude to the initial surface load amplitude, F is the ratio of the initial internal load amplitude to the total amplitude of both initial loads. While f varies between 0 and ∞, F varies between 0 and 1. Purely surface loading gives $f = F = 0$, purely internal loading gives $f = \infty$ and $F = 1$, while equal surface and internal loading gives $f = 1$ and $F = 0.5$. Note that f and F are wavenumber-dependent parameters (Kirby and Swain, 2009).

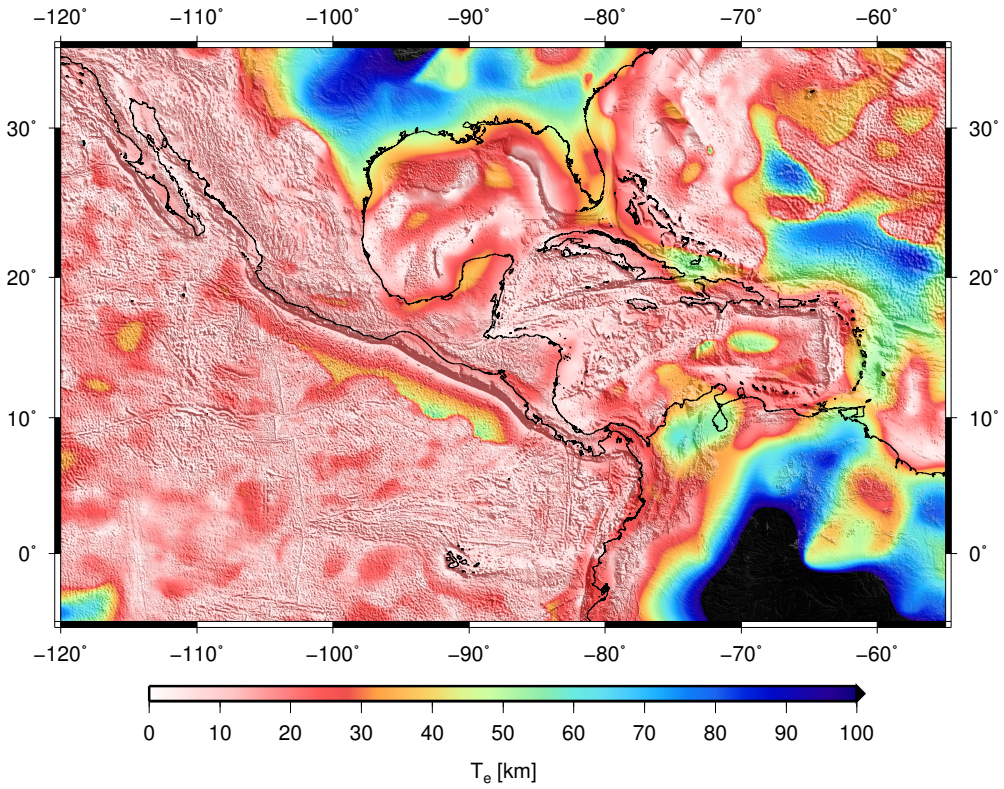

Supplementary Figure 4: T_e over Central America and surrounding regions from the wavelet method with $|\mathbf{k}_0| = 2.668$.

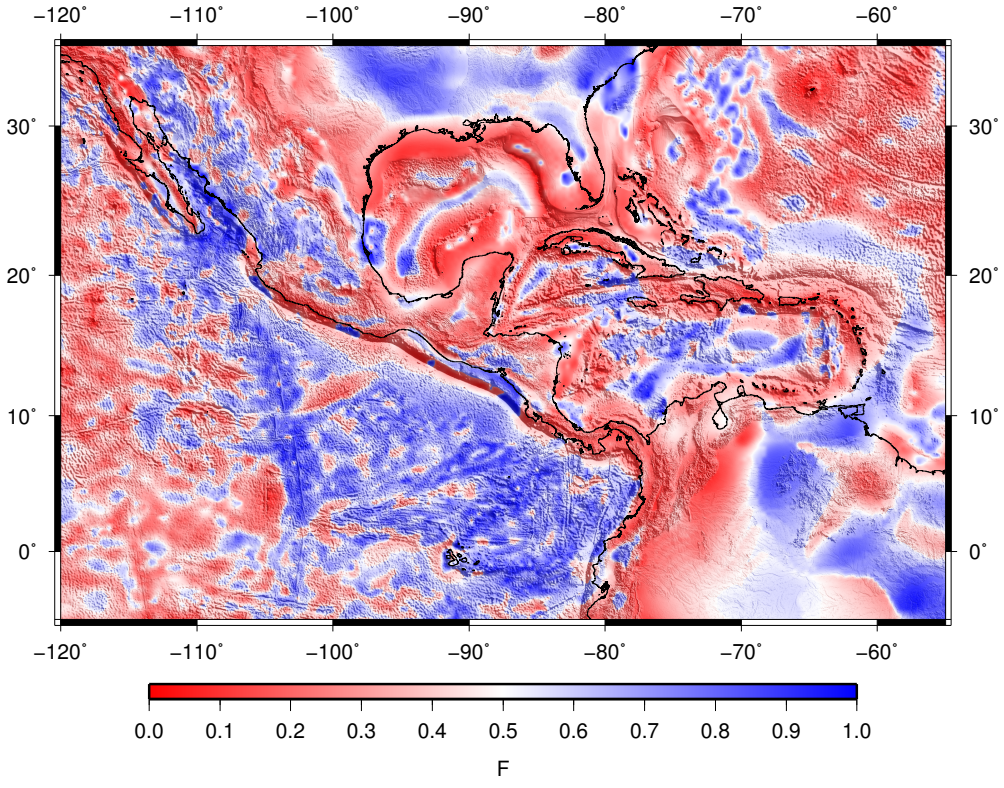

Supplementary Figure 5: Loading ratio, F, corresponding to the T_e results in Suppl. Fig. 4.

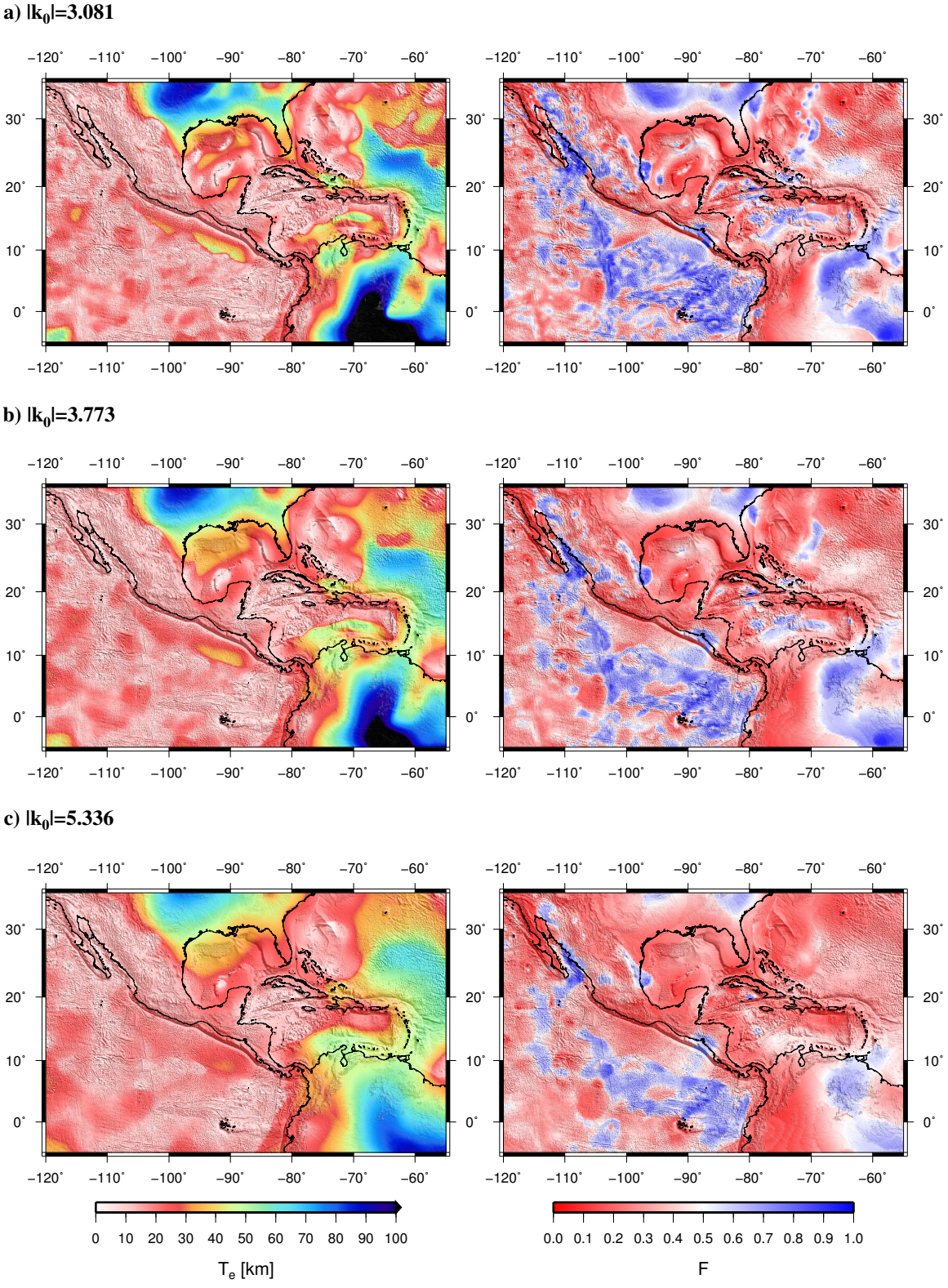

Supplementary Figure 6: T_e and loading ratio, F, corresponding to the T_e results over Central America and surrounding regions from wavelets with the following $|\mathbf{k}_0|$ values: (a) 3.081, (b) 3.773, and (c) 5.336.

3.3.4. Bias in T_e estimation

A fundamental assumption of the load deconvolution method developed by Forsyth (1985) is that surface and subsurface loads are statistically uncorrelated. In many cases, however, surface and subsurface loading are likely to be tectonically related processes and, therefore, spatially correlated (Forsyth, 1985). Subsurface loads include mafic intrusions, accreted lower crustal material, thermal anomalies and compositional variations, which cause lateral variations of density at depth and may have a strong influence on T_e estimates (Stark et al., 2003). Meanwhile, surface loading is caused by topography and large-scale variations in surface density (e.g., mountains and sedimentary basin). Macario et al. (1995) showed that when the degree of correlation of initial surface and subsurface loading increases, the T_e values estimated using Forsyth's (1985) deconvolution method can be biased downward. Kirby and Swain (2009) present an extensive analysis of load correlation and its effect on T_e using the load deconvolution method of Forsyth (1985), showing that the real part of the Bouguer coherency identifies wavelengths over which loads are correlated.

Furthermore, erosion and sedimentation may play an important role in modifying the relationship between surface topography and subsurface density anomalies (e.g., Forsyth, 1985; McKenzie and Fairhead, 1997). Both processes can reduce the landscape to a perfectly flat surface, removing the topographic expression of subsurface loads. The presence of topographically unexpressed internal loading, known as "noise" or "gravitational noise" (McKenzie and Fairhead, 1997; McKenzie, 2003; Kirby and Swain, 2009), biases the T_e upward. As pointed out by Kirby and Swain (2009), this problem can occur in regions of subdued topography, and predominantly affects areas where the coherence method indicates high T_e. We analyse the bias in T_e estimation related to the effect of "gravitational noise" following the approach of Kirby and Swain (2009), based on the maximum normalized imaginary component of free-air coherency ($\overline{\Gamma}^2_{F,I}$). Suppl. Fig. 7 shows a map of T_e from the wavelet method (with $|\mathbf{k}_0| = 2.668$) wherein we have masked out regions where the corresponding noise levels are high (i.e., where the load-deconvolution method fails) and are likely to bias T_e. It should be noted that "gravitational noise" does exist in the study area, which casts doubt upon T_e values in some regions, especially where we have recovered very high values. Note that while large "gravitational noise" indicates a failure of the plate loading model (and T_e estimation from gravity-topography spectra), it does not imply that the lithosphere is weak (Audet and Bürgmann, 2011). Kirby and Swain (2011) found that the size of the area affected increases as $|\mathbf{k}_0|$ decreases, and that the lower $\mathbf{k}$-resolution of low-$|\mathbf{k}_0|$ wavelets results in the noise spectrum being smeared over a larger bandwidth than with high-$|\mathbf{k}_0|$ wavelets.

We refer the interested reader to McKenzie and Fairhead (1997), Banks et al. (2001), McKenzie (2003), Stark et al. (2003), Pérez-Gussinyé et al. (2004, 2009a, 2009b), Crosby (2007), Kirby and Swain (2008, 2009, 2011), Audet and Bürgmann (2011) and Artemieva (2011) for an extended discussion about the influence of the initial correlations between the surface and subsurface loads and/or of the "gravitational noise" on T_e estimates.

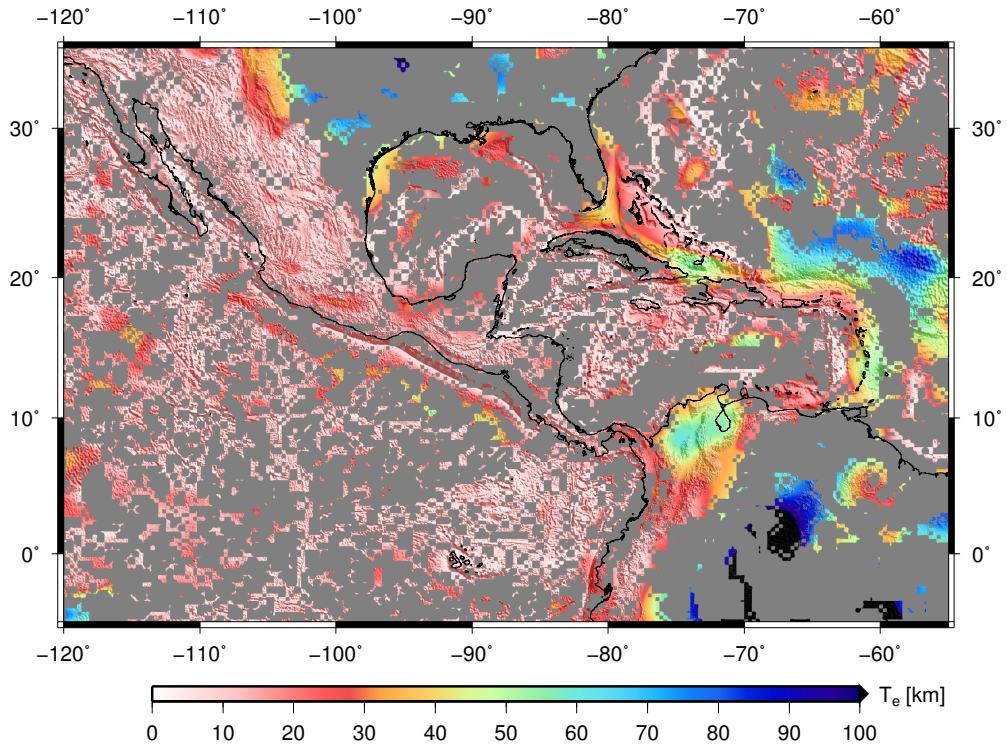

Supplementary Figure 7: Map of T_e of Central America and surrounding regions from the wavelet method (with $|\mathbf{k}_0| = 2.668$) with regions of $\overline{\Gamma}^2_{F,I} > 0.5$ masked in grey; where $\overline{\Gamma}^2_{F,I}$ is the maximum value of the normalized free-air SIC.

References

Addison, P.S., 2002. The Illustrated Wavelet Transform Handbook, Institute of Physics Publishing, Bristol, UK.

Addison, P.S., Watson, J.N., Feng, T., 2002. Low-oscillation complex wavelets. J. Sound Vibr., 254, 733-762.

Antoine, J.-P., Murenzi, R., Vandergheynst, P., Ali, S.T., 2004. Two-Dimensional Wavelets and their Relatives. Cambridge University Press, Cambridge

Artemieva, I., 2011. The Lithosphere: An Interdisciplinary Approach. Cambridge University Press (773 pp.).

Audet, P., Bürgmann, R., 2011. Dominant role of tectonic inheritance in supercontinent cycles. Nature Geoscience 4, 184–187.

Audet, P., Jellinek, A.M., Uno, H., 2007. Mechanical controls on the deformation of continents at convergent margins. Earth Planet. Sci. Lett. 264, 151–166.

Banks, R.J., Francis, S.C., Hipkin, R.G., 2001. Effects of loads in the upper crust on estimates of the elastic thickness of the lithosphere. Geophysical Journal International 145, 291–299.

Crosby, A.G., 2007. An assessment of the accuracy of admittance and coherence estimates using synthetic data. Geophys. J. Int., 171, 25–54.

Dallard, T., Spedding, G.R., 1993. 2-D wavelet transforms: generalisation of the Hardy space and application to experimental studies. Eur. J. Mech., 12, 107-134.

Daly, E., Brown, C., Stark, C.P., Ebinger, C.J., 2004. Wavelet and multitaper coherence methods for assessing the elastic thickness of the Irish Atlantic margin. Geophys. J. Int., 159, 445–459.

Deng, Y., Zhang, Z., Fan, W., Pérez-Gussinyé, M., 2013. Multitaper spectral method to estimate the elastic thickness of South China: Implications for intracontinental deformation. Geoscience Frontiers, in press. http://dx.doi.org/10.1016/j.gsf.2013.05.002.

Forsyth, D.W., 1985. Subsurface loading estimates of the flexural rigidity of continental lithosphere. J. Geophys. Res. 90, 12,623–12,632.

Kirby, J.F., Swain, C.J., 2008. An accuracy assessment of the fanwavelet coherence method for elastic thickness estimation. Geochemistry, Geophysics, Geosystems 9 (3), Q03022. (Correction. 2008. Geochemistry, Geophysics, Geosystems. 9(5), Q05021).

Kirby, J.F., Swain, C.J., 2009. A reassessment of spectral Te estimation in continental interiors: the case of North America. Journal of Geophysical Research 114, B08401.

Kirby, J.F., Swain, C.J., 2011. Improving the spatial resolution of effective elastic thickness estimation with the fan wavelet transform. Computers and Geosciences 37, 1345–1354.

Kirby, J.F., Swain, C.J., 2013. Power spectral estimates using two-dimensional Morlet-fan wavelets with emphasis on the long wavelengths: jackknife errors, bandwidth resolution and orthogonality properties. Geophysical Journal International 194, 78-99.

Lowry, A.R., Smith, R.B., 1994. Flexural rigidity of the Basin and Range-Colorado Plateau-Rocky Mountain transition from coherence analysis of gravity and topography. Journal of Geophysical Research 99 (B10), 20, 123–20, 140.

Macario, A., Malinverno, A., Haxby, W.F., 1995. Onthe robustness of elastic thickness estimates obtained using the coherence method. J. Geophys. Res. 100 (D8), 15,163–15,172.

McKenzie, D., 2003. Estimating Te in the presence of internal loads. Journal of Geophysical Research 108 (B9), 2438.

McKenzie, D.P., Fairhead, J.D., 1997. Estimates of the effective elastic thickness of the continental lithosphere from Bouguer and free air gravity anomalies, J. geophys. Res., 102(B12), 27 523–27 552.

Percival, D.B., Walden, A.T., 1993. Spectral Analysis for Physical Applications, Multitaper and Conventional Univariate Techniques, pp. 1-190, Cambridge Univ. Press, New York.

Pérez-Gussinyé, M., Lowry, A.R., Watts, A.B., Velicogna, I., 2004. On the recovery of the effective elastic thickness using spectral methods: examples from synthetic data and from the Fennoscandian Shield. J. Geophys. Res. 109.

Pérez-Gussinyé, M., Lowry, A.R., Watts, A.B., 2007. Effective elastic thickness of South America and its implications for intracontinental deformation. Geochem. Geophys. Geosyst. 8 (5), Q05009.

Pérez-Gussinyé, M., Lowry, A.R., Phipps Morgan, J., Tassara, A., 2008. Effective elastic thickness variations along the Andean margin and their relationship to subduction geometry. Geochem. Geophys. Geosyst. 9, Q02003.

Pérez-Gussinyé, M., Swain, C.J., Kirby, J.F., Lowry, A.R., 2009a. Spatial variations of the effective elastic thickness, Te, using multitaper spectral estimation and wavelet methods: examples from synthetic data and application to South America. Geochem. Geophys. Geosyst. 10, Q04005.

Pérez-Gussinyé, M., Metois, M., Fernández, M., Vergés, J., Fullea, J., Lowry, A.R., 2009b. Effective elastic thickness of Africa and its relationship to other proxies for lithospheric structure and surface tectonics. Earth Planet. Sci. Lett. 287, 152–167.

Press, W.H., Teukolsky, S.A., Vetterling, W.T., Flannery, B.P., 1992. 2nd Edn. Numerical Recipes in Fortran 77. Cambridge University Press, Cambridge, 933 pp.

Simons, F.J., Zuber, M.T., Korenaga, J., 2000. Isostatic response of the Australian lithosphere: estimation of effective elastic thickness and anisotropy using multitaper spectral analysis. Journal of Geophysical Research 105 (B8), 19,163–19,184.

Stark, C.P., Stewart, J., Ebinger, C.J., 2003. Wavelet transform mapping of effective elastic thickness and plate loading: validation using synthetic data and application to the study of southern African tectonics. J. Geophys. Res. 108 (B12), 2558.

Thomson, D.J., 1982. Spectrum estimation and harmonic-analysis. Proceedings of the IEEE 70 (9), 1055–1096.

Thomson, D.J., Chave, A.D., 1991. Jackknifed error estimates for spectra, coherences, and transfer functions. In: Haykin, S. (Ed.), Advances in Spectrum Analysis and Array Processing, vol. 1(2). Prentice Hall, Englewood Cliffs, NJ, pp. 58–113.

Walden, A. T., McCoy, E. J., Percival, D. B., 1995. The effective bandwidth of a multitaper spectral estimator. Biometrika, 82(1), 201-214.

Capítulo 4

Análisis integrado de la topografía y gravedad en el estudio de la estructura cortical y litosférica de los planetas terrestres: Estructura de la litosfera de Venus

4. Análisis integrado de la topografía y gravedad en el estudio de la estructura cortical y litosférica de los planetas terrestres: Estructura de la litosfera de Venus

4.1. Introducción

El análisis de los datos de topografía y gravedad es una potente herramienta para constreñir aspectos fundamentales sobre la geodinámica de los planetas terrestres, que permite "sondear" la estructura y el comportamiento mecánico de sus litosferas y, en concreto, su respuesta ante cargas y descargas (Wieczorek, 2007; Watts et al., 2013). En particular, un parámetro muy útil que describe este comportamiento es el espesor elástico efectivo de la litosfera (T_e), el cual, a su vez, puede ser usado para constreñir la estructura y evolución térmica de un cuerpo planetario (p.ej., Zuber et al., 2000; McGovern et al., 2002; Ruiz et al., 2011) (véase el Capítulo 5). Los avances más recientes, tanto en el análisis espectral de la gravedad y topografía como en la modelización litosférica de la Tierra, han permitido caracterizar la variación espacial del espesor elástico efectivo en ésta con una resolución sin precedentes (Audet, 2014; Kirby, 2014).

Venus y la Tierra tienen un tamaño similar, una densidad y composición equivalentes, y distancias respecto al Sol comparables. A pesar de estas similitudes, la tectónica y la evolución dinámica de Venus son muy diferentes a las de la Tierra. La litosfera venusiana es estable y no muestra evidencias de tectónica de placas en el presente (p.ej., Solomon y Head, 1982; Solomon et al., 1992). Las observaciones realizadas por la misión Venus Express aportan evidencias de vulcanismo reciente, o incluso actual, en su superficie (Smrekar et al., 2010). No obstante, la historia térmica de Venus continúa siendo un enigma y hay planteadas muchas preguntas fundamentales sobre la estructura y evolución de su litosfera, referidas a aspectos claves para comprender Venus en el marco de los planetas terrestres (p.ej., VEXAG, 2014).

En este contexto, el artículo que se presenta en este capítulo aborda el análisis de la estructura litosférica de Venus mediante el cálculo del espesor cortical (T_c) y el espesor elástico efectivo a partir del análisis de la topografía y la gravedad, con el objetivo de reevaluar la variación regional en la estructura y el comportamiento mecánico de su litosfera. Este estudio fue concebido, desde un punto de vista metodológico, como una continuación del anterior (ver Capítulo 3), y pretende obtener una visión mucho más amplia del concepto de litosfera. En este artículo se presenta un modelo global de espesor de corteza, necesario para el análisis litosférico, obtenido a partir de la inversión de los datos de topografía y gravedad. El análisis espectral de la coherencia entre la topografía y la anomalía de Bouguer ha permitido obtener un mapa global de las variaciones espaciales de T_e y analizar la importancia relativa de los mecanismos de las cargas superficiales e internas asociados. Finalmente,

se discuten las implicaciones de los resultados en el conocimiento del comportamiento mecánico de la litosfera venusiana a largo plazo.

Los resultados muestran que la corteza de Venus tiene un espesor característico de 20-25 km, con espesores mayores asociados a las tierras altas (mesetas o "plateaus" corticales y grandes macizos volcánicos). Esto sugiere que la mayor parte de la corteza venusiana se formó en condiciones similares, y diferentes a las que prevalecían cuando se formaron gran parte de las tierras altas. El espesor elástico efectivo obtenido varía entre 14 (el mínimo T_e recuperable en el caso de Venus) y 94 km, pero claramente dominado por valores bajos y moderados. Las variaciones de espesor elástico deducidas de nuestro modelo podrían reflejar variaciones regionales en la historia de enfriamiento de la litosfera de Venus, así como procesos mantélicos con una limitada manifestación superficial. Las mesetas corticales están cerca de un estado de compensación isostático, consistente con una litosfera elástica delgada, y mostrando una corteza de mayor espesor bajo ellas, mientras que las tierras bajas exhiben valores de espesor elástico altos, quizás indicativos de una litosfera más fría que cuando se formaron las tierras altas. Por otra parte, existen grandes macizos volcánicos que muestran una señal muy compleja, con un amplio rango de valores de espesor elástico y de mecanismos de carga asociados. Finalmente, nuestros resultados revelan una importante contribución de la parte superior del manto a la resistencia de la litosfera en este planeta.

4.2. Lithospheric structure of Venus from gravity and topography

Alberto Jiménez-Díaz [a,b], Javier Ruiz [a], Jon F. Kirby [c],

Ignacio Romeo [a], Rosa Tejero [a,b], Ramón Capote [a]

[a] *Departamento de Geodinámica, Facultad de Ciencias Geológicas, Universidad Complutense de Madrid. 28040 Madrid, Spain*

[b] *Instituto de Geociencias, IGEO (CSIC, UCM). 28040 Madrid, Spain*

[c] *Department of Spatial Sciences, Curtin University, GPO Box U1987, Perth WA 6845, Australia*

Submitted to *Icarus* (under review), 2014.

Abstract

There are many fundamental and unanswered questions on the structure and evolution of the Venusian lithosphere, which are key issues for understanding Venus in the context of the terrestrial planets. Here we investigate the lithospheric structure of Venus by calculating its crustal and effective elastic thicknesses (T_c and T_e, respectively) from an analysis of gravity and topography, in order to improve our knowledge of the large scale and long-term mechanical behaviour of its lithosphere. We found that the Venusian crust is usually 20-25 km thick with thicker crust under the highlands. Our effective elastic thickness values range between 14 km (corresponding to the minimum resolvable T_e value) and 94 km, but are dominated by low to moderate values. T_e variations deduced from our model could represent regional variations in the cooling history of the lithosphere and/or mantle processes with limited surface manifestation. The crustal plateaus are near-isostatically compensated, consistent with a thin elastic lithosphere, showing a thickened crust beneath them, whereas the lowlands exhibit higher T_e values, maybe indicating a cooler lithosphere than that when the Venusian highlands were emplaced. Meanwhile, the large volcanic rises show a complex signature, with a broad range of T_e and subsurface-to-surface load ratio (F) values. Finally, our results also reveal a significant contribution of the upper mantle to the strength of the lithosphere in many regions.

4.2.1. Introduction

Venus and the Earth share a similar size, nearly equivalent density and bulk composition, and comparable distances from the Sun. Despite these similarities, Venus's tectonics and dynamic evolution are very different from those of the Earth. The Venusian lithosphere is stagnant and shows no evidence for present-day global plate tectonics (e.g., Solomon and Head, 1982; Solomon et al., 1992). Recent data provided from the Venus Express Mission show evidence of geologically young, and even ongoing, volcanism on the Venusian surface (Smrekar et al., 2010). However, the thermal history of Venus remains an enigma and there are many fundamental and unanswered questions on the structure

and evolution of its lithosphere (e.g., Smrekar et al., 1997; Stofan et al., 1997; Phillips et al., 1997; Grimm and Hess, 1997), which are key issues for understanding Venus in the context of the terrestrial planets (Garvin et al., 2009; Sotin et al., 2014; VEXAG, 2014).

The analysis of gravity and topography data provides useful constraints to solve many fundamental questions on the geodynamics of terrestrial planets, probing the structure and mechanical behaviour of their lithospheres, for example how they respond to loading and unloading (Wieczorek, 2007; Audet, 2011, 2014; Watts et al., 2013). In particular, a useful parameter that describes this behaviour is the effective elastic thickness (T_e) of the lithosphere, which, in turn, can be used in order to constrain the thermal structure and evolution of a planetary body (e.g., Zuber et al., 2000; McGovern et al., 2002; Ruiz et al., 2011). T_e is a proxy for the strength of the lithosphere, integrating contributions from brittle and ductile layers and from elastic cores of the lithosphere (for a review see Watts and Burov, 2003).

Although previous research provided important constraints on the effective elastic thickness of Venus (e.g., Johnson and Sandwell, 1994; Smrekar, 1994, Simons et al., 1994, 1997; McKenzie and Nimmo, 1997; Smrekar and Stofan, 1999; Barnett et al., 2000, 2002; Hoogenboom et al., 2004, 2005), work on global mapping of T_e is very scarce. Anderson and Smrekar (2006) presented the first global map of T_e for Venus based on the spatio-spectral localization technique of Simons et al. (1997) by using three end-member models of loading (top loading, bottom loading, or hot spot) and fitting their results to specified classes of results. Recently, Audet (2014) used a spherical wavelet analysis of gravity and topography and thin shell loading models, and presented preliminary mappings of T_e for the Moon, Mars and Venus, in order to analyse both the promises and the limitations of fully spherical techniques.

Recent advances in joint spectral analysis of gravity and topography and improvements in lithospheric modelling of the Earth have led to mapping of T_e at unprecedented resolution (for reviews see Audet, 2014; Kirby, 2014). Given these recent methods developed for the Earth, it is a natural step to make a reliable T_e mapping for Venus at higher resolution. Performing this task would be of interest to re-evaluate regional variations in, and improve the characterization of, the structure and rheological behaviour of the lithosphere of this planet.

Thus, we have calculated maps of the spatial variations of Venusian T_e, as well as of their associated surface and subsurface loading mechanisms, from the analysis of the Bouguer coherence using wavelet transforms (Kirby and Swain, 2009, 2011), modelled with a simple thin elastic plate subject to both surface and subsurface loads, following the load deconvolution procedure of Forsyth (1985). We have performed our mapping in the Cartesian domain, dividing the surface of Venus into 36 overlapping areas (or 'tiles'). This procedure is useful: indeed, Audet (2014) showed that the Cartesian analysis is just as good as a spherical analysis over small regions if the data edges of the Cartesian grid are excluded. Before this, we present a global model of crustal thickness, which is required for the lithospheric analysis, derived from topography and gravity. Finally, we discuss the implications of our results for the large scale and long-term evolution and behaviour of the Venusian crust and lithosphere.

4.2.2. Global gravity and topography of Venus

Gravity and topography data acquired by the Magellan spacecraft between 1990 and 1994 remain the most complete set for constraining the structure of the Venusian lithosphere. We apply potential theory to model the crustal thickness of Venus from the relationship between gravity and topography data (Section 4.2.3). This analysis has been developed in spherical coordinates making use of spherical harmonics. Thus, we use the spherical harmonic models SHTJV360u (Rappaport et al., 1999) and SHGJ180u (Konopliv et al., 1999) for topography and gravity respectively (available at http://pds-geosciences.wustl.edu; see Fig. 4.1). While SHTJV360u and SHGJ180u are supplied to degree and order 360 and 180, respectively, the topography and gravity used in spectral flexural analyses must have the same bandwidth, because the coherence (and admittance) compares these data in the spectral domain. Therefore we expand the gravity and topography coefficients up to degree and order 180 only, which corresponds to a minimum wavelength of ≈211 km at the Venusian equator. This corresponds to a flexural wavelength such that the minimum resolvable T_e is ≈14 km (estimated through $\lambda_{flex} \approx 29T_e^{3/4}$; see Swain and Kirby, 2003), which is useful taking into account the limited data resolution and large errors in the gravity model (see Audet, 2014). However, we note that the accuracy of the SHGJ180u gravity data is quite low, with large uncertainties at spherical harmonics beyond 60-70 (see for example, Anderson and Smrekar, 2006; Wieczorek, 2007; James et al., 2013).

Effective elastic thickness modelling has been developed in the Cartesian domain by using a continuous planar wavelet analysis of gravity and topography data (see Section 4.2.4). Although Audet (2011, 2014) recently developed a continuous spherical wavelet transform for estimating T_e, he found that the differences between the spherical and planar methods were small ($<10\,\%$ of the absolute T_e value) and concentrated at the data area edges (Audet, 2014). In order to reduce the effects of distortion from curvature of a planet's surface, we divided the surface of Venus into 36 overlapping areas (or 'tiles') from north to south and west to east, and projected the gravity and topography in each of them to a Cartesian frame using an oblique Mercator map projection, providing a global coverage. Each tile had dimensions of 6000 km (easting) x 6000 km (northing), and a grid spacing of 20 km in both directions. The Bouguer gravity anomaly and topography are mirrored about their edges prior to Fourier transformation with the purpose of reducing leakage at them, which, when used with the wavelet transform, does not generally bias the results significantly (see Kirby and Swain, 2008, for a discussion on mirroring). The planar wavelet analysis for coherence and subsequent inversion for T_e were then carried out on each tile. After inversion, T_e and subsurface-to-surface load ratio (F; see Section 4.2.4) data at the edges of each tile (ten percent of a side length) were removed to mitigate possible remnant edge effects near the grid boundaries. As a final step, T_e and F results were back-projected onto geographic 1° x 1° grids, and merged and gridded using GMT's 'surface' algorithm (Smith and Wessel, 1990) to produce global T_e and F maps that combine the information from all tiles.

All maps are generated using GMT (Wessel et al., 2013), and are presented in Robinson projection with east-positive longitude convention and centered on 180° longitude.

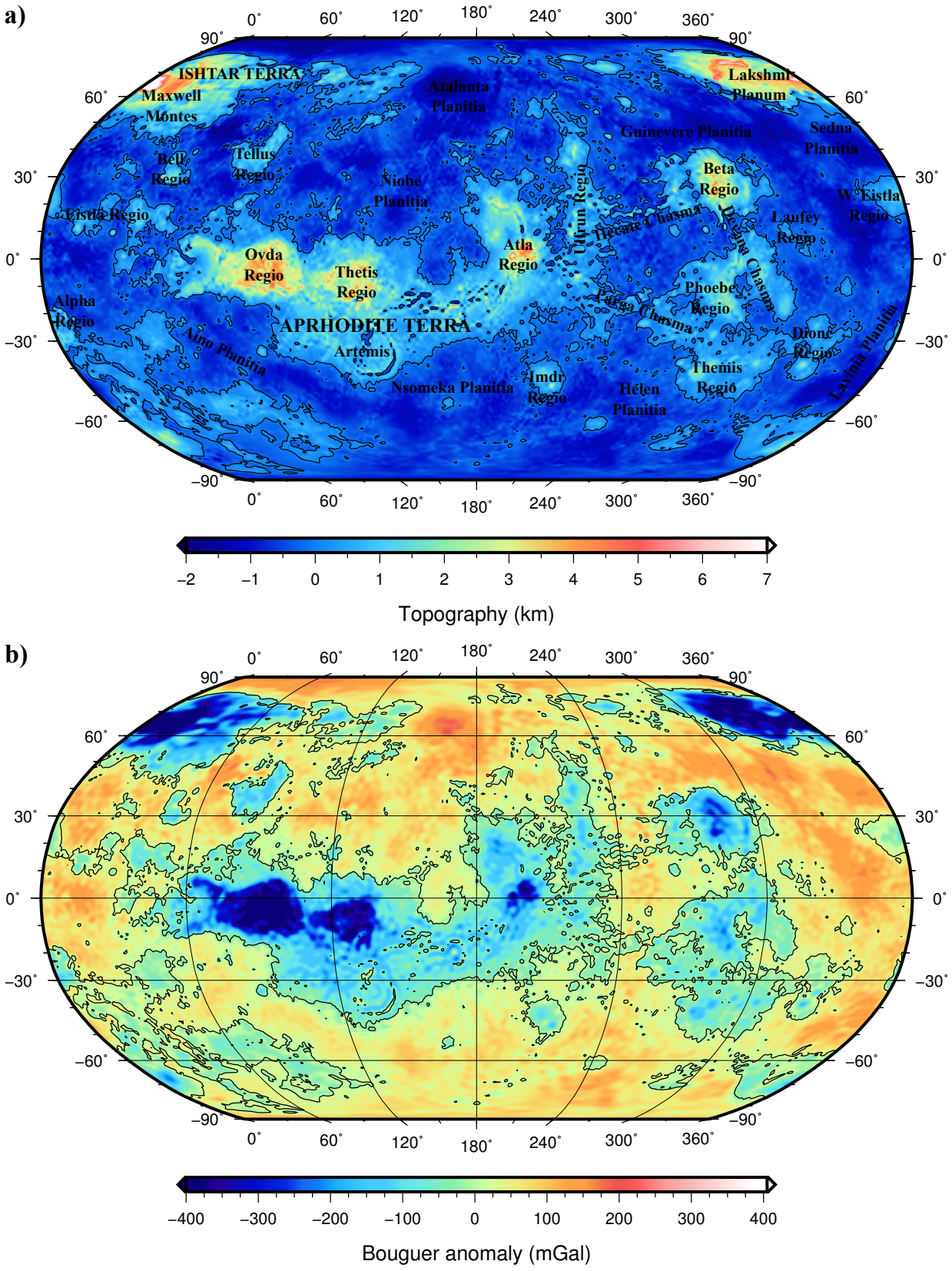

Figure 4.1: (a) Topography and (b) Bouguer gravity anomaly of Venus derived from the spherical harmonic models SHTJV360u (Rappaport et al., 1999) and SHGJ180u (Konopliv et al., 1999), respectively, to degree and order 180. The map projection is Robinson with east-positive longitude convention and centered on 180º longitude. Black contour in (b) is the zero topography contour.

4.2.3. Crustal thickness modelling

We use the relationship between global topography and gravity data to model the crustal thickness (T_c) of Venus following the potential theory procedure of Wieczorek and Phillips (1998), which was originally derived for estimating T_c of the Moon and later used in other crustal thickness modelling of the Moon (Wieczorek, 2007), Mars (Zuber et al., 2000; Neumann et al., 2004; Wieczorek, 2007; Cheung and King, 2014), and Venus (Wieczorek, 2007; James et al., 2013). To constrain the thickness of the Venusian crust, we assume (1) that the observed gravitational anomalies arise only from a combination of surface topography and variations at the crust-mantle interface (i.e., the "Moho"), and (2) constant crustal and mantle densities to overcome the non-uniqueness associated with potential modelling. Under these assumptions, we first calculate the Bouguer gravity anomaly from surface topography and the free air anomaly, and then calculate by downward continuation the relief along the crust-mantle interface necessary to explain the observed Bouguer gravity anomaly (for reviews see Wieczorek and Phillips, 1998; Wieczorek, 2007). In order to mitigate errors in downward continuing the Bouguer anomaly, we applied a minimum amplitude filter (see Wieczorek and Phillips, 1998) for the Moho relief at degree $l = 70$. Finally, we obtain the crustal thickness by subtracting the relief on the Moho from surface topography.

Since we cannot constrain the crustal thickness model with a given value at a specific location on Venus (for example, by using the minimum T_c at deep impact basins as Hellas or Isidis on Mars; e.g., Neumann et al., 2004), we assume a mean T_c to "anchor" our model satisfying the condition that the inverted crustal thickness is not negative anywhere on the planet. Furthermore, the phase transition from basalt to dense eclogite limits large T_c values such that they cannot result in crust anywhere extending below the basalt-eclogite phase change depth, predicted to occur at depths of $\sim$70-100 km depending on the temperature gradient (e.g., Namiki and Solomon, 1993; Jull and Arkani-Hamed, 1995; Ghent et al., 2004). With these constraints, we assume an average crustal thickness of 25 km consistent with the range of 5-50 km obtained by previous studies (e.g., Zuber, 1987; Grimm, 1994; Phillips, 1994; Konopliv and Sjogren, 1994; Simons et al., 1994, 1997; Grimm and Hess, 1997).

The obtained global crustal thickness model is shown in Fig. 4.2. The Venusian crust exhibits a good spatial correlation between topography and crustal thickness, with highland regions and crustal plateaus being locally thicker than the surrounding plains and lowland regions, and large volcanic rises characterized by intermediate to high T_c values. The crustal thickness variation pattern agrees well with results of previous global crustal thickness modelling (Anderson and Smrekar, 2006; Wieczorek, 2007; James et al., 2013). Our model (which is based upon the premise of an average crustal thickness of 25 km, and crust and mantle densities of, respectively, 2900 and 3300 kg m^{-3}) finds a crustal thickness that varies from $\approx$10 to $\approx$95 km, with the smallest values associated with Atalanta, Sedna and Lavinia planitiae, while Lakshmi Planum and Maxwell Montes (which reach a maximum elevation of 11 km) on Ishtar Terra are characterized by the higher values of T_c.

The global crustal structure is distinctly unimodal (Fig. 4.3a). It has one major peak at approximately 20-22 km, with a trail of values higher than the average crustal thickness of 25 km, and with

less than 20% of crust being thinner than 20 km. Pole-to-pole longitudinal transects of the crustal structure, as well as an equatorial transect (Fig. 4.3b,c), clearly show the thickening beneath the highland plateaus, and thin crust beneath the lowland plains, where the transition in thickness between highlands and lowlands is relatively abrupt. In general, the Moho relief gives the impression of a crust usually 20-25 km thick with superposition of thicker (even very thicker) crust associated with the highlands. This suggests that most of the Venusian crust was emplaced under similar conditions, and different to those generating the crustal plateaus.

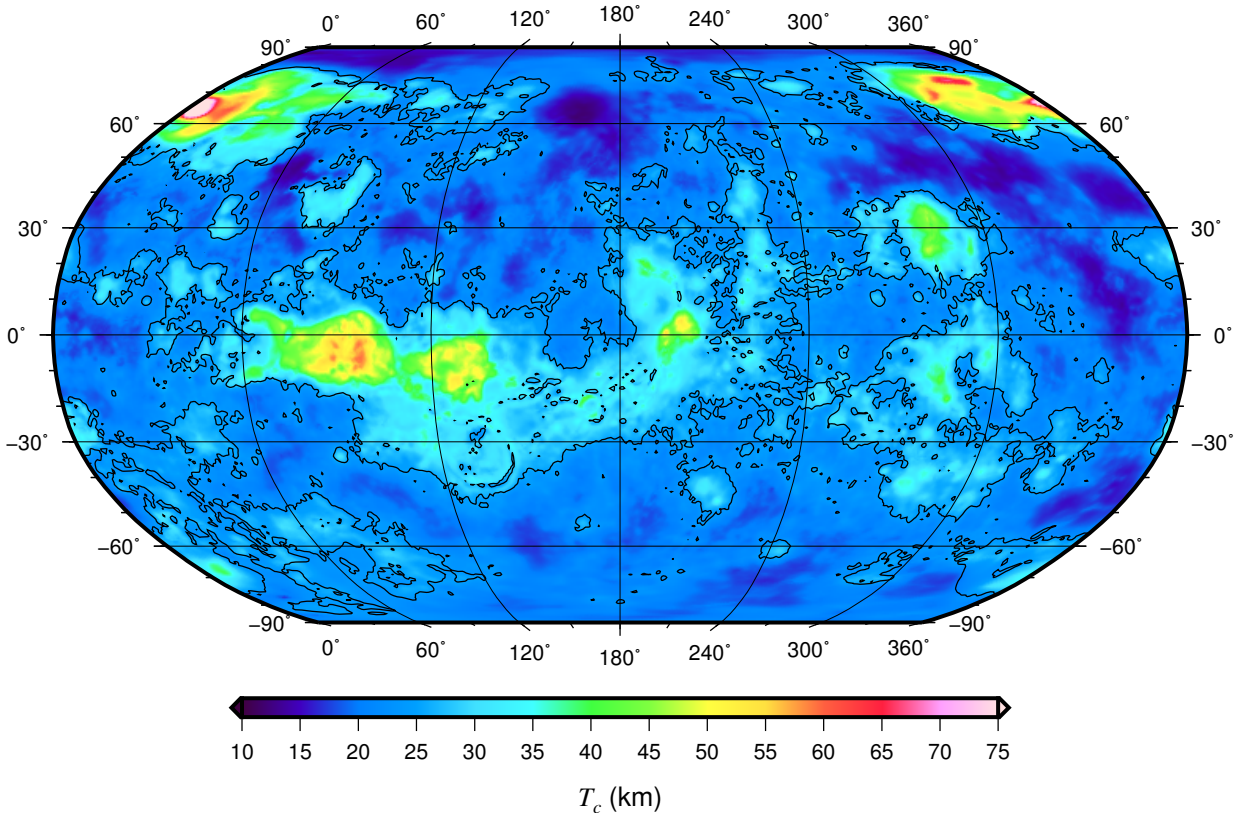

Figure 4.2: Crustal thickness model for Venus assuming a mean crustal thickness of 25 km, and crust and mantle densities of, respectively, 2900 and 3300 kg m^{-3}.

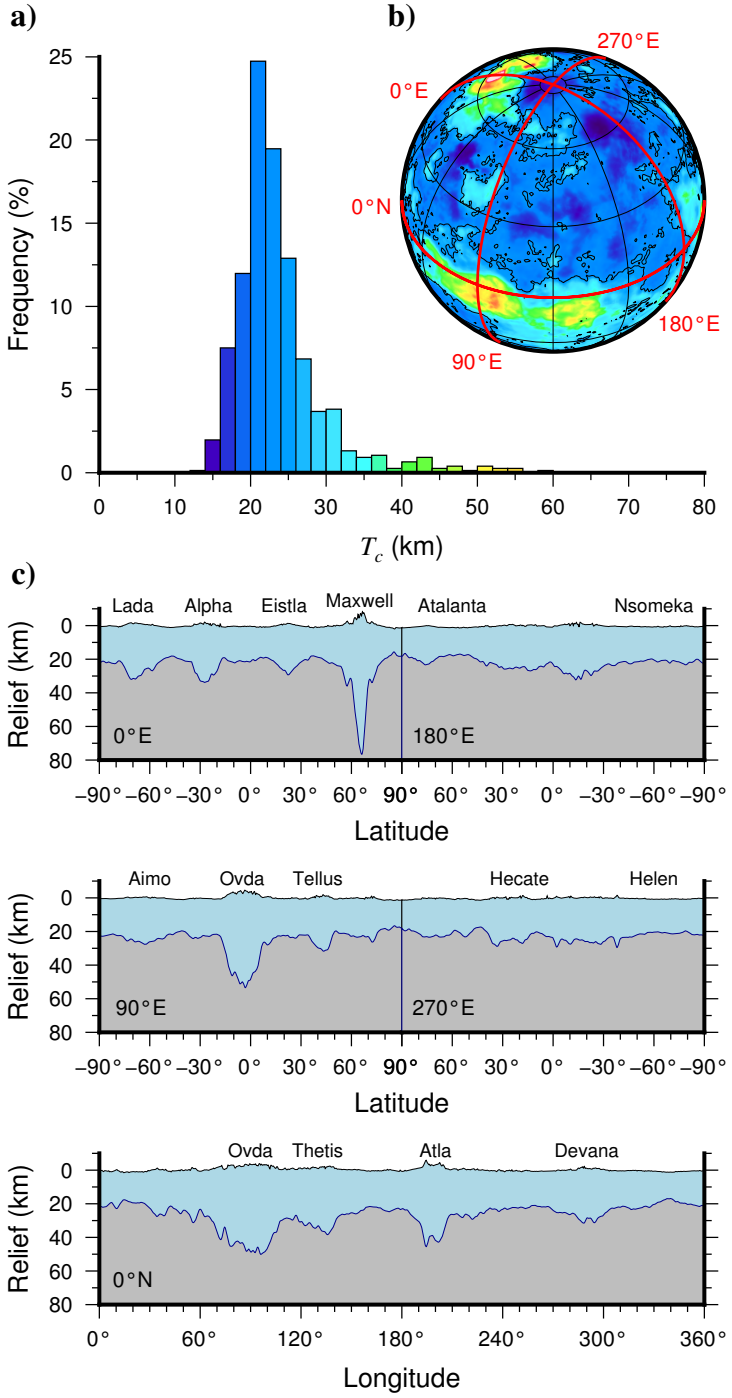

Figure 4.3: (a) Histogram of crustal thickness. (b) Crustal thickness model in an orthographic projection centered on 120° longitude and 40º latitude. The red lines correspond to the crustal structure profiles shown in (c). (c) Pole-to-pole longitudinal transects of the crustal structure, as well as an equatorial transect, where light blue corresponds to crust and gray corresponds to mantle.

4.2.4. Estimating the effective elastic thickness of the lithosphere

To estimate the effective elastic thickness we calculate the coherence function relating the topography and Bouguer anomaly (i.e., the Bouguer coherence) by using the wavelet transform (Kirby and Swain, 2009, 2011), modelled with a simple thin elastic plate subject to both surface and subsurface loads, following the load deconvolution procedure of Forsyth (1985). The Bouguer coherence gives information on the wavelength band over which topography and Bouguer anomaly are correlated, such that it generally tends to zero at short wavelengths, where the topography is not compensated and loads are supported predominantly by the elastic strength of the lithosphere (Forsyth, 1985). At long wavelengths, the response to loading approaches the Airy limit and the coherence tends to one. The wavelengths at which the coherence rapidly increases from 0 to 1 depend on the effective elastic thickness of the lithosphere, such that when the lithosphere is weak and T_e is small, local compensation for loading occurs at relatively shorter wavelengths, and vice versa.

First, as mentioned in Section 4.2.2, we divided the gravity and topography data into 36 tiles, map-projected the data, and performed the following planar wavelet analysis on each tile. The wavelet coherence method convolves a range of scaled wavelets with the data under consideration to map and invert the coherence at each grid point, and achieves good wavenumber resolution over long length scales and good spatial resolution over short length scales. Here we employ a Morlet wavelet in the fan wavelet transform (Kirby and Swain, 2011). The value of the central wavenumber of the Morlet wavelet, denoted by $|\mathbf{k}_0|$, governs the resolution of the wavelet in the space and wavenumber domains (Kirby and Swain, 2011). Large values of $|\mathbf{k}_0|$ give the Morlet wavelets a high wavenumber-domain resolution but poor space-domain resolution, while small values of $|\mathbf{k}_0|$ give a poorer wavenumber-domain resolution but better space-domain resolution (Kirby and Swain, 2011, 2013). The $|\mathbf{k}_0|$ value used in this study is 5.336, which has a good resolution in the wavenumber domain and a reasonably good resolution in the space domain.

In the load-deconvolution method of Forsyth (1985), T_e is estimated by comparing the observed coherence curve with coherence functions predicted for a range of T_e values. For each given T_e, we calculate, via deconvolution of the observed Bouguer anomaly and topography, the initial surface and subsurface loads and compensating deflections that generate a predicted topography and gravity that best fit the observed topography and gravity anomaly, and a predicted coherence that best fits the observed coherence (Forsyth, 1985). We follow Kirby and Swain (2009) and invert the square of the real part of the wavelet coherency (SRC), rather than the coherence, because it is less sensitive to correlations between the initial loads on the plate and to the presence of topographically unexpressed internal loading (commonly known as "gravitational noise"), both of which can cause incorrect recovery of T_e (e.g., McKenzie and Fairhead, 1997; McKenzie, 2003; Kirby and Swain, 2009; Audet and Bürgmann, 2011; Kirby, 2014). Furthermore, the deconvolution requires detailed information on the internal structure of the lithosphere. We follow Forsyth's (1985) original formulation of the predicted coherence method, assuming that all internal loading occurs at the crust-mantle interface. To define the lateral variation of the Moho relief, we use the global crustal thickness model obtained

in this study (see Section 4.2.3). Table 4.1 shows the values of the crustal and mantle densities used in the coherence inversion, together with the values of other required constants. Finally, the T_e value that minimizes the differences between the predicted and observed quantities is the optimal one for the analyzed area.

Additionally, we can also estimate the ratio between the initial internal and surface load amplitudes (the loading ratio, f; Forsyth, 1985) at the wavelength of the Bouguer coherence rollover. We can display the loading ratio results in terms of the internal load fraction, F, using (McKenzie, 2003) . Thus, whereas f is the ratio of the initial internal load amplitude to the initial surface load amplitude, F is the ratio of the initial internal load amplitude to the total amplitude of both initial loads. While f varies between 0 and ∞, F varies between 0 and 1. Purely surface loading gives $f = F = 0$, purely internal loading gives $f = \infty$ and $F = 1$, while equal surface and internal loading gives $f = 1$ and $F = 0.5$ (note that f and F are wavenumber-dependent parameters; Kirby and Swain, 2009).

The T_e and F values in each tile were then merged to provide seamless coverage over the planet, as described in Section 4.2.2.

Constant	Symbol	Value	Units
Young's modulus	E	100	GPa
Poisson's ratio	υ	0.25	
Newtonian gravitational constant	G	6.67259×10^{-11}	$m^3\ kg^{-1}\ s^{-2}$
Gravity acceleration	g	8.87	$m\ s^{-2}$
Mean planetary radius	R	6052	km
Mean crustal thickness	T_c	25	km
Crust density	ρ_c	2900	$kg\ m^{-3}$
Mantle density	ρ_m	3300	$kg\ m^{-3}$

Table 4.1: Symbols and values of constants.

4.2.5. Results of effective elastic thickness mapping

The effective elastic thickness results are shown in Fig. 4.4a. T_e values range between 14 (the minimum resolvable T_e value; see Section 4.2.2) and 94 km, although low to moderate values clearly dominate (Fig. 4.4c). Error in T_e estimates are usually lower than 20 per cent (see Appendix A). The most noticeable feature on the T_e map is the low to moderate T_e ($<$50 km) large region associated with Ishtar, western Aphrodite (Ovda Regio) and Lada terrae, Alpha, Bell, Tellus and Eistla regiones, and parts of Lavinia, Atalanta and Niobe planitiae. Otherwise, the Beta-Atla-Themis (BAT) region and the southern planitiae show more variable T_e results, including very high values. The Artemis region (following the terminology of Hansen, 2002) is characterized by moderate T_e values ($\sim$45 km), in continuity with those of the surrounding plains. These T_e values increase smoothly towards Nsomeka Planitia, which along with Aino and Helen planitiae show higher T_e values with patches and regions of moderate to low T_e. In the northern hemisphere of Venus, Guinevere Planitia also shows this pattern. On the other hand, the large volcanic rises show a complex signature, but Atla, Themis, Dione, Imdr

and Laufey regiones seem to be uniformly strong. Within the BAT region, our results show moderate to high T_e values associated with Phoebe Regio. Our results also show a zone of high T_e associated with Dali Chasma and the Atahensik Corona region. Otherwise, the graben-fissure systems in Hecate Chasma and Ulfrun Regio areas, as well as Beta Regio and Devana Chasma areas, have T_e values that are higher than the typical values in the surrounding plains.

Fig. 4.4b shows best fitting F values corresponding to the T_e results in Fig. 4.4a. Interestingly, surface loads dominate a great part of the BAT region (associated with moderate to high T_e values; see Fig. 4.4), with some exceptions as south of Atla Regio or surrounding of Phoebe Regio. Themis, Laufey, and western and central Eistla regiones are also dominated by surface loads. Nevertheless, Tellus, Alpha, Dione, Imdr and eastern Eistla regiones exhibit a more complex signature, characterized by moderate F values. On the other hand, our load ratio estimates indicate that subsurface loading dominates (at least slightly) on Aphrodite Terra (associated with low to moderate T_e values). Ishtar Terra is also dominated by subsurface loads; nonetheless, Lakshmi Planum is associated with a small load ratio, indicating that surface loads dominate. Lada Terra exhibits a more complex signature, with a broad range of F values. Finally, planitiae and lowlands regions in both hemispheres show a broad range of F values.

Our pattern of T_e variations is consistent with previous studies. However, we found some important differences in the results, possibly related to the approach and parameters used in the analysis. Anderson and Smrekar (2006) estimated T_e from a global mapping of the admittance using the spatio-spectral localization technique of Simons et al. (1997) and three end-member models of loading (top loading, bottom loading, or hot spot), fitting their results to specified classes of results. The authors found T_e values varying between 0-100 km, with $T_e < 20$ km for approximately half of the planet, while our results show a similar range but predominantly dominated by moderate T_e values, peaking around 35-40 km.

Our results also show differences with the global T_e and F maps recently obtained by Audet (2014) for Venus. It is important to note that while Audet (2014) estimated T_e using the continuous spherical wavelet transform and equations for the flexure of a thin elastic shell, and a joint inversion of the real admittance and coherency with analytical expressions, we use the continuous planar wavelet transform and equations for the flexure of a thin elastic plate, and the Bouguer coherence method with the load deconvolution procedure to estimate T_e and F, the latter obtained as a function of wavelength. Also, the study by Audet (2014) used 5-degree mean gravity anomalies and topography, and for this reason his analysis does not show the small-scale variability observed in our results, which were computed on a 20 km grid then averaged onto a 1-degree grid.

Figure 4.4: Results of the inversion of the squared-real Bouguer coherency ($|\mathbf{k}_0|$ = 5.336). (a) Effective elastic thickness, T_e. (b) Loading ratio, F, corresponding to the T_e results in (a). (c) Histograms of T_e and F. (d) Plot of T_e against F.

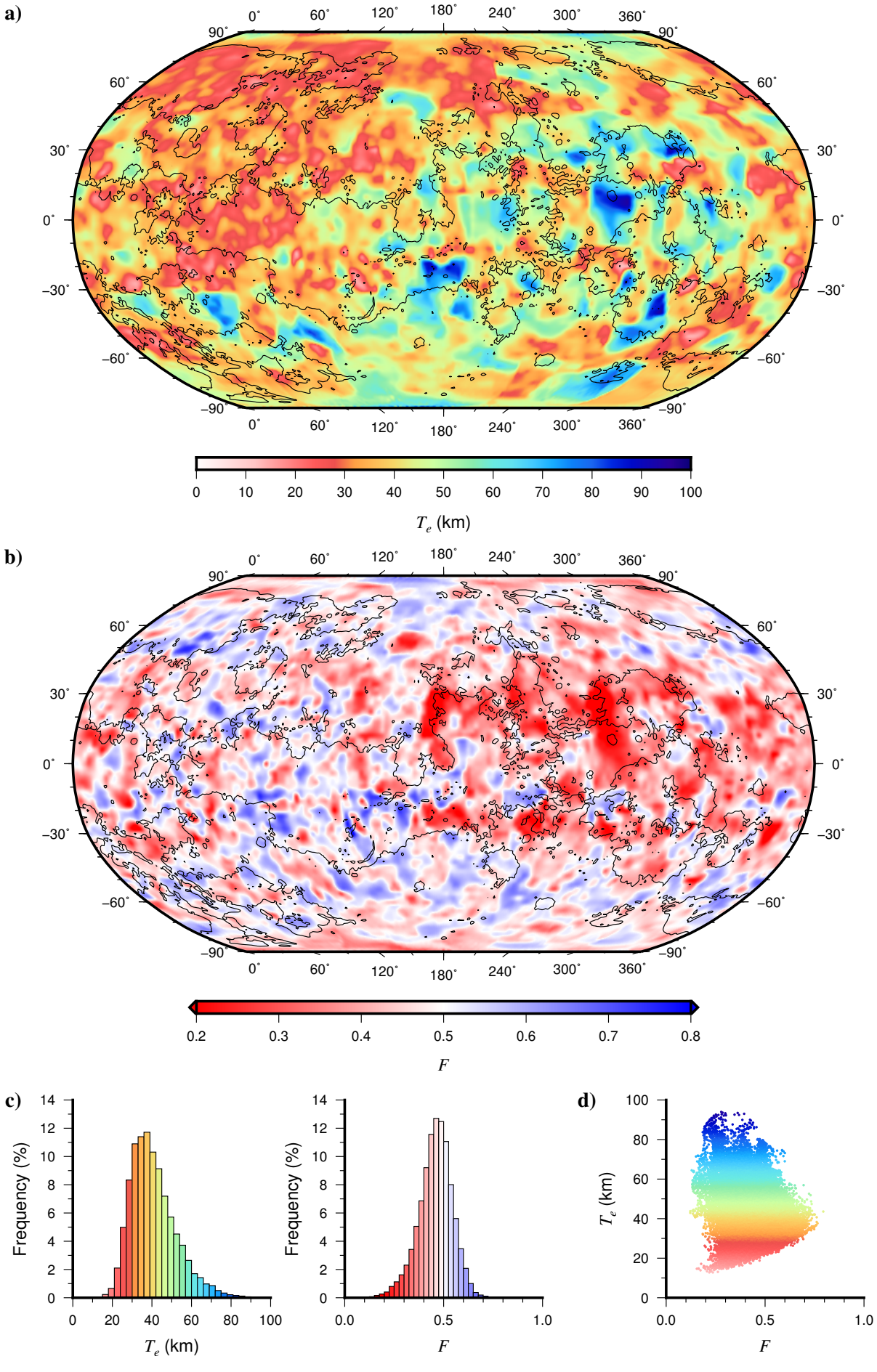
a)
0˚ 60˚ 120˚ 180˚ 240˚ 300˚ 360˚
90˚ 60˚ 30˚ 0˚ −30˚ −60˚ −90˚
0 10 20 30 40 50 60 70 80 90 100
T_e (km)
b)
0.2 0.3 0.4 0.5 0.6 0.7 0.8
F
c)
Frequency (%)
0 2 4 6 8 10 12 14
0 20 40 60 80 100
T_e (km)
Frequency (%)
0.0 0.5 1.0
F
d)
T_e (km)
0 20 40 60 80 100
0.0 0.5 1.0
F

4.2.6. Discussion

Our patterns of T_e and F variations show a high variability. This could suggest that Venus would remain an active planet with complex geologic processes, as previously suggested by Anderson and Smrekar (2006). However, this might be true only taking into account the relatively young ages typical of the Venusian surface (e.g., Basilevsky and Head, 1998; Guest and Stofan, 1999; Ivanov and Head, 2011), because a very high range of T_e values could be indicating a temporal trend. Indeed, the range of T_e values obtained for Mars (for a compilation see Ruiz, 2014) is larger than for Venus, but it seems mostly to be a consequence of secular planetary evolution (e.g., McGovern et al., 2002), related to cooling and thickening of the lithosphere (Ruiz, 2014). This can be so because the observed T_e values derive from the state of the lithosphere when the topography was formed (or, in the case of the T_e calculated from spectral methods, when the relation between topography and gravity was established) (Watts, 2001). There are evidences that crustal plateaus are the (at least slightly) older terrains on Venus (e.g., Ivanov and Head, 2011), which would be consistent with a lower elastic thickness and near-isostatic compensation (see Fig. 4.4). This is consistent with their small gravity anomalies, low geoid-to-topography ratios (GTRs), and shallow apparent depths of compensation (ADCs); all indicating a thickened crust beneath them (e.g., Smrekar and Phillips, 1991; Kucinskas and Turcotte, 1994; Grimm, 1994; Simons et al., 1997; Anderson and Smrekar, 2006; James et al., 2013).

Fig. 4.5 shows an equatorial transect of our crustal thickness and effective elastic thickness models. Higher T_e values generally occur in areas of normal crustal thickness (≈20-25 km), which is consistent with the topography lowlands being formed when the lithosphere of Venus was cooler than that at the time of the formation of the crustal plateaus. In general, most T_e estimates are higher than the crustal thickness, suggesting a significant contribution of the upper mantle to the strength of the lithosphere in many areas. It must be recalled that the effective elastic thickness does not, in general, represent an actual layer, rather it is a measurement of lithospheric strength which integrates contributions from mechanically strong portions of the crust and mantle (see Watts and Burov, 2003).

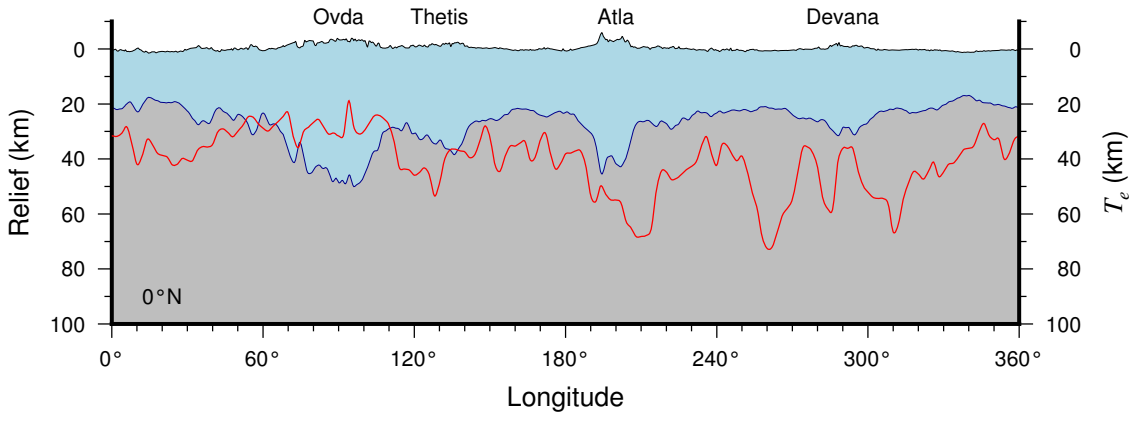

Figure 4.5: Equatorial transect of our crustal thickness model (figure format is the same as Fig. 4.3c). The red line corresponds to the variation of the effective elastic thickness (right axis) along the same profile.

Mantle rocks are stronger than crustal rocks, but being under higher temperatures, which reduces their strength. For a sufficiently high heat flow the upper mantle does not contribute to T_e, and the lithosphere is thin and restricted to the crust; conversely, if the heat flow is sufficiently low, the upper mantle is cold and strong, and contributes to the strength of the lithosphere, and hence to the effective elastic thickness, which is therefore higher. Thus at least part of the regional variations of T_e could be due to differences in the cooling history of the lithosphere in these regions, although deep geodynamic processes with little surface manifestation also could be operating (see Anderson and Smrekar, 2006). In this sense, mantle processes could be responsible we find a similar pattern of low to moderate T_e associated with a large region that encloses very different geological features, and of different relative ages, as crustal plateaus and planitiae.

The large volcanic rises show a complex T_e signature, which along with their large ADCs and GTRs (e.g., Kucinskas and Turcotte, 1994; Smrekar, 1994; Moore and Schubert, 1997; James et al., 2013), suggest that the topography would be supported through a combination of several mechanisms (see also Kucinskas and Turcotte, 1994; Moore and Schubert, 1997; Vezolainen et al., 2004; Pauer et al., 2006). James et al. (2013) recently found that the topography of certain regions, such as Atla and Eistla regiones, is mainly supported by dynamic loading, or in the case of Thetis Regio, by contributions from both crustal thickening and dynamic support from the mantle.

We have examined the effective elastic thickness in relation to the crater density (Fig. 4.6) by using a global database of impact craters on its surface (Schaber et al., 1998). The impact crater population on Venus, which gives a mean surface age of 300-1000 Ma (McKinnon et al., 1997), shows a nearly uniform spatial distribution (Schaber et al., 1992; Phillips et al., 1992; Strom et al., 1994). In Fig. 4.6 we plot the crater density (points) obtained with sampling windows of 10^6 km^2 against the mean value of T_e in each window. We found that most of craters are located in regions with low or moderate T_e, although this possible correlation could be biased by the distribution of

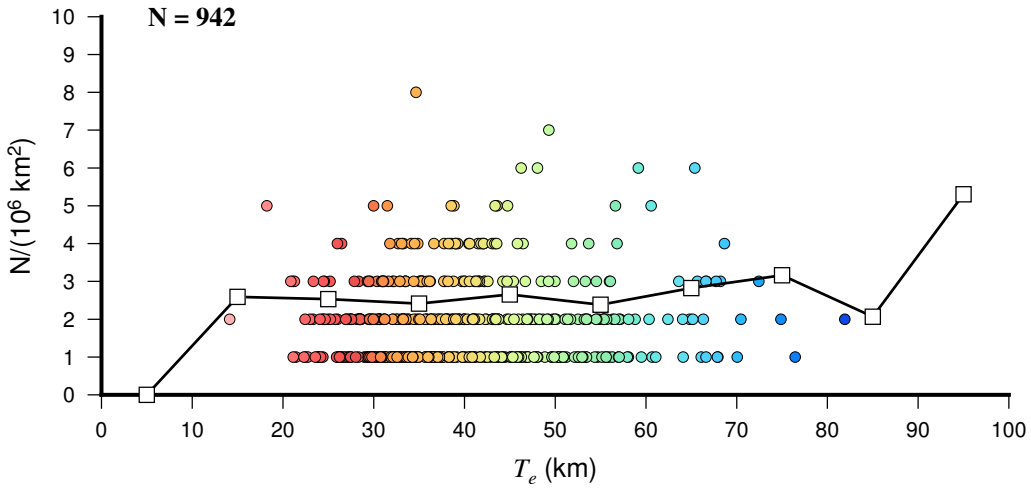

Figure 4.6: Plot of crater density obtained with sampling windows of 10^6 km^2 against the mean value of T_e in each window (points); and crater density calculated counting the number of craters for T_e intervals of 10 km (white squares and black line).

T_e, clearly dominated by that range of low to moderate values. Alternatively, we also plot a second analysis of the crater density (overlapping white squares and black line) calculated by counting the number of craters for T_e intervals of 10 km providing the crater density of each interval (in 10^6 km^2), to avoid the effect of windowing. This analysis shows a higher (at least relatively) crater density associated with moderate to high T_e values. Although the high T_e intervals show a comparatively low number of craters, the corresponding areas are so small that the crater density is slightly increased; therefore these results may be biased upward. Unfortunately this implies that there is no evidence of a clear correlation between T_e and the crater density, consistent with the previous observations of Barnett et al. (2002).

However, the spatial and temporal distribution of surface volcanism may provide essential information on the geologic history and geodynamic evolution of Venus. Comparison of the spatial variations of T_e with volcanoes (from the USGS Venus Volcano Catalog; Schaber et al., 1998) indicates that most of the volcanoes are located in regions with low or moderate T_e, associated with a wide range of F values, while a low volcano density in areas characterized by high T_e values is evident (Fig. 4.7a). It should be noted that these patterns are largely controlled by the spatial distribution of the volcanic features on the planetary surface, where the BAT (Beta, Atla, Themis) region is characterized by a concentration of volcanic activity (see e.g., Crumpler et al., 1997). Our results

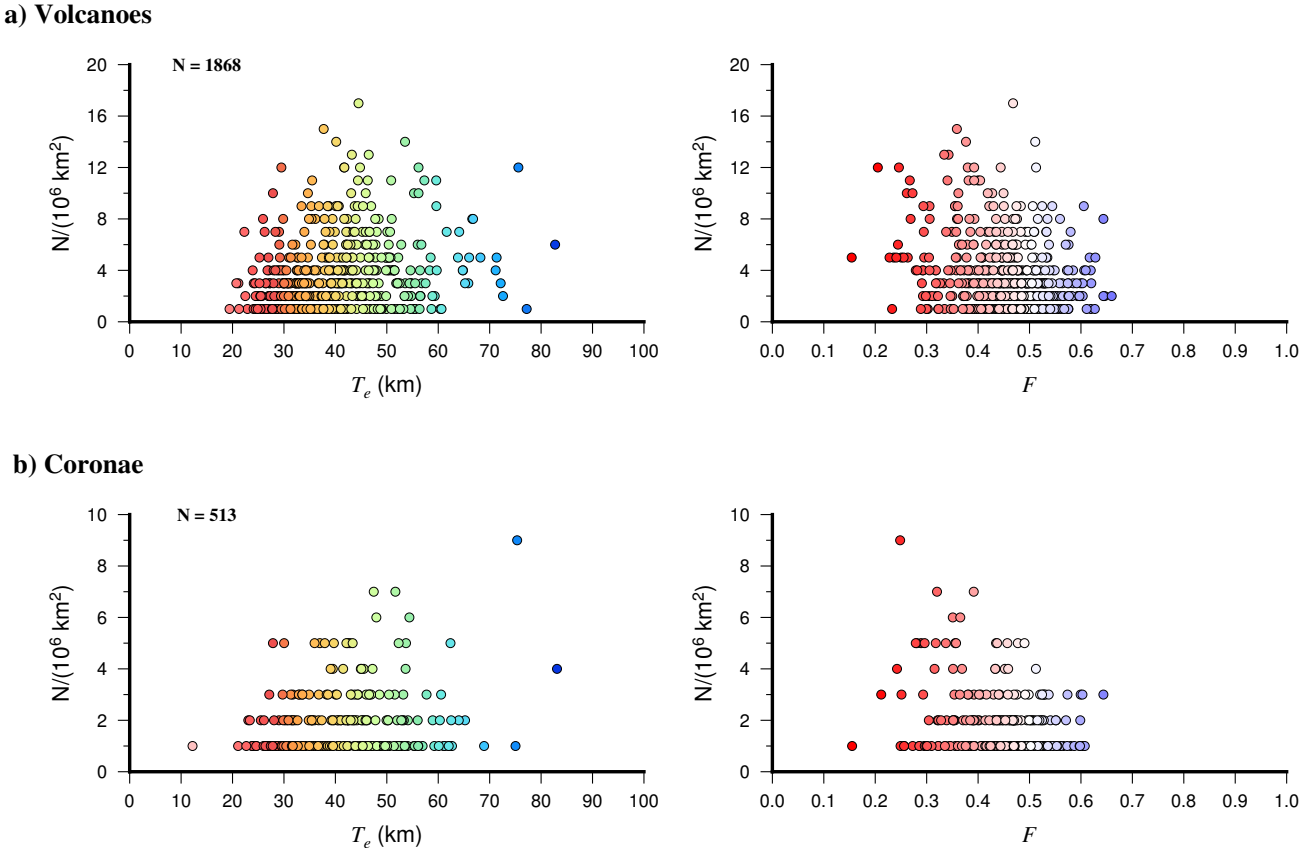

Figure 4.7: Density of (a) volcanoes (Schaber et al., 1998) and (b) coronae (Stofan et al., 2001) against T_e and F corresponding to the results in Fig. 4.4. Figure format is the same as Fig. 4.6.

indicate that on average surface loads prevail on volcanoes. However, coronae may provide a potentially useful probe of lithospheric properties since they load the lithosphere, occur in large numbers, and are nearly global in distribution (Smrekar et al., 2003; Hoogenboom et al., 2004). In Fig. 4.7b we examine our T_e and F estimates from the mapping for coronae (Stofan et al., 2001). Although we do not show it here, there are no significant differences in lithospheric properties between Type 1 and Type 2 coronae (see Coronae Type definition by Stofan et al., 2001), confirming the previous observations of Smrekar and Stofan (2003). Coronae are frequently located in regions with low to moderate T_e in our maps, and their absence in areas characterized by high T_e values, as in the case for volcanoes, is also evident. Regarding the initial loads, coronae show a wide range of F values (between 0.1 and 0.7), but more frequently exhibit surface loading. In summary, the comparison of the spatial variations of T_e with volcanoes and coronae (analysed by sampling windows) indicates that most of these are located in regions with low or moderate T_e, associated with a wide range of F values. Reasons for this pattern could be (i) that comparatively low T_e values are expected for magmatically active regions (McGovern et al., 2002), and/or (ii) the difficulty of these features for progressing in a stronger, and maybe colder and more ancient, lithosphere.

4.2.7. Conclusions

In this paper we investigated the lithospheric strength of Venus by calculating its effective elastic thickness from the analysis of gravity and topography. We have first presented a crustal thickness model, in which the Venusian crust is usually 20-25 km thick with thicker crust under the highlands. This suggests that most of the Venusian crust was emplaced under similar conditions, and different to those generating the crustal plateaus.

We find effective elastic thickness values up to ≈95 km for Venus, but they are mostly of low to moderate value. T_e variations and patterns deduced from our model could represent regional variations in the cooling history of the lithosphere and/or mantle processes with limited surface manifestation. The crustal plateaus are near-isostatically compensated, consistent with a thin elastic lithosphere, showing a thickened crust beneath them, whereas the lowlands exhibit higher T_e values, maybe indicating a cooler lithosphere than that when the Venusian highlands were emplaced. Meanwhile, the large volcanic rises show a complex signature, with a broad range of T_e and F values. Our results also reveal a significant contribution of the upper mantle to the strength of the lithosphere.

Comparison of the spatial variations of T_e with volcanoes and coronae indicate that most of these features are located in regions with low or moderate T_e, and are associated with a wide range of F values, consistent with magmatically active regions having thinner lithospheres. Otherwise, there is not a good correlation between T_e and crater density.

As shown, the effective elastic thickness is a very interesting indicator of the strength and mechanical behaviour of the lithosphere. Recent advances in mapping of T_e represent a great opportunity, as well as a great challenge, for future work. Limitations due to resolution of the available data sum up the importance of future missions to map out the gravity and topography of Venus with suffi-

ciently high resolution in order to produce regional lithospheric models and solve key gaps in the understanding of the lithospheric structure and evolution of Venus.

Acknowledgements

We thank Valle López for her encouragements and help during the realization of this work. We also thank USGS for the on-line distribution of the databases used in this study, and Mark A. Wieczorek and Matthias Meschede for making their SHTOOLS software package available (Wieczorek and Meschede, 2015), which was used to process the Magellan data products obtained from the PDS Geosciences Node (http://pds-geosciences.wustl.edu). All figures were plotted using GMT (Wessel et al., 2013). A.J.-D. work was supported by a grant of the Complutense University of Madrid. J.R. work was supported by a contract Ramón y Cajal co-financed from the the Spanish Ministry of Economy and Competitiveness and the European Social Fund. This work was supported by the project CGL2011-23857 from the Spanish Ministry of Economy and Competitiveness.

Appendix A. Misfit results

Fig. 4.8 shows the gravity misfit (the difference between calculated and modelled gravity, see Section 4.2.3), derived from the crustal thickness modelling, corresponding to the results in Fig. 4.2 and 4.3. In Fig. 4.9 we show the T_e error corresponding to results in Fig. 4.4. In the load-deconvolution method (Forsyth, 1985), the initial loads acting on the plate are recreated with an assumed value of T_e, and the predicted SRC is computed. T_e at a grid node is found by minimizing the predicted against the observed wavelet coherence, using Brent's method of 1-D minimization (Press et al., 1992), with the observed-predicted differences weighted by the inverse of equivalent Fourier wavenumber (i.e., reciprocal-wavenumber weighting of the observed-minus-predicted SRC) (Kirby and Swain, 2006). This inverse-wavenumber method generally gives smoother T_e results, as it down-weights the noisy coherencies that sometimes occur at high wavenumbers. The loading ratio is then computed as a consequence of this procedure from the recreated initial loads − it is hence wavenumber-dependent. Errors on T_e are computed (95% confidence limits), but this method cannot give errors on f, and hence on F.

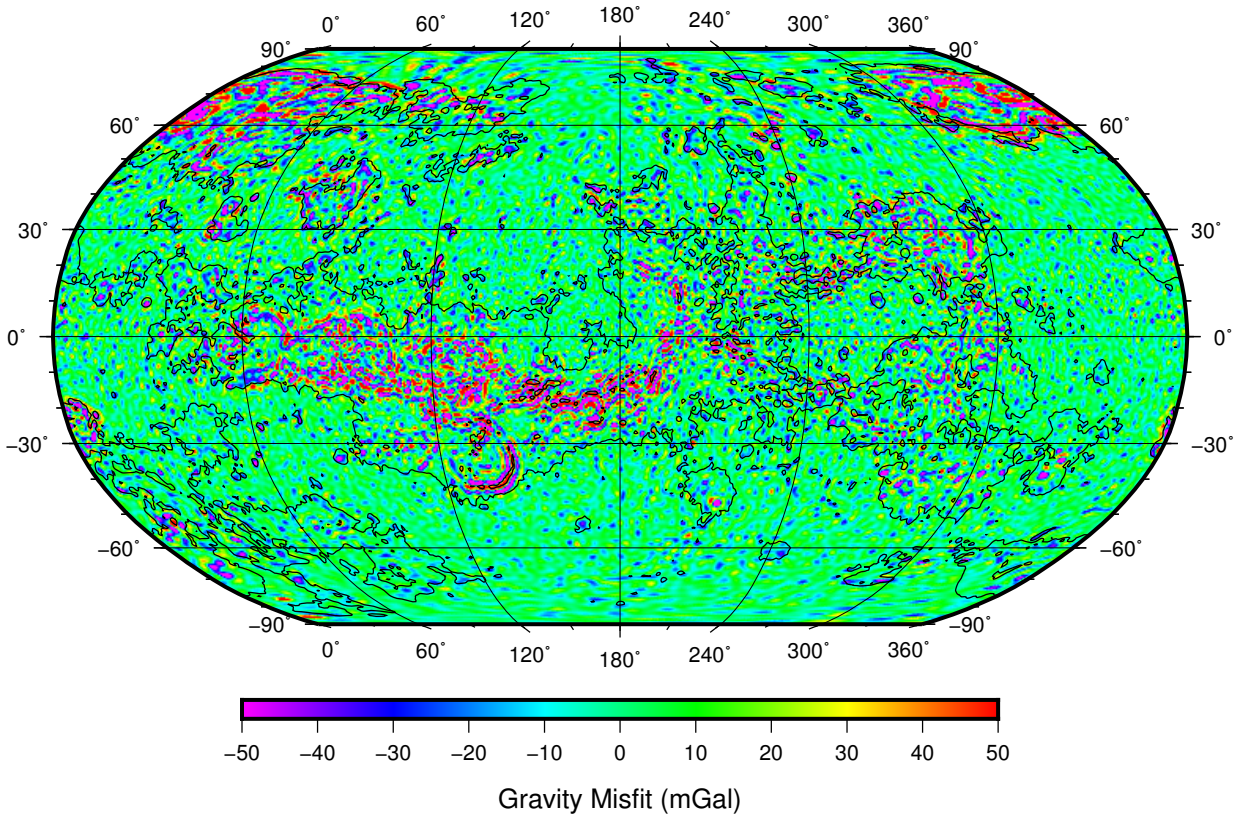

Figure 4.8: Gravity misfit derived from the crustal thickness modelling at spherical harmonic degree and order 180, corresponding to the results in Fig. 4.2 and Fig. 4.3.

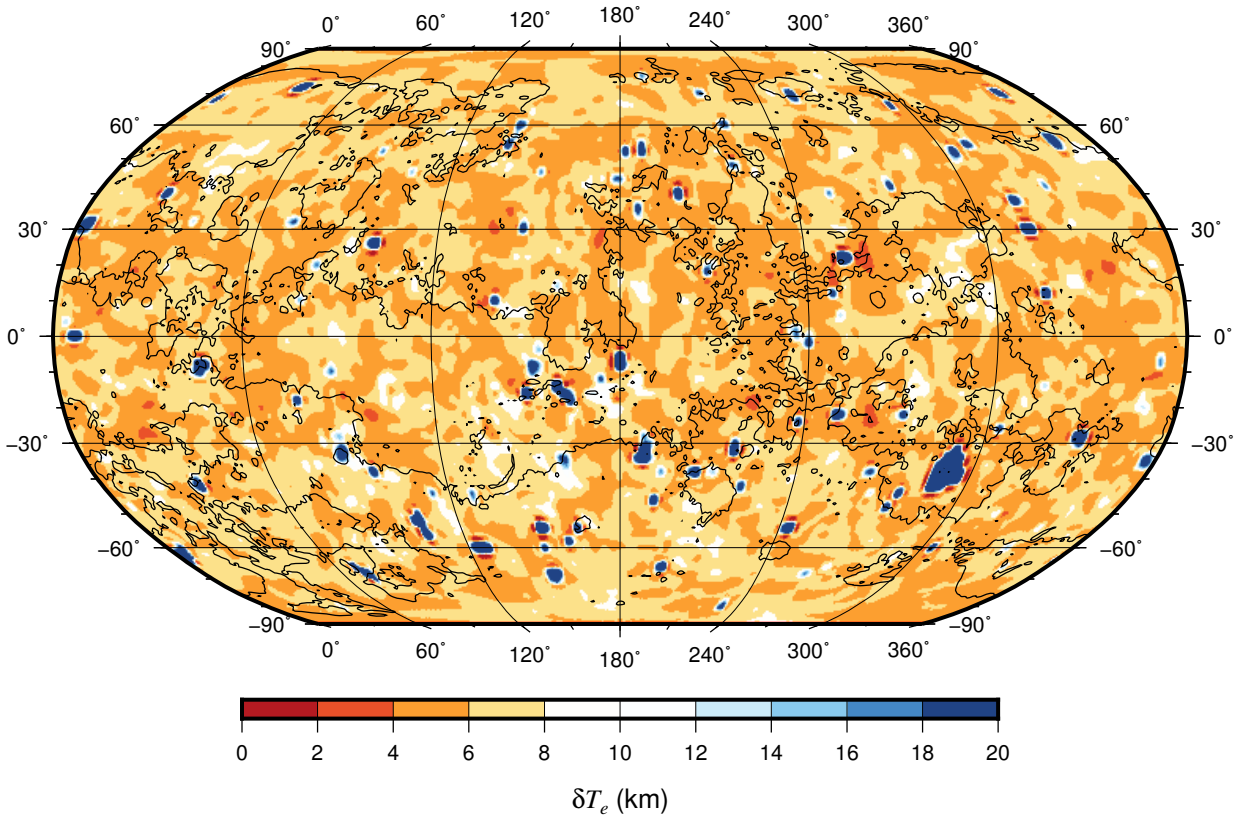

Figure 4.9: T_e error corresponding to the results in Fig. 4.4.

References

Anderson, F.S., Smrekar, S.E., 2006. Global mapping of crustal and lithospheric thickness on Venus. J. Geophys. Res. 111, E08006.

Audet, P., 2011. Directional wavelet analysis on the sphere: application to gravity and topography of the terrestrial planets. J. Geophys. Res. 116, E01003.

Audet, P., 2014. Toward mapping the effective elastic thickness of planetary lithospheres from a spherical wavelet analysis of gravity and topography. Phys. Earth Planet. Inter. 226, 48-82.

Audet, P., Bürgmann, R., 2011. Dominant role of tectonic inheritance in supercontinent cycles. Nat. Geosci. 4, 184-187.

Barnett, D.N., Nimmo, F., McKenzie, C., 2000. Elastic thickness estimates for Venus using line of sight accelerations from Magellan Cycle 5. Icarus 146, 404-419.

Barnett, D.N., Nimmo, F., McKenzie, D., 2002. Flexure of Venusian lithosphere measured from residual topography and gravity. J. Geophys. Res. 107 (E2).

Basilevsky, A.T., Head, J.W., 1998. The geologic history of Venus: A stratigraphic view. J. Geophys. Res. 103, 8531- 8544.

Cheung, K.K., King, S.D., 2014. Geophysical evidence supports migration of Tharsis volcanism on Mars. J. Geophys. Res. 119, 1078-1085.

Crumpler, L.S., Aubele, J.C., Senske, D.A., Keddie, S.T., Magee, K.P., Head, J.W., 1997. Volcanoes and centers of volcanism on Venus, in: Bougher, W., Hunten, D.M., Phillips, R.J. (Eds.), Venus II. Univ. of Arizona Press, Tucson, pp. 697-756.

Forsyth, D.W., 1985. Subsurface loading estimates of the flexural rigidity of continental lithosphere. J. Geophys. Res. 90, 12,623-12,632.

Garvin, J.B., Glaze, L.S., Campbell, B., Ford, P., Lemoine, F., Neumann, G., Phillips, R., Raney, K., 2009. Venus: Constraining Crustal Evolution from Orbit Via High-Resolution Geophysical and Geological Reconnaissance. Venus White Paper for Planetary Sciences Decadal Survey, Inner-Planets Panel, 8 pp.

Ghent, E.D, Dipple, G.M., Russell, J.K., 2004. Thermodynamic models for eclogitic mantle lithosphere. Earth Planet. Sci. Lett. 218, 451-462.

Grimm, R.E., 1994. The deep structure of Venusian plateau highlands. Icarus 112, 89-103.

Grimm, R.E., Hess, P.C., 1997. The crust of Venus, in: Bougher, W., Hunten, D.M., Phillips, R.J. (Eds.), Venus II. Univ. of Arizona Press, Tucson, pp. 1205-1244.

Guest, J.E., Stofan, E.R., 1999. A new view of the stratigraphic history of Venus. Icarus 139, 55-66.

Hansen, V.L., 2002. Artemis; surface expression of a deep mantle plume on Venus. Geological Society of America Bulletin 114, 839-848.

Hoogenboom, T., Houseman, G., Martin, P., 2005. Elastic thickness estimates for coronae associated with chasmata on Venus. J. Geophys. Res. 110, E09003.

Hoogenboom, T., Smrekar, S.E., Anderson, F.S., Houseman, G., 2004. Admittance survey of type 1 coronae on Venus. J. Geophys. Res. 109, E03002.

Ivanov, M.A., Head, J.W., 2011. Global geological map of Venus. Planetary and Space Science 59, 1559-1600.

James, P.B., Zuber, M.T., Phillips, R.J., 2013. Crustal thickness and support of topography on Venus. J. Geophys. Res. 118, 859-875.

Johnson, C.L., Sandwell, D.T., 1994. Lithospheric flexure on Venus. Geophys. J. Int. 119, 627-647.

Jull, M.G., Arkani-Hamed, J., 1995. The implications of basalt in the formation and evolution of mountains on Venus. Phys. Earth Planet. Inter. 89, 163-175.

Kirby, J.F., Swain, C.J., 2006. Mapping the mechanical anisotropy of the lithosphere using a 2D wavelet coherence, and its application to Australia. Physics of the Earth and Planetary Interiors 158(2-4), 122-138.

Kirby, J.F., Swain, C.J., 2008. An accuracy assessment of the fanwavelet coherence method for elastic thickness estimation. Geochemistry, Geophysics, Geosystems 9 (3), Q03022. (Correction. 2008. Geochemistry, Geophysics, Geosystems 9(5), Q05021).

Kirby, J.F., Swain, C.J., 2009. A reassessment of spectral Te estimation in continental interiors: the case of North America. Journal of Geophysical Research 114, B08401.

Kirby, J.F., Swain, C.J., 2011. Improving the spatial resolution of effective elastic thickness estimation with the fan wavelet transform. Computers & Geosciences 37, 1345-1354.

Kirby, J.F., Swain, C.J., 2013. Power spectral estimates using two-dimensional Morlet-fan wavelets with emphasis on the long wavelengths: jackknife errors, bandwidth resolution and orthogonality properties. Geophys. J. Int. 194, 78-99.

Kirby, J.F., 2014. Estimation of the effective elastic thickness of the lithosphere using inverse spectral methods: The state of the art. Tectonophysics 631, 87-116.

Konopliv, A.S., Banerdt, W.B., Sjogren, W.L., 1999. Venus gravity: 180th degree and order model. Icarus 139, 3-18.

Konopliv, A.S., Sjogren, W.L., 1994. Venus spherical harmonic gravity model to degree and order 60. Icarus 112, 42-54.

Kucinskas, A.B., Turcotte, D.L., 1994. Isostatic compensation of equatorial highlands on Venus. Icarus 112, 104-116.

McGovern, P.J., Solomon, S.C., Smith, D.F., Zuber, M.T., Simons, M., Wieczorek, M.A., Phillips, R.J., Neumann, G.A., Aharonson, O., Head J.W., 2002. Localized gravity/topography admittance and correlation spectra on Mars: Implications for regional and global evolution. J. Geophys. Res. 107, 5136.

McKenzie, D., 2003. Estimating Te in the presence of internal loads. Journal of Geophysical Research 108 (B9), 2438.

McKenzie, D., Nimmo, F., 1997. Elastic thickness estimates for Venus from line of sight accelerations. Icarus 130, 198-216.

McKenzie, D.P., Fairhead, J.D., 1997. Estimates of the effective elastic thickness of the continental lithosphere from Bouguer and free air gravity anomalies. J. Geophys. Res., 102(B12), 27 523-27 552.

McKinnon, W.B., Zahnle, K., Ivanov, B.A., Melosh, H.J., 1997. Cratering on Venus: modeling and observations, in: Bougher, W., Hunten, D.M., Phillips, R.J. (Eds.), Venus II. Univ. of Arizona Press, Tucson, pp. 969-1014.

Moore, W.B., Schubert, G., 1997. Venusian crustal and lithospheric properties from nonlinear regressions of highland geoid and topopgraphy. Icarus 128, 415-428.

Namiki, N., Solomon S.C., 1993. The gabbro-eclogite phase transition and the elevation of mountain belts on Venus. J. Geophys. Res. 98, 15,025-15,031.

Neumann, G.A., Zuber, M.T., Wieczorek, M.A., McGovern, P.J., Lemoine, F.G., Smith, D.E., 2004. Crustal structure of Mars from gravity and topography. J. Geophys. Res. 109, E08002.

Pauer, M., Fleming, K., Čadek, O., 2006. Modeling the dynamic component of the geoid and topography of Venus. J. Geophys. Res. 111, E11012.

Phillips, R.J., 1994. Estimating lithospheric properties at Atla Regio. Icarus 112, 147-170.

Phillips, R.J., Johnson, C.L., Mackwell, S.J., Morgan, P., Sandwell, D.T., Zuber, M.T., 1997. lithospheric mechanics and dynamics of Venus, in: Bougher, W., Hunten, D.M., Phillips, R.J. (Eds.), Venus II. Univ. of Arizona Press, Tucson, pp. 1163-1204.

Phillips, R.J., Raubertas, R.F., Arvidson, R.E., Sarkar, I.C., Herrick, R.R., Izenberg, N., Grimm, R.E., 1992. Impact craters and Venus resurfacing history. J. Geophys. Res. 97, 15923-15948.

Press, W.H., Teukolsky, S.A., Vetterling, W.T., Flannery, B.P., 1992. Numerical Recipes in Fortran 77, 2nd Ed., Cambridge University Press, Cambridge.

Rappaport, N.J., Konopliv, A.S., Kucinskas, A.B., 1999. An improved 360 degree and order model of Venus topography. Icarus 139, 19-31.

Ruiz, J., 2014. The early heat loss evolution of Mars and their implications for internal and environmental history. Sci. Rep. 4, 4338.

Ruiz, J., McGovern, P.J., Jiménez-Díaz, A., López, V., Williams, J.P., Hahn, B.C., Tejero, R., 2011. The thermal evolution of Mars as constrained by paleo-heat flows. Icarus 215, 508-517.

Schaber, G.G., Kirk, R.L., Strom, R.G., 1998. Data base of impact craters on Venus based on analysis of Magellan radar images and altimetry data. U.S. Geol. Surv. Open File Rep. 98-104.

Schaber, G.G., Strom, G.H., Moore, H.J., Soderblom, L.A., Kirk, R.L., Chadwick, D.J., Dawson, D.D., Gaddis, L.R., Boyce, J.M., Russell, J., 1992. Geology and distribution of impact craters on Venus: what are they telling us? J. Geophys. Res. 97 (E8), 13257-13301.

Simons M, Hager, B.H., Solomon, S.C., 1994. Global variations in the geoid/topography admittance of Venus. Science 264, 798-803.

Simons, M., Solomon, S.C., Hager, B.H., 1997. Localization of gravity and topography: constraints on the tectonics and mantle dynamics of Venus. Geophys. J. Int. 131, 24-44.

Smith, W.H.F., Wessel, P., 1990. Gridding with continuous curvature splines in tension. Geophysics 55, 293-305.

Smrekar, S.E., 1994. Evidence for active hotspots on Venus from analysis of Magellan gravity data. Icarus 112, 2-26.

Smrekar, S.E., Comstock, R., Anderson, F.S., 2003. A gravity survey of Type 2 coronae on Venus. J. Geophys. Res. 108 (E8), 5090.

Smrekar, S.E., Phillips, R.J., 1991. Venusian highlands: Geoid to topography ratios and their implications. Earth Planet. Sci. Lett. 107, 582-597.

Smrekar, S.E., Stofan, E.R., 1999. Origin of corona-dominated topographic rises on Venus. Icarus 139, 100-115.

Smrekar, S.E., Stofan, E.R., 2003. Effects of lithospheric properties on the formation of Type 2 coronae on Venus. J. Geophys. Res. 108 (E8), 5091.

Smrekar, S.E., Stofan, E.R., Kiefer, W.S., 1997. Large volcanic rises on Venus, in: Bougher, W., Hunten, D.M., Phillips, R.J. (Eds.), Venus II. Univ. of Arizona Press, Tucson, pp. 845-878.

Smrekar, S.E., Stofan, E.R., Mueller, N., Treiman, A., Elkins-Tanton, L., Helbert, J., Piccioni, G., Drossart, P., 2010. Recent Hotspot Volcanism on Venus from VIRTIS Emissivity Data. Science 328, 605-608.

Solomon, S.C., Head, J.W., 1982. Mechanisms for lithospheric heat transport on Venus: Implications for tectonic style and volcanism. J. Geophys. Res. 87, 9,236-9,246.

Solomon, S.C., Smrekar, S.E., Bindschadler, D.L., Grimm, R.E., Kaula, W.M., McGill, G.E., Phillips, R.J., Saunders, R.S., Schubert, G., Squyres, S.W., and Stofan, E.R., 1992, Venus tectonics: An overview of Magellan observations. J. Geophys. Res. 97, 13,199-13,255.

Sotin, C., Davaille, A., Lenardic, A., Smrekar, S.E., 2014. Venus' interior structure and dynamics. EPSC Abstracts, Vol. 9, EPSC2014-711.

Stofan, E.R., Hamilton, V.E., Janes, D.M., Smrekar, S.E., 1997. Coronae on Venus: Morphology and Origin, in: Bougher, W., Hunten, D.M., Phillips, R.J. (Eds.), Venus II. Univ. of Arizona Press, Tucson, pp. 931-965.

Stofan, E.R., Smrekar, S.E., Tapper, S.W., Guest, J.E., Grindrod, P.M., 2001. Preliminary analysis of an expanded corona database for Venus. Geophys. Res. Lett. 28, 4267-4270.

Strom, R.G., Schaber, G.G., Dawson, D.D., 1994. The global resurfacing of Venus. J. Geophys. Res. 99 (E5), 10899-10926.

Swain, C.J., Kirby, J.F., 2003. The effect of 'noise' on estimates of the elastic thickness of the continental lithosphere by the coherence method, Geophys. Res. Lett. 30(11), 1574.

VEXAG, 2014. Goals, Objectives, and Investigations for Venus Exploration 2014, Venus Exploration Analysis Group (VEXAG), [http://www.lpi.usra.edu/vexag], 21 pp.

Vezolainen, A.V., Solomatov, V.S., Basilevsky, A.T., Head, J.W., 2004. Uplift of Beta Regio: Three-dimensional models. J. Geophys. Res. 109, E08007.

Watts, A.B., 2001. Isostasy and Flexure of the Lithosphere. Cambridge University Press. 472 pp.

Watts, A.B., Burov, E.B., 2003. Lithospheric strength and its relation to the elastic and seismogenetic layer thickness. Earth Planet. Sci. Lett. 213, 113-131.

Watts, A.B., Zhong, S.J., Hunter, J., 2013. Lithosphere behaviour on seismic through geologic time-scales. Annual Reviews Earth & Planetary Sciences 41, 443-468.

Wessel, P., Smith, W.H.F., Scharroo, R., Luis, J.F., Wobbe, F., 2013. Generic Mapping Tools: Improved version released, EOS Trans. AGU, 94, 409-410.

Wieczorek, M.A., 2007. Gravity and topography of the terrestrial planets, Treatise on Geophysics, Vol. 10, 165-206.

Wieczorek, M.A., Meschede, M., 2015. SHTOOLS - Tools for working with spherical harmonics (v3.0), ZENODO, doi:10.5281/zenodo.15967.

Wieczorek, M.A., Phillips, R.J., 1998. Potential anomalies on a sphere: applications to the thickness of the lunar crust. J. Geophys. Res. 103, 1715-1724.

Zuber, M.T., 1987. Constraints on the lithospheric structure of Venus from mechanical models and tectonic surface features. J. Geophys. Res. 92, E541-E551.

Zuber, M.T., Solomon, S.C., Phillips, R.J., Smith, D.E., Tyler, G.L., Aharonson, O., Balmino, G., Banerdt, W.B., Head, J.W., Lemoine, F.G., 2000. Internal structure and early thermal evolution of Mars from Mars Global Surveyor topography and gravity. Science 287, 1788-1793.

Capítulo 5

La (reconstrucción de la) historia térmica de los planetas terrestres: Estructura y evolución de la litosfera de Marte

5. La (reconstrucción de la) historia térmica de los planetas terrestres: Estructura y evolución de la litosfera de Marte

5.1. Introducción

Uno de los grandes objetivos de las ciencias planetarias es comprender la evolución interna de los planetas y satélites mayores del Sistema Solar, y como ha afectado a las condiciones en su superficie, por ejemplo a nivel geológico o climático. Uno de los aspectos básicos de la evolución interna es la historia térmica del cuerpo en cuestión, que se relaciona con la estructura y grado de diferenciación internos, o con el grado y estilo de la actividad volcánica y tectónica. En este contexto, Marte es el objeto del Sistema Solar, aparte de la Tierra, cuyo estudio despierta más interés, dado que es el que presenta (o presentó en el pasado) condiciones ambientales más parecidas a las de nuestro propio planeta, aunque el conocimiento de su historia evolutiva es todavía muy incompleto. Sin embargo, este planeta preserva un excelente registro de deformaciones sucedidas a lo largo de casi toda la historia del Sistema Solar (unos cuatro mil millones de años), y contamos además con excelentes datos de topografía y gravedad para su estudio obtenidos a partir de varias misiones de las agencias espaciales norteamericana y europea (NASA y ESA, respectivamente, por sus siglas en inglés).

El conocimiento (aunque sea aproximado) de la relación entre la estructura térmica de la litosfera y su comportamiento mecánico, así como sus cambios temporales, aporta importantes informaciones sobre la evolución térmica de un planeta. En efecto, la relación entre temperatura y comportamiento mecánico de las rocas permite calcular el flujo térmico de los cuerpos planetarios a partir de indicadores geológicos de temperatura en profundidad, como el espesor elástico efectivo de la litosfera, parámetro que se relaciona con la resistencia total de la litosfera frente a la deformación (McNutt, 1984; Watts y Burov, 2003), o la profundidad de grandes fallas (Schultz y Watters, 2001; Ruiz et al., 2008). Los resultados así obtenidos corresponden a la época en que se formaron las estructuras geológicas usadas como indicador, y por tanto esta aproximación puede potencialmente dar información sobre la evolución térmica de un planeta al ayudar a la caracterización del flujo térmico en distintas épocas (Zuber et al., 2000; McGovern et al., 2002), y puede potencialmente ayudar a deducir la intensidad y distribución de fuentes internas de calor (Phillips et al., 2008; Ruiz et al., 2010). Esto además resulta muy útil en ausencia de medidas directas de flujo térmico.

En el artículo que se presenta en este capítulo se calculan, de una manera matemáticamente consistente, paleo flujos térmicos derivados del espesor elástico efectivo de la litosfera o de la profundidad de grandes fallas para veintidós regiones de Marte de diferente época y contexto geológico, con el

objetivo de constreñir la historia térmica del planeta rojo. Para ello, se han implementado conductividades térmicas realistas para la corteza y el manto litosférico (incluyendo una conductividad térmica dependiente de la temperatura, apropiada para el olivino, para el manto litosférico), así como dos casos extremos de abundancia y distribución de elementos radiactivos productores de calor (HPE): se han utilizado valores refinados de HPE basados en las medidas de la sonda *Mars Odyssey* GRS (Hahn et al., 2011) y ausencia de HPE en la litosfera para calcular límites superiores e inferiores, respectivamente, de los flujos térmicos superficiales. Además, se han tenido en cuenta las respectivas contribuciones de la corteza y el manto litosférico a la resistencia total de la litosfera en los cálculos de flujo térmicos derivados del espesor elástico efectivo. Finalmente, se comparan los resultados obtenidos con estimaciones de HPE derivadas de modelos composicionales y con las predicciones derivadas de modelos de la historia térmica de Marte, con el objetivo de constreñir su evolución térmica.

De esta manera se ha podido realizar una primera aproximación a su evolución térmica, mostrando que este planeta ha disipado menos calor que el producido en su interior por radioactividad, lo que implica que se ha enfriado muy poco (e incluso podría haberse calentado internamente), al menos durante algunas fases de su historia. Estas conclusiones son consistentes con una serie de observaciones geológicas y geofísicas independientes como son la presencia de un núcleo metálico total o parcialmente líquido, una reducida presencia de estructuras compresivas indicando una cantidad limitada de contracción térmica, y la abundancia de depósitos volcánicos de origen reciente.

5.2. The thermal evolution of Mars as constrained by paleo-heat flows

Javier Ruiz [a], Patrick J. McGovern [b], Alberto Jiménez-Díaz [a], Valle López [c,d],

Jean-Pierre Williams [e], Brian C. Hahn [f], Rosa Tejero [a,d]

[a] *Departamento de Geodinámica, Facultad de Ciencias Geológicas, Universidad Complutense de Madrid. 28040 Madrid, Spain*

[b] *Lunar and Planetary Institute, 3600 Bay Area Boulevard, Houston, TX 77058, USA*

[c] *Instituto de Geología Económica, CSIC-UCM, 28040 Madrid, Spain*

[d] *Instituto de Geociencias, CSIC-UCM, 28040 Madrid, Spain*

[e] *Department of Earth and Space Sciences, University of California, Los Angeles, CA 90095, USA*

[f] *Department of Earth and Planetary Sciences, University of Tennessee, Knoxville, TN 37996*

Icarus 215, 508-517, 2011

Abstract

Lithospheric strength can be used to estimate the heat flow at the time when a given region was deformed, allowing us to constrain the thermal evolution of a planetary body. In this sense, the high (>300 km) effective elastic thickness of the lithosphere deduced from the very limited deflection caused by the north polar cap of Mars indicates a low surface heat flow for this region at the present time, a finding difficult to reconcile with thermal history models. This has started a debate on the current heat flow of Mars and the implications for the thermal evolution of the planet. Here we perform refined estimates of paleo-heat flow for 22 martian regions of different periods and geological context, derived from the effective elastic thickness of the lithosphere or from faulting depth beneath large thrust faults, by considering regional radioactive element abundances and realistic thermal conductivities for the crust and mantle lithosphere. For the calculations based on the effective elastic thickness of the lithosphere we also consider the respective contributions of crust and mantle lithosphere to the total lithospheric strength. The obtained surface heat flows are in general lower than the equivalent radioactive heat production of Mars at the corresponding times, suggesting a limited contribution from secular cooling to the heat flow during the majority of the history of Mars. This is contrary to the predictions from the majority of thermal history models, but is consistent with evidence suggesting a currently fluid core, limited secular contraction for Mars, and recent extensive volcanism. Moreover, the interior of Mars could even have been heating up during part of the thermal history of the planet.

5.2.1. Introduction

A very interesting and productive debate on the present-day heat flow and thermal state of Mars, and their implications for the thermal evolution of the planet, is currently occurring (Phillips et al.,

2008; Kiefer and Li, 2009; Grott and Breuer, 2009, 2010; Ruiz et al., 2010; Dombard and Phillips, 2010). The very high (>300 km) effective elastic thickness of the lithosphere implied by the very limited (if any) deflection caused by the loading due to the north polar cap of Mars (Phillips et al., 2008) indicates a low surface heat flow at the present-time that is difficult to reconcile with most thermal history models. This low heat flow could be indicative of sub-chondritic heat-producing elements abundances (Phillips et al., 2008), a limited influence of secular cooling and fossil heat (Ruiz et al., 2010), or simply a regional variability of surface heat flow (Phillips et al., 2008; Kiefer and Li, 2009; Grott and Breuer, 2009, 2010). This debate clearly shows the profound implications that current or ancient surface heat flow estimates, deduced from geological or geophysical indicators of the thermal state of the lithosphere, have for understanding the thermal history of Mars.

Previous works estimated surface heat flows for diverse regions and epochs of Mars from the effective elastic thickness of the lithosphere (Solomon and Head, 1990; Anderson and Grimm, 1998; Zuber et al., 2000; Nimmo, 2002; Kiefer, 2004; McGovern et al., 2002, 2004; Grott et al., 2005; Ruiz et al., 2006a,b, 2008, 2010; Kronberg et al., 2007; Ruiz, 2009; Dohm et al., 2009a; Ritzer and Hauck, 2009) or from the depth to the brittle–ductile transition (BDT) beneath large thrust faults (Schultz and Watters, 2001; Grott et al., 2007; Ruiz et al., 2008, 2009); such heat flow estimates correspond to the time when the lithosphere was loaded or faulted. These previous works find a general decrease of heat flows with time, as expected for a cooling planet (McGovern et al., 2002, 2004; Montesi and Zuber, 2003), although there were some indications of regional variations in surface heat flows since comparatively higher heat flows are found for volcanic regions (McGovern et al., 2004).

However, the values of material parameters used to derive heat flow estimates varies widely, limiting the ability to integrate the results of different studies to collectively constrain the thermal history of Mars. Specifically, the amount and distribution of lithospheric heat-producing elements (HPE) and the values of the thermal conductivity of crust and mantle can affect the results substantially (Ruiz et al., 2006a, 2010). Heat flow estimates typically have not included HPE in the calculations: this omission reduces the calculated surface heat flow but increases calculated mantle heat flow and temperatures in the lower crust. Similarly, most workers used a very high mantle lithosphere thermal conductivity, which overestimates the surface heat flow for high effective elastic thicknesses but underestimates temperatures in the mantle lithosphere.

In this work we carefully calculate in a consistent manner paleo-heat flow for 22 martian regions of different ages and geological contexts (Fig. 5.1). We improve the heat flow calculations by taking into account realistic thermal conductivities for the crust and mantle lithosphere (including a temperature-dependent thermal conductivity, appropriate for olivine, for the mantle lithosphere), and two extreme cases for the abundance and distribution of HPE: we use refined HPE values based on Mars Odyssey GRS measurement and zero lithospheric HPE to calculate upper and lower limits, respectively, for the surface heat flows. For the heat flow calculations that use the effective elastic thickness of the lithosphere we also consider the respective contributions of crust and mantle components to the total strength of the lithosphere. Finally, we compare our results with estimates of radioactive heat production deduced from compositional models and with predictions from thermal history models, in order

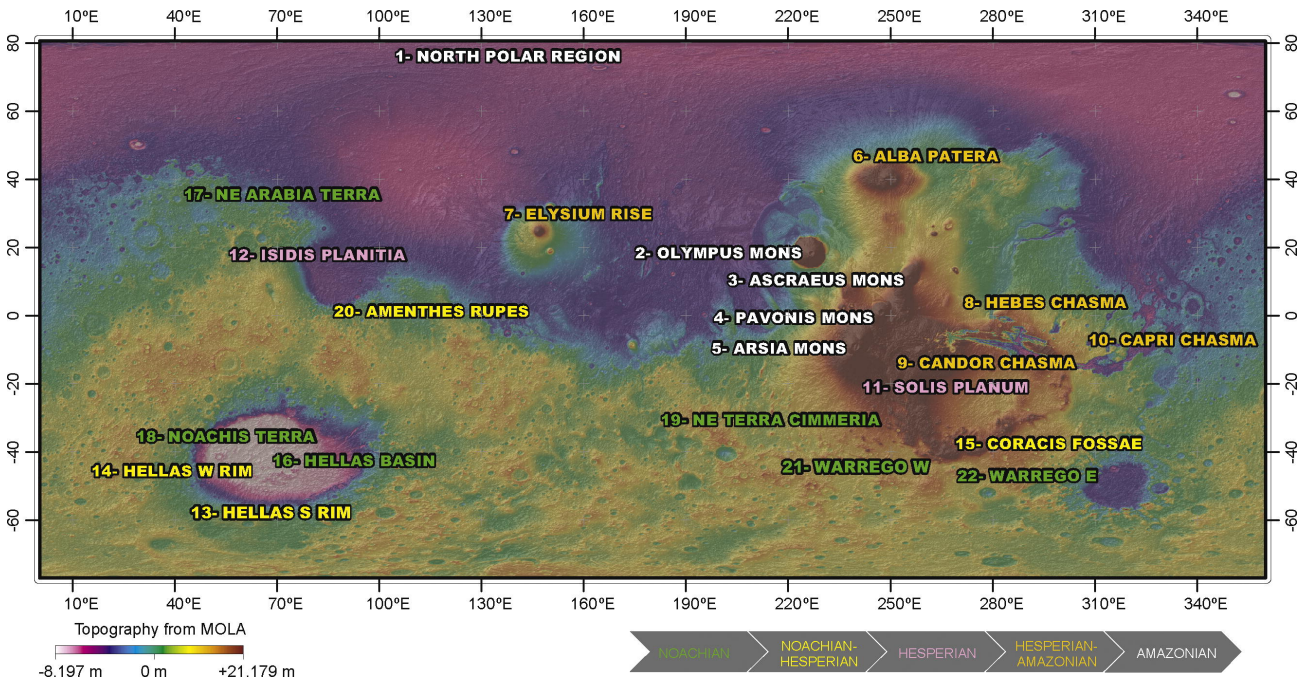

Figure 5.1: MOLA topography map showing the analyzed regions.

to obtain constrains on the thermal evolution of Mars. Since heat flow upper limits are more useful to constrain thermal evolution, we have been very careful to provide very robust upper limit calculations for the analyzed regions.

5.2.2. Strength of the lithosphere

The effective elastic thickness is a measure of the total strength of the lithosphere, integrating contributions from brittle and ductile layers and from elastic cores of the lithosphere (for a review see Watts and Burov (2003)). Effective elastic thickness estimates can be converted to estimates of heat flow following the equivalent strength envelope procedure described by McNutt (1984). This methodology is based on the condition that the bending moment M of the mechanical lithosphere must be equal to the bending moment of the equivalent elastic layer of thickness T_e, and so,

$$\frac{EKT_e^3}{12(1-\upsilon^2)} = \int_0^{T_m} \sigma(z)(z-z_n)dz, \tag{5.1}$$

where E is the Young's modulus, K is the topography curvature, T_e is the effective elastic thickness, υ is the Poisson's ratio, T_m is the mechanical thickness of the lithosphere, $\sigma(z)$ is the least, at depth z, of the brittle strength, the ductile strength, or the fiber stress due to plate flexure, and z_n is the depth to the neutral stress plane. Additionally, the condition of zero net axial force is imposed,

$$\int_0^{T_m} \sigma(z)dz = 0. \tag{5.2}$$

The case of a rheologically stratified lithosphere with mechanically decoupled crust and mantle is more complicated (see, for example, McNutt et al., 1988; Burov and Diament, 1992; Ruiz et al., 2006c), and the total bending moment is given by

$$M = M_{crust} + M_{mantle}, \tag{5.3}$$

where the subindex refers to the crust and mantle lithosphere contributions to the total bending moment. Also, in this case the condition of zero net axial force must be imposed on both the crust and lithospheric mantle.

The brittle strength is calculated according to the expression (e.g., Ranalli, 1997)

$$(\sigma_1 - \sigma_3)_b = \alpha \rho g (1 - \lambda) z, \tag{5.4}$$

where α is a coefficient depending on the stress regime (which is 3 and 0.75 for pure compression and tension respectively; e.g., Ranalli, 1997), ρ is the density, g is the acceleration due to the gravity (3.72 m s^{-2} for Mars), λ is the pore pressure, and z is the depth. The brittle strength of the crust is here calculated directly from Eq. (5.4) by using the density of the crust. The brittle strength of the lithospheric mantle is calculated for a density of 3500 kg m^{-3} and starting from the brittle strength at the base of the crust. The ductile strength (which does not depend on the stress regime) is given by

$$(\sigma_1 - \sigma_3)_d = \left(\frac{\dot{e}}{A} \right)^{1/n} exp \left(\frac{Q}{nRT} \right), \tag{5.5}$$

where $\dot{e}$ is the strain rate, A, Q, and n are laboratory-determined constants, R (= 8.31447 J mol^{-1} K^{-1}) is the gas constant, and T is the absolute temperature. The fiber stress is in turn calculated from

$$\sigma_{fib} = \frac{EK(z - zn)}{1 - \upsilon^2}. \tag{5.6}$$

The link between the strength envelope procedure and heat flow comes from the dependence of the ductile strength on temperature.

We analyze regions for which estimates of effective elastic thickness and topography curvatures of the equivalent elastic layer are available (see Table 5.1). Also, the elastic parameters in these estimates must be consistent with the nominal values of E = 100 GPa and υ = 0.25, which are widely used for Mars (e.g., McGovern et al., 2002; Phillips et al., 2008). The density of the crust is taken as 2900 kg m^{-3}, unless a different value has been inferred from geophysical modeling (e.g., McGovern et al., 2004) for a given region, and the mantle lithosphere density is taken as 3500 kg m^{-3}. The admittance modeling of McGovern et al. (2004), from which derive the majority of effective elastic thicknesses in Table 5.1, was performed for a mean crustal thickness of 50 km, whereas the crustal thickness maps of Neumann et al. (2004, 2008) were constructed for a mean crustal thickness of 45 km. Thus, for our calculations we assume local crustal thicknesses based on regional trends in Neumann et al. (2008) but increased by 5 km, in order to be consistent with the mean value of McGovern et al. (2004). Positive and negative topography curvatures are concave downward and upward, respectively, which implies that the part of the elastic plate above the neutral stress plane is under tension or compression,

Feature	Centered on	Surface age	T_e (km)	Curvature (10^{-7} m^{-1}) [h]	Crustal density (kg m^{-3})	Crustal thickness (km)
1. North Pole [a]	90ºN, 0ºE	Current	>300	0	2900	30
2. Olympus Mons [b]	19ºN, 226.5ºE	A	>70	-1.6	2900	55
3. Ascraeus Mons [b]	11.5ºN, 256ºE	A	≤80 [g]	-0.69	2900	70
4. Pavonis Mons [b]	0.5ºN, 247ºE	A	<100	-1.0	2900	75
5. Arsia Mons [b]	9ºS, 239ºE	A	>20	-13	2900	85
6. Alba Patera [b]	42ºN, 249ºE	A–H	38–65	-1.8 to -0.55	2900	65
7. Elysium rise [b]	25ºN, 147ºE	A–H	15–45	-9.9 to -2.3	2900	45
8. Hebes Chasma [b,c]	1ºS, 284ºE	A–H	≥60	-1.2	2900	65
9. Candor Chasma [b,c]	8ºS, 295ºE	A–H	≥80	-1.2	2200	70
10. Capri Chasma [b,c]	12ºS, 310ºE	A–H	>100	-0.6	2500	55
11. Solis Planum [b]	25ºS, 270ºE	H	24–37	+6.4 to +3.0	2900	70
12. Isidis Planitia [d]	13ºN, 87ºE	H	100–180	-0.09 to -0.02	2900	10
13. Hellas S rim [b]	64ºS, 66ºE	H–N	20–120	+6.4 to + 0.34	2900	55
14. Hellas W rim [b]	42ºS, 39ºE	H–N	<20	-3.9	2650	55
15. Coracis Fossae [e]	34.5ºS, 274.5ºE	H–N [f]	10.3–12.5	+6.4 to + 4.9	2900	75
16. Hellas Basin [b]	42ºS, 66ºE	N	<13	-7.6	2750	15
17. NE Arabia Terra [b]	36ºN, 40ºE	N	<16	-2.4	2500	50
18. Noachis Terra [b]	35ºS, 26ºE	N	<12	-3.1	2800	65
19. Terra Cimmeria [b]	30ºS, 180ºE	N	<12	-4.2	2950	60

[a] Phillips et al. (2008).

[b] McGovern et al. (2004); the maximum lithospheric curvature in the vicinity of each feature/region was determined directly from the lithospheric deflection, for themodels that correspond to the upper and/or lower bounds on effective elastic thickness.

[c] There are alternative best fit T_e values (McGovern et al., 2004), but we use values maximizing the heat flow range.

[d] Ritzer and Hauck (2009).

[e] Grott et al. (2005).

[f] A surface age of 3.5–3.9 Ga has been reported for this feature by Grott et al. (2005).

[g] The effective elastic thickness range for this feature is 2–80 km (McGovern et al., 2004); because the very low lower bound, we have only calculated the lower limit heat flows for this feature.

[h] Curvature values correspond to the quoted T_e values; positive and negative values indicate, respectively, concave upward and downward curvatures.

Table 5.1: Values used for the calculation of heat flows from the effective elastic thickness (T_e) of the lithosphere.

respectively (e.g., Turcotte and Schubert, 2002). This determines the value of the parameter a used for each case in Eq. (5.4). For several regions in Table 5.1 T_e upper (lower) limits are unavailable; for these regions we cannot obtain lower (upper) limits for the heat flow.

We perform calculations for zero pore pressure and hydrostatic pore pressure. Increasing the pore pressure decreases the total strength of the lithosphere, and the heat flow must be lowered in order to maintain the total strength consistent with a given T_e. Thus, for equal T_e, zero and hydrostatic pore pressures serve to place upper and lower limits, respectively, to the obtained surface heat flow.

For creep parameters of the martian crust we use the constants for the flow law of diabase: A = 0.0612 MPa^{-n} s^{-1}, n = 3.05 and Q = 276 kJ mol^{-1} (Caristan, 1982). The use of a wet diabase law is appropriate for a basaltic martian crust and is consistent with extensive evidence for water-

related geological activity in early Mars (e.g., Head et al., 2001; Dohm et al., 2009b); moreover, the water amount needed to ''wet'' the diabase is certainly modest (lower than 1%; see Caristan, 1982). The ductile strength of the mantle lithosphere is calculated for dry and wet olivine dislocation creep rheologies, which give upper and lower limits, respectively, to the surface heat flow. For wet olivine, we use the flow law of the Anita Bay dunite: A = 9550 MPa^{-n} s^{-1}, n = 3.35 and Q = 444 kJ mol^{-1} (Chopra and Paterson, 1984). This flow law places a lower limit on the strength of wet olivine due to its relative weakness (compared with other wet dunites, such as Aheim dunite). For dry olivine we use the flow law obtained for artificially dried dunites (which is valid for both Anita Bay and Aheim dunites): A = 28840 MPa^{-n} s^{-1}, n = 3.6 and Q = 535 kJ mol^{-1} (Chopra and Paterson, 1984). Zhao et al. (2009) have recently reported that anhydrous olivine is considerably weaker when it is proportionally iron-rich, as expected for the martian mantle, which would reduce mantle strength and hence the obtained heat flows. Thus, the use of rheology of Chopra and Paterson (1984) provides a generous upper limit for heat flows obtained from lithospheric strength. (There are not similar published experiments for iron-rich wet olivine.) Strain rates of 10^{-16} and 10^{-19} s^{-1} are used in the calculations, based on the range usually considered for Mars (McGovern et al., 2002, 2004). To make a comparison, terrestrial strain rates are typically $\sim 10^{-16}$ s^{-1} in active continental interiors (e.g., Tesauro et al., 2007), and $\sim 10^{-19}$–10^{-17} s^{-1} in stable plate interiors (Ku- mar and Gordon, 2009).

The base of the mechanical lithosphere is here defined as the depth at which the ductile strength reaches a low value of 10 MPa (see Ranalli, 1994; Ruiz et al., 2006a), and below which there are no further significant increases in strength, although varying the exact value selected does not produce substantial changes in the calculations due to the exponential dependence of ductile strength on temperature (see McNutt, 1984).

The depth of the brittle–ductile transition (BDT) can also be used in order to calculate surface heat flows (Ruiz and Tejero, 2000). This depth can be deduced by estimating the depth of faults that are thought to extend down until the crustal BDT, and hence the temperature at the BDT depth is obtained by equating the brittle and ductile strength for the depth $z = z_{BDT}$,

$$T_{BDT} = \frac{Q}{R}\left[ln\frac{A(\sigma_1 - \sigma_3)^n_{BDT}}{\dot{e}}\right]^{-1}, \tag{5.7}$$

where $(\sigma_1 - \sigma_3)_{BDT}$ is the strength at the BDT depth from Eq. (5.4). The heat flow is then obtained by matching T_{BDT} to a temperature profile. Here we use this procedure for three prominent lobate scarps (Table 5.2), interpreted to be the surface expression of large thrust faults. It must be noted that pore fluid pressure reduces brittle strength, and hence increases temperature at the BDT depth. Thus, upper and lower limits for the surface heat flow are calculated, respectively, for hydrostatic conditions and zero pore pressure, the opposite to the case for calculations based on the effective elastic thickness of the lithosphere.

Feature	Centered on	Surface age	BDT depth (km)	Crustal density (kg m^{-3})	Crustal thickness (km)
20. Amenthes Rupes [a]	2ºN, 249ºE	H–N	27–35	2900	50
21. Warrego W [b]	41ºS, 263ºE	N [c]	27–35	2900	80
22. Warrego E [b]	43ºS, 267ºE	N [c]	21–28	2900	75

[a] Ruiz et al. (2008).

[b] Grott et al. (2005).

[c] A surface age of 3.7–4.0 Ga has been reported Grott et al. (2005) for this feature.

Table 5.2: Values used for the calculation of heat flows from the brittle–ductile transition (BDT) depth.

5.2.3. Temperature profiles

Surface heat flows obtained from lithospheric strength are higher, for a fixed T_e or BDT depth, if lithospheric radioactive heat sources are included in the calculations than if purely thermal gradients are used (see Ruiz et al., 2006a, 2008, 2009). Thus, we calculate surface heat flow upper limits by including HPE in the crust and the mantle lithosphere, whereas lower limits are obtained by using zero lithospheric heat sources.

The significant homogeneity of elemental abundances measure by Mars Odyssey GRS suggests that the martian crust is much less geochemically varied than the Earth's crust (Taylor et al., 2006), which is consistent with a strong mixing by cratering (e.g. Taylor et al., 2006), and with the absence of large-scale crustal recycling, at least since the early part of the history of Mars (e.g., Frey, 2006). Indeed, some authors have suggested that Mars experienced an early phase of plate tectonics (e.g., Sleep, 1994; Baker et al., 2007), although high-resolution topography and radar sounding have revealed a large population of buried impact basins on Mars, implying a similar, and very early (>4 Ga), age of the basement throughout the entire planet (Frey, 2006; Watters et al., 2006). Temperature profiles in the crust are therefore calculated by assuming a homogeneous distribution of radioactive heat sources. Although it is possible that crustal HPE abundances decrease with depth, a homogeneous distribution gives higher surface heat flow and therefore is useful for our upper limit calculations. Also, we use a constant thermal conductivity for the crust, and therefore the temperature at a given depth z is given by

$$T_z = T_s + \frac{Fz}{k_c} - \frac{\rho_c H_c z^2}{2k_c}, \tag{5.8}$$

where T_s is the surface temperature, F is the surface heat flow, k_c is the thermal conductivity of the crust, ρ_c is the density of the crust, and H_c is the crustal heat production rate per unit mass. We use a surface temperature of 220 K, the present-day mean surface temperature on Mars (Kieffer et al., 1977), which is consistent with the inference of low near-surface temperatures deduced for most of the past 4 Ga from ALH84001 thermochronology (Shuster and Weiss, 2005). Also, we use k_c = 2 W m^{-1} K^{-1}, a value appropriate for intact basaltic rocks; this value is in the uppermost part of the range for intact (non-porous) basalts (see the compilation by Beardsmore and Cull (2001)).

Crustal potassium and thorium abundances for each analyzed region (Table 5.3) have been obtained from 5º x 5º pixel maps of GRS abundances renormalized considering the volatile content, in order to reflect a volatile/alteration-free composition, more likely to be representative of the total crust, and not surface contamination (Hahn et al., 2011). Uranium abundances are estimated using a Th/U ratio of 3.8. Potassium and thorium abundance values of the pixels corresponding to the analyzed features are good regional approximations due to the regional scale of the GRS footprint; the footprint of the GRS instrument from which 50% of the gamma ray signal originates is between 480 and 600 km in diameter (roughly 8–10º measured at the equator) depending upon energy (e.g., Boynton et al., 2007). For the North Polar Region, where GRS measurements are absent, we use global averages. For Hellas south rim, for which there are potassium and thorium GRS measurements but no volatile values, we use the same volatile abundances as for Hellas west rim. Heat dissipation rates are calculated for decay constants from Van Schmus (1995), and regional ages are listed in Table 5.1.

Feature	K (ppm)	Th (ppm)	U (ppm)
1. North Pole	3652 [a]	0.69 [a]	0.18 [a]
2. Olympus Mons	3390	0.63	0.17
3. Ascraeus Mons	3220	0.67	0.18
4. Pavonis Mons	3540	0.68	0.18
5. Arsia Mons	3630	0.63	0.17
6. Alba Patera	3070	0.51	0.13
7. Elysium rise	2900	0.53	0.14
8. Hebes Chasma	3670	0.54	0.14
9. Candor Chasma	3850	0.54	0.14
10. Capri Chasma	4310	0.65	0.17
11. Solis Planum	2540	0.42	0.11
12. Isidis Planitia	4590	0.86	0.23
13. Hellas S rim	2850	0.36	0.10
14. Hellas W rim	3750	0.77	0.20
15. Hellas Basin	3030	0.36	0.09
16. Coracis Fossae	2960	0.51	0.13
17. NE Arabia Terra	3640	0.79	0.21
18. Noachis Terra	3850	0.75	0.20
19. Terra Cimmeria	4830	0.97	0.26
20. Amenthes Rupes	3540	0.68	0.18
21. WarregoW	3100	0.60	0.16
22. Warrego E	3260	0.57	0.15

[a] Average values for the martian crust

Table 5.3: Heat-producing element abundances.

The effective elastic thicknesses from the admittance study of McGovern et al. (2004) were estimated for regions including surfaces of different epochs (see also Tanaka, 1986). For these regions we use the age range embracing the appropriate periods. Absolute ages for period boundaries are derived from the cratering chronologies of Hartmann and Neukum (2001); when Hartmann's and

Neukum's chronologies differ (for the Late Hesperian epoch or younger) we use the mean value as representative.

The thermal conductivity of olivine (the main mineral in the mantle) is strongly temperature-dependent, and therefore we calculate temperature profiles in the mantle lithosphere from

$$\frac{dT}{dz} = \frac{F_{cb} - \rho_m H_m (z - b_c)}{k_m(T)}, \tag{5.9}$$

where $F_{cb} = \rho_c H_c b_c$ is the heat flow at the base of the crust, ρ_m and H_m are, respectively, the density and heat production rate per mass unity of the mantle lithosphere, b_c is the base of the crust, and k_m is the thermal conductivity of the mantle lithosphere. The value of H_m is poorly constrained, and here we use $H_m = 0.1 H_{c(av)}$, where $H_{c(av)}$ is the average value for the martian crust. This choice is based on a ratio between crustal and primitive mantle HPE abundances higher than $\sim$10 for Mars (Taylor and McLennan, 2009), and represents a reasonable upper limit for H_m (melt extraction would reduce mantle HPE abundances), which in turn results in an upper limit to the obtained surface heat flow (the lower limit is obtained for $H_c = 0$ and $H_m = 0$).

For k_m we use the thermal conductivity of olivine, the main mineral in lithospheric mantle rocks, according to the expression (McKenzie et al., 2005)

$$k_m = \frac{a}{1 + c(T - 273)} + \sum_{i=0}^{3} d_i T^i, \tag{5.10}$$

where a = 5.3, c = 0.0015, d_0 = 1.753 x 10^{-2}, d_1 = -1.0364 x 10^{-4}, d_2 = 2.2451 x 10^{-7} and d_3 = -3.4071 x 10^{-11}, for calculating an upper limit for the thermal conductivity of olivine as a function of temperature. Results obtained from Eq. (5.10) are similar to those of Hofmeister (1999) for forsterite olivine. The thermal conductivity of some silicate minerals somewhat decreases with the increasing of the proportion of iron (Hofmeister, 1999). The martian mantle is considered to be iron-rich (e.g., Halliday et al., 2001), and for this reason Eq. (5.10) gives an upper limit to the thermal conductivity of the mantle lithosphere of Mars. However, there are not, to our knowledge, similar expressions to Eq. (5.10) accounting for iron content of olivine. Eq. (5.10) applied to the martian mantle lithosphere would overestimate the thermal conductivity (by less than 1 W m^{-1} K^{-1}), which is useful for calculation of surface heat flow upper limits; on the other hand, for the calculation of surface heat flow lower limits this effect is balanced by the assumption of zero lithospheric heat sources.

For the case of the North Polar Region we additionally consider the effect of the polar cap above (but not included in) the lithosphere. The polar cap is assumed to be composed of water–ice. The thermal conductivity of cold water–ice is high, and the presence of rocks or other ices (e.g., CO_2) would reduce the bulk thermal conductivity, and hence the calculated heat flow. For this reason, non-water–ice components are not taken into account in our upper-limit calculation. The thermal conductivity of water– ice is strongly temperature-dependent, and therefore the temperature profile in the polar cap is given by

$$T_{pcb} = T_s exp\left(\frac{F b_{cp}}{k_0}\right), \tag{5.11}$$

where T_s is the surface temperature, F is the surface heat flow (equal to the heat flow reaching the polar cap from below), b_{cp} is the thickness of the polar cap, and k_0 = 621 W m^{-1} (Petrenko and Whitworth, 1999). Here we use T_s = 155 K and b_{cp} = 2 km as representative of the martian polar regions (Plaut et al., 2007; Phillips et al., 2008; Wieczorek, 2008).

5.2.4. Results

Surface heat flows are calculated by constructing thermal profiles (Section 5.2.3) that satisfy the constraints imposed by indicators of lithospheric strength (Section 5.2.2). Calculations based on faulting depth only consider the thermal structure of the crust above the BDT depth, since the lithosphere below it does not influence the results. Calculations based on the effective elastic thickness of the lithosphere consider the entire thickness of the mechanical lithosphere. Also, the condition of non-negative sublithospheric heat flow is imposed for calculations using lithospheric heat sources. A negative sublithospheric heat flow could occur if assumed lithospheric HPE abundances are higher than the actual ones for a particular region (for example, the crust could be stratified, with a HPE-poor lower crust; see Ruiz et al., 2006b, 2009). If the sublithospheric heat flow is negative, then the thermal profile is adjusted to enforce zero sublithospheric heat flow and permit a ductile strength higher than 10 MPa at the base of the mechanical lithosphere. This is appropriate for calculating a generous upper limit to the surface heat flow since, as above noted, higher lithospheric strength increases the surface heat flow for a given T_e.

Results are shown in Fig. 5.2 as a function of age. Fig. 5.2 also shows the average surface heat flow corresponding to the total radioactive heat production of Mars after the compositional model of Wänke and Dreibus (1988). From Fig. 5.2 it is evident that most of the estimated heat flow upper limits, and all the lower limits, are below the radioactive heat flow curve (although lower limits from features for which an upper limit is not available give a limited constraint on the thermal history). Also, the obtained heat flows are lower than predicted for the majority of thermal history models of Mars (e.g., Hauck and Phillips, 2002; Williams and Nimmo, 2004; Grott and Breuer, 2010; Fraeman and Korenaga, 2010).

Our results can also be interpreted in terms of the Urey number *Ur*, the ratio of the internal heat production to the total surface heat loss in a planet. Fig. 5.2 indicates very low heat flows relative to expected heat output, consistent with very little secular cooling, i.e., a bulk-Mars *Ur* for Mars approaching 1.0 or perhaps even exceeding that value. Current estimates of the bulk-Earth *Ur* are in the range 0.35–0.53 (e.g., Jaupart et al., 2007; Korenaga, 2008), and somewhat higher (but usually $<$0.75) values are predicted for most martian thermal history models (see Fig. 5.3).

If $Ur > 1$ the martian interior (as an average) would be heating up. For illustrative purposes, we have estimated the mantle temperature change for constant representative values for the Urey number by integrating the mantle heat balance equation from McGovern and Schubert (1989) using martian interior heat production values deduced from the HPE abundances of Wänke and Dreibus (1988). We obtain mantle temperature increases of 160 and 320 K for, respectively, Urey numbers of 1.2 and 1.5

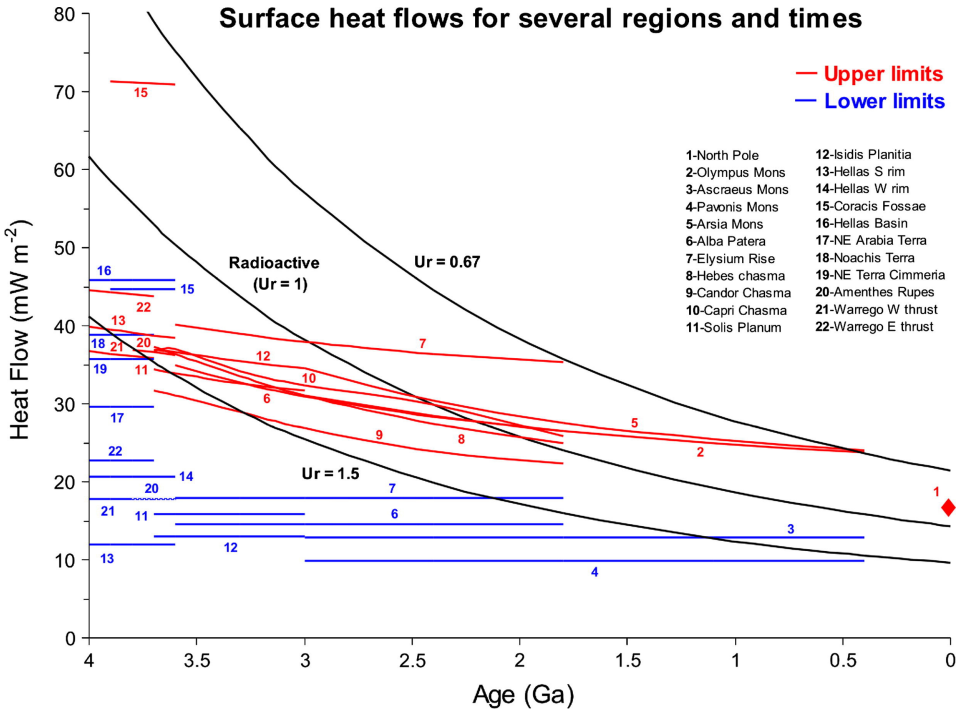

Figure 5.2: Upper (red) and lower (blue) limits for the surface heat flows for several regions and times of Mars. For several regions only upper or lower limits are obtained, since lower or upper limits on effective elastic thickness are not available. Curves and horizontal lines indicate uncertainty related to surface age (and hence also to radioactive heating in the lithosphere), not to temporal evolution. The black curves show surface heat flows for three values of the Urey number (the ratio of the internal heat production to the total surface heat loss in a planet), calculated according to the composition model of Wänke and Dreibus (1988). Thus, the curve labeled ‘‘Radioactive (Ur = 1)’’ corresponds to the average surface heat flow which is equivalent to the total radioactive heat production of Mars.

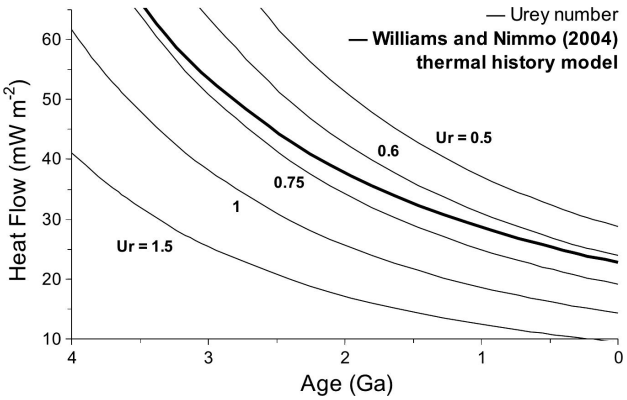

Figure 5.3: Heat flows as a function of age and Urey number compared with the predictions of a thermal history model of Mars (calculated according to Williams and Nimmo (2004)), which obtain results similar to those of other thermal history models for Mars (e.g., Hauck and Phillips, 2002; Grott and Breuer, 2010). The Urey number is between 0.75 and 0.6 through the entire history of Mars.

integrated over the entire history of Mars. These values would be in any case generous upper limits given that the time period for which Ur could have been higher than 1 is likely to be significantly less than 4.6 Gyr. Under appropriate conditions ($Ur > 1$ and surface heat flow higher than the radioactive contribution from the lithosphere), heating of the convective mantle and cooling (and thickening) of the lithosphere could simultaneously occur.

Fig. 5.4 shows upper limits to the surface heat flow as a function of feature age and type of terrain (Fig. 5.5 shows the location, period and relative value of these upper limits). The only terrains for which surface heat flow could clearly exceed the equivalent radioactive heat flow are volcanic regions (Coracis Fossae is a rift zone with associated magmatism; Dohm et al., 2001; Grott et al., 2005), although uncertainties in feature age and effective elastic thickness preclude a definitive conclusion. Also, regional heat flow variations related to differences in crustal HPE abundances and/or crustal thickness (which influences the total amount of crustal HPE in the lithospheric column), are also expected (e.g., Grott and Breuer, 2010; Hahn et al., 2011), although our results lack the resolution to reveal these variations.

The estimates of effective elastic thickness for Isidis Planitia are comparatively high (Ritzer and Hauck, 2009), but the obtained surface heat flow is similar to other regions due to the very low curvatures and thin crust (which increases the mantle contribution to the total strength of the lithosphere) in this region. Similarly, the very high lower limits of the effective elastic thickness estimated for the North Polar Region (Phillips et al., 2008) gives a heat flow upper limit slightly higher than the

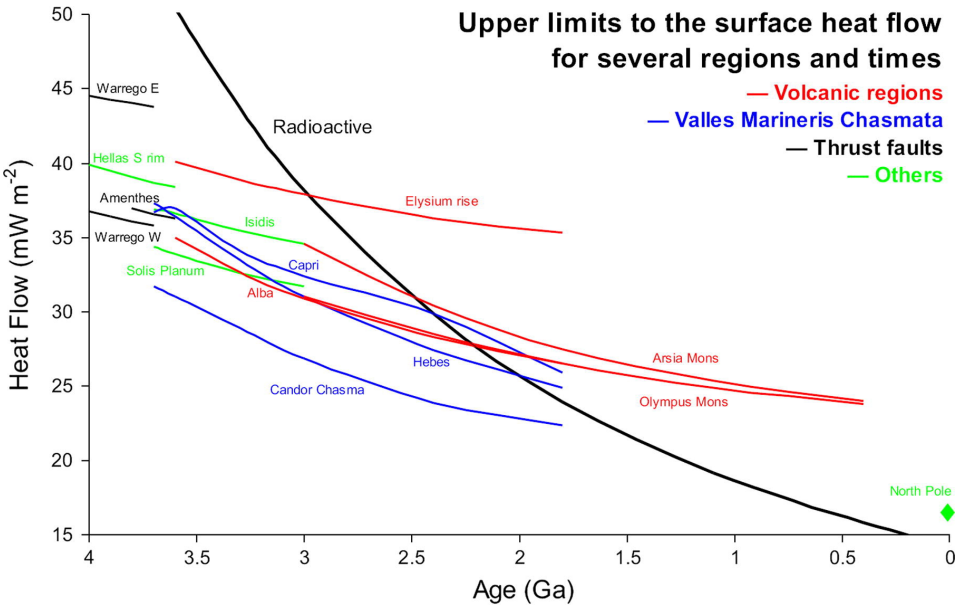

Figure 5.4: Upper limits for the surface heat flows for several regions and times of Mars. Several categories of geological features are also indicated. Coracis Fossae, a rift zone with associated magmatism is not represented due to scale considerations (see Fig. 5.3). Curves indicate uncertainty related to surface age (and hence to radioactive heating in the lithosphere), not to temporal evolution. The black curve is the average heat flow equivalent to the total radioactive heat production of Mars according to the composition model of Wänke and Dreibus (1988).

equivalent radioactive heat flow due to the absence of flexure (and also to a relatively thin crust) in this region. On the other hand, the heat flow lower limits obtained for non-volcanic Noachian terrains (for which only upper limits are available for the effective elastic thickness) do not rule out a very high surface heat flow when the large-scale topography of these regions was formed. However, the absence of upper limit estimates for the surface heat flow in these regions greatly diminishes their relevance as constraints on the thermal evolution of Mars.

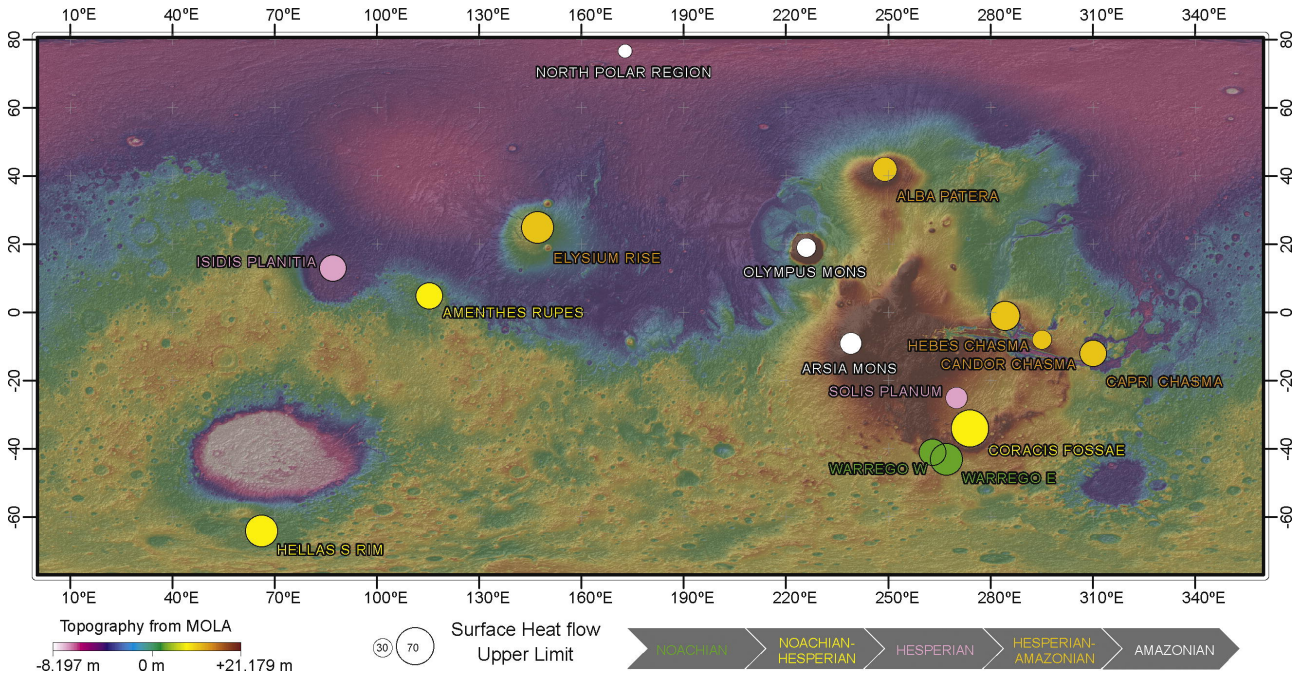

Figure 5.5: Regional distribution of upper limits for the surface heat flow shown on MOLA topography. Most estimates correspond to the Tharsis region of Mars, where geological activity is concentrated.

5.2.5. Discussion

Our results indicate that the contribution from secular cooling to the surface heat flow has been limited during the majority of the history of Mars, contrary to the predictions of most thermal history models (e.g., Hauck and Phillips, 2002; Grott and Breuer, 2010). Further, the heat flow estimates in Fig. 5.2 suggest that the martian mantle was heating up during a significant fraction of the history of the planet (at least during Hesperian and Early Amazonian periods). These results are robust due to the conservative assumptions applied in generating our heat flow upper bounds.

Fig. 5.6 shows upper limits for sublithospheric heat flows (in essence the heat flow from the convective mantle), calculated in the same way as upper limits in Figs. 5.2 and 5.4 except by assuming $H_c = 0$ and $H_m = 0$: in absence of lithospheric heat sources the surface heat flow equals the sublithospheric heat flow. Calculated upper limits for sublithospheric heat flows are again lower than predicted from the majority of thermal history models (e.g., Hauck and Phillips, 2002; Grott and

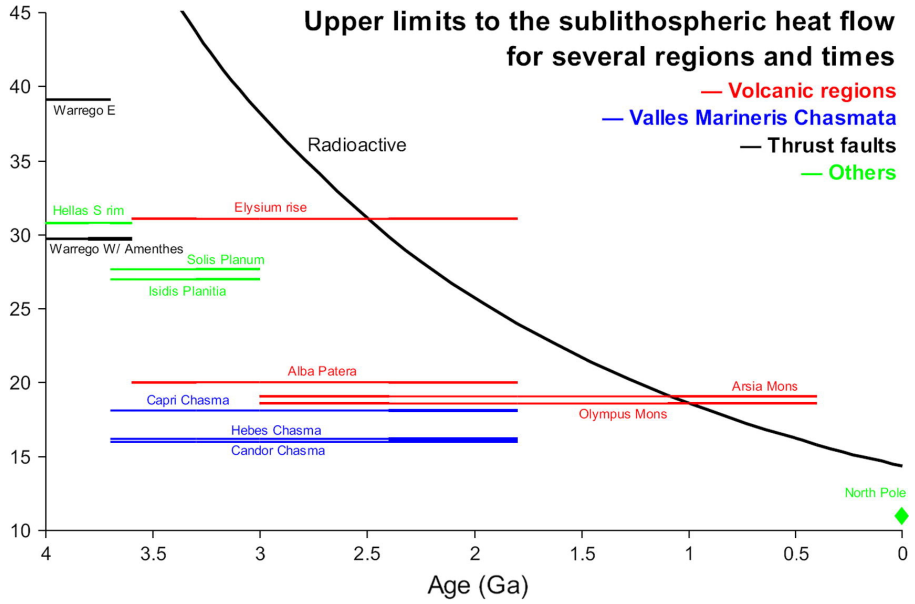

Figure 5.6: Upper limits for the sublithospheric heat flow for several regions and times of Mars, calculating by imposing the condition of zero lithospheric heat sources. Coracis Fossae is not represented due to scale considerations (the sublithospheric heat flow upper limit is 68 mW m^{-2} for this feature). Several categories of geological features are also indicated. Black curve as in Fig. 5.4.

Breuer, 2010). These low sublithospheric heat flow values also suggest that mantle convection has been less efficient than has been appreciated in many studies of martian thermal evolution.

Our results are consistent with several independent geophysical and geological observations. For example, high mantle temperatures reduce core cooling, possibly contributing to the present-day existence of a, at least partly, fluid core (deduced from the response to the solar tide; Yoder et al., 2003), and to the simultaneous absence of an endogenic magnetic field (e.g., Acuña et al., 2001) due to the reduction (or even suppression) of core convection (e.g., Nimmo and Stevenson, 2000). Our results are also consistent with a lower amount of global contraction since the Early Noachian than expected from thermal history models, as deduced from thrust faults recorded on the surface (Nahm and Schultz, 2011); indeed, the lack of mantle cooling (and maybe mantle heating) limits the thermal contraction that can drive surface contraction. Finally, the evidences for recent extensive volcanism (Hauber et al., 2011) also suggest the retention of a substantial amount of internal heat.

Our results are also supported by parameterized mantle convection models that couple convective vigor with the rheologic weakening effect of interior volatiles suggesting that high Urey ratios are also favored by inefficient cycling of volatiles to and from the mantle (McGovern and Schubert, 1989; Sandu et al., 2011), as might be expected for Mars, which has lacked a plate tectonic cycle to efficiently degas and (especially) replenish the mantle volatiles at least since the early part of the evolution of Mars. Further, High Urey ratios might typify all planets lacking the thermal efficiency of plate tectonics.

Alternatively, a substantial amount of heat could be transported by hydrothermal cooling of the upper crust (Parmentier and Zuber, 2007). However, hydrothermal circulation could only operate

above the brittle–ductile transition, since below porosity is mostly eliminated by viscous creep (Hanna and Phillips, 2005). This implies that, for a given temperature at the BDT, the obtained temperature profile below the BDT depth (and the sublithospheric heat flow) is the same if hydrothermal cooling is occurring or not (although in our calculations surface heat flows are increased with respect to the value at the BDT depth due to radioactive heating in the brittle crust). Magmatic activity could enhance hydrothermal circulation and heat flow on space scales lower than resolved by admittance studies, but to justify in this way average heat flows higher than those obtained here for the majority of the history and regions of Mars seems unrealistic.

On the other hand, Baratoux et al. (2011a,b) have recently modeled melting pressures and degrees of partial melting from GRS data for 12 Hesperian and Amazonian volcanic provinces, and hence potential mantle temperatures and (using linear thermal gradients and a constant thermal conductivity for the entire lithosphere) heat flows, suggesting bulk-Mars $Ur \sim$0.6–0.7 or lower, in accordance with most thermal history models. However, volcanic regions are expected to be associated with higher than average heat flows (see Figs. 5.2 and 5.4), making any Ur value based on those regions a lower limit. Thus, the melting pressures and degrees of partial melting obtained by Baratoux et al. (2011a,b) do not alter our conclusions.

5.2.6. Conclusions

Our results strongly suggest that Mars has been losing less heat than conventionally thought during, at least, a substantial part of its history. This would be indicative of less efficient mantle convection than commonly thought (perhaps related to stagnant lid convection with inefficient volatile cycling) and/or a reduced contribution from fossil heat to the surface heat flow, which would result in a lower heat flow from the convective mantle, and possibly elevated lower mantle and core temperatures. Also, there is evidence favoring a heterogeneous heat flow depending on the geological province (volcanic versus non-volcanic provinces), although it cannot presently be definitively demonstrated. Moreover, if the interior of Mars is in fact heating up ($Ur > 1$), there is the potential for a future increase in mantle convective vigor and/or melting, and there may ultimately be a resurgence of volcanic and tectonic activity.

It is clear that a better understanding of the thermal evolution of Mars requires a feedback between thermal history models and heat flow calculations based on the evolution of the strength of the lithosphere.

Acknowledgments

We thank James Dohm and an anonymous reviewer for their comments and suggestions; also, we thank Matthias Grott for his comments on an early version of this work. J.R. was supported by a contract Ramón y Cajal co-financed from the Ministerio de Ciencia e Innovación of Spain and the Fondo Social Europeo (ESF). LPI contribution number LPI-001630.

References

Acuña, M.H. et al., 2001. Magnetic field of Mars: Summary of results from the aerobraking and mapping orbits. J. Geophys. Res. 106, 23403–23417.

Anderson, S., Grimm, R.E., 1998. Rift processes at the Valles Marineris, Mars: Constraints from gravity on necking and rate-depending strength evolution. J. Geophys. Res. 103, 11113–11124.

Baker, V.R., Maruyama, S., Dohm, J.M., 2007. Tharsis superplume and the geological evolution of early Mars. In: Yuen, D.A., Maruyama, S., Karato, S.-I., Windley, B.F. (Eds.), Superplumes: Beyond Plate Tectonics. Springer, Berlin, pp. 507–523.

Baratoux, D., Toplis, M.J., Monnereau, M., Gasnault, O., 2011a. Thermal history of Mars inferred from orbital geochemistry of volcanic provinces. Nature 472, 338–341.

Baratoux, D., Toplis, M.J., Monnereau, M., Gasnault, O., 2011b. Corrigendum: Thermal history of Mars inferred from orbital geochemistry of volcanic provinces. Nature 475, 254.

Beardsmore, G.R., Cull, J.P., 2001. Crustal Heat Flow: A Guide to Measurement and Modelling. Cambridge University Press, Cambridge, 324 pp.

Boynton, W.V. et al., 2007. Concentration of H, Si, Cl, K, Fe, and Th in the low and mid latitude regions of Mars. J. Geophys. Res. 112, E12S99.

Burov, E.B., Diament, M., 1992. Flexure of the continental lithosphere with multilayered rheology. Geophys. J. Int. 109, 449–468.

Caristan, Y., 1982. The transitions from high temperature creep to fracture in Marylan diabase. J. Geophys. Res. 87, 6781–6790.

Chopra, P.N., Paterson, M.S., 1984. The role of water in the deformation of dunite. J. Geophys. Res. 89, 7861–7876.

Dohm, J.M., Tanaka, K.L., Hare, T.M., 2001. Geologic map of the Thaumasia region of Mars. USGS Misc. Inv. Ser. Map I-2650, scale 1:5000,000.

Dohm, J.M. et al., 2009a. Claritas rise, Mars: Pre-Tharsis magmatism? J. Volcanol. Geotherm. Res. 185, 139–156.

Dohm, J.M. et al., 2009b. GRS Evidence and the possibility of paleooceans on Mars. Planet. Space Sci. 57, 664–684.

Dombard, A.J., Phillips, R.J., 2010. Viscoelastic finite-element simulations of the flexure under the north polar cap of Mars. Proc. Lunar Planet. Sci. Conf. 41. Abstract 1865.

Fraeman, A.A., Korenaga, J., 2010. The influence of mantle melting on the evolution of Mars. Icarus 210, 43–57.

Frey, H.V., 2006. Impact constraints on, and a chronology for, major events in early Mars history. J. Geophys. Res. 111, E08S91.

Grott, M., Breuer, D., 2009. Implications of large elastic thicknesses for the composition and current thermal state of Mars. Icarus 201, 540–548.

Grott, M., Breuer, D., 2010. On the spatial variability of the martian elastic lithosphere thickness: evidence for mantle plumes? J. Geophys. Res. 115, E03005.

Grott, M., Hauber, E., Werner, S.C., Kronberg, P., Neukum, G., 2005. High heat flux on ancient Mars: Evidence from rift flank uplift at Coracis Fossae. Geophys. Res. Lett. 32, L21201.

Grott, M., Hauber, E., Werner, S.C., Kronberg, P., Neukum, G., 2007. Mechanical modelling of thrust faults in the Thaumasia region, Mars, and implications for the Noachian heat flux. Icarus 186, 517–526.

Hahn, B.C., McLennan, S.M., Klein, E.C., 2011. Martian surface heat production and crustal heat flow from Mars Odyssey gamma-ray spectrometry. Geophys. Res. Lett. doi:10.1029/2011GL047435, in press.

Halliday, A.N., Wänke, H., Birck, J.L., Clayton, R.N., 2001. The accretion, composition and early differentiation of Mars. Space Sci. Rev. 96, 197–230.

Hanna, J.C., Phillips, R.J., 2005. Hydrological modeling of the martian crust with application to the pressurization of aquifers. J. Geophys. Res. 110, E01004.

Hartmann, W.K., Neukum, G., 2001. Cratering chronology and the evolution of Mars. Space Sci. Rev. 96, 165–194.

Hauber, E., Broz, P., Jagert, F., Jodlowski, F., Platz, T., 2011. Very recent and wide- spread basaltic volcanism on Mars. Geophys. Res. Lett. 38, L10201.

Hauck, S.A., Phillips, R.J., 2002. Thermal and crustal evolution of Mars. J. Geophys. Res. 107, 5052.

Head, J.W. et al., 2001. Geological processes and evolution. Space Sci. Rev. 96, 263– 292.

Hofmeister, A.M., 1999. Mantle values of thermal conductivity and the geotherm from phonon lifetimes. Science 283, 1699–1706.

Jaupart, C., Labrosse, S., Mareschal, J.C., 2007. Temperatures, heat and energy in the mantle of the Earth. In: Bercovici, S. (Ed.), Treatise on Geophysics: Mantle Dynamics, vol. 7. Elsevier, Amsterdam, pp. 253–303.

Kiefer, W.S., 2004. Gravity evidence for a extinct magma chamber beneath Syrtis Major, Marts: A look at the magmatic plumbing system. Earth Planet. Sci. Lett. 222, 349–361.

Kiefer, W.S., Li, Q., 2009. Mantle convection controls the observed lateral variations in lithospheric thickness on present-day Mars. Geophys. Res. Lett. 36, L18203.

Kieffer, H.H. et al., 1977. Thermal and albedo mapping of Mars during the Viking primary mission. J. Geophys. Res. 82, 4249–4291.

Korenaga, J., 2008. Urey ratio and the structure and evolution of Earth's mantle. Rev. Geophys. 46, 1–32.

Kronberg, P. et al., 2007. Acheron Fossae, Mars: Tectonic rifting, volcanism, and implications for lithospheric thickness. J. Geophys. Res. 112, E04005.

Kumar, R.R., Gordon, R.G., 2009. Horizontal thermal contraction of oceanic lithosphere: The ultimate limit to the rigid plate approximation. J. Geophys. Res. 114, B01403.

McGovern, P.J., Schubert, G., 1989. Thermal evolution of the Earth: Effects of volatile exchange between atmosphere and interior. Earth Planet. Sci. Lett. 96, 27–37.

McGovern, P.J. et al., 2002. Localized gravity/topography admittance and correlation spectra on Mars: Implications for regional and global evolution. J. Geophys. Res. 107, 5136.

McGovern, P.J. et al., 2004. Correction to localized gravity/topography admittance and correlation spectra on Mars: Implications for regional and global evolution. J. Geophys. Res. 109, E07007.

McKenzie, D., Jackson, J., Priestley, K., 2005. Thermal structure of oceanic and continental lithosphere. Earth Planet. Sci. Lett. 233, 337–349.

McNutt, M.K., 1984. Lithospheric flexure and thermal anomalies. J. Geophys. Res. 89, 11180–11194.

McNutt, M.K., Diament, M., Kogan, M.G., 1988. Variations of elastic plate thickness at continental thrust belts. J. Geophys. Res. 93, 8825–8838.

Montesi, L.G.J., Zuber, M.T., 2003. Clues to the lithospheric structure of martian from winkle ridge sets and localization instability. J. Geophys. Res. 108, 5048.

Nahm, A.L., Schultz, R.A., 2011. Magnitude of global contraction on Mars from analysis of surface faults: Implications for martian thermal history. Icarus 211, 389–400.

Neumann, G.A. et al., 2004. The crustal structure of Mars from gravity and topography. J. Geophys. Res. 109, E08002.

Neumann, G.A., Lemoine, F.G., Smith, D.E., Zuber, M.T., 2008. Marscrust3-A crustal thickness inversion from recent MRO gravity solutions. Proc. Lunar Planet. Sci. Conf. 39. Abstract 2167.

Nimmo, F., 2002. Admittance estimates of mean crustal thickness and density at the martian hemispheric dichotomy. J. Geophys. Res. 107, 5117.

Nimmo, F., Stevenson, D.J., 2000. Influence of early plate tectonics on the thermal evolution and magnetic field of Mars. J. Geophys. Res. 105, 11969–11979.

Parmentier, E.M., Zuber, M.T., 2007. Early evolution of Mars with mantle compositional stratification or hydrothermal crustal cooling. J. Geophys. Res. 112, E02007.

Petrenko, V.F., Whitworth, R.W., 1999. Physics of Ice. Oxford Univ. Press, Oxford, 366pp.

Phillips, R.J. et al., 2008. Mars north polar deposits: Stratigraphy, age, and geodynamical response. Science 320, 1182–1185.

Plaut, J.J. et al., 2007. Subsurface radar sounding of the south polar layered deposits of Mars. Science 316, 92–95.

Ranalli, G., 1994. Nonlinear flexure and equivalent mechanical thickness of the lithosphere. Tectonophysics 240, 107–114.

Ranalli, G., 1997. Rheology of the lithosphere in space and time. Geol. Soc. Spec. Pub. 121, 19–37.

Ruiz, J., 2009. The very early thermal state of Terra Cimmeria: Implications for magnetic carriers in the crust of Mars. Icarus 203, 454–459.

Ruiz, J., Tejero, R., 2000. Heat flows through the ice lithosphere of Europa. J. Geophys. Res. 105, 23283–23289.

Ruiz, J., McGovern, P.J., Tejero, R., 2006a. The early thermal and magnetic state of the cratered highlands of Mars. Earth Planet. Sci. Lett. 241, 2–10.

Ruiz, J., Tejero, R., McGovern, P.J., 2006b. Evidence for a differentiated crust at Solis Planum, Mars, from lithospheric strength and heat flow. Icarus 180, 308–313.

Ruiz, J., Gómez-Ortiz, D., Tejero, R., 2006c. Effective elastic thicknesses of the lithosphere in the Central Iberian Peninsula from heat flow: Implications for the rheology of the continental lithospheric mantle. J. Geodyn. 41, 500–509.

Ruiz, J. et al., 2008. Ancient heat flow, crustal thickness, and lithospheric mantle rheology in the Amenthes region, Mars. Earth Planet. Sci. Lett. 270, 1–12.

Ruiz, J., Williams, J.P., Dohm, J.M., Fernández, C., López, V., 2009. Ancient heat flows and crustal thickness at Warrego rise, Thaumasia Highlands, Mars: Implications for a stratified crust. Icarus 203, 47–57.

Ruiz, J., López, V., Dohm, J.M., 2010. The present-day thermal state of Mars. Icarus 207, 631–637.

Sandu, C., Lenardic, A., McGovern, P., 2011. The effects of volatile cycling on planetary thermal evolution. J. Geophys. Res., submitted for publication.

Schultz, R.A., Watters, T.R., 2001. Forward mechanical modeling of the Amenthes Rupes thrust fault on Mars. Geophys. Res. Lett. 28, 4659–4662.

Shuster, D.L., Weiss, B.P., 2005. Martian surface paleotemperatures from thermochronology of meteorites. Science 309, 594–597.

Sleep, N.H., 1994. Martian plate tectonics. J. Geophys. Res. 99, 5639–5655.

Solomon, S.C., Head, J.W., 1990. Heterogeneities in the thickness of the elastic lithosphere of Mars: Constraints on heat flow and internal dynamics. J. Geophys. Res. 95, 11073–11083.

Tanaka, K.L., 1986. The stratigraphy of Mars. J. Geophys. Res. 91, E139–E158.

Taylor, S.R., McLennan, S.M., 2009. Planetary Crusts: Their Composition, Origin and Evolution. Cambridge Univ. Press, Cambridge.

Taylor, G.J. et al., 2006. Bulk composition and early differentiation of Mars. J. Geophys. Res. 111, E03S10. doi:10.1029/2005JE002645 (Printed 112 (E3), 2007).

Tesauro, M., Kaban, M.K., Cloetingh, S.A.P.L., Hardebol, N.J., Beekman, F., 2007. 3D strength and gravity anomalies of the European lithosphere. Earth Planet. Sci. Lett. 263, 56–73.

Turcotte, D.L., Schubert, G., 2002. Geodynamics, second ed. Cambridge Univ. Press, Cambridge, 456pp.

Van Schmus, W.R., 1995. Natural radioactivity of the crust and mantle. In: Ahrens, T.J. (Ed.), Global Earth Physics: A Handbook of Physical constants. AGU Reference Shelf 1. American Geophysical Union, Washington, DC, pp. 283–291.

Wänke, H., Dreibus, G., 1988. Chemical composition and accretion history of terrestrial planets. Philos. Trans. Roy. Soc. London: Ser. A 325, 545–557.

Watters, T.R. et al., 2006. MARSIS radar sounder evidence of buried basins in the northern lowlands of Mars. Nature 444, 905–908.

Watts, A.B., Burov, E.B., 2003. Lithospheric strength and its relation to the elastic and seismogenetic layer thickness. Earth Planet. Sci. Lett. 213, 113–131.

Wieczorek, M.A., 2008. Constraints on the composition of the martian south polar cap from gravity and topography. Icarus 196, 506–517.

Williams, J.-P., Nimmo, F., 2004. Thermal evolution of the martian core: Implications for an early dynamo. Geology 32, 97–100.

Yoder, C.F., Konopliv, A.S., Yuan, D.N., Standish, E.M., Folkner, W.M., 2003. Fluid core size of Mars from detection of the solar core. Science 300, 299–303.

Zhao, Y.-H., Zimmerman, M.E., Kohlstedt, D.L., 2009. Effect of iron content on the creep behavior of olivine: 1. Anhydrous conditions. Earth Planet. Sci. Lett. 287, 229–240.

Zuber, M.T. et al., 2000. Internal structure and early thermal evolution of Mars from Mars Global Surveyor. Science 287, 1788–1793.

Capítulo 6

Discusión y conclusiones

6. Discusión y conclusiones

6.1. Marco conceptual integrador

Aunque los distintos artículos presentados en esta memoria de Tesis Doctoral se ocupan de dominios geodinámicos y problemáticas concretas y diferentes, todos ellos persiguen un objetivo común. Como se comentó al inicio de esta memoria (véase el Capítulo 1), la investigación presentada en los capítulos anteriores pone de manifiesto, mediante el estudio de casos concretos, la profunda relación que existe entre la estructura mecánica de la litosfera y su estado térmico, y cómo cada aumento en el conocimiento de uno de estos aspectos puede ser utilizado para mejorar nuestro conocimiento del otro, de manera que no es posible una correcta comprensión de la primera sin un adecuado conocimiento del segundo y viceversa. Así, los resultados presentados en los artículos, cuando son tomados conjuntamente, brindan una imagen más amplia del concepto de litosfera que la que puede encontrarse en cada uno de los artículos individuales, y permiten una valoración más global de las aportaciones derivadas del trabajo realizado en esta investigación.

La Figura 6.1 muestra de una manera integrada el marco conceptual de esta investigación, individualizando los conceptos aplicados en cada uno de los casos de estudio abordados, y que ponen de manifiesto la interrelación existente entre el estado térmico de la litosfera y la estructura mecánica de la misma. El estudio de esta interrelación es precisamente el objetivo fundamental de esta Tesis Doctoral. En el Capítulo 2 se hace especial énfasis sobre la importancia de un conocimiento adecuado de los parámetros térmicos implicados, del flujo térmico superficial, y de la estructura térmica local para una mejor compresión de la estructura mecánica de la litosfera en una región determinada de la Tierra, el centro de la península ibérica. Por su parte, en los Capítulo 3 y 4 se remarca la gran utilidad del análisis integrado de topografía y gravedad como herramienta (mediante el cálculo del espesor cortical y el espesor elástico efectivo) para caracterizar el comportamiento mecánico de la litosfera a largo plazo, primero en Centroamérica, y después de forma global en Venus. Por último, en el Capítulo 5 se explora de nuevo la relación entre la estructura térmica y mecánica de la litosfera procediendo en orden inverso a lo que se hace en el Capítulo 2, deduciendo sus propiedades térmicas en función de indicadores de la estructura mecánica, como son el espesor elástico efectivo de la litosfera o la profundidad de la transición frágil-dúctil en la corteza, con el fin de reconstruir la historia térmica de una región o un planeta, en este caso, de Marte. De este modo, tomados en conjunto, todos los trabajos incluidos en esta investigación muestran la universalidad de los métodos que sirven para estudiar la estructura térmica y mecánica de la litosfera, y refuerzan la confianza en la aplicación de este tipo de metodologías al estudio de la litosfera de la Tierra y de otros cuerpos planetarios.

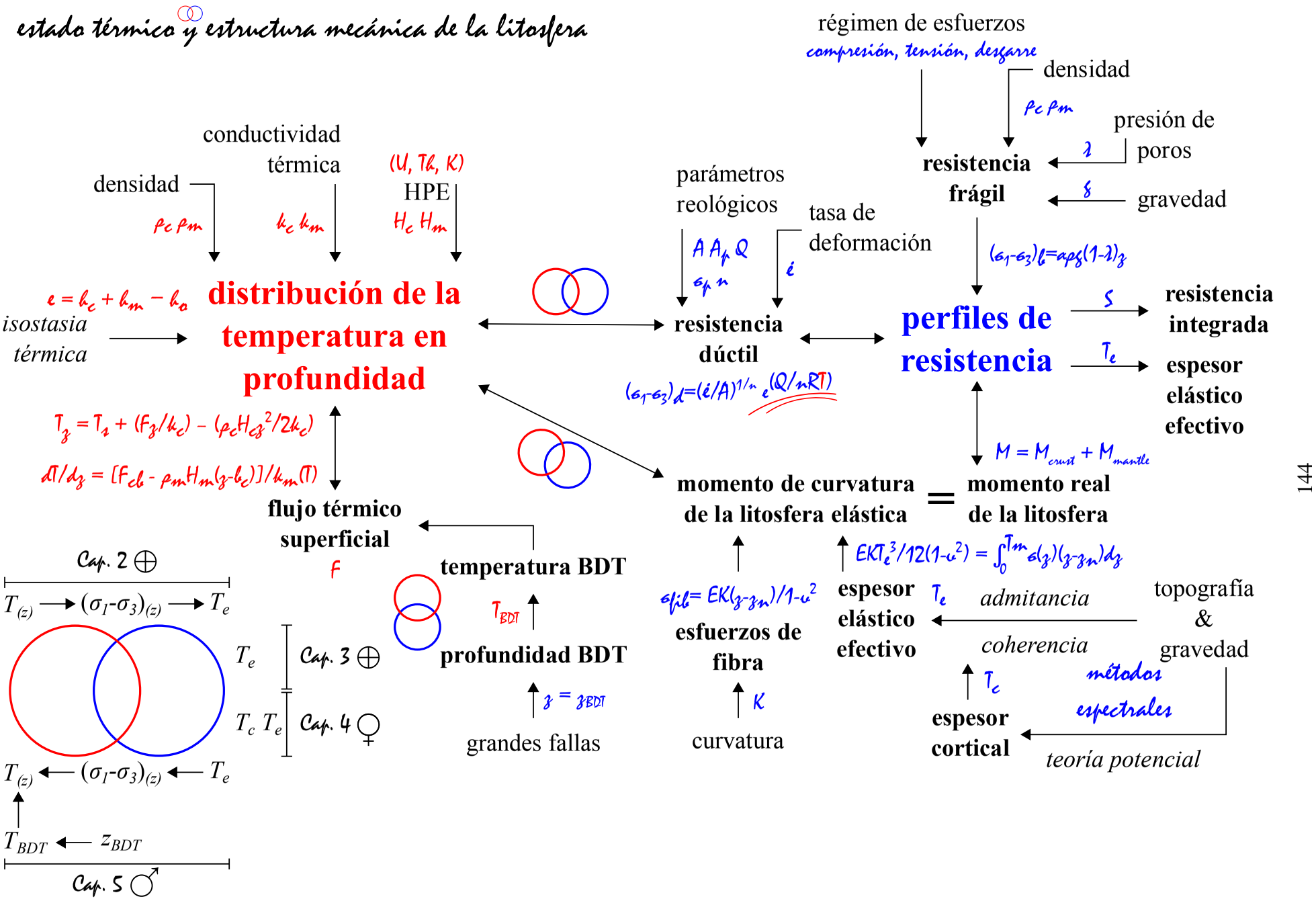

Figura 6.1: Marco conceptual de la investigación.

Finalmente, como es habitual en cualquier investigación, la que se recoge en esta memoria no supone más que un primer paso para el estudio de la estructura térmica y mecánica de la litosfera, y para avanzar en el conocimiento y comprensión de la dinámica de la Tierra y del resto de los planetas de tipo terrestre (ejemplificados en esta Tesis Doctoral por Venus y Marte), y de cómo se ha desarrollado su evolución interna. Cada uno de los trabajos aquí recopilados plantea preguntas que constituyen nuevos retos a afrontar, y que han abierto el camino a nuevas investigaciones, algunas de ellas en proceso y otras en las que se espera trabajar a corto o medio plazo. A continuación se exponen, de forma breve, algunas de estas lineas de trabajo futuras.

6.2. Sobre la anisotropía mecánica de la litosfera

La resistencia de la litosfera juega un papel relevante en el control de la deformación que resulta de la acción de cargas a largo plazo sobre la misma (Burov y Diament, 1995; Watts, 2001), y es clave para entender la distribución de orógenos, fallas y terremotos. Como se ha visto en los capítulos anteriores, la resistencia es a menudo cuantificada por medio del espesor elástico efectivo (T_e) de la litosfera. Debido a la presencia de esfuerzos tectónicos y/o de una fábrica tectónica preexistente, la litosfera muestra frecuentemente variaciones azimutales en su resistencia (anisotropía mecánica), que deben relacionarse con la anisotropía de T_e (p.ej., Stephenson y Beaumont 1980; Lowry y Smith, 1995; Simons et al. 2000; Audet y Mareschal, 2004; Kirby y Swain, 2006). La anisotropía mecánica estimada a partir del análisis de la coherencia refleja las variaciones azimutales en la compensación de la flexión de la litosfera (Simons et al., 2003). Así, las direcciones de debilidad mecánica se alinean con grandes gradientes de espesor elástico efectivo y con límites tectónicos, de modo que la variación espacial de T_e puede mostrar donde se localiza la deformación, especialmente en la litosfera continental (Audet et al., 2007; Audet y Bürgmann, 2011).

En el Capítulo 3 se ha analizado la variación espacial del espesor elástico efectivo de la litosfera en Centroamérica y las regiones circundantes, analizando la función coherencia entre topografía y gravedad por medio de la transformación continua de ondículas (Transformada Wavelet Continua, CWT por sus siglas en inglés, o método *Wavelet*; para una descripción detallada del método véase la Sección 3.3.3). Siguiendo esta metodología podemos realizar un análisis de la anisotropía adaptando el método original de Forsyth (1985) a un modelo de placa ortotrópica, e invertir la coherencia en dos dimensiones (p.ej., Kirby y Swain, 2006; Audet y Mareschal, 2007). De esta manera, podemos calcular la rigidez flexural máxima y mínima en dos direcciones perpendiculares, D_{max} y D_{min}, y sus análogos geométricos T_e^{max} y T_e^{min}, además de la orientación de la "dirección débil" (β_w), calculado en sentido antihorario desde el eje x, siendo la dirección de menor rigidez. Estos parámetros de anisotropía suelen presentarse como un patrón espacial de ejes débiles, que muestra la dirección de menor rigidez y la magnitud de anisotropía, definida por el ratio $(T_e^{max} - T_e^{min})/T_e^{max}$ (Kirby y Swain, 2006), y que puede visualizarse como el porcentaje de anisotropía (PCA, o p_a; Kirby y Swain, 2014b):

$$p_a = 100\left(1 - \frac{T_e^{min}}{T_e^{max}}\right). \tag{6.1}$$

La Figura 6.2 muestra la magnitud de anisotropía de T_e en Centroamérica y las regiones circundantes, obtenida a partir del análisis anisotrópico con el método *Wavelet*. Los datos de topografía, anomalía de Bouguer, características de la litosfera, y parámetros elásticos son los mismos que los utilizados en el Capítulo 3.

La anisotropía mecánica es casi ubicua en toda la región, de manera que la mayoría de las áreas presentan una anisotropía de T_e moderada o alta. Comparando los resultados de la Figura 6.2a con la variación espacial de T_e obtenida con este mismo método (Figura 6.2b), no hay una clara correlación en la magnitud de anisotropía y los valores de T_e. Hay regiones que muestran poca anisotropía asociadas a valores de T_e altos como, por ejemplo, las plataformas estables de Norteamérica y Sudamérica. Por el contrario, hay otras regiones con valores de T_e bajos asociados a una anisotropía de T_e baja o moderada como, por ejemplo, parte de la Dorsal del Pacífico Oriental, el punto caliente de las Galápagos, las crestas del Coco y de Carnegie, o la región norte del Bloque Maya. Si destaca una banda estrecha que muestra una fuerte anisotropía ($>60\,\%$) asociada al patrón de valores de T_e altos de la zona de subducción Mesoamericana, al igual que en otras zonas de grandes gradientes de espesor elástico efectivo, consistentes con las observaciones de Audet y Bürgmann (2011).

En la Figura 6.3 se muestran la dirección débil de la anisotropía mecánica (β_w), representada como barras o "ejes", cuya longitud es proporcional a la magnitud de anisotropía de T_e, superpuestos a la variación espacial de T_e para dos regiones dentro del área de estudio. Esta figura muestra claramente diferentes agrupaciones de direcciones homogéneas. En ocasiones, los límites entre estos grupos muestran un cambio suave y gradual en las direcciones, pero en otros casos, este cambio es abrupto. β_w se orienta NE-SO en la región norte del Bloque Maya, claramente asociada a la banda de valores de T_e moderados y altos, y que conecta hacia el Oeste con una banda estrecha de valores relativamente altos asociados al borde sur del Cinturón Volcánico Transmexicano, donde rotan a adquiriendo una orientación NO-SE coherente con el patrón de T_e. Los resultados son relativamente dispersos dentro del Bloque de Chortís. Sin embargo, β_w es casi perpendicular a los principales límites de la Depresión de Nicaragua. En Sudamérica, la dirección mecánica débil es predominantemente NO-SE al norte de los Andes, que hacia el sureste rota adquiriendo una dirección NE-SO sobre la región norte del Cratón Amazónico, y conectando hacia el noreste con el patrón observado en la Fosa de las Antillas Menores.

En el Pacífico, los resultados de β_w son en general aleatorios. No obstante, destaca una clara alineación de las direcciones débiles a lo largo de la Fosa Mesoamericana, asociada a la estrecha banda de valores de T_e altos (y a una fuerte magnitud de anisotropía de T_e, descrita anteriormente). En el Mar del Caribe, los resultados son menos dispersos, observándose varios grupos donde β_w está bien orientada como, por ejemplo, en la Cuenca de Colombia (con una orientación NO-SE), o en la región central de la cuenca de Venezuela (con una orientación E-O). Además, al igual que en la Fosa Mesoamericana, β_w se alinea claramente con la Fosa de las Antillas Menores. Por último, cabe destacar que β_w muestra una alta relación angular con la linea de costa. Esta tendencia hacia la ortogonalidad ha sido descrita en estudios previos sobre la anisotropía de T_e realizados para otras regiones (p.ej., Simons et al., 2003; Kirby y Swain, 2006; Audet y Bürgmann, 2011; Mao et al. 2012).

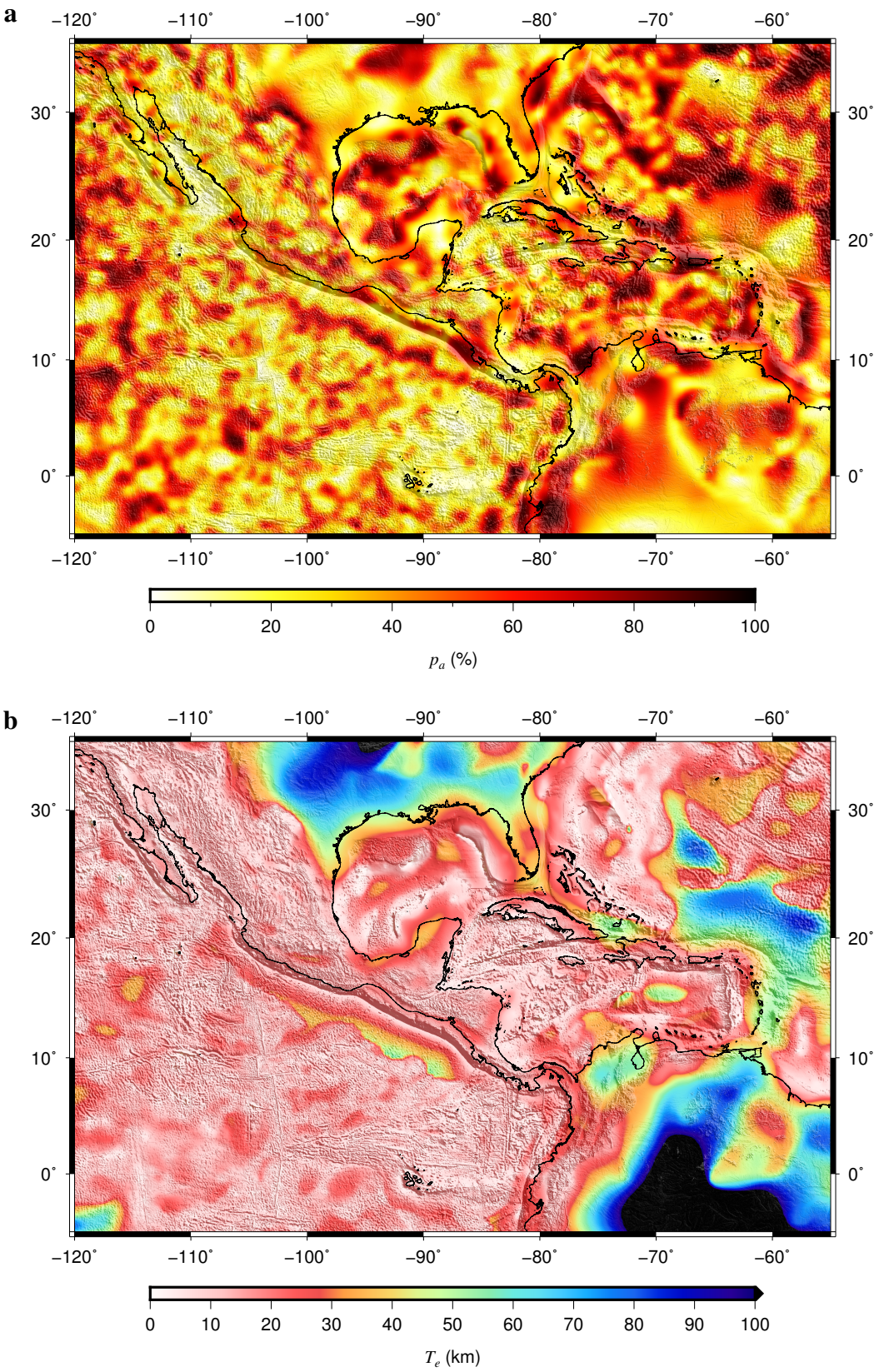

Figura 6.2: (a) Anisotropía de T_e (p_a) en Centroamérica y las regiones circundantes, obtenida a partir del análisis anisotrópico con el método *Wavelet* ($|\mathbf{k}_0|$ = 2.668). (b) Variación espacial de T_e a partir del análisis isotrópico realizado con el mismo método, correspondiente a los resultados presentados en el Capítulo 3 (véase la Figura 3.3 y la Figura Suplementaria 4).

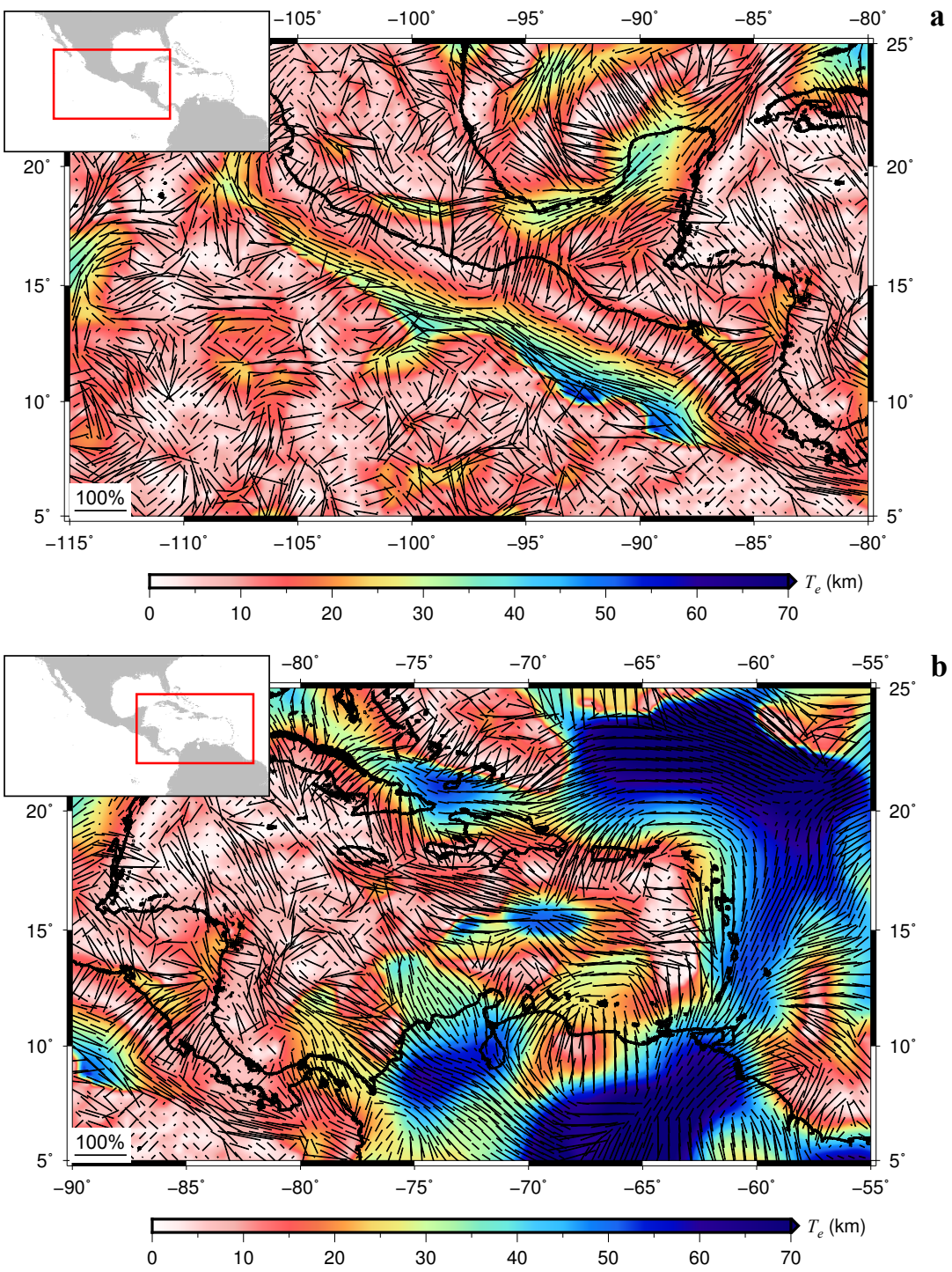

Figura 6.3: La dirección débil de la anisotropía mecánica (β_w), representada como barras cuya longitud es proporcional a la magnitud de anisotropía de T_e, superpuestas a la variación espacial de T_e para dos regiones dentro del área de estudio.

6.2.1. T_e, anisotropía de T_e y deformación litosférica

La magnitud y la variación espacial de T_e puede controlar el grado, el estilo y la localización de la deformación en respuesta a las cargas tectónicas a largo plazo y, potencialmente, la distribución de la actividad sísmica (p.ej., Lowry y Smith, 1995; Tassara et al., 2007; Audet y Bürgmann, 2011; Mao et al., 2012; Chen et al., 2013). Así, la relación entre el espesor elástico efectivo y la rigidez de la litosfera nos permite estudiar como la litosfera responde ante los esfuerzos tectónicos, por ejemplo, comparando la distribuciones de T_e y de la sismicidad (véase la Sección 3.2.4.4). Tomando la Figura 3.6 como punto de partida, podemos comparar además la distribución de la sismicidad con la magnitud de anisotropía de T_e.

Recientemente, Mao et al. (2012) analizaron la variación espacial de T_e y su anisotropía en el sur de China y las regiones circundantes, y observaron que la mayor parte de la actividad sísmica se concentra en áreas con una magnitud de anisotropía de T_e moderada o alta ($p_a > 50\,\%$), sugiriendo que una estructura mecánica altamente anisótropa promovería la localización de la deformación y de dominios de rotura frágil. En la Figura 6.4 se comprara la distribución de la sismicidad superficial (profundidad < 50 km) frente la distribución espacial de T_e (mostrado anteriormente en la Figura 6.6),

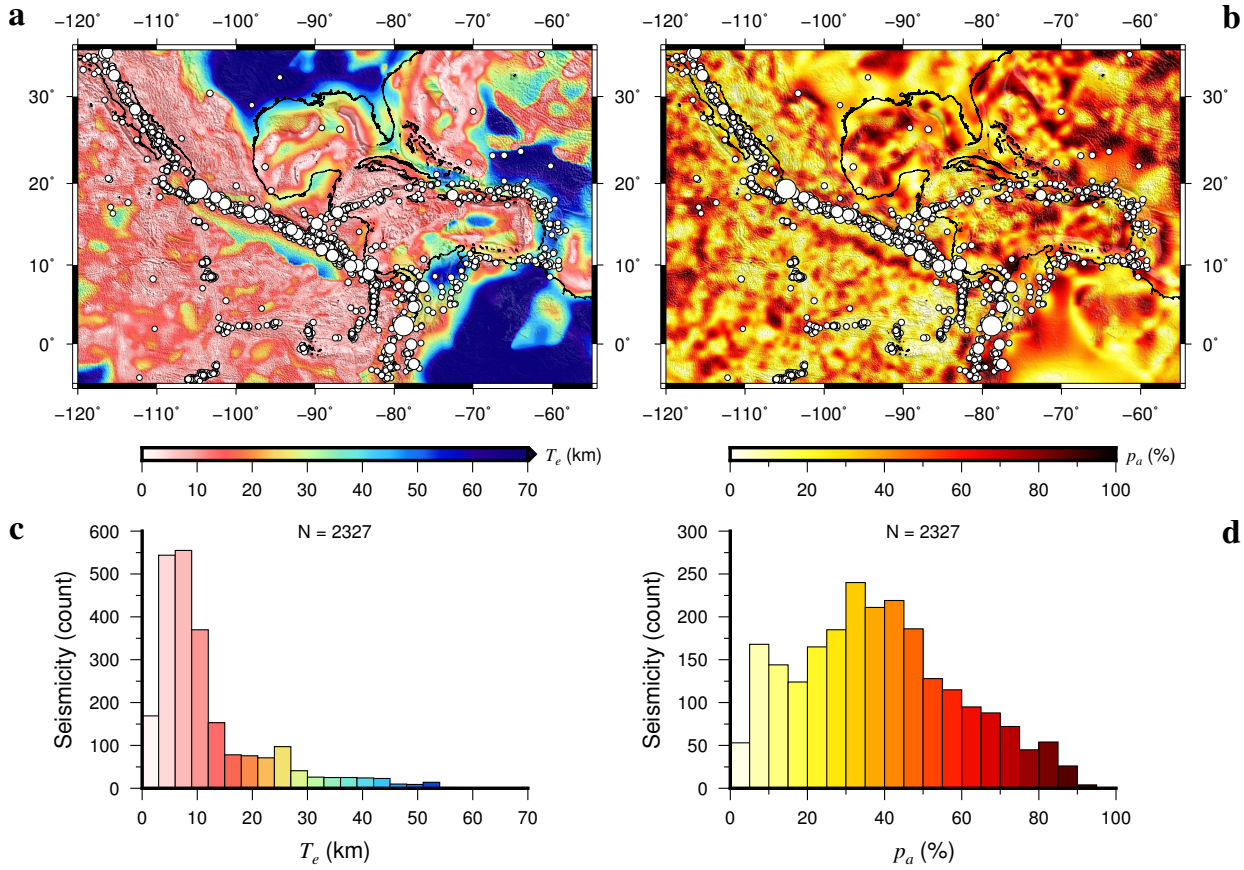

Figura 6.4: Correlación entre la distribución de la sismicidad superficial (profundidad < 50 km; Global CMT catalog, Ekström et al., 2012) con T_e (a) y con la magnitud de anisotropía de T_e (b). Los histogramas muestran los terremotos superficiales frente a T_e (c) y frente a la magnitud de anisotropía de T_e (d).

y frente a la distribución de la magnitud de anisotropía de T_e en Centroamérica. Puede observarse como muchos de los terremotos se concentran en regiones con una baja o moderada magnitud de anisotropía de T_e, de modo que, a diferencia de lo observado por Mao et al. (2012), en nuestra zona de estudio no hay una clara correlación entre la distribución de la actividad sísmica y la anisotropía de T_e. De hecho, en esta región parece que la anisotropía mecánica juega un papel menor en la concentración de la actividad sísmica, y que son las principales estructuras activas las que controlan a deformación litosférica superficial. No obstante, esta diferencia no es sorprendente teniendo en cuenta que ambas regiones se caracterizan por historias evolutivas y contextos geodinámicos muy diferentes.

6.2.2. Prospectiva

Como se ha comentado anteriormente, hay diversos factores dinámicos y estructurales que podrían ser responsables de la anisotropía de T_e (Audet y Burgmann, 2011). Los efectos dinámicos están relacionados con los esfuerzos actuales, por ejemplo, esfuerzos tectónicos intraplaca (Lowry y Smith, 1995) o la tracción basal debida a la convección sublitosférica (Stephenson y Beaumont, 1980). Los efectos estructurales se relacionan principalmente con una fábrica tectónica preexistente, como la foliación o la orientación cristalográfica preferente (Simons et al., 2003). Es necesario, por tanto, un análisis más detallado y profundo de la anisotropía de T_e, y especialmente de las orientaciones de las direcciones mecánicas débiles (β_w) y su relación con otros indicadores de la deformación de la litosfera (como, por ejemplo, la dirección del máximo esfuerzo compresivo horizontal, la anisotropía sísmica, las velocidades GPS) para distinguir que efectos controlan la anisotropía mecánica y entender, a su vez, cómo la estructura mecánica controla la deformación de la litosfera en una región dada (p.ej., Lowry y Smith, 1995; Simons et al. 2003; Audet y Mareschal 2004; Kirby y Swain 2006; Audet y Mareschal 2007; Audet y Bürgmann, 2011; Mao et al., 2012; Zamani et al., 2013; Chen et al., 2014). Este análisis debe realizarse, además, con mucha cautela. Recientemente, Kirby y Swain (2014b) han observado que el control estructural sobre la anisotropía observado en trabajos previos podría ser potencialmente erróneo, ya que se basan en la hipótesis de que la dirección de los gradientes de T_e y la dirección mecánica débil son independientes. Según estos autores, si existe cierto grado de dependencia, y muchas de las observaciones podrían ser artefactos de los métodos de análisis. Un ejemplo inmediato para esta región podrían ser los patrones de β_w alineados con los gradientes de T_e a lo largo de las fosas Mesoamericana y de las Antillas Menores.

Por otra parte, este tipo de análisis también resultaría de especial interés para el caso de la península ibérica. Como se ha comentado en la Sección 2.2.5.2, varios estudios han estimado T_e para esta región por medio de métodos espectrales (p.ej., Gómez-Ortiz et al., 2005; Pérez-Gussinyé et al., 2005). No obstante, hasta la fecha no hay un estudio específico de la variación espacial de T_e (y F), y de la anisotropía mecánica de la litosfera para esta región (y que podría ser extensible a la región norteafricana y mediterránea). En la Figura 6.5 se muestran resultados preliminares de la variación espacial de T_e y de la anisotropía de T_e (dirección débil, β_w) para la región de la península ibérica, a partir del análisis espectral de la coherencia entre la topografía y la gravedad (anomalía de Bou-

guer) con el método *Wavelet* ($|\mathbf{k}_0|$ = 2.668). Los datos de topografía derivan del modelo *RET2012* (http://geodesy.curtin.edu.au/research/models/Earth2012/), un modelo global de topografía equivalente donde las masas de agua de los océanos y los grandes lagos, así como las capas de hielo, se comprimen a una capa de roca equivalente (de densidad 2670 kg m^{-3}) que se suma a la topografía (véase p.ej., Hirt et al., 2012). El uso de un modelo de topografía equivalente permite aplicar las ecuaciones de deconvolución de cargas "en tierra" a todo el conjunto de datos (Stark et al., 2003; Kirby y Swain, 2008; véase la Sección 3.2.2.3). Los datos de anomalía de Bouguer se han obtenido del modelo global en armónicos esféricos *WGM2012* (Balmino et al., 2011; disponible en: http://bgi.omp.obs-mip.fr/data-products/Grids-and-models/). El modelo global *CRUST1.0* (Laske et al., 2013; disponible en: http://igppweb.ucsd.edu/~gabi/crust1.html#download) proporciona la información requerida sobre la estructura interna de la corteza y el manto superior (variación lateral de la densidad interna y de la profundidad de las diferentes interfaces). Otros parámetros utilizados en la inversión son: módulo de Young, $E = 100$ GPa; coeficiente de Poisson, ν = 0.25; aceleración de la gravedad, g = 9.79 m s^{-2}; constante de gravitación universal, G = 6.67259 x 10^{-11} m^3 kg^{-1} s^{-2}.

Como primera valoración de este análisis, la mayor parte de la región se caracteriza por valores de espesor elástico efectivo muy bajos ($T_e < 15$ km; Fig. 6.5a), destacando un domino de valores de T_e moderados y altos en la zona centro y suroeste peninsular, que se prolonga hacia el norte de África, y que se encuentra limitado por fuertes gradientes de T_e, especialmente en la zona sur. El rango de valores de T_e observado en el centro de la Península Ibérica, entre 20 y 40 km, es consistente con los valores de T_e obtenidos por diferentes métodos para esta zona (15-40 km; véase la Sección 2.2.5.2). Respecto a las direcciones β_w, en la Fig. 6.5b se observan diferentes agrupaciones de direcciones homogéneas. Al igual que se observaba en Centroamérica (véase la Fig. 6.3), en muchas ocasiones los límites entre estos grupos muestran un cambio suave y gradual en las direcciones, pero en otros casos, este cambio es abrupto. Destaca un patrón de β_w con orientación NE-SO en la región central y suroeste, asociado al dominio de valores de T_e moderados y altos, y que hacia el norte rotan adquiriendo patrones casi radiales, formando grupos más locales con una distribución más compleja. En el Este y en el Mediterráneo los resultados son más dispersos, aunque destaca un cierto patrón NE-SO desde Mallorca hacia el mar de Alborán. De nuevo, se observa una cierta tendencia a la ortogonalidad de β_w con respecto a la linea de costa.

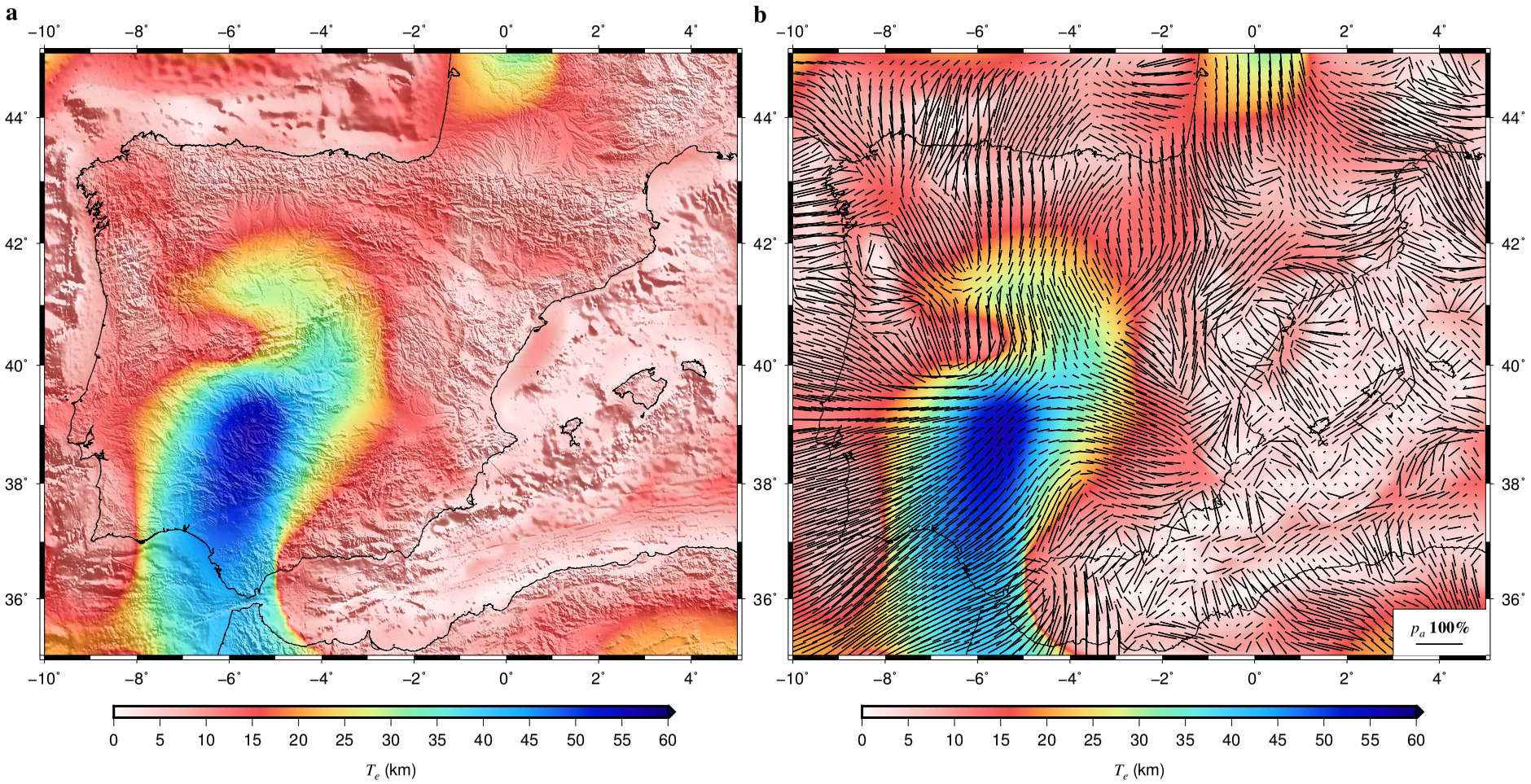

Figura 6.5: Resultados preliminares de la variación espacial de T_e en la península ibérica (a), y de la dirección débil de la anisotropía mecánica (β_w), superpuesta a la variación espacial de T_e (b), obtenidos con el método *Wavelet* ($|\mathbf{k}_0| = 2.668$).

6.3. Sobre la evolución interna (y climática) de Marte

En el Capítulo 5 se ha mostrado como el cálculo de paleo flujos térmicos a partir de la resistencia litosférica (usando como indicadores la profundidad de grandes fallas o el espesor elástico efectivo de la litosfera) puede ser usado para constreñir la evolución térmica de un cuerpo planetario, puesto que los resultados así obtenidos corresponden a la época en que se formaron las estructuras geológicas usadas como indicador (p.ej., Zuber et al., 2000; McGovern et al., 2002). Analizando de esta forma veintidós regiones de Marte de diferente época y contexto geológico, se ha podido hacer una primera aproximación a la evolución térmica del planeta rojo, mostrando que ha disipado menos calor que el producido en su interior por radioactividad, lo que implica que se ha calentado internamente, al menos durante algunas fases de su historia. Recientemente, Ruiz (2014) ha mostrado que hace alrededor de 3700 millones de años Marte experimentó una reducción sustancial en su flujo térmico y un aumento rápido en el espesor de la litosfera, lo que pone de manifiesto que en dicho tiempo se produjeron importantes cambios en la dinámica interna del planeta rojo.

6.3.1. Espesor de corteza (T_c)

Como se ha expuesto en el Capítulo 5, las estimaciones previas de T_e a partir del análisis de la topografía y gravedad fueron realizadas asumiendo un espesor medio de corteza de 50 km (McGovern et al., 2004), mientras que en el modelo de espesor de corteza de Marte más reciente se asume un espesor cortical medio de 45 km (Neumann et al., 2008). Así, en los cálculos de los paleo flujos térmicos presentados en el Capítulo 5 (véase también Ruiz, 2014), se asumen los espesores corticales basados en las tendencias regionales del modelo cortical de Neumann et al. (2008), pero aumentados 5 km con el fin de ser consistentes, en lineas generales, con el valor medio asumido por McGovern et al. (2004). Por otra parte, en el Capítulo 4 se ha presentado un modelo global del espesor de corteza para Venus, obtenido a partir del análisis de la topografía y la gravedad siguiendo el procedimiento de la teoría potencial de Wieczorek y Phillips (1998), el mismo procedimiento que siguen Neumann et al. (2008) para realizar su modelo de Marte. Siguiendo esta línea de trabajo, podemos realizar un cálculo independiente más riguroso del espesor de corteza para Marte consistente con los otros observables utilizados en el análisis litosférico, con el fin de reevaluar y mejorar la caracterización del comportamiento mecánico a largo plazo de la litosfera del planeta rojo, y así ampliar y refinar los resultados sobre su estructura y evolución térmica en futuros estudios.

Para constreñir el espesor de la corteza marciana, asumimos (1) que las anomalías de gravedad observadas derivan únicamente de la combinación de la superficie topográfica y de la variación del relieve de la interfase corteza-manto (Moho), y (2) densidades de corteza y manto constantes para superar la no-unicidad asociada con la modelización potencial. Como datos, usamos el modelo de forma de Marte *MarsTopo719* (Wieczorek, 2007), y el modelo del potencial gravitatorio *MRO110b2* (Konopliv et al., 2011), ambos en armónicos esféricos. Los datos de topografía, con mayor resolución que los datos de gravedad, son útiles únicamente hasta la resolución de éstos, por lo que los coeficientes de ambos modelos son truncados más allá del grado (l) y orden (m) 90 en nuestro análisis dada

la dramática disminución en la correlación espectral que se observa entre la gravedad observada y la topografía a partir de este grado (p.ej., Baratoux et al., 2014). El modelo asume un espesor cortical medio de 50 km (más acorde con las evidencias geofísicas y geoquímicas; Wieczorek y Zuber, 2004; Ruiz et al., 2009), una densidad de 2900 kg m^{-3} para la corteza de naturaleza basáltica, consistente con los mejores ajustes en los análisis de admitancia (McGovern et al., 2004), y una densidad de 3500 kg m^{-3} para el manto litosférico, consistente con los modelos de composición para un manto enriquecido en hierro; valores ampliamente utilizados para Marte (p.ej., Zuber et al., 2000; McGovern et al., 2004; Ruiz et al., 2011). Con estas asunciones, primero calculamos la anomalía de Bouguer a partir de la topografía superficial y de la anomalía de aire libre, y después calculamos de forma iterativa (continuación o prolongación descendente) el relieve a lo largo de la interfase corteza-manto necesario para explicar la anomalía de Bouguer observada (para una descripción detallada véase Wieczorek y Phillips, 1998; Wieczorek, 2007). Con el fin de mitigar los errores y contrarrestar el efecto desestabilizador en el cálculo de la anomalía de Bouguer por la prolongación descendente, aplicamos un filtro definido para tener un valor de 0.5 en el grado 50 (p.ej., Wieczorek y Phillips, 1998). Finalmente, obtenemos el espesor cortical sustrayendo el relieve en el Moho de la superficie topográfica. Las Figuras 6.6 y 6.7 muestran los resultados de espesor de corteza obtenidos para Marte.

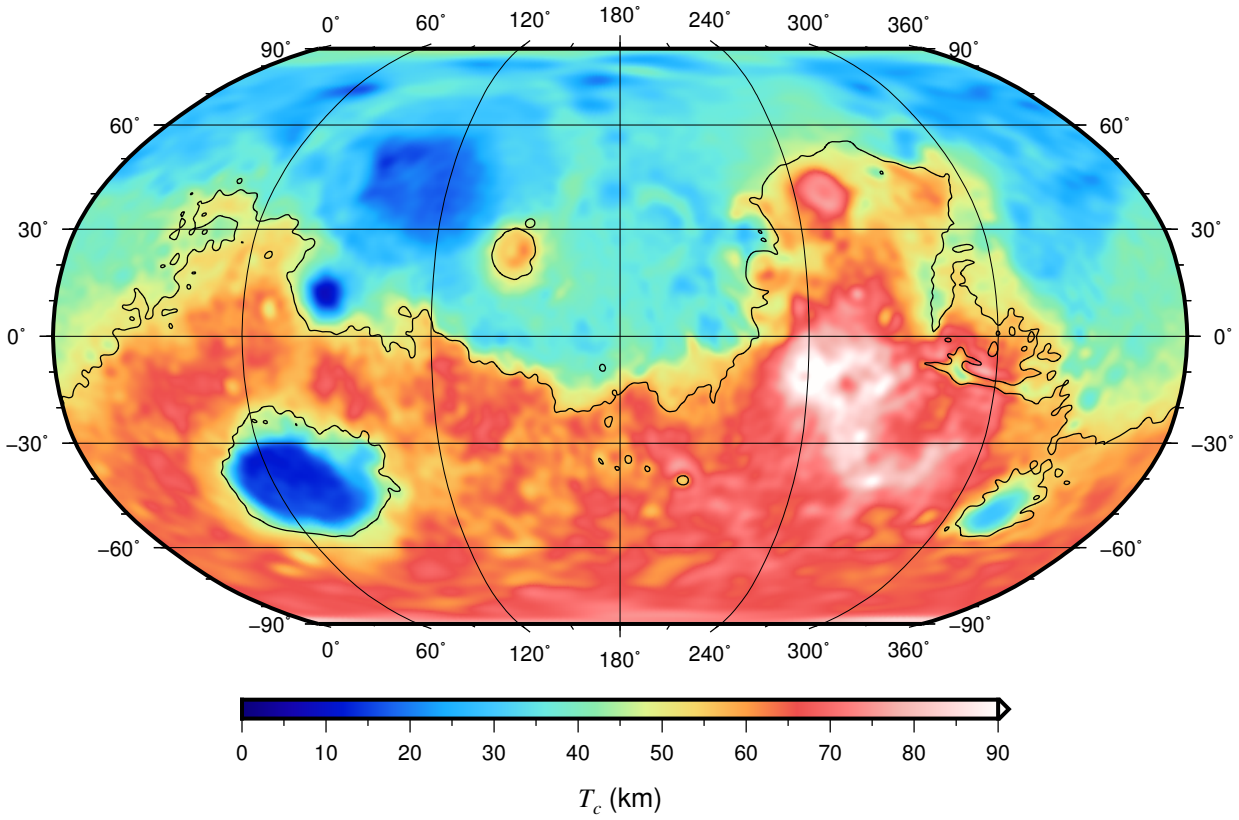

Figura 6.6: Modelo de espesor de corteza para Marte asumiendo un espesor cortical medio de 50 km, y unas densidades para la corteza y el manto litosférico de, respectivamente, 2900 y 3500 kg m^{-3}. La linea negra corresponde al contorno de cota 0 del modelo de forma de Marte *MarsTopo719* (Wieczorek, 2007).

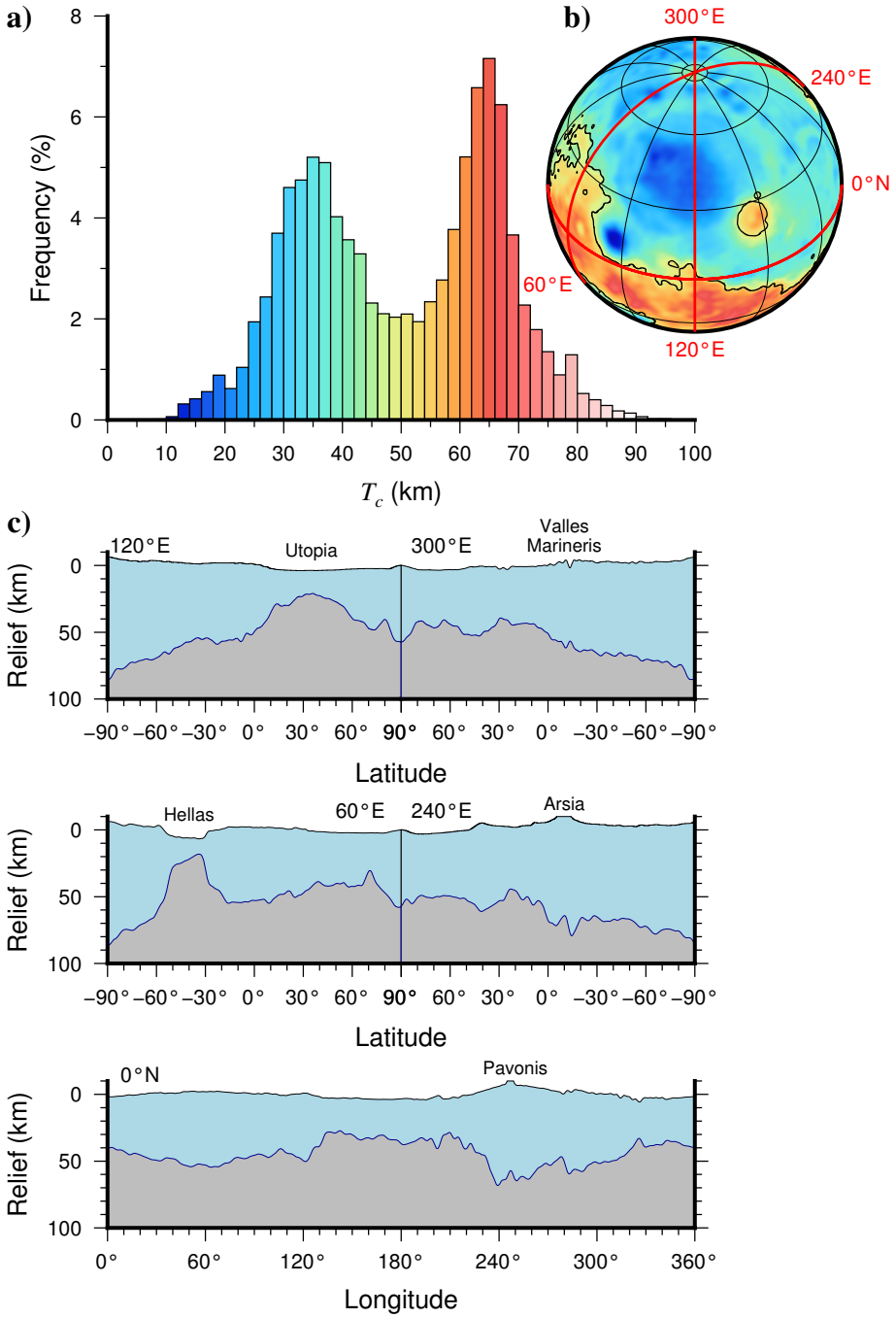

Figura 6.7: (a) Histograma del espesor cortical. (b) Modelo de espesor de corteza para Marte en proyección ortográfica centrado en 120º de longitud y 40º de latitud. Las lineas rojas corresponden a los perfiles corticales mostrados en (c). (c) Cortes polo a polo de la estructura cortical, así como un corte ecuatorial, donde la corteza está representada en azul, y el manto en gris.

El modelo de espesor de corteza obtenido (Figura 6.6) varía entre 8.2 km y 97.5 km, con los valores más bajos localizados en el centro de Isidis y en el noroeste de Hellas Planitia, y muestra una distribución claramente bimodal, con picos en aproximadamente 35 km y 65 km, respectivamente, y donde la dicotomía cortical se demarca por el mínimo local cerca de los 50 km (Figura 6.7a). Si bien estos resultados son consistentes con los modelos obtenidos en trabajos previos (p.ej., Zuber et al., 2000; Neumann et al., 2004, 2008; Wieczorek, 2007), como cabe espesar, se aprecia la influencia del

espesor medio asumido de 50 km. Como referencia, en el modelo de Neumann et al. (2004), obtenido para un espesor medio de 45 km, los picos de la distribución bimodal se alcanzan en aproximadamente 32 km y 58 km, respectivamente, y con un mínimo local representativo de la dicotomía cortical en 40 km. Estas diferencias no son homogéneas a lo largo del planeta, con valores más cercanos (menos de 3 km) entre ambos modelos en las tierras bajas, en Argyre y Hellas Planitiae, y una mayor diferencia (superior a 5 km) en algunas regiones de las tierras altas, especialmente en la región de Tharsis.

6.3.2. Prospectiva

La evolución del clima de un planeta depende de factores como la cantidad de insolación que recibe, y sus variaciones latitudinales y temporales, debidas por ejemplo, a cambios en la órbita y el eje de rotación, o a la proporción entre el calor recibido y reflejado por la atmósfera y la superficie. Pero también depende de diversas formas de la evolución interna del propio planeta. Por ejemplo, la actividad volcánica puede inyectar a la atmósfera importantes cantidades de vapor de agua y otros gases que producen efecto invernadero. Por otra parte, en el caso de la Tierra, la pérdida de calor del núcleo genera complejas corrientes de material cargado eléctricamente en su interior que son responsables de la generación del campo magnético terrestre. Este a su vez sirve de pantalla protectora frente a la acción de las partículas cargadas que forman el viento solar y los rayos cósmicos, que podrían arrastrar la atmósfera de nuestro planeta y ocasionar su pérdida parcial o total. En Marte no ha existido un campo magnético similar desde las primeras etapas de su historia (al menos desde hace entre 3600 y 4100 millones de años, aunque no existe acuerdo en cuanto a este dato; p.ej., Milbury et al., 2012; Lillis et al., 2013). La ausencia de este campo, junto con la baja gravedad de este planeta (de aproximadamente un tercio de la terrestre) ha llevado a que la atmósfera marciana, que pudo haber sido mucho más densa en el pasado, sea actualmente muy tenue, con una presión superficial de menos de un uno por ciento de la terrestre.

Por otra parte, también existen evidencias de que Marte experimentó una disminución importante en la intensidad de actividad hidrogeológica hace unos 3700 millones de años, lo que se interpreta como un cambio desde condiciones relativamente húmedas en la superficie a otras frías y áridas, parecidas a las actuales, lo que queda atestiguado por la disminución drástica de la erosión o degradación, por efecto del agua, de las formas geológicas de su superficie (Mangold et al., 2012). Algunos estudios recientes han propuesto que la desaparición del campo magnético de Marte y aridificación del planeta estuvieron relacionados (p.ej., Sandu y Kiefer, 2012). En efecto, el fin del campo magnético habría supuesto la pérdida de protección, y por tanto la reducción, de la atmósfera, y esto a su vez el final de condiciones relativamente húmedas de Marte.

Como se ha mencionado previamente, hace alrededor de 3700 millones de años Marte también experimentó una reducción sustancial en su flujo térmico y un aumento rápido en el espesor de la litosfera (Ruiz, 2014). Así, esos grandes cambios ocurridos en la dinámica interna del planeta rojo, coinciden aproximadamente en el tiempo con la disminución en la intensidad de la erosión hídrica de rasgos geológicos, y también con cambios en la composición de los materiales sedimentarios y de la

lava expulsada por los volcanes (Baratoux et al., 2013; Wilson y Mustard, 2013); además, como se ha indicado antes, la desaparición del campo magnético interno del planeta pudo haberse producido en una época similar. Por tanto, cada vez es más evidente que la historia ambiental de Marte se encuentra íntimamente ligada a su evolución interna.

No obstante, el conocimiento de la historia evolutiva de Marte es todavía muy incompleto. En este sentido, ampliar los análisis del antiguo estado térmico de la litosfera a otras regiones de Marte contribuiría a constreñir mejor la historia térmica del planeta. Además, un análisis detallado sobre los efectos de la evolución interna del planeta en la deformación que se observa sobre la superficie, tanto a escala global como local y su variación en el tiempo, contribuiría a su vez a una mejor comprensión de la dinámica y evolución interna de Marte, y de cómo influye en la evolución climática y ambiental del planeta rojo. Desde el punto de vista de la planetología comparada, esta linea de trabajo sería de gran importancia al aportar una mayor perspectiva para la comprensión de los resultados con los otros planetas de tipo terrestre, Mercurio, Venus y nuestra propia Tierra. La comparación con la Tierra, por ejemplo, debe resultar en una mejor comprensión de su dinámica global, y los factores que determinan el origen y mantenimiento de la tectónica de placas, mecanismo de disipación del calor interno único a nuestro planeta, y todavía no bien comprendido; también podría aportar valiosas informaciones sobre la evolución climática a largo plazo de la Tierra y Venus.

Uno de los aspectos más interesantes a investigar en futuros trabajos es la influencia de la abundancia de hierro en el manto de Marte sobre las propiedades térmicas y mecánicas de la litosfera, y las estimaciones de flujo térmico. En el Capítulo 5 se ha calculado el flujo térmico de Marte a partir de indicadores de resistencia de la litosfera para diversas regiones y épocas, alcanzando la conclusión general de que este planeta ha disipado menos calor que el generado por radioactividad, por lo que su interior ha debido calentarse en cierta medida durante al menos parte de su historia geológica. Específicamente, en ese estudio se buscaba obtener límites superiores muy generosos para el flujo térmico, con el fin de hacer muy robusta la conclusión general de que el interior de este planeta ha perdido durante su evolución menos calor de lo generalmente aceptado. Así, en los cálculos se utilizaron parámetros que maximizaban la resistencia de la litosfera (como el uso de una ley de flujo describiendo una reología muy dura para el olivino, el mineral que domina la deformación en el manto litosférico), y valores muy altos para la conductividad térmica de las rocas (lo que maximiza el flujo térmico conductivo obtenido).

Sin embargo, el manto de Marte es sustancialmente más rico en hierro que el de la Tierra, y recientemente se ha mostrado (Zhao et al., 2009) que la resistencia del olivino se reduce de forma muy significativa con su contenido en hierro. Esta reducción de la resistencia implica que el manto litosférico debe ser menos caliente para justificar los valores de espesor elástico efectivo deducidos para Marte. De forma similar, la conductividad térmica del olivino se reduce con la proporción de hierro, lo que a su vez implica un menor flujo térmico para un perfil de temperaturas dado. Por tanto, se deberían tener en cuenta estos efectos en los nuevos cálculos de flujo térmico de Marte a partir de indicadores de resistencia de la litosfera.

Por otra parte, los experimentos de laboratorio de deformación de rocas suelen a hacerse a altas

temperaturas para producir deformaciones apreciables en un tiempo relativamente corto. Pero experimentos recientes (Mei et al., 2010) han mostrado que en temperaturas relativamente bajas, apropiadas para las condiciones del manto litosférico, el olivino es más débil que lo predicho por extrapolación de los datos de alta temperatura. Así, sería conveniente testar por primera vez la aplicación de la ley de flujo de baja temperatura a Marte, ya aplicada preliminarmente para algunos casos en la Tierra (véase el Capítulo 2). Aunque los relativamente bajos niveles de esfuerzos y tasas de deformación en la litosfera de Marte podrían limitar la relevancia de la ley de flujo de baja temperatura en el manto litosférico de este planeta, es importante llevar a cabo una evaluación cuantitativa.

Por tanto, estos resultados (junto con los derivados de otras lineas de trabajo) permitirán establecer restricciones mucho más ajustadas a la historia térmica de Marte que las disponibles hasta ahora. Estos resultados también se podrían comparar con estimaciones de producción de calor derivadas de modelos geoquímicos de composición (que se basan en meteoritos procedentes de Marte y en observaciones de elementos radioactivos desde naves en órbita alrededor del planeta rojo), y con modelos convectivos de evolución interna. Todo ello debe redundar en una mejor compresión de cómo Marte ha "gestionado" su calor interno a lo largo de su evolución. Además, otro punto muy interesante sería analizar cómo la evolución del flujo térmico afecta a las condiciones en el subsuelo de Marte, y su importancia, por ejemplo, para la existencia de agua líquida en el subsuelo, o incluso de circulación hidrotermal.

6.4. Sobre la estimación del espesor elástico efectivo de la litosfera (T_e) mediante métodos espectrales

A lo largo de esta memoria se ha mostrado como el espesor elástico efectivo es un indicador muy útil de la resistencia y el comportamiento mecánico de la litosfera. Como se ha comentado anteriormente, los métodos espectrales han alcanzado estos últimos años un grado aún mayor de sofisticación, y cada vez se pueden contemplar más problemáticas y escenarios en el análisis de la litosfera. Estos avances en la estimación de T_e ofrecen grandes oportunidades (y suponen además grandes retos) para futuros trabajos.

En las últimas décadas ha tenido lugar un interesante debate sobre la reología de la litosfera de las áreas continentales de la Tierra, en concreto sobre la resistencia a la deformación de la corteza y el manto litosférico, y sobre su contribución a la resistencia de la litosfera (véase p.ej., Watts y Burov, 2003; Afonso y Ranalli, 2004; Burov y Watts, 2006). Dentro de este debate (y en lo que concierne a la estimación del espesor elástico efectivo de la litosfera mediante a métodos espectrales; véase p.ej., Audet, 2014; Kirby, 2014), antes de la introducción del método de Forsyth en 1985, los valores de T_e estimados en áreas continentales eran bajos, obteniéndose desde valores muy bajos cercanos a una compensación tipo Airy hasta un par de decenas de kilómetros. Después del método de Forsyth (1985), con el uso de la coherencia de Bouguer y la deconvolución de cargas, los estudios continentales empezaron obtener valores de T_e muy altos ($>$100 km) en muchos lugares donde previamente

se habían obtenido valores bajos. McKenzie y Fairhead (1997) se mostraron en desacuerdo con estos altos valores de T_e y su implicación de que el manto litosférico continental era resistente. El debate que se inició con este trabajo continua hasta nuestros días, y concierne a las propiedades reológicas últimas de la litosfera, y por tanto, al debate mayor sobre la contribución de la corteza y el manto litosférico a la resistencia de la litosfera (el modelo "sándwich de gelatina" o "*jelly sandwich*", con un manto litosférico muy resistente, frente al modelo "crema catalana" o "*crème brûlée*", con una corteza superior resistente, y un manto litosférico débil; véase p.ej., Burov and Watts, 2006). Así, McKenzie y Fairhead (1997), y más tarde McKenzie (2003), se opusieron al uso del método de Forsyth, y específicamente al uso de la coherencia de Bouguer y de la deconvolución de cargas, e instaban a usar una inversión analítica de la admitancia de aire libre para estimar T_e.

Son muchos los estudios donde se analizan diversos aspectos de esta problemática, especialmente la que concierne al uso de la admitancia de aire libre o la coherencia de Bouguer, a los modelos de carga, o al papel de la erosión en la estimación de T_e en regiones continentales (Simons et al., 2000; Armstrong y Watts, 2001; Watts y Burov, 2003, Pérez-Gussinyé et al., 2004; Pérez-Gussinyé y Watts, 2005; Kirby y Swain, 2009; McKenzie, 2010; entre otros). En este sentido, McKenzie (2010) cuestionó si el núcleo de T_e alto en el escudo Canadiense que se observa en el mapa de T_e obtenido con la admitancia de aire libre de Kirby y Swain (2009) podría ser un artefacto debido a la contaminación en las señales de topografía y gravedad en longitudes de onda largas por efecto de la convección del manto y el ajuste isostático glacial (*glacial isostatic adjustment*, GIA), y este autor señala que estos dos procesos deberían tenerse en cuenta al usar la admitancia. Así, en un estudio reciente, Kirby y Swain (2014a) han desarrollado una expresión analítica para la admitancia (Q_{CGF}) que combina las contribuciones de la convección del manto, del GIA y de la flexión litosférica, para estimar T_e con admitancia de aire libre usando el método *Wavelet* en el escudo Canadiense (véase la Ec. A16 y Ec. A17 de Kirby y Swain, 2014a).

Al margen del debate sobre los valores de T_e en áreas continentales, la implementación de estas contribuciones a la admitancia abre nuevas y muy interesantes lineas de trabajo. Por ejemplo, ciertas regiones de Venus como Atla Regio parecen estar soportadas dinámicamente, o en el caso de Thetis Regio, por una contribución de dos mecanismos: engrosamiento cortical y soporte dinámico desde el manto (James et al., 2013). Así, sería muy interesante analizar el papel de la convección del manto y su contribución al soporte de la topografía venusiana, y su efecto en la estimación del espesor elástico efectivo de la litosfera, así como sobre los mecanismos de carga asociados (F), que se obtuviesen. A su vez, la contribución del efecto del GIA abre una linea muy interesante de trabajo sobre el papel que juegan los casquetes de hielo en las regiones polares de Marte, caracterizadas por valores de T_e muy altos ($\geq$ 300 km; Phillips et al., 2008). La carga de la litosfera debido al peso asociado a los casquetes de hielo en las regiones polares de Marte es un fenómeno reciente (estimado en unos pocos millones de años; Laskar et al., 2002; Phillips et al., 2008), y debido a la falta de actividad tectónica a gran escala en el presente, las estimaciones de T_e en estas regiones representan los únicos indicadores para caracterizar el estado térmico actual de Marte. Por otra parte, la aplicación de la admitancia combinada (Q_{CGF}) también resultaría de especial interés en un estudio de T_e y F para la península

ibérica, donde la contribución de la convección de manto podría tener una gran influencia.

Por otra parte, uno de los avances más significativos en la estimación de T_e mediante métodos espectrales ha sido la reciente implementación del análisis *Wavelet* en un sistema de coordenadas esférico (*continuous spherical wavelet transform*, CSWT; Audet, 2011, 2014). Este nuevo método permite estimar el espesor elástico efectivo de la listosfera de forma global sin algunas de las restricciones del análisis planar CPWT, y al usar las ecuaciones de flexión de una lámina elástica, extiende además este tipo de estudios a otros cuerpos planetarios como la Luna, Marte o Mercurio. Si bien este método cuenta aún con ciertas limitaciones (véase Audet, 2014), abre el camino a multitud de nuevos estudios sobre las propiedades mecánicas (y sobre la estructura y evolución térmica) de las litosferas planetarias.

Finalmente, los avances tanto en el análisis espectral de la gravedad y topografía como en la modelización litosférica de la Tierra han permitido caracterizar la variación espacial del espesor elástico efectivo en ésta con una resolución sin precedentes (Audet, 2014; Kirby, 2014). Recientemente, Tesauro et al. (2012) presentaron un mapa global de T_e estimado a partir de un análisis reológico. No obstante, el procedimiento seguido por estos autores para obtener los mapas de resistencia litosférica y de espesor elástico efectivo presentados tiene limitaciones, como por ejemplo la generalización de las leyes y parámetros reológicos, o no tener en cuenta la curvatura en el cálculo de T_e. Sin embargo, aunque contamos con mapas globales de T_e estimados por métodos espectrales para las regiones continentales (p.ej., Audet y Bürgmann, 2011; Audet, 2014), para la litosfera oceánica (y extendido de forma preliminar a los continentes; Kalnins, 2011), e incluso mapas casi globales de T_e continental y oceánico a partir de los resultados obtenidos por ambos métodos de análisis (p.ej., Mouthereau et al., 2013, basado en los datos recopilados en Watts, 2007), hasta la fecha no hay un mapa global de T_e continental y oceánico obtenido por métodos espectrales. Por tanto, obtener este mapa global constituye un enorme desafío, y debe ser un objetivo prioritario de futuras investigaciones.

6.5. Conclusiones

Cada uno de los trabajos individuales que configuran esta Tesis Doctoral aborda cuestiones y problemas científicos de un gran interés en si mismo, constituyendo por tanto unidades autónomas de investigación que pueden ser analizadas, comprendidas y valoradas independientemente. De estos estudios se han podido extraer las siguientes conclusiones principales:

En el Capítulo 2 se ha abordado el estudio del estado térmico y resistencia de la litosfera de una zona intraplaca: el centro de la península ibérica. Para la elaboración de este trabajo se ha contado con datos geoquímicos inéditos que han permitido caracterizar la producción de calor de la corteza en el área de estudio. Por otra parte, el concepto de isostasia térmica y su uso para constreñir los perfiles de temperatura, junto con el uso de una nueva ley reológica para el manto litosférico, representa una buena aproximación que no se utiliza con frecuencia en trabajos similares. Esto ha permitido obtener interesantes resultados acerca del flujo térmico superficial y resistencia de la litosfera para esta zona. Se han obtenido valores de flujo térmico superficial de 84 mW m^{-2} y 82 mW m^{-2} para el Sistema Central y Cuenca del Tajo, respectivamente. Además, se han obtenido temperaturas de 700 ºC y 630-650 ºC en el límite corteza-manto (Moho), así como flujos térmicos mantélicos de 24 mW m^{-2} y 26 mW m^{-2}, bajo el Sistema Central y Cuenca del Tajo, respectivamente. Por otra parte, las estimaciones de resistencia litosférica varían dentro de la zona de estudio, obteniéndose los valores máximos en el norte de la Cuenca del Tajo, y los valores mínimos asociados al Sistema Central, claro reflejo del estado térmico de la litosfera en esas regiones. Los perfiles de resistencia muestran variaciones en la profundidad de la transición frágil-dúctil en función de las reologías y del régimen de esfuerzos considerado, y para todos los casos, el Moho representa una importante discontinuidad mecánica entre la corteza inferior y la parte superior del manto litosférico. Por último, se han obtenido valores de espesor elástico efectivo de 16-28 km en el Sistema Central, y de 20-34 km y 17-30 km, respectivamente, en el norte y sur de la Cuenca del Tajo, en función de las reologías, consistentes con el rango de valores obtenidos en estudios previos.

En el Capítulo 3 se han presentado mapas de alta resolución de las variaciones espaciales del espesor elástico efectivo (T_e) en Centroamérica y las regiones circundantes, obtenidos a partir del análisis de la coherencia entre la topografía y la gravedad (anomalía de Bouguer) por medio de dos métodos espectrales (conocidos por sus nombres en inglés como los métodos *Multitaper* y *Wavelet*, respectivamente). Los resultados muestran que, independientemente de las diferencias técnicas entre los dos métodos, hay una gran correspondencia en la variación espacial de T_e recuperada por ambos. Aunque los valores absolutos de T_e pueden variar en los mapas obtenidos por ambos procedimientos, la estructura cualitativa y la ubicación de sus principales gradientes son muy similares, de modo que la estimación de T_e es relativamente insensible a la elección del método espectral usado. El patrón de las variaciones de T_e en Centroamérica y regiones circundantes concuerda bien con las provincias tectónicas de la región, y está estrechamente correlacionado con los principales límites tectónicos. Las zonas de subducción Mesoamericana y de las Antillas Menores se caracterizan por una banda de altos valores de T_e en la placa subducente previos a la fosa. Estos altos valores de T_e están relacionados

con el dominio de cargas internas (y en el caso del extremo meridional de la zona de subducción de las Antillas Menores, también se asocian con la presencia de una gran cantidad de sedimentos), y deben ser interpretados con cautela. Por otra parte, hay una buena correlación, a pesar de algunas incertidumbres, entre el flujo térmico superficial y los resultados de T_e en el área de estudio. Estos resultados sugieren que aunque esta región es geológicamente muy compleja, el estado térmico de la litosfera tiene una profunda influencia en su comportamiento mecánico, de manera que el espesor elástico efectivo de la misma está fuertemente controlado por su estructura térmica.

En el Capítulo 4 se ha abordado el análisis de la estructura litosférica de Venus mediante el cálculo del espesor cortical (T_c) y del espesor elástico efectivo a partir del análisis de la topografía y la gravedad, con el objetivo de reevaluar la variación regional en (y mejorar la caracterización de) la estructura y el comportamiento mecánico de su litosfera. Los resultados muestran que la corteza de Venus tiene un espesor característico de unos 20-25 km, con espesores mayores asociados a las tierras altas (constituidas por mesetas o "plateaus" corticales y grandes macizos volcánicos). Esto sugiere que la mayor parte de la corteza venusiana se formó en condiciones similares, y diferentes a las que prevalecían cuando se formaron gran parte de las tierras altas. El espesor elástico efectivo obtenido varía entre 14 (el mínimo T_e recuperable en el caso de Venus) y 94 km, pero claramente dominado por valores bajos y moderados. Las variaciones de espesor elástico deducidas de nuestro modelo podrían reflejar variaciones regionales en la historia de enfriamiento de la litosfera de Venus, así como procesos mantélicos con una limitada manifestación superficial. Las mesetas corticales están cerca de un estado de compensación isostático, consistente con una litosfera elástica delgada en la época de su formación, y mostrando una corteza de mayor espesor bajo ellas, mientras que las tierras bajas exhiben valores de espesor elástico altos, quizás indicativos de una litosfera más fría que cuando se formaron las tierras altas. Por otra parte, existen grandes macizos volcánicos que muestran una señal muy compleja, con un amplio rango de valores de espesor elástico y de mecanismos de carga asociados. Finalmente, nuestros resultados revelan una importante contribución de la parte superior del manto a la resistencia de la litosfera en este planeta.

En el Capítulo 5 se han calculado, de una manera matemáticamente consistente, paleo flujos térmicos derivados del espesor elástico efectivo de la litosfera o de la profundidad de grandes fallas para veintidós regiones de Marte de diferente época y contexto geológico, con el objetivo de constreñir la historia térmica del planeta rojo. De esta manera se ha podido realizar una primera aproximación a su evolución térmica, mostrando que este planeta ha disipado menos calor que el producido en su interior por radioactividad, lo que implica que globalmente se ha enfriado muy poco (e incluso podría haberse calentado internamente), al menos durante algunas fases de su historia. Estas conclusiones son consistentes con una serie de observaciones geológicas y geofísicas independientes como son la presencia de un núcleo metálico total o parcialmente líquido, una reducida presencia de estructuras compresivas indicando una cantidad limitada de contracción térmica, y la abundancia de depósitos volcánicos de origen reciente.

6.6. Reflexión final

La investigación presentada en los capítulos anteriores pone de manifiesto, mediante el estudio de casos concretos y el empleo de diferentes metodologías, la profunda interrelación que existe entre la estructura mecánica de la litosfera y su estado térmico, y cómo cada aumento en el conocimiento de uno de estos aspectos puede ser utilizado para mejorar nuestro conocimiento del otro, de manera que no es posible una correcta comprensión de la primera sin un adecuado conocimiento del segundo y viceversa.

Tomados en conjunto, los trabajos incluidos en esta investigación muestran la universalidad de los métodos que sirven para estudiar la estructura térmica y mecánica de la litosfera, refuerzan la confianza en la aplicación de este tipo de metodologías al estudio de la litosfera en diferentes contextos geodinámicos, así como de diferentes cuerpos planetarios, y proporcionan una visión mucho más amplia del concepto de litosfera.

Como es habitual en cualquier investigación, la que se recoge en esta memoria no supone más que un primer paso para el estudio de la estructura térmica y mecánica de la litosfera, y para avanzar en el conocimiento y comprensión de la dinámica de la Tierra y del resto de los planetas terrestres, y de cómo se ha desarrollado su evolución interna. Cada uno de los trabajos aquí recopilados plantea preguntas que constituyen nuevos retos a afrontar, y que abren el camino a futuras investigaciones.

Bibliografía

Afonso, J.C., Ranalli, G., 2004. Crustal and mantle strengths in continental lithosphere: is the jelly sandwich model obsolete? Tectonophysics, 394, 221–232.

Anguita, F., Castilla, G., 2010. Planetas. Editorial Rueda, S.L., Madrid (p. 474).

Armstrong, G.D., Watts, A.B., 2001. Spatial variations in Te in the southern Appalachians, eastern United States. J. Geophys. Res. 106 (B10), 22,009–22,026.

Artemieva, I., 2011. The Lithosphere: An Interdisciplinary Approach. Cambridge University Press (p. 773).

Audet, P., Mareschal, J-C., 2004. Anisotropy of the flexural response of the lithosphere in the Canadian Shield, Geophys. Res. Lett., 31, L20601.

Audet, P., Jellinek, A.M., Uno, H., 2007. Mechanical controls on the deformation of continents at convergent margins. Earth Planet. Sci. Lett. 264, 151–166.

Audet, P., Mareschal, J-C., 2007. Wavelet analysis of the coherence between Bouguer gravity and topography: application to the elastic thickness anisotropy in the Canadian shield. Geophysical Journal International 168, 287–298.

Audet, P., 2011. Directional wavelet analysis on the sphere: application to gravity and topography of the terrestrial planets. J. Geophys. Res. 116, E01003.

Audet, P., Bürgmann, R., 2011. Dominant role of tectonic inheritance in supercontinent cycles. Nature Geoscience 4, 184–187.

Audet, P., 2014. Toward mapping the effective elastic thickness of planetary lithospheres from a spherical wavelet analysis of gravity and topography. Phys. Earth Planet. Inter. 226, 48-82.

Balmino, G., Vales, N., Bonvalot, S., Briais, A., 2011. Spherical harmonic modeling to ultra-high degree of Bouguer and isostatic anomalies. Journal of Geodesy. DOI 10.1007/s00190-011-0533-4.

Baratoux, D., Toplis, M. J., Monnereau, M., Sautter, V., 2013. The petrological expression of early Mars volcanism. J. Geophys. Res. 118, 59–64.

Baratoux, D., Samuel, H., Michaut, C., Toplis, M.J., Monnereau, M., Wieczorek, M., Garcia, R., Kurita, K., 2014. Petrological constraints on the density of the Martian crust. J. Geophys. Res., 119, 1707-1727.

Bürgmann, R., Dresen, G., 2008. Rheology of the lower crust and upper mantle: evidence from rock mechanics, geodesy, and filed observations. Annu. Rev. Earth Planet. Sci. 36, 531–567.

Burov, E.B., Diament, M., 1995. The effective elastic thickness of (Te) continental lithosphere. What does it really means? J. Geophys. Res. 100 (B3), 3905–3927.

Burov, E.B., Watts, A.B., 2006. The long-term strength of continental lithosphere: "jelly sandwich" or "crème brûlée"? GSA Today 16 (1), 4–10.

Burov, E., 2011. Lithosphere, Mechanical Properties, in Encyclopedia of Solid Earth Geophysics, Gupta, Harsh K. (Ed.) Springer (p. 1539).

Chapman, D.S., Furlong, K.P., 1992. Thermal state of continental lower crust. In: Fountain, D.M., Arculus, R., Kay, R.W. (Eds.), Continental Lower Crust. Elsevier Science, Amsterdam, pp. 179–199.

Chen, B., Chen, C., Kaban, M.K., Du, J., Liang, Q., Thomas, M., 2013. Variations of the effective elastic thickness over China and surroundings and their relation to the lithosphere dynamics. Earth and Planetary Science Letters 363, 61-72.

Chen, B., Liu, J., Kaban, M.K., Sun, Y., Chen, C., Du, J., 2014. Elastic thickness, mechanical anisotropy and deformation of the southeastern Tibetan Plateau. Tectonophysics 637, 45–56.

DeMets, C., Gordon, R.G., Argus, D.F., 2010. Geologically current plate motions. Geophys. J. Int. 181, 1–80. See also: Erratum. Geophys. J. Int. 187 (2011) 538.

Ekström, G., Nettles, M., Dziewoński, A., 2012. The global CMT project 2004–2010: centroid-moment tensors for 13,017 earthquakes. Physics of the Earth and Planetary Interiors 200–201, 1–9.

Forsyth, D.W., 1985. Subsurface loading estimates of the flexural rigidity of continental lithosphere. J. Geophys. Res. 90, 12,623–12,632.

Gómez-Ortiz, D., Tejero, R., Ruiz, J., Babín-Vich, R., González-Casado, J.M., 2005. Estimating the effective elastic thickness of the Iberian Peninsula's lithosphere based on multitaper spectral analysis. Geophys. J. Int. 160, 729–735.

Hahn, B.C., McLennan, S.M., Klein, E.C., 2011. Martian surface heat production and crustal heat flow from Mars Odyssey Gamma-Ray spectrometry. Geophys. Res. Lett. 38, L14203.

Hirt, C., Kuhn, M., Featherstone, W.E., Goettl, F., 2012. Topographic/isostatic evaluation of new-generation GOCE gravity field models. Journal of Geophysical Research B05407.

James, P.B., Zuber, M.T., Phillips, R.J., 2013. Crustal thickness and support of topography on Venus. J. Geophys. Res. 118, 859-875.

Jiménez-Díaz, A., Ruiz, J., Villaseca, C., Tejero, R., Capote, R., 2012. The thermal state and strength of the lithosphere in the Spanish Central System and Tajo Basin from crustal heat production and thermal isostasy. Journal of Geodynamics 58, 29-37.

Jiménez-Díaz, A., Ruiz, J., Pérez-Gussinyé, M., Kirby, J.F., Álvarez-Gómez, J.A., Tejero, R., Capote, R., 2014. Spatial variations of effective elastic thickness of the lithosphere in Central America and surrounding regions. Earth and Planetary Science Letters 391, 55-66.

Jiménez-Díaz, A., Ruiz, J., Kirby, J.F., Romeo, I., Tejero, R., Capote, R. 2014. Lithospheric structure of Venus from gravity and topography. Submitted to Icarus (under review).

Kalnins, L.M., 2011. Spatial Variations in the Effective Elastic Thickness of the Lithosphere and their Tectonic Implications. Ph.D. Thesis. University of Oxford.

Katayama, I., Karato, S.-I., 2008. Low-temperature, high-stress deformation of olivine under water-saturated conditions. Phys. Earth Planet. Inter. 168, 125–133.

Keefner, J.W., Mackwell, S.J., Kohlstedt, D.L., Heidelbach, F., 2011. Dependence of dislocation creep of dunite on oxygen fugacity: implications for viscosity variations in Earth's mantle. J. Geophys. Res. 116, B05201.

Kirby, J.F., 2014. Estimation of the effective elastic thickness of the lithosphere using inverse spectral methods: The state of the art. Tectonophysics 631, 87-116.

Kirby, J.F., Swain, C.J., 2006. Mapping the mechanical anisotropy of the lithosphere using a 2D wavelet coherence, and its application to Australia. Physics of the Earth and Planetary Interiors 158, 122–138.

Kirby, J.F., Swain, C.J., 2008. An accuracy assessment of the fanwavelet coherence method for elastic thickness estimation. Geochemistry, Geophysics, Geosystems 9 (3), Q03022. (Correction. 2008. Geochemistry, Geophysics,Geosystems. 9(5), Q05021).

Kirby, J.F., Swain, C.J., 2009. A reassessment of spectral Te estimation in continental interiors: the case of North America. Journal of Geophysical Research 114, B08401.

Kirby, J.F., Swain, C.J., 2014a. The long-wavelength admittance and effective elastic thickness of the Canadian Shield, J. Geophys. Res. Solid Earth, 119, 5187–5214.

Kirby, J.F., Swain, C.J., 2014b. On the robustness of spectral methods that measure anisotropy in the effective elastic thickness. Geophys. J. Int. 199, 391–401.

Kohlstedt, D.L., Evans, B., Mackwell, S.J., 1995. Strength of the lithosphere: constraints imposed by laboratory experiments. J. Geophys. Res. 100, 17587–17602.

Konopliv, A.S., Asmar, S.W., Folkner, W.M., Karetekin, Ö., Nunes, D.C., Smrekar, S.E., Yoder, C.F., Zuber, M.T., 2011. Mars high resolution gravity fields from MRO, Mars seasonal gravity, and other dynamical parameters. Icarus 211, 401–428.

Laskar, J., Levrard, B., Mustard, J.F., 2002. Orbital forcing of the martian polar layered deposits. Nature 419, 375–377.

Laske, G., Masters., G., Ma, Z., Pasyanos, M., 2013. Update on CRUST1.0 - A 1-degree Global Model of Earth's Crust. Geophys. Res. Abstracts 15, Abstract EGU2013-2658.

Lillis, R. J., Robbins, S., Manga, M., Halekas, J. S., Frey, H. V., 2013 Time history of the Martian dynamo from crater magnetic field analysis. J. Geophys. Res. 118, DOI:10.1002/jgre.20105.

Lowry, A.R., Smith, R.B., 1995. Strength and rheology of the western U.S. Cordillera. J. Geophys. Res. 100, 17,947–17,963.

Mangold, N., Adeli, S., Conway, S., Ansan, V., Langlais, B., 2012. A chronology of early Mars climatic evolution from impact crater degradation. J. Geophys. Res. 117, E04003.

Mao, X., Wang, Q., Liu, S., Xu, M., Wang, L., 2012. Effective elastic thickness and mechanical anisotropy of South China and surrounding regions. Tectonophysics 550-553, 47–56.

Martín-Velázquez, S., De Vicente, G., 2011. Reduca (Geología). Serie Tectónica 3 (1), 1-41.

McGovern, P.J., Solomon, S.C., Smith, D.F., Zuber, M.T., Simons, M., Wieczorek, M.A., Phillips, R.J., Neumann, G.A., Aharonson, O., Head J.W., 2002. Localized gravity/topography admittance and correlation spectra on Mars: Implications for regional and global evolution. J. Geophys. Res. 107, 5136.

McGovern, P.J., Solomon, S.C., Smith, D.F., Zuber, M.T., Simons, M., Wieczorek, M.A., Phillips, R.J., Neumann, G.A., Aharonson, O., Head J.W., 2004. Correction to localized gravity/topography admittance and correlation spectra on Mars: Implications for regional and global evolution. J. Geophys. Res. 109, E07007.

McKenzie, D., 2003. Estimating Te in the presence of internal loads. Journal of Geophysical Research 108 (B9), 2438.

McKenzie, D., 2010. The influence of dynamically supported topography on estimates of Te. Earth and Planetary Science Letters 295, 127–138.

McKenzie, D., Jackson, J., Priestley, K., 2005. Thermal structure of oceanic and continental lithosphere. Earth Planet. Sci. Lett. 233, 337–349.

McKenzie, D.P., Fairhead, J.D., 1997. Estimates of the effective elastic thickness of the continental lithosphere from Bouguer and free air gravity anomalies, J. geophys. Res., 102(B12), 27 523–27 552.

McNutt, M.K., 1984. Lithospheric flexure and thermal anomalies. J. Geophys. Res. 89, 11,180-11,194.

Mei, S., Suzuki, A.M., Kohlstedt, D.L., Dixon, N.A., Durham, W.B., 2010. Experimental constraints on the strength of the lithospheric mantle. J. Geophys. Res. 115, B08204.

Milbury, C., Schubert, G., Raymond, C. A., Smrekar, S. E., Langlais, B., 2012. The history of Mars' dynamo as revealed by modelling magnetic anomalies near Tyrrhenus Mons and Syrtis Major. J. Geophys. Res. 117, E10007.

Mouthereau, F., Watts, A.B., Burov, E., 2013. Structure of orogenic belts controlled by lithosphere age. Nature Geoscience 6, 785–789. doi:10.1038/ngeo1902

Neumann, G.A., Zuber, M.T., Wieczorek, M.A., McGovern, P.J., Lemoine, F.G., Smith, D.E., 2004. Crustal structure of Mars from gravity and topography. J. Geophys. Res., 109, E08002.

Neumann,G.A., Lemoine, F.G., Smith, D.E., Zuber, M.T., 2008. Marscrust3-A crustal thickness inversion from recent MRO gravity solutions. Lunar Planet. Sci. Conf. 39, 2167.

Pérez-Gussinyé, M., Lowry, A.R., Watts, A.B., Velicogna, I., 2004. On the recovery of the effective elastic thickness using spectral methods: examples from synthetic data and from the Fennoscandian Shield. J. Geophys. Res. 109.

Pérez-Gussinyé, M., Watts, A.B., 2005. The long-term strength of Europe and its implications for plate forming processes. Nature 436, 381–384.

Phillips, R.J. et al., 2008. Mars north polar deposits: Stratigraphy, age, and geodynamical response. Science 320, 1182–1185.

Ranalli, G., 1997. Rheology of the lithosphere in space and time. Geol. Soc. Spec. Pub. 121, 19–37.

Ranalli, G., Murphy, D.C., 1987. Rheological stratification of the lithosphere. Tectonophysics 132, 281–295.

Ross, M.I., Scotese, C.R., 1988. A hierarchical tectonic model of the Gulf of Mexico and Caribbean region. Tectonophysics 155, 139–168.

Ruiz, J., 2006. La estructura térmica y mecánica de la litosfera de los cuerpos planetarios. Tesis Doctoral, Universidad Complutense de Madrid. Madrid (p. 184).

Ruiz, J., 2014. The early heat loss evolution of Mars and their implications for internal and environmental history. Sci. Rep. 4, 4338.

Ruiz, J., Fernández, C., Gomez-Ortiz, D., Dohm, J.M., López V., Tejero, R., 2008. Ancient heat flow, crustal thickness, and lithospheric mantle rheology in the Amenthes region, Mars. Earth Planet. Sci. Lett. 270, 1-12.

Ruiz, J., Gómez-Ortiz, D., Tejero, R., 2006. Effective elastic thicknesses of the lithosphere in the Central Iberian Peninsula from heat flow: implications for the rheology of the continental lithospheric mantle. J. Geodyn. 41, 500–509.

Ruiz, J., López, V., Dohm, J.M., 2010. The present-day thermal state of Mars. Icarus 207, 631–637.

Ruiz, J., McGovern, P.J., Jiménez-Díaz, A., López, V., Williams, J.P., Hahn, B.C., Tejero, R., 2011. The thermal evolution of Mars as constrained by paleo-heat flows. Icarus 215, 508-517.

Ruiz, J., Williams, J.P., Dohm, J.M., Fernández, C., López, V., 2009. Ancient heat flows and crustal thickness at Warrego rise, Thaumasia Highlands, Mars: Implications for a stratified crust. Icarus 203, 47–57.

Sandiford, M., 1994. Preamble, in Lithospheric dynamics, edited by Sandiford, M., Foden, J. (p. 117).

Sandu, C., Kiefer, W. S., 2012. Degassing history of Mars and the lifespan of its magnetic dynamo. Geophys. Res. Lett. 39, L03201.

Schubert, G., 2015. Treatise on Geophysics, 2nd Edition. Elsevier (p. 5604).

Schultz, R.A., Watters, T.R., 2001. Forward mechanical modeling of the Amenthes Rupes thrust fault on Mars. Geophys. Res. Lett. 28, 4659-4662.

Simons, F.J., van der Hilst, R.D., Zuber, M.T., 2003. Spatiospectral localization of isostatic coherence anisotropy in Australia and its relation to seismic anisotropy: implications for lithospheric deformation. Journal of Geophysical Research 108 (B5), 2250.

Simons, F.J., Zuber, M.T., Korenaga, J., 2000. Isostatic response of the Australian lithosphere: estimation of effective elastic thickness and anisotropy using multitaper spectral analysis. Journal of Geophysical Research 105 (B8), 19,163–19,184.

Smrekar, S.E., Stofan, E.R., Mueller, N., Treiman, A., Elkins-Tanton, L., Helbert, J., Piccioni, G., Drossart, P., 2010. Recent Hotspot Volcanism on Venus from VIRTIS Emissivity Data. Science 328, 605-608.

Solomon, S.C., Head, J.W., 1982. Mechanisms for lithospheric heat transport on Venus: Implications for tectonic style and volcanism. J. Geophys. Res. 87, 9,236-9,246.

Solomon, S.C., Smrekar, S.E., Bindschadler, D.L., Grimm, R.E., Kaula,W.M., McGill, G.E., Phillips, R.J., Saunders, R.S., Schubert, G., Squyres, S.W., and Stofan, E.R., 1992, Venus tectonics: An overview of Magellan observations. J. Geophys. Res. 97, 13,199-13,255.

Spohn, T., Breuer, D., Johnson, T., 2014. Encyclopedia of the Solar System, 3rd Edition. Elsevier (p. 1336).

Stark, C.P., Stewart, J., Ebinger, C.J., 2003. Wavelet transform mapping of effective elastic thickness and plate loading: validation using synthetic data and application to the study of southern African tectonics. J. Geophys. Res. 108 (B12), 2558.

Stephenson, R., Beaumont, C., 1980, Small-scale convection in the upper mantle and the isostatic response of the Canadian shield, in Mechanisms of Continental Drift and Plate Tectonics, pp. 111–122, eds Davies, P.A. & Runcorn, S.K., Academic Press, San Diego, CA.

Stüwe, K., 2007. Geodynamics of the lithosphere. An introduction, 2nd Edition. Springer–Verlag, Berlin (p. 493).

Sykes, L.R., McCann,W.R., Kafka, A.L., 1982. Motion of Caribbean Plate during last 7 million years and implications for early Cenozoic movements. J. Geophys. Res. 87 (B13), 10656–10676.

Tassara, A., Swain, C.J., Hackney, R.I., Kirby, J.F., 2007. Elastic thickness structure of South America estimated using wavelets and satellite-derived gravity data. Earth and Planetary Science Letters 253, 17–36.

Tesauro, M., Kaban, M.K., Cloetingh, S.A.P.L., 2012. Global strength and elastic thickness of the lithosphere. Global and Planetary Change 90–91, 51–57.

Turcotte, D.L., Schubert, G., 2014. Geodynamics, 3rd Edition. Cambridge Univ. Press, Cambridge (p. 612).

VEXAG, 2014. Goals, Objectives, and Investigations for Venus Exploration 2014, Venus Exploration Analysis Group (VEXAG), [http://www.lpi.usra.edu/vexag], 21 pp.

Watts, A.B., 2007. An overview, in Treatise of Geophysics. Volume 6: Crust and lithosphere dynamics, edited by A. B. Watts, pp. 1-48, Elsevier.

Watts, A.B., 2001. Isostasy and Flexure of the Lithosphere. Cambridge University Press. 472 pp.

Watts, A.B., Burov, E.B, 2003. Lithospheric strength and its relation to the elastic and seismogenetic layer thickness. Earth Planet. Sci. Lett. 213, 113-131.

Watts, A.B., Zhong, S.J., Hunter, J., 2013. Lithosphere behaviour on seismic through geologic timescales. Annual Reviews Earth & Planetary Sciences 41, 443-468.

Wieczorek, M.A., 2007. Gravity and topography of the terrestrial planets, Treatise on Geophysics, Vol. 10, 165-206.

Wieczorek, M.A., Phillips, R.J., 1998. Potential anomalies on a sphere: applications to the thickness of the lunar crust. J. Geophys. Res. 103, 1715-1724.

Wieczorek, M.A., Zuber, M.T., 2004. Thickness of the Martian crust: Improved constraints from geoid-to-topography ratios. J. Geophys. Res., 109, E01009.

Wilson, J. H., Mustard, J. F., 2013. Exposures of olivine-rich rocks in the vicinity of Ares Vallis: implications for Noachian and Hesperian volcanism. J. Geophys. Res. 118, 916–929.

Zamani, A., Samiee, J., Kirby, J.F., 2013. Estimating the mechanical anisotropy of the Iranian lithosphere using the wavelet coherence method. Tectonophysics 601, 139–147.

Zhao, Y.H., Zimmerman, M.E., Kohlstedt, D.L., 2010. Effect of iron content on the creep behavior of olivine: 1. Anhydrous conditions. Earth Planet. Sci. Lett. 287, 229-240.

Zuber, M.T., Solomon, S.C., Phillips, R.J., Smith, D.E., Tyler, G.L., Aharonson, O., Balmino, G., Banerdt, W.B., Head, J.W., Lemoine, F.G., 2000. Internal structure and early thermal evolution of Mars from Mars Global Surveyor topography and gravity. Science 287, 1788-1793.

Anexo I

Jiménez-Díaz, A., Ruiz, J., Villaseca, C., Tejero, R., Capote, R. The thermal state and strength of the lithosphere in the Spanish Central System and Tajo Basin from crustal heat production and thermal isostasy. *Journal of Geodynamics* 58, 29-37, 2012.

Journal of Geodynamics 58 (2012) 29–37

Contents lists available at SciVerse ScienceDirect

Journal of Geodynamics

journal homepage: http://www.elsevier.com/locate/jog

The thermal state and strength of the lithosphere in the Spanish Central System and Tajo Basin from crustal heat production and thermal isostasy

Alberto Jiménez-Díaz [a,b,*], Javier Ruiz [a], Carlos Villaseca [b,c], Rosa Tejero [a,b], Ramón Capote [a]

[a] Departamento de Geodinámica, Facultad de Ciencias Geológicas, Universidad Complutense de Madrid, José Antonio Nováis 2, 28040 Madrid, Spain
[b] Instituto de Geociencias, CSIC-UCM, José Antonio Nováis 2, 28040 Madrid, Spain
[c] Departamento de Petrología y Geoquímica, Facultad de Ciencias Geológicas, Universidad Complutense de Madrid, José Antonio Nováis 2, 28040 Madrid, Spain

ARTICLE INFO

Article history:
Received 17 July 2011
Received in revised form
23 December 2011
Accepted 8 January 2012
Available online 16 January 2012

Keywords:
Heat flow
Thermal structure
Strength envelopes, Rheology
Continental lithosphere
Iberian Peninsula

ABSTRACT

In this work we have modeled the thermal structure of the lithosphere of the Spanish Central System and the Tajo Basin, and their implications for lithospheric strength. For this, we have used refined heat-producing elements (HPE) values to obtain new estimates of heat production rates in the Spanish Central System and Tajo Basin areas, which have been used joined to the relation between topography and thermal structure of the lithosphere to calculate the best-fit surface heat flows in the study area. Moreover, we have implemented a temperature-dependent thermal conductivity (appropriate for olivine) for the lithospheric mantle to improve the calculations of temperature profiles in the mantle. The geotherms so obtained, together with the implementation of a new rheological law for the upper lithospheric mantle, have been used to calculate refined estimations of the strength and effective elastic thickness of the lithosphere. We have obtained surface heat flow values of 84 mW m^{-2} and ~82 mW m^{-2} for the Spanish Central System and the Tajo Basin, respectively. The thermal state of the lithosphere affects mantle temperatures, and hence may be playing an important role in the uplift and maintenance of the Spanish Central System.

1. Introduction

The thermal state and the rheological behavior of the continental lithosphere depend on many factors (e.g., Afonso and Ranalli, 2004; Chapman and Furlong, 1992; Kohlstedt et al., 1995; Ranalli, 1997; Ranalli and Murphy, 1987). Due to the relationship between thermal and mechanical structure of the lithosphere, it is necessary to have an adequate knowledge of the thermal parameters, local heat flow and thermal structure, to reduce the uncertainty in strength estimates. For example, the amount and distribution of lithospheric heat-producing elements (HPE) and the values of the thermal conductivities of crust and mantle may affect the results substantially. Thus, the mechanical behavior and rheological stratification of the lithosphere in continental areas are largely a consequence of local conditions (e.g., Afonso and Ranalli, 2004; Furlong and Chapman, 1987; Ruiz et al., 2006; Watts and Burov, 2003). On the other hand, recent laboratory experiments conducted under controlled microstructural and chemical conditions have shown a significant effect of important parameters on the rheological properties of major silicate rocks (Bürgmann and Dresen, 2008), and have yielded new rheological laws describing the first-order mechanical behavior of the lithospheric materials (e.g., Katayama and Karato, 2008; Keefner et al., 2011; Mei et al., 2010).

The aim of this work is to model the thermal structure and their implications for lithospheric strength of the Spanish Central System (SCS) and the Tajo Basin (TB). The SCS constitutes the most prominent topographic elevation in the interior of the Iberian Peninsula separating the Duero and Tajo watersheds. It is flanked by two Cenozoic intracontinental sedimentary basins, the Duero Basin to the north and the TB to the south (Fig. 1). The SCS is a thick-skinned double-vergence (pop-up) intraplate range built as a result of polyphase Alpine tectonic evolution (De Vicente and Vegas, 2009; De Vicente et al., 2004, 2007, 2009; Fernández-Lozano et al., 2011; Martín-Velázquez et al., 2009), in which the deformation partitioning of the basement in the intraplate convergence setting of Iberia has had a profound influence on the development of topography.

The surface heat flow map of the Iberian Peninsula performed by Fernàndez et al. (1998) provides some values at the SCS-TB boundary and the north and south of the TB. In contrast, the SCS is not well characterized due to the unavailability of heat flow measurement, and it is necessary to approach the study of the thermal state of the range through other methodologies. In this sense, Tejero and Ruiz

* Corresponding author at: Departamento de Geodinámica, Facultad de Ciencias Geológicas, Universidad Complutense de Madrid, José Antonio Nováis 2, 28040 Madrid, Spain.
E-mail address: ajimenezdiaz@geo.ucm.es (A. Jiménez-Díaz).

0264-3707/$ – see front matter © 2012 Elsevier Ltd. All rights reserved.
doi:10.1016/j.jog.2012.01.005

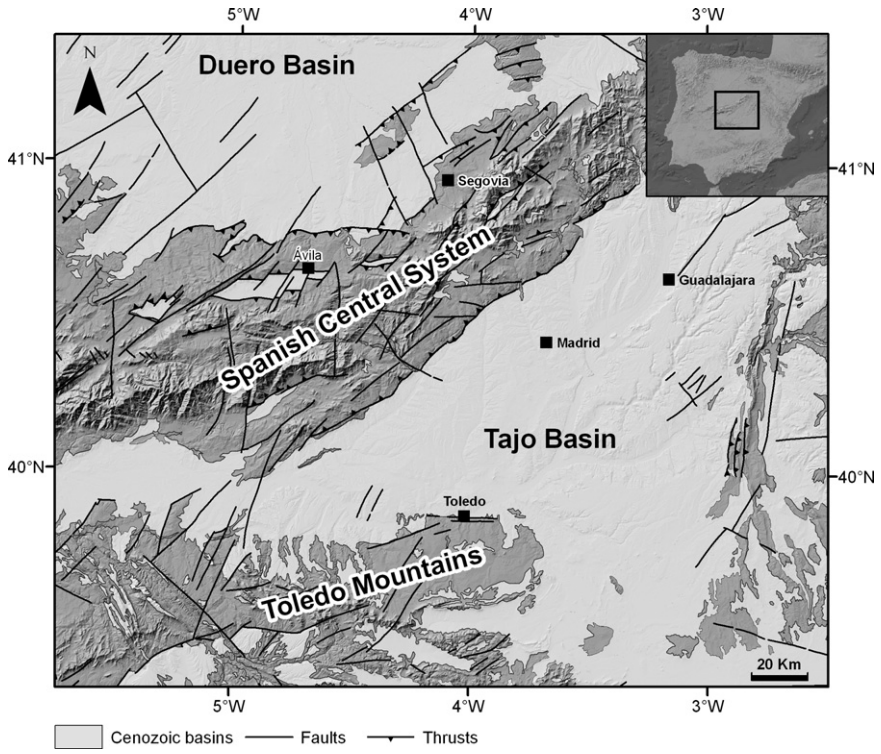

Fig. 1. Geographical and geological settings of the study area showing the two mountains ranges (Spanish Central System and Toledo Mountains) separated by the Tajo Basin. Map background is from the Neotectonic Map of Spain (IGME and ENRESA, 1998).

(2002) modeled the thermal structure of the lithosphere of this area by using thermal isostasy to improve the calculated geotherms, considering surface heat flow values of 70 and 65–70 mW m^{-2} for the SCS and the TB, respectively.

On the other hand, several works have focused on characterizing the lithospheric strength from estimating the effective elastic thickness of the lithosphere through flexure modeling (Van Wees et al., 1996), the coherence between topography and Bouguer anomaly (Gómez-Ortiz et al., 2005a; Pérez-Gussinyé and Watts, 2005) or from rheological models (Martín-Velázquez et al., 2008; Ruiz et al., 2006; Tejero and Ruiz, 2002; Tesauro et al., 2007, 2009).

In the present work, we have used the relation between topography and thermal structure to calculate the best-fit surface heat flows. We included a temperature-dependent thermal conductivity (appropriate for olivine) for the lithospheric mantle to improve the calculations. Moreover, we have used refined HPE values based on bulk rock composition of main lithological formations of the SCS and the Toledo Mountains (e.g. Villaseca et al., 1998, 1999, 2005; this study), and these values have been used to obtaining estimates of heat production rates. Finally, we have used our result for the thermal structure in order to analyze the strength of the lithosphere in the study area. To make this, we have implemented a new rheological law for the upper lithospheric mantle, largely controlled by low-temperature plasticity of olivine-rich rocks (Mei et al., 2010). All of this provides an opportunity to refine existing thermal and rheological models and lithospheric strength determinations of the study area.

2. Temperature profiles

The thermal structure of the lithosphere depends on heat flow, heat sources distribution and thermal conductivity of lithospheric rocks. The temperature profile within the lithosphere has been calculated assuming steady-state conditions and radioactive heat sources homogeneously distributed in three crustal layers and in the lithospheric mantle. The temperature at depth z in each crust layer is

$$T_z = T_s + \frac{F_S z}{k} - \frac{Hz^2}{2k}, \tag{1}$$

where T_s and F_s are the temperature and heat flow at the layer top, k is the thermal conductivity, and H is the volumetric heat production rate. The calculations assume k = 2.5, 2.5 and 2.1 W m^{-1} K^{-1} for upper, middle and lower crust, respectively, and the surface temperature was taken as 288 K.

The thermal conductivity of olivine (the main mineral in the mantle) is strongly temperature-dependent; therefore temperature profiles in the mantle lithosphere are calculated from (see Ruiz et al., 2011)

$$\frac{dT}{dz} = \frac{F_{cb} - \rho_m H_m (z - b_c)}{k_m(T)}, \tag{2}$$

where $F_{cb} = F - \rho_c H_c b_c$ is the heat flow at the base of the crust, ρ_m and H_m are, respectively, the density and heat production rate per mass unity of the mantle lithosphere, b_c is the base of the crust, and k_m is the thermal conductivity of the mantle lithosphere. For k_m we use the thermal conductivity of olivine, which is a function of temperature according to the expression (McKenzie et al., 2005)

$$k_m = \frac{a}{1 + c(T - 273)} + \sum_{i=0}^{3} d_i T^i, \tag{3}$$

where $a = 5.3$, $c = 0.0015$, $d_0 = 1.753 \times 10^{-2}$, $d_1 = -1.0364 \times 10^{-4}$, $d_2 = 2.2451 \times 10^{-7}$ and $d_3 = -3.4071 \times 10^{-11}$. Results obtained from Eq. (3) are similar to those of Hofmeister (1999) for forsterite olivine. For solving Eqs. (2) and (3), we used the Newton iterative method.

Moreover, the use of concept of thermal isostasy is useful in order to constrain continental temperature profiles (e.g., Fernàndez et al., 1998; Hasterok and Chapman, 2007, 2011; Lachenbruch and

Morgan, 1990; Tejero and Ruiz, 2002), by providing a link between the thermal structure of the lithosphere and the elevation of the surface. Elevation above sea level (e) can be expressed by

$$e = h_c + h_m - h_o, \tag{4}$$

where h_c and h_m are the individual contributions of crust and mantle components to the buoyancy of the lithosphere. h_o is the buoyant height of sea level above the free asthenosphere surface ($h_o \approx 2.4$ km; Lachenbruch and Morgan, 1990). Crust contribution is estimated from

$$h_c = \frac{1}{\rho_a}(\rho_a - \rho_c)b_c, \tag{5}$$

where b_c is crust thickness, ρ_c is mean crust density and ρ_a is asthenosphere density (3200 kg m^{-3}). Mantle contribution is related to the thermal state of the lithosphere mantle by

$$h_m = a(\bar{T}_m - T_a)b_m, \tag{6}$$

where α is the thermal volumetric expansion coefficient (3.5×10^{-5} K^{-1}), b_m is the thickness of the lithospheric mantle until the asthenosphere temperature T_a, assumed to be the isotherm of 1350 °C, and $\bar{T}_m$ is the mean lithosphere mantle temperature given by

$$\bar{T}_m = \frac{1}{b_m}\int_0^{b_m} T(z)dz, \tag{7}$$

which we use here in order to determine the depth of the lithosphere–asthenosphere boundary (*LAB*). Here we use crustal structure and composition derived from seismic data (Banda et al., 1981; ILIHA DSS Group, 1993; Suriñach and Vegas, 1988), and crustal density derived from gravity data analysis (Gómez-Ortiz et al., 2005b). Mantle heat flow was estimated by subtracting crustal contribution from surface heat flow. We applied the thermal isostasy model by iterative calculation to fit the calculated elevation to the observed mean elevation (~1250 m and ~650 m for SCS and TB, respectively). Table 1 summarizes the parameters used in the calculations.

3. Crustal heat production

Uranium, Thorium and Potassium (collectively termed as heat-producing elements, HPE) abundance determines heat production rates of crustal rocks. Thus, heat production is calculated from HPE abundance by the addition of the contribution of each element as follows (Rybach, 1988)

$$H\ (\mu\text{W m}^{-3}) = 10^{-5}\rho(9.52C_U + 2.56C_{Th} + 3.48C_K), \tag{8}$$

where C_U and C_{Th} are in ppm and C_K in percent, and ρ is the density (in kg m^{-3}). This method has been used to estimate heat production rates of the crust of Central Iberia (Spain), where 196 samples of metamorphic and igneous rocks of Variscan basement were collected and their content on HPE determined. They represent main outcropping lithologies mostly orthogeneiss and granites. Furthermore, granulite xenoliths carried by Upper Permian alkaline lamprophyres have been interpreted as samples of the lower crust below the SCS (Villaseca et al., 1999). Table 2 summarizes HPE abundances collected from 196 sites covering the Spanish Central System and the Toledo Mountains.

HPE abundances and heat production values for the SCS complex comprises outcropping metamorphic rocks mostly of two types: metasedimentary sequences and felsic orthogneissic rocks. These Cambrian-Lower Ordovician metaigneous rocks are the dominant country rocks, and they show higher heat production rates than metasedimentary types because they are enriched in U and K (Table 2). Metabasic rocks have been also described in the SCS,

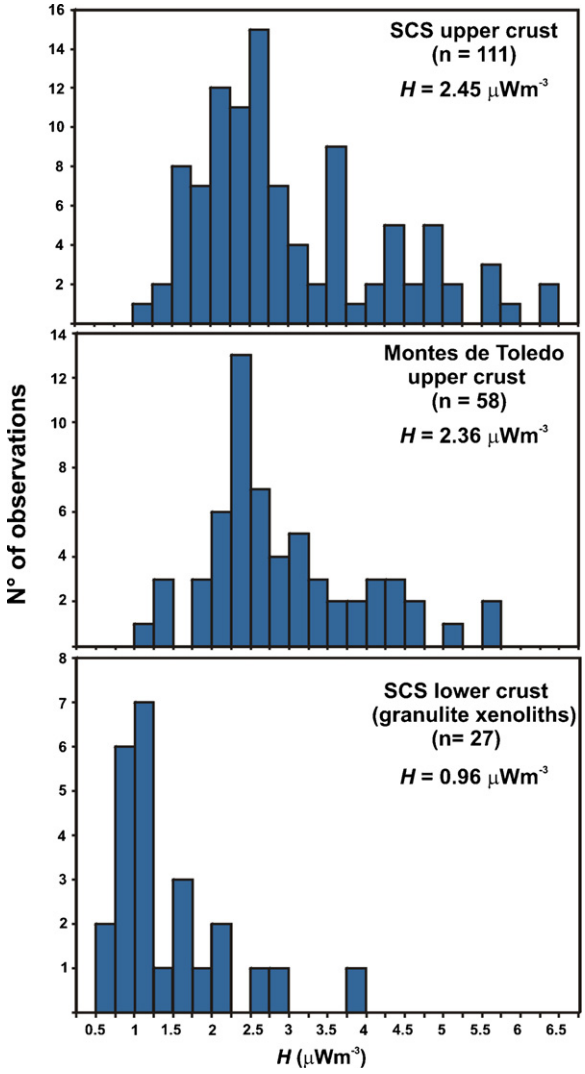

Fig. 2. Estimates of heat production rates of rocks from the Spanish Central System upper crust, Toledo Mountains upper crust and Spanish Central System lower crustal granulite xenoliths.

but defining a very minor surface; regional geologic maps suggest that felsic orthogneisses constitute approximately the 80% of the metamorphic rock exposures at least in his eastern half sector. Otherwise, most of the SCS is occupied by a huge granitic batolith. Proportions determined by mapped lithologies suggest that granites might be 75% of the SCS. The SCS Variscan granites are characterized by an averaged heat production of 2.49 μW m^{-3} (pondered by granite type and area, Table 2), higher values than those of orthogneissic wall-rocks. This approach yields an averaged heat production value of 2.45 μW m^{-3} for the outcropping SCS rocks (Fig. 2).

In the south, Toledo Mountains is also comprised by metamorphic rocks intruded by Variscan granite plutons. Country rocks are dominated by Neoproterozoic-Low Palaeozoic metasedimentary sequences (the Schist-Greywacke Complex), most of low-grade metamorphism (San José et al., 1990). The estimated average heat production rate of 2.36 μW m^{-3} (Table 2 and Fig. 2) for the whole Toledo Mountains area is lower to that obtained for the whole granite-high-grade metamorphic complex of the SCS, mostly due to the lower abundance of granites in the Toledo Mountains area (Table 2). HPE abundances for Tajo sedimentary rocks are not available, although representative heat production rates can be estimated from the surrounding orogenic areas as their

Table 1
Parameters used to construct the geotherms and strength envelopes. Crustal structure and composition derived from seismic data (Banda et al., 1981; ILIHA DSS Group, 1993; Suriñach and Vegas, 1988), crustal density derived from gravity data analysis (Gómez-Ortiz et al., 2005b) and rheological parameters from Ranalli (1997).

	Thickness (km)	Thermal conductivity ($W m^{-1} K^{-1}$)	Heat production ($\mu W m^{-3}$)	Density ($kg m^{-3}$)	A ($MPa^{-n} s^{-1}$)	Q ($kJ mol^{-1}$)	n
Spanish Central System							
Upper crust (dry granite)	11	2.5	2.45	2670	1.8×10^{-9}	123	3.2
Upper crust (wet granite)					2.0×10^{-4}	137	1.9
Middle crust (quarzdiorite)	14	2.5	1.75	2800	1.3×10^{-3}	219	2.4
Lower crust (felsic granulite)	9	2.1	0.96	2900	8.0×10^{-3}	243	3.1
Tajo Basin							
Sediments layer	2/1[a]	2.5	2.40	2400	6.7×10^{-6}	156	2.4
Upper crust (dry quarzite)	12/13[a]	2.5	2.36	2780	6.7×10^{-6}	156	2.4
Upper crust (wet quarzite)					3.2×10^{-4}	154	2.3
Middle crust (quarzdiorite)	9	2.5	1.65	2800	1.3×10^{-3}	219	2.4
Lower crust (felsic granulite)	8	2.1	0.96	2900	8.0×10^{-3}	243	3.1

[a] Thickness for north/south Tajo Basin, respectively.

sedimentary source regions (averaged heat production of 2.40 $\mu W m^{-3}$; Table 1).

The averaged heat production rate of the lower crust is estimated to be 0.96 $\mu W m^{-3}$; value slightly lower than preliminary estimates (Villaseca et al., 2005), but clearly higher than values usually considered for the lower crust (Furlong and Chapman, 1987; Hasterok and Chapman, 2011; Rudnick and Gao, 2003; Vilà et al., 2010). This is consequence of the markedly felsic composition of the SCS lower crust, dominated by felsic meta-igneous (95 vol%) and pelitic (5 vol%) granulites (Villaseca et al., 1999). The felsic nature of the SCS lower crust is best shown in comparison with other lower-crustal xenoliths suites which, on average, are more mafic than granulite terranes (Villaseca et al., 1999 and references therein).

Heat production of the middle crust is not well characterized due to the unavailability of direct measurement, and thus, there is considerable uncertainty with regard to this parameter. The mid-crustal layer is not pervasive globally, and where it exists, tends to have radiogenic heat generation more similar to lower rather than to upper crust (Hasterok and Chapman, 2011 and references therein). On the other hand, the middle crust of the area is made of intrusive felsic materials (Villaseca et al., 1999) similar to those forming the upper crust in many continental areas, and seismic velocities findings point to a granodioritic composition of the middle crust (Banda et al., 1981). Unknown of the depth distribution of rocks compelled us to consider layer homogeneity, and we have assumed an intermediate (density weighted) heat production rate between upper and lower crust. Finally, for the lithospheric mantle we use a standard heat production rate of 0.02 $\mu W m^{-3}$ (e.g., Chapman and Furlong, 1992; Hasterok and Chapman, 2011).

4. Strength of the lithosphere

The concept of strength envelopes is useful to illustrate a first-order approximation of the rheological properties of lithosphere (e.g., Brace and Kohlstedt, 1980; Kohlstedt et al., 1995; Ranalli, 1997; Ranalli and Murphy, 1987). Thus, the strength of the lithosphere at any depth is the minimum between the strengths for brittle and ductile deformation. Assuming a prefractured medium with fractures ideally oriented, the brittle strength is calculated according to the expression (e.g., Ranalli, 1997; Ranalli and Murphy, 1987)

$$(\sigma_1 - \sigma_3)_b = \beta \rho g (1 - \lambda) z, \tag{9}$$

where β is a coefficient depending on the stress regime (0.75 for tension and 3 for compression), ρ is the density, g is the acceleration due to the gravity (9.8 $m s^{-2}$), λ is the pore fluid factor defined as the ratio of pore fluid pressure to lithostatic pressure (Sibson, 1974), and z the depth. The density of the brittle crust, adequate for rocks in the upper crust, is taken as 2670 $kg m^{-3}$ for the SCS and 2780 $kg m^{-3}$ for the TB (Gómez-Ortiz et al., 2005b). In addition, a sedimentary layer is considered in the TB (Table 1). We use the same hydrostatic pore fluid factor ($\lambda = 0.37$) for the whole lithosphere.

The ductile strength does not depend on the stress regime but it is strongly strain rate- and temperature-dependent (Burov and Diament, 1995; Ranalli and Murphy, 1987; Stüwe, 2002), and can be described by a thermally activated power law,

$$(\sigma_1 - \sigma_3)_d = \left(\frac{\dot{e}}{A}\right)^{1/n} \exp\left(\frac{Q}{nRT}\right), \tag{10}$$

where $\dot{e}$ is the strain rate, A, Q, and n are laboratory-determined constants, R is the gas constant (8.31447 $J mol^{-1} K^{-1}$), and T is the

Table 2
Estimates of heat production of rocks from the Spanish Central System and Toledo Mountains.

	Area (%)	Numbers of samples	U (ppm)	Th (ppm)	K (%)	H ($\mu W m^{-3}$)
Spanish Central System						
Metamorphic rocks						
Metabasites	<0.1	6	1.37	5.70	0.54	0.86
Metapelites	20	8	2.65	14.82	2.76	2.00
Metagranites	80	41	4.61	12.25	3.69	2.42
Granitic rocks						
Monzogranites	85	25	3.07	15.63	3.72	2.22
Leucogranites	15	31	8.61	21.23	3.83	4.04
LC Granulite Xenoliths						
Charnockites	<1	4	1.18	2.61	1.87	0.69
Pelites	5	6	0.78	9.14	2.32	1.21
Metaigneous	95	17	0.70	6.54	2.55	0.95
Toledo Mountains						
Metasediments	55	5	3.66	10.97	2.63	1.98
Granites MTB	35	42	6.38	14.76	3.55	2.99
ACT Migmatites	10	11	3.39	12.88	4.97	2.27

absolute temperature. Strength envelopes are calculated for a strain rate of $10^{-15}\,s^{-1}$.

The ductile strength of the upper crust is calculated using flow laws for wet/dry granite and wet/dry quartzite for the SCS and TB, respectively. The lower crust of the central Iberian Peninsula is of a felsic granulite nature (Villaseca et al., 1999), and bearing in mind its flow law it should not appreciably contribute to the strength of the lithosphere. It is therefore not taken into account in the present work (see Tejero and Ruiz, 2002; Ruiz et al., 2006). In turn, the middle crust of the area is made of intrusive felsic materials (Villaseca et al., 1999) similar to those forming the upper crust in many continental areas; its mechanical behavior is therefore likely to be similar (Ruiz et al., 2006).

For the estimation of the strength of the lithospheric mantle we use dry and wet olivine rheologies, which give upper and lower limits, respectively. The behavior of the upper lithospheric mantle is in turn largely controlled by low-temperature plasticity of olivine-rich rocks (Mei et al., 2010), resulting in a rheology significantly weaker than that usually used for the lithosphere mantle. Under anhydrous conditions, Mei et al. (2010) define a flow law for a quasi steady state deformation of olivine under low-temperature and high-stress, which can be written in terms of differential stress as

$$(\sigma_1-\sigma_3)=\left(\frac{\dot{e}}{A_p}\right)^{1/2}\exp\left[\frac{E_k(0)}{2RT}\left(1-\sqrt{\frac{(\sigma_1-\sigma_3)}{\sigma_p}}\right)\right], \qquad (11)$$

where $A_p = 1.4\times10^{-7}\,s^{-1}\,MPa^{-2}$, $E_k(0)$ is the zero-stress activation energy ($320\pm50\,kJ\,mol^{-1}$), and σ_p is Peierls stress ($5.9\pm0.2\,GPa$). Thus, for dry olivine we use the minimum strength obtained from Eq. (11) and from the high temperature flow law obtained for artificially dried dunites: $A = 28{,}840\,MPa^{-n}\,s^{-1}$, $n = 3.6$ and $Q = 535\,kJ\,mol^{-1}$ (Chopra and Paterson, 1984). For wet olivine, we use the flow law of the Anita Bay dunite: $A = 9550\,MPa^{-n}\,s^{-1}$, $n = 3.35$ and $Q = 444\,kJ\,mol^{-1}$ (Chopra and Paterson, 1984). This flow law places a lower limit on the strength of wet olivine due to its relative weakness (compared with other wet dunites, such as Aheim dunite).

Finally, the total lithospheric strength (Ranalli, 1997) can be defined as

$$S=\int_0^{b_L}(\sigma_1-\sigma_3)(z)dz, \qquad (12)$$

where $(\sigma_1-\sigma_3)$ is the minor, at z depth, between the brittle and ductile strength, and b_L is the mechanical thickness of the lithosphere. The base of the mechanical lithosphere is here defined as the depth at which the ductile strength reaches a low value of 10 MPa (McNutt, 1984; Ranalli, 1994), and below which there are no further significant increases in strength, although the exact value selected does not produce significant changes in the calculations due to the exponential dependence of ductile strength on temperature. Table 1 summarizes the rheological model parameters.

5. Results

5.1. Thermal modeling

Fig. 3 shows the geotherms obtained by our thermal model. For the SCS, we have obtained a value of $F_s = 84\,mW\,m^{-2}$, with elevation adjustment of ±1 m (Table 3 and Fig. 3). For the north and south TB, we have obtained values of $F_s = 81\,mW\,m^{-2}$ and $F_s = 83\,mW\,m^{-2}$ respectively, with elevation adjustment of ±2 m in both cases (Table 3 and Fig. 3). We have calculated the surface heat flow from the thermal isostasy model obtaining through iterative calculation the surface heat flow best-fitting the observed mean elevation. In this sense, a heat flow uncertainty of $\pm0.1\,mW\,m^{-2}$ and $\pm0.01\,mW\,m^{-2}$ results in an elevation uncertainty of ±10 m and ±2 m, respectively.

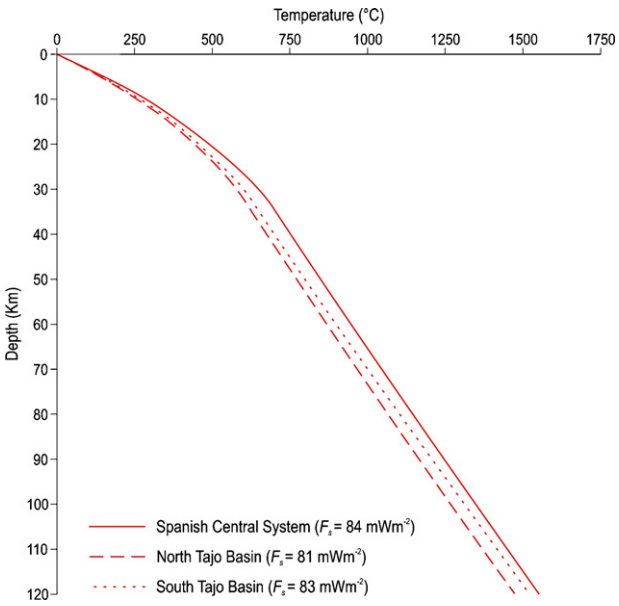

Fig. 3. Geotherm constructed for the Spanish Central System and the Tajo Basin. Variables used in estimations are provided in Table 1. See text for details.

At the crust-mantle boundary (*Moho*) under the SCS, we have obtained a temperature of 700 °C and a mantle heat flow of $24\,mW\,m^{-2}$. For the north and south TB, at *Moho* depth, the temperature and the mantle heat flow decrease to 630 °C and $25\,mW\,m^{-2}$, and to 650 °C and $27\,mW\,m^{-2}$, respectively. The lithosphere–asthenosphere boundary (*LAB*) is located at 99 km in the SCS and at 100 km and 95 km in the north and south TB, respectively.

The differences between the coldest geotherm (North TB) and the hottest geotherm (SCS) remain almost constant, and even show a certain convergence of the curves in depth, indicating an effective lateral homogenization of the temperature in the sublithospheric mantle. Table 3 summarizes the values of the thermal models obtained in this study.

5.2. Mechanical structure and strength envelopes

Strength envelopes for the study area have been constructed using the geotherms presented in the previous section. For the SCS, two crustal brittle–ductile transitions (BDT) appear under tensional stress (Fig. 4), the upper BDT within the upper crust at a depth between 6 and 7 km, depending on rheology, while the lower BDT is found in the middle crust at depth of 13 km. On the other hand, under compression stress, the upper BDT depth is between 5 and 6 km, but there is no BDT in the middle crust. In the case of the TB, a BDT appear within the upper crust but there is no BDT in the middle crust (Fig. 4). Under tensional stress, BDT is located at a depth between 6 and 10 km, depending on rheology. Under compression stress, BDT depth is between 5 and 8 km, depending on rheology. The lithospheric mantle remained in the ductile field for a wet peridotite rheology for the whole area (Fig. 4). For dry peridotite and tensional stresses, only the north TB presents a brittle portion in the lithospheric mantle with a BDT depth of ~32 km. Under compression conditions, the entire lithospheric mantle presents ductile behavior. Finally, all the strength envelopes show that the *Moho* always represents a strong mechanical discontinuity between the lower crust and the uppermost lithospheric mantle (Fig. 4).

Table 3
Summary of values obtained from thermal modeling.

	Surface heat flow ($mW\,m^{-2}$)	Mantle heat flow ($mW\,m^{-2}$)	*Moho* temperature (°C)	Thermal lithospheric thickness (km)
Spanish Central System	84	24	700	98
Tajo Basin (North)	81	25	630	100
Tajo Basin (South)	83	27	650	95

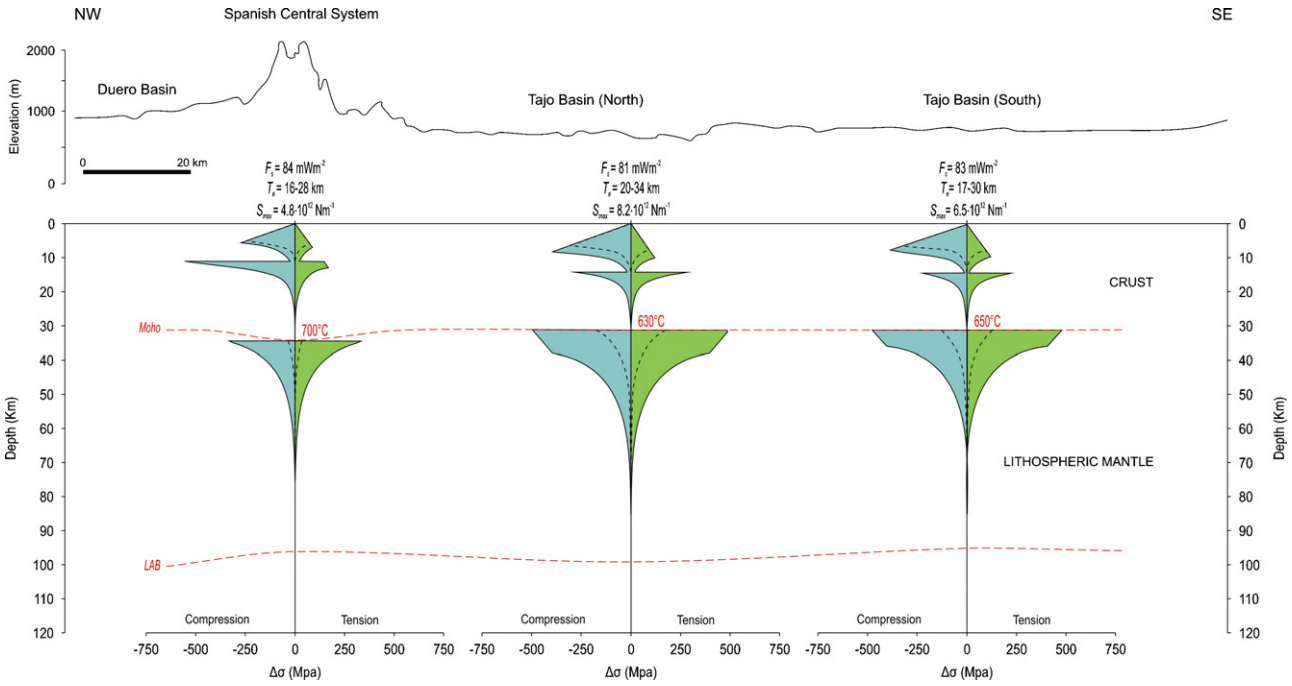

Fig. 4. Results of thermal models and strength envelopes, calculated for a strain rate of $10^{-15}\,s^{-1}$, plotted along a NW–SE transverse section of the area. Outer black line binds differential stress estimated for dry rock composition. Inner dashed line denotes differential stress for wet rock composition of the upper crust (quartzite or granite) and lithospheric mantle (peridotite). F_s: surface heat flow. T_e: effective elastic thickness for wet/dry rheology. S_{max}: maximum total lithospheric strength. *Moho*: crust–mantle boundary. *LAB*: lithosphere–asthenosphere boundary.

Fig. 5 shows total lithospheric strength for compressional and tensional stresses and, in each case, for dry and wet rheologies. Total strength ranges from $\sim 8.2 \times 10^{12}$ to $\sim 1.2 \times 10^{12}\,N\,m^{-1}$. In general, higher total lithospheric strengths are associated with the north TB, while minimum values corresponded to the SCS. These values are consistent with mean integrated strength values estimated under compressional conditions by Tesauro et al. (2009) for the continental lithosphere in Iberia. In the same way, the contribution of the lithospheric mantle to the total lithospheric strength ranges from $\sim 7 \times 10^{12}$ to $\sim 2 \times 10^{11}\,N\,m^{-1}$. These values are consistent with the wavelengths (<250 km) of the lithospheric folds, which suggests low mean mantle strength values ($<10^{13}\,N\,m^{-1}$; Sokoutis et al., 2005), proposed by Muñoz-Martín et al. (2010) from the spectral analysis of the gravity and elevation for continental lithosphere at the Africa–Eurasia boundary.

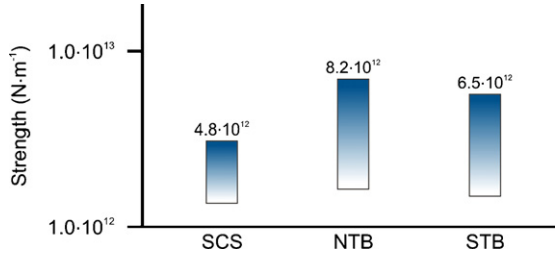

Fig. 5. Total lithospheric strength values for dry and wet rocks in compression and tension plotted for the different tectonic units. Higher strength values were obtained for dry rheology and compressive differential stress. Minimum strength values correspond to wet rheology and tensional differential stress.

Our results can also be interpreted in term of the effective elastic thickness of the lithosphere (T_e), a measure of the total strength of the lithosphere which integrates the contributions from brittle and ductile layers and from elastic cores of the lithosphere (for a review see Watts and Burov, 2003). We have calculated T_e from the strength envelopes constructed for the SCS and the TB. Following Burov and Diament (1995), the total effective elastic thickness of an unflexed plate constituted by n detached layers is

$$T_e = \left(\sum_{i=1}^{n} t_{ei}^3 \right)^{1/3}. \quad (13)$$

where t_{ei} is the mechanical thickness of the layer i. We take the base of each mechanical layer as the depth in which the strength goes down to a value of 10 MPa (see above). If strength levels at the base layer are higher than 10 MPa, the layer is considered welded to the layer below. The calculations were performed for both wet and dry rheology. For the SCS, the results are 16 km for wet rheology and 28 km for dry rheology. For the north and south TB, the obtained values are 17–20 and 30–34 km for wet and dry rheology, respectively. The lower values for the SCS are greatly resulting of the weaker upper mantle in this zone, which has a more limited contribution to the total strength of the lithosphere.

The effective elastic thickness depends on the thermal state of the lithosphere, which determines the thickness and contribution

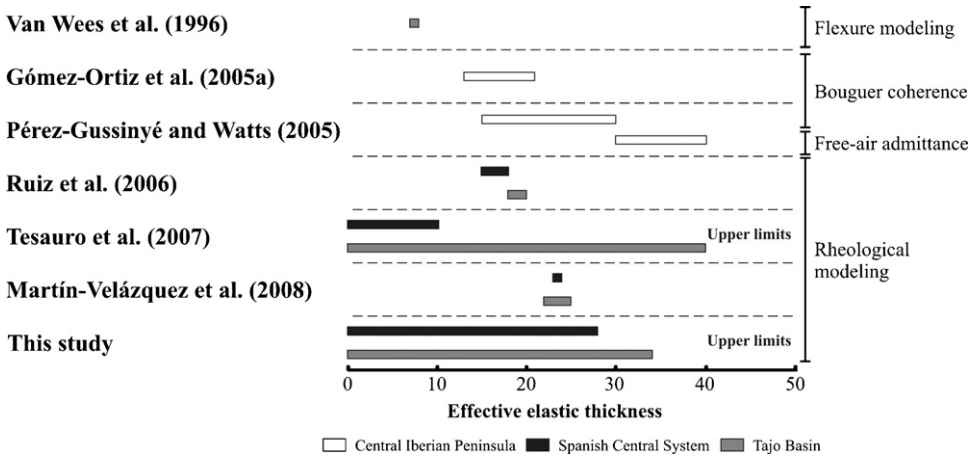

Fig. 6. Compilation of effective elastic thickness values obtained for the study area.

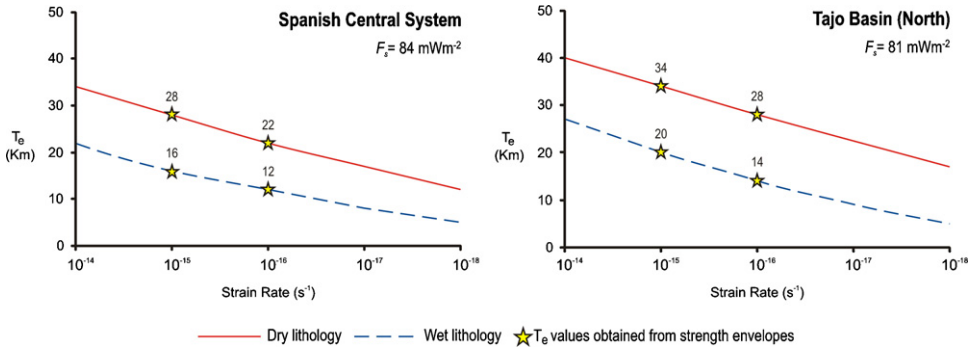

Fig. 7. Effective elastic thickness, in terms of strain rate, in the Spanish Central System and Tajo Basin (North). Dry and wet rheologies for the crust and mantle are used in the calculation.

of mechanically competent layers, and on the local curvature of the plate (which in turn depends on the rheological structure and distribution of the external loads applied to the plate; e.g., Burov and Watts, 2006; Watts and Burov, 2003). Since curvature reduces the bending moment of the lithosphere, assuming an unflexed lithosphere our values of T_e (obtained for dry rheology, which represent the maximum strength) can be considered upper limits.

Several works have focused on characterizing the lithospheric strength in the study area from estimating the effective elastic thickness of the lithosphere following different procedures (Fig. 6). Van Wees et al. (1996) calculated a value of T_e of 7 km for the TB through flexure modeling, Gómez-Ortiz et al. (2005a) obtained values of 14–21 km for the central Iberian Peninsula from the coherence between topography and Bouguer anomaly, and Pérez-Gussinyé and Watts (2005) obtained best-fits of 15–30 km for the Iberian peninsula also from Bouguer coherence (but with the method of the free-air admittance these authors obtained higher T_e values). Ruiz et al. (2006) used the relationship between rheology of the lithosphere and heat flow to calculate theoretical T_e values of 18–20 km for the TB and 15–18 km for the SCS. The map of effective elastic thickness of the European lithosphere performed by Tesauro et al. (2007) shows an increase from 5–10 km in the SCS to 35 km within the basin. Tesauro et al. (2007) assumed an unflexed lithosphere, so their values of T_e actually are upper limits as our results. For the TB, there is good correspondence between the values obtained by these authors and our results. Although for the case of SCS we obtain higher T_e values. Finally, Martín-Velázquez et al. (2008), by means of a finite elements model, obtained an elastic thickness of 24 km for the SCS and 23–25 km for the TB (for wet and dry rheology, respectively).

6. Discussion and conclusions

In the present work we have used refined HPE values to obtain new estimates of heat production rates in the SCS and TB areas, which have been used joined to the relation between topography and thermal structure of the lithosphere to calculate the best-fit surface heat flows in the study area (see Sections 2 and 3). Moreover, we have implemented a temperature-dependent thermal conductivity (appropriate for olivine) for the lithospheric mantle to improve the calculations of temperature profiles in the mantle. The main influence of these procedures is that higher surface heat flows are needed to achieve similar temperatures at *Moho* depth, and small variations in surface heat flow have great influence in the temperature distribution within the lithosphere. The geotherms so obtained, together with the implementation of a new rheological law for the upper lithospheric mantle (see Section 4), have been used to calculate refined estimations of the strength and effective elastic thickness of the lithosphere. Thus, our results refine the thermo-mechanical models and lithospheric strength determinations for the study area.

Surface heat flow obtained for the north TB show good agreement with measurements of Fernàndez et al. (1998), which fall within the range between 62 and 94 mW m^{-2} with a mean value of 77 ± 5 mW m^{-2} ($n = 6$). In contrast, the south TB presents values of surface heat flow clearly higher than the observed range of values in that region (with a mean value of 48 ± 7 mW m^{-2} for $n = 6$, Fernàndez et al., 1998). This difference may be due to local effects. Surface heat flow determinations for the south TB were carried out on water, geothermal and mining explorations wells (Fernàndez et al., 1998). These wells can be affected by thermal

disturbances due to water circulation (Marzán et al., 1996). In the south TB, geothermal gradient values observed are dispersed, and the thermal regime may be affected by surface water flow in porous levels and hydraulic connection between aquifers through the well (Marzán et al., 1996). Moreover, an average of 48 mW m^{-2} leads to an increase of the total lithospheric strength ($S \approx 1 \times 10^{15}$ N m^{-1}), and effective elastic thickness (Te ≈ 150 km), much higher than any previous estimates for the Central Iberian Peninsula (see Section 5.2).

Some authors use the mean value (and sometimes the median value) for the heat production rate in their models (e.g., Hasterok and Chapman, 2011). A heat production rate weighted by the areal distribution characterizes better our crust model that a purely statistical value, where less abundant rocks, but with higher sampling, would have greater weight in the calculations (see Table 2). We also consider a heat production rate weighted by the areal distribution more correct, therefore considering a radioactive heat sources homogeneously distributed. To check the influence on the results of our models, we have considered the effect of using mode values without taking into account the areal distribution of samples in order to study the model response. These slightly higher estimates of heat production rates (2.6 μW m^{-3} for the upper crust, and 1.1 μW m^{-3} for the lower crust), leads to an average increase of 4 mW m^{-2} in the surface heat flow, 20 °C of the temperature at the crust-mantle boundary (*Moho*), and enlarge 1 km in the thermal lithospheric thickness. In turn, the mantle heat flow is reduced by 1 mW m^{-2}. This change in the thermal state, results in a decrease in 1 km of the T_e, and a reduction over 10–20% of the total lithospheric strength, depending on the stress regime. Thus, we consider our results robust.

In the case of the SCS, the crustal thickening (especially of the lower crust, which has a relatively high content of HPE; see Section 3), may be an important factor in its thermal structure. This thickening can be translated into a lithospheric mantle with a minor contribution in the calculation of surface heat flow, but proportionally hotter. So, the HPE-enriched and hot lower crust could reduce the heat loss from the lithospheric mantle. Recently, Boschi et al. (2010) and Faccenna and Becker (2010) have proposed the existence of a vigorous mantle upwelling in the western Mediterranean (from southern Iberia to the French Massif Central), based on interpreting residual topography (after correcting by isostasy) as dynamical topography due to mantle flow. In their models, the mantle upwelling would be driven by density variations caused by temperature differences derived from seismic tomography. However, thermal insulation of the upper mantle due to an HPE-enriched lower crust might be an important factor by contributing to mantle high temperatures. This state, together with an important contribution from crustal shortening and thickening, erosion during the endorheic–exorheic drainage transition, and lithospheric folding process (Casas-Sainz and De Vicente, 2009; De Vicente and Vegas, 2009; De Vicente et al., 2007, 2011; Fernández-Lozano et al., 2011) may be playing an important role in the uplift and maintenance of the SCS.

Moreover, the implementation of a new rheological law related to behavior of dry olivine in lithospheric conditions (see Section 4) results in a lithospheric mantle significantly weaker, with a consequent reduction of its contribution to the total effective strength. In the TB, the lithospheric mantle has a large contribution to the strength and the effective elastic thickness of the lithosphere. Consequently the strength of the mantle top would be in clear contrast with that of the weaker lower crust. Otherwise, the lithospheric mantle under the SCS is significantly weaker, clear reflection of its thermal state.

One non-well determined factor is the pore pressure. For crustal rocks, a hydrostatic pore fluid factor (equal to a column of water of height z) is usually assumed. In the absence of information pertaining to high temperature regimes and greater depths, the pore fluid factor is usually taken uniform for the whole lithosphere (e.g., Afonso and Ranalli, 2004; Mahatsente et al., 2012; Tesauro et al., 2009). In this study, the pore pressure is assumed as 0.37 (see Section 4). Previous works have assumed a hydrostatic pore fluid factor for the study area, ranging from 0.36 to 0.4 (Ruiz et al., 2006; Tejero and Ruiz, 2002; Tesauro et al., 2009). This range leads to a variation of the total lithospheric strength over 1–4% depending on stress regimen. In addition, if an increase of the pore fluid factor to values of 0.6 and 0.8 is considered in order to simulate the presence of super-hydrostatic pressures, leads to a decrease of the total lithospheric strength over 15–25% and 40–50% depending on stress regimen, respectively. This pattern is similar to that observed by Tesauro et al. (2009). It must be noted that pore fluid pressure reduces brittle strength, and hence increases temperature at the BDT depth (Ruiz et al., 2011).

On the other hand, the ductile strength is largely strain rate dependent. As in previous works (e.g., Martín-Velázquez et al., 2008; Ruiz et al., 2006; Tejero and Ruiz, 2002), our strength envelopes are here calculated for a strain rate of 10^{-15} s^{-1}, but other authors consider a value of 10^{-16} s^{-1} as a characteristic strain rate value for intraplate Europe (Tesauro et al., 2007). Fig. 7 shows the effective elastic thickness calculated for the SCS and TB in terms of strain rate. If we considered a strain rate of 10^{-16} s^{-1}, the results are 12–22 km and 14–28 km, respectively for the SCS and the TB (depending on wet or dry rheology). Other of the main uncertainties could be due to not considering the effect of the horizontal regional stresses, which could have a strong effect on the T_e (Cloetingh and Burov, 1996).

Finally, future investigations should also consider other important influences on the rheological properties of major silicate rocks. For example, oxygen fugacity under anhydrous conditions (Keefner et al., 2011) or water fugacity under water-saturated conditions (Katayama and Karato, 2008) could significantly affect upper mantle rheology. This kind of consideration further will constrain the mechanical behavior of lithospheric materials, and their implications for the thermal and mechanical state of the lithosphere.

Acknowledgements

The authors would like to thank the Editor Randell Stephenson and two anonymous reviewers for their comprehensive revision and comments, which were of great help in the preparation of the final version of this paper. We also thank Giorgio Ranalli and Alfonso Muñoz Martín for their useful comments and suggestions that helped to improve the manuscript and Viazmelya Monroy for her assistance with the English language of this article. AJ-D was supported by a grant of the Complutense University of Madrid (Spain). JR was supported by a contract Ramón y Cajal cofinanced from the Ministerio de Ciencia e Innovación of Spain and the Fondo Social Europeo (ESF). This work was carried out in the projects CGL2008-03463, CGL2008-05952 and CGL2009-14405-C02-02 of the Ministerio de Ciencia e Innovación of Spain and the GR35/10-A-910492-UCM.

References

Afonso, J.C., Ranalli, G., 2004. Crustal and mantle strengths in continental lithosphere: is the jelly sandwich model obsolete? Tectonophysics 394, 221–232.

Banda, E., Suriñach, E., Aparicio, A., Sierra, J., Ruiz de la Parte, E., 1981. Crust and upper mantle structure of the central Iberian Meseta (Spain). Geophys. J. Int. 67, 779–789.

Boschi, L., Faccenna, C., Becker, T.W., 2010. Mantle structure and dynamic topography in the Mediterranean Basin. Geophys. Res. Lett. 37, L20303, doi:10.1029/2010GL045001.

Brace, W.F., Kohlstedt, D.L., 1980. Limits on lithospheric stress imposed by laboratory experiments. J. Geophys. Res. 94, 3967–3990.

Bürgmann, R., Dresen, G., 2008. Rheology of the lower crust and upper mantle: evidence from rock mechanics, geodesy, and filed observations. Annu. Rev. Earth Planet. Sci. 36, 531–567, doi:10.1146/annurev.earth.36.031207.124326.
Burov, E.B., Diament, M., 1995. The effective elastic thickness of (Te) continental lithosphere. What does it really means? J. Geophys. Res. 100 (B3), 3905–3927.
Burov, E.B., Watts, A.B., 2006. The long-term strength of continental lithosphere: jelly sandwich or crème brûlée? GSA Today 16 (1), 4–10.
Casas-Sainz, A.M., De Vicente, G., 2009. On the tectonic origin of Iberian topography. Tectonophysics 474, 214–235, doi:10.1016/j.tecto. 2009.01.030.
Chapman, D.S., Furlong, K.P., 1992. Thermal state of continental lower crust. In: Fountain, D.M., Arculus, R., Kay, R.W. (Eds.), Continental Lower Crust. Elsevier Science, Amsterdam, pp. 179–199.
Chopra, P.N., Paterson, M.S., 1984. The role of water in the deformation of dunite. J. Geophys. Res. 89, 7861–7876.
Cloetingh, S.E.B., Burov, E.B., 1996. Thermomechanical structure of European continental lithosphere: constraints from rheological profiles and EET estimates. Geophys. J. Int. 124, 695–723.
De Vicente, G., Cloetingh, S., Van Wees, J.-D., Cunha, P.P., 2011. Tectonic classification of Cenozoic Iberian foreland basins. Tectonophysics 502, 38–61.
De Vicente, G., Vegas, R., Muñoz-Martín, A., Van Wees, J.D., Casas-Sáinz, A., Sopeña, A., Sánchez-Moya, Y., Arche, A., López-Gómez, J., Olaiz, A., Fernández-Lozano, J., 2009. Oblique strain partitioning and transpression on an inverted rift The Castilian Branch of the Iberian Chain. Tectonophysics 470, 224–242.
De Vicente, G., Vegas, R., 2009. Large-scale distributed deformation controlled topography along the western Africa–Eurasia limit: tectonic constrains. Tectonophysics 474, 124–143.
De Vicente, G., Vegas, R., Muñoz Martín, A., González-Casado, J.M., Carbó, A., Álvarez, J., Cloetingh, S., Andriessen, P., Elorza, F.J., Olaiz, A., 2004. Estructura alpina del Antepaís Ibérico. Cadenas sin cobertera. El Sistema Central. In: Vera, J.A. (Ed.), Geología de España. SGE-IGME, Madrid, pp. 621–626.
De Vicente, G., Vegas, R., Muñoz Martín, A., Silva, P.G., Andriessen, P., Cloetingh, S., González Casado, J.M., Van Wees, J.D., Álvarez, J., Carbó, A., Olaiz, A., 2007. Cenozoic thick-skinned deformation and topography evolution of the Spanish Central System. Global Planet. Change 58, 335–338.
Faccenna, C., Becker, T.W., 2010. Shaping mobile belts by smallscale convection. Nature 465, 602–605, doi:10.1038/nature09064.
Fernàndez, M., Marzám, I., Correia, A., Ramalho, E., 1998. Heat flow, heat production, and lithospheric thermal regime in the Iberian Peninsula. Tectonophysics 291, 29–53.
Fernández-Lozano, J., Sokoutis, D., Willingshofer, E., Cloetingh, S., De Vicente, G., 2011. Cenozoic deformation of Iberia: a model for intraplate mountain building and basin development based on analogue modeling. Tectonics 30, TC1001, doi:10.1029/2010TC002719.
Furlong, K.P., Chapman, D.S., 1987. Crustal heterogeneities and the thermal structure of the continental crust. Geophys. Res. Lett. 14, 314–317.
Gómez-Ortiz, D., Tejero, R., Ruiz, J., Babín-Vich, R., González-Casado, J.M., 2005a. Estimating the effective elastic thickness of the Iberian Peninsula's lithosphere based on multitaper spectral analysis. Geophys. J. Int. 160, 729–735.
Gómez-Ortiz, D., Tejero-López, R., Babín-Vich, R., Rivas-Ponce, A., 2005b. Crustal density structure in the Spanish Central System derived from gravity data analysis (central Spain). Tectonophysics 403, 131–149, doi:10.1016/j.tecto.2005.04.006.
Hasterok, D., Chapman, D., 2007. Continental thermal isostasy. I: methods and sensitivity. J. Geophys. Res. 11, 2, doi:10.1029/2006JB004663.
Hasterok, D., Chapman, D., 2011. Heat production and geotherms for the continental lithosphere. Earth Planet. Sci. Lett., doi:10.1016/j.epsl.2011.04.034.
Hofmeister, A.M., 1999. Mantle values of thermal conductivity and the geotherm from phonon lifetimes. Science 283, 1699–1706.
IGME-ENRESA, 1998. Neotectonic Map of Spain Sc: 1/1.000.000 (J. Baena, Coord.). Madrid, Spain.
ILIHA DSS Group, 1993. A deep seismic sounding investigation of the lithospheric heterogeneity and anisotropy beneath the Iberian Peninsula. Tectonophysics 221, 35–51.
Katayama, I., Karato, S.-I., 2008. Low-temperature, high-stress deformation of olivine under water-saturated conditions. Phys. Earth Planet. Inter. 168, 125–133, doi:10.1016/j.pepi.2008.05.019.
Keefner, J.W., Mackwell, S.J., Kohlstedt, D.L., Heidelbach, F., 2011. Dependence of dislocation creep of dunite on oxygen fugacity: implications for viscosity variations in Earth's mantle. J. Geophys. Res. 116, B05201, doi:10.1029/2010JB007748.
Kohlstedt, D.L., Evans, B., Mackwell, S.J., 1995. Strength of the lithosphere: constraints imposed by laboratory experiments. J. Geophys. Res. 100, 17587–17602.
Lachenbruch, A.H., Morgan, P., 1990. Continental extension, magmatism and elevation; formal relations and rules of thumb. Tectonophysics 174, 39–62.
Mahatsente, R., Ranalli, G., Bolte, D., Götze, H.-J., 2012. On the relation between lithospheric strength and ridge push transmission in the Nazca plate. J. Geodyn. 53, 18–26, doi:10.1016/j.jog.2011.08.002.
Martín-Velázquez, S., De Vicente, G., Elorza, F.J., 2008. Resistencia, espesor elástico efectivo y deformación de la litosfera Ibérica (Sistema Central y cuencas del Duero y Tajo). Geo-Temas 10, 1523–1526.
Martín-Velázquez, S., De Vicente, G., Elorza, F.J., 2009. Intraplate stress state from finite element modelling: the southern border of the Spanish Central System. Tectonophysics 473, 417–427.
Marzán, I., Fernández, M., Cabal, J., 1996. Estudio geotérmico en la mitad Occidental de España. Geogaceta 20, 745–748.
McKenzie, D., Jackson, J., Priestley, K., 2005. Thermal structure of oceanic and continental lithosphere. Earth Planet. Sci. Lett. 233, 337–349.
McNutt, M.K., 1984. Lithospheric flexure and thermal anomalies. J. Geophys. Res. 89, 11180–11194.
Mei, S., Suzuki, A.M., Kohlstedt, D.L., Dixon, N.A., Durham, W.B., 2010. Experimental constraints on the strength of the lithospheric mantle. J. Geophys. Res. 115, B08204, doi:10.1029/2009JB006873.
Muñoz-Martín, A., De Vicente, G., Fernandez-Lozano, J., Cloetingh, S., Willingshofer, E., Sokoutis, D., Beekman, F., 2010. Spectral analysis of the gravity and elevation along the western Africa–Eurasia plate tectonic limit: continental versus oceanic lithospheric folding signals. Tectonophysics 495, 298–314, doi:10.1016/j.tecto.2010.09.036, ISSN 0040-1951.
Pérez-Gussinyé, M., Watts, A.B., 2005. The long-term strength of Europe and its implications for plate-forming processes. Nature 436, doi:10.1038/nature03854.
Ranalli, G., 1994. Nonlinear flexure and equivalent mechanical thickness of the lithosphere. Tectonophysics 240, 107–114.
Ranalli, G., 1997. Rheology of the lithosphere in space and time. Geol. Soc. Spec. Pub. 121, 19–37.
Ranalli, G., Murphy, D.C., 1987. Rheological stratification of the lithosphere. Tectonophysics 132, 281–295.
Rudnick, R.L., Gao, S., 2003. Composition of the continental crust. In: Rudnick, R.L. (Ed.), The Crust (In: Holland, H.D., Turekian, K.K.(Eds.), Vol. 3 Treatise of Geochemistry. Elsevier-Pergamon, Oxford, pp. 1–64.
Ruiz, J., Gómez-Ortiz, D., Tejero, R., 2006. Effective elastic thicknesses of the lithosphere in the Central Iberian Peninsula from heat flow: implications for the rheology of the continental lithospheric mantle. J. Geodyn. 41, 500–509.
Ruiz, J., McGovern, P.J., Jiménez-Díaz, A., López, V., Williams, J.-P., Hahn, B.C., Tejero, R., 2011. The thermal evolution of Mars as constrained by paleo-heat flows. Icarus 215, 508–517, doi:10.1016/j.icarus.2011.07.029.
Rybach, L., 1988. Determination of heat production rate. In: Haenel, R., Rybach, L., Stegena, L. (Eds.), Handbook of Terrestrian Heat-flow Density Determination. Kluwer, pp. 125–142.
San José, M.A., Pieren, A., García-Hidalgo, J.F., Vilas, L., Herranz, P., Peláez, J.R., Perejón, A., 1990. Ante-Ordovician Stratigraphy. Authocthonous sequences of Central-Iberian Zone. In: Dallmayer, R.D., Martínez-García, E. (Eds.), Pre-Mesozoic Geology of Iberia. Springer-Verlag, Berlín, pp. 145–159.
Sibson, R.H., 1974. Frictional constraints on thrust, wrench and normal faults. Nature 249, 542–544.
Sokoutis, D., Burg, J.P., Bonini, M., Corti, G., Cloetingh, S., 2005. Lithospheric-scale structures from the perspective of analogue continental collision. Tectonophysics 406, 1–15.
Stüwe, K., 2002. Geodynamics of the Lithosphere. An Introduction. Springer-Verlag, Berlin, p. 449.
Suriñach, E., Vegas, R., 1988. Lateral inhomogeneities of the Hercyninan crust in central Spain. Phys. Earth Planet. Inter. 51, 226–234.
Tejero, R., Ruiz, J., 2002. Thermal and mechanical structure of the central Iberian Peninsula lithosphere. Tectonophysics 350, 49–62.
Tesauro, M., Kaban, M.K., Cloetingh, S., 2009. A new thermal and rheological model of the European lithosphere. Tectonophysics 476, 478–495.
Tesauro, M., Kaban, M.K., Cloetingh, S., Hardebol, N.J., Beekman, F., 2007. 3D strength and gravity anomalies of the European lithosphere. Earth Planet. Sci. Lett. 263, 56–73.
Van Wees, J.D., Cloetingh, S., de Vicente, G., 1996. The role of pre-existing faults in basin evolution: constraints from 2D finite element and 3D flexure models. Geol. Soc. Spec. Pub. 99, 297–320.
Vilà, M., Fernández, M., Jiménez-Munt, I., 2010. Radiogenic heat production variability of some common lithological groups and its significance to lithospheric thermal modeling. Tectonophysics 490, 152–164, doi:10.1016/j.tecto.2010.05.003, ISSN: 0040-1951.
Villaseca, C., Barbero, L., Rogers, G., 1998. Crustal origin of Hercynian peraluminous granitic batholiths of Central Spain: petrological, geochemical and isotopic (Sr, Nd) constraints. Lithos 43, 55–79.
Villaseca, C., Downes, H., Pin, C., Barbero, L., 1999. Nature and composition of the lower continental crust in central Spain and the granulite–granite linkage: inferences from granulitic xenoliths. J. Petrol. 40, 1465–1496.
Villaseca, C., Orejana, D., Pérez-Soba, C., Reyes, J., 2005. Estimación del régimen térmico y producción de calor de los niveles litosféricos del Sistema Central Español. Geogaceta 38, 215–218.
Watts, A.B., Burov, E.B., 2003. Lithospheric strength and its relation to the elastic and seismogenetic layer thickness. Earth Planet. Sci. Lett. 213, 113–131.

Anexo II

Jiménez-Díaz, A., Ruiz, J., Pérez-Gussinyé, M., Kirby, J.F., Álvarez-Gómez, J.A., Tejero, R., Capote, R. Spatial variations of effective elastic thickness of the lithosphere in Central America and surrounding regions. *Earth and Planetary Science Letters* 391, 55-66, 2014.

Earth and Planetary Science Letters 391 (2014) 55–66

Contents lists available at ScienceDirect

Earth and Planetary Science Letters

www.elsevier.com/locate/epsl

Spatial variations of effective elastic thickness of the lithosphere in Central America and surrounding regions

Alberto Jiménez-Díaz [a,b,*], Javier Ruiz [a], Marta Pérez-Gussinyé [c], Jon F. Kirby [d], José A. Álvarez-Gómez [a], Rosa Tejero [a,b], Ramón Capote [a]

[a] Departamento de Geodinámica, Facultad de Ciencias Geológicas, Universidad Complutense de Madrid, 28040 Madrid, Spain
[b] Instituto de Geociencias, IGEO (CSIC, UCM), 28040 Madrid, Spain
[c] Department of Earth Sciences, Royal Holloway, University of London, Egham Hill, TW20 0EX Egham, United Kingdom
[d] Department of Spatial Sciences, Curtin University, GPO Box U1987, Perth WA 6845, Australia

ARTICLE INFO

Article history:
Received 4 August 2013
Received in revised form 22 January 2014
Accepted 26 January 2014
Available online 8 February 2014
Editor: Y. Ricard

Keywords:
effective elastic thickness
spectral methods
lithosphere structure
Central America
Caribbean plate

ABSTRACT

As a proxy for long-term lithospheric strength, the effective elastic thickness (T_e) can be used to understand the relationship between lithospheric rheology and geodynamic evolution of complex tectonic settings. Here we present, for the first time, high-resolution maps of spatial variations of T_e in Central America and surrounding regions from the analysis of the coherence between topography and Bouguer gravity anomaly using multitaper and wavelet methods. Regardless of the technical differences between the two methods, there is a good overall agreement in the spatial variations of T_e recovered from both methods. Although absolute T_e values can vary in both maps, the qualitative T_e structure and location of the main T_e gradients are very similar. The pattern of the T_e variations in Central America and surrounding regions agrees well with the tectonic provinces in the region, and it is closely related to major tectonic boundaries, where the Middle American and Lesser Antilles subduction zones are characterized by a band of high T_e on the downgoing slab seaward of the trenches. These high T_e values are related to internal loads (and in the case of the southernmost tip of the Lesser Antilles subduction zone also associated with a large amount of sediments) and should be interpreted with caution. Finally, there is a relatively good correlation, despite some uncertainties, between surface heat flow and our T_e results for the study area. These results suggest that although this area is geologically complex, the thermal state of the lithosphere has profound influence on its strength, such that T_e is strongly governed by thermal structure.

1. Introduction

The knowledge of lateral variations in lithosphere strength can aid in understanding how surface deformation relates to deep Earth processes. As a proxy for long-term lithospheric strength, the effective elastic thickness of the lithosphere (T_e) corresponds to the thickness of an idealized elastic plate bending under the same applied loads (Watts, 2001), and is related to the integrated mechanical strength of the lithosphere (Burov and Diament, 1995). The knowledge of T_e in different places provides a measurement of the spatial variation of the lithospheric strength, which is strongly controlled by local and regional conditions. Although T_e does not represent an actual depth to the base of the mechanical lithosphere, its spatial variations reflect relative lateral variations in lithospheric mechanical thickness (see McNutt, 1984). Thus it can be used to understand the relationship between lithospheric rheology and geodynamic evolution of complex tectonic settings.

T_e primarily depends on the thickness and structure of the crust, the composition of the crust and the lithospheric mantle, the degree of their coupling, the thermal state of the lithosphere, the state of stress, plate curvature, and the presence of melts, fluids and faults (e.g., Lowry and Smith, 1995; Burov and Diament, 1995; Lowry et al., 2000; Watts, 2001; Artemieva, 2011). The oceanic lithosphere generally behaves like a single mechanical layer due to the thin crust, which is usually coupled to the lithospheric mantle, and T_e is to first order controlled by the thermal age of the lithosphere at the time of loading (Watts, 2001; Kalnins and Watts, 2009). By contrast, the thermal state and rheological behavior of the lithosphere in continental areas are largely a consequence of local conditions (e.g., Ranalli, 1997; Afonso and Ranalli, 2004; Bürgmann and Dresen, 2008; Hasterok and Chapman, 2011; Mareschal and Jaupart, 2013), such that there is a complex relationship between T_e and its controlling parameters (Watts and Burov, 2003; Burov and Watts, 2006; Burov, 2011).

* Corresponding author at: Departamento de Geodinámica, Facultad de CC. Geológicas, Universidad Complutense de Madrid, c/ José Antonio Nováis, 2. 28040 Madrid, Spain. Tel.: +34 91 394 4821; fax: +34 91 394 4631.
E-mail address: ajimenezdiaz@geo.ucm.es (A. Jiménez-Díaz).

0012-821X/$ – see front matter
http://dx.doi.org/10.1016/j.epsl.2014.01.042

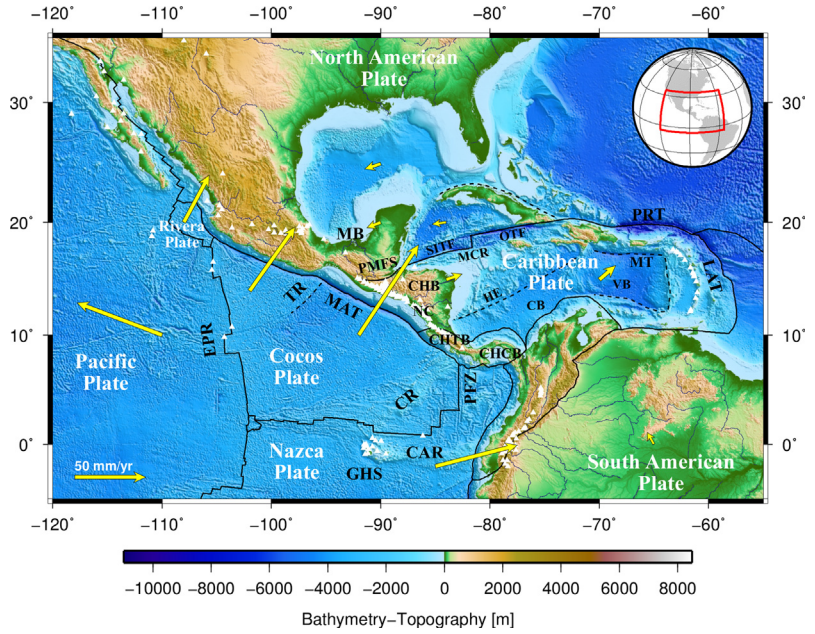

Fig. 1. Geotectonic setting of Central America and surrounding regions. Shaded relief image of bathymetry and topography is from ETOPO1 digital data (Amante and Eakins, 2009), and boundaries of lithospheric plates are based on the PB2002 model (Bird, 2003). Yellow arrows denote vectors of the plate motion from the MORVEL model (DeMets et al., 2010) with respect to the NNR reference frame as calculated at the given position with the Plate Motion Calculator (http://www.unavco.org/community_science/science-support/crustal_motion/dxdt/model.html). Triangles show the position of Holocene volcanoes (Siebert and Simkin, 2002). Abbreviations: CAR, Carnegie Ridge; CB, Colombian Basin; CHB, Chortis Block; CHCB, Chocó Block; CHTB, Chorotega Block; CR, Cocos Ridge; EPR, East Pacific Rise; GHS, Galápagos Hotspot; HE, Hess Escarpment; LAT, Lesser Antilles Trench; MAT, Middle America Trench; MB, Maya Block; MCR, Mid-Cayman Rise; MT, Muertos Trough; ND, Nicaraguan Depression; OTF, Oriente Transform Fault; PFZ, Panamá Fracture Zone; PMFS, Polochic–Motagua Fault System; PRT, Puerto Rico Trench; SITF, Swan Island Transform Fault; TR, Tehuantepec Ridge; VB, Venezuelan Basin. (For interpretation of the references to color in this figure legend, the reader is referred to the web version of this article.)

In this study we present, for the first time, high-resolution maps of spatial variations of T_e in Central America and surrounding regions from the analysis of the Bouguer coherence using both multitaper and wavelet methods. The Central America–Caribbean region is characterized by the interaction of six lithospheric plates (Fig. 1). The Caribbean plate moves eastward relative to its two neighboring plates, North and South America plates (DeMets et al., 2010), and its perimeter is characterized by a high variability and complexity of geodynamic and tectonic processes (e.g., Sykes et al., 1982; Ross and Scotese, 1988). Therefore, this area represents a good natural laboratory to study the spatial variations of T_e, test the response of spectral methods to different factors and geodynamic conditions, and examine relationships between surface deformation, lithospheric structure and mantle dynamics.

In the following sections we first introduce the methodology and data employed for estimating T_e. We then present our results and compare them to previous estimates of T_e in the study area. Finally, we examine the relationships between T_e with other proxies for lithospheric and sub-lithospheric structure to improve our knowledge of the long-term rheology and mechanical behavior of the lithosphere in the study area. We also discuss how the lithospheric structure derived from our T_e analysis relates to surface deformation.

2. T_e estimation by spectral methods

To estimate the effective elastic thickness we calculate the coherence function relating the topography and Bouguer anomaly, commonly known as Bouguer coherence, using multitaper and wavelet methods. This function gives information on the wavelength band over which topography and Bouguer anomaly are correlated. In the coherence deconvolution method of Forsyth (1985), T_e is estimated by comparing the observed coherence curve with coherence functions predicted for a range of T_e values. For each given T_e, we calculate via deconvolution the initial surface and subsurface loads and compensating deflections that generate a predicted topography and gravity that best fit the observed topography and gravity anomaly, and a predicted coherence that best fits the observed coherence (Forsyth, 1985). The T_e value that minimizes the differences between the predicted and observed quantities is the optimal one for the analyzed area. The Bouguer coherence generally tends to zero at short wavelengths, where the topography is not compensated and loads are supported predominantly by the elastic strength of the lithosphere (Forsyth, 1985). At long wavelengths, the response to loading approaches the Airy limit and the coherence tends to one. The wavelengths at which the coherence rapidly increases from 0 to 1 depend on the effective elastic thickness of the lithosphere, such that when the lithosphere is weak and T_e is small, local compensation for loading occurs at relatively shorter wavelengths and vice versa.

In this section we describe briefly the methodology and data employed to estimate T_e. For an extensive description of the methods, choice of parameters and biases in T_e estimation, see Supplementary Material associated with the online version of this article.

2.1. Multitaper method

To recover spatial variations in T_e we divide the analysis area into overlapping windows, such that in each window the coherence is calculated and inverted assuming a spatially constant T_e, moving the centre of each window 50 km for each new estimate. Calculation of the observed and predicted coherence involves transformation into the Fourier domain of the topography and Bouguer gravity anomaly to estimate their auto- and cross-power spectra. Because both data sets are non-periodic and finite, the Fourier transformation presents problems of frequency leakage (Thomson, 1982; Simons et al., 2000), resulting in estimated spectra that differ from the true spectra. To reduce leakage, the data are first multiplied by a set of orthogonal tapers in the space domain, the Fourier transform of the data-taper product taken for

each taper, and the power spectrum determined at each taper. The final estimate of the signal's true power spectrum is then the weighted average of the individual power spectra over all tapers. However, the choice of taper influences the resulting power spectra and hence the coherence function (Pérez-Gussinyé et al. 2007, 2008). The set of orthogonal tapers is defined by the bandwidth product NW that controls the wavelength resolution and spectral leakage (where N is the number of samples within the data window and W is the half bandwidth of the central lobe of the power spectral density of the first-order taper) and by the number of tapers K that governs the estimation variance (see Simons et al., 2000). The choice of bandwidth parameter NW in the multitaper technique is important. As the bandwidth increases, the resolution (i.e. the minimum separation in wave number between approximately uncorrelated spectral estimates) decreases (Walden et al., 1995). For a given bandwidth, W, there are up to $K = 2NW - 1$ tapers with good leakage properties (Percival and Walden, 1993). The variance of the spectral estimates decreases with the number of tapers as $1/K$, so the bandwidth and resolution are chosen depending on the individual function under analysis (Percival and Walden, 1993). In this study we apply the multitaper method using $NW = 3$ and $K = 3$, which are also used in several recent studies for T_e estimation (see e.g. Daly et al., 2004; Audet et al., 2007; Pérez-Gussinyé et al., 2009a; Kirby and Swain, 2011).

The effect of calculating T_e within a finite-size window is to limit the maximum wavelength of the gravity and topography that can be recovered. The choice of window size is critical in the multitaper estimation of T_e because it compromises the trade-off between resolution and variance of the estimates (Pérez-Gussinyé et al., 2004; Audet et al., 2007), such that large windows are better able to retrieve high T_e but degrade the spatial resolution and potentially merge tectonic provinces, while small windows provide high spatial resolution and analyze perhaps just one province but cannot resolve long flexural wavelengths. As the resulting T_e estimate depends on window size, we use three different window sizes (400×400 km, 600×600 km and 800×800 km, respectively) to obtain high spatial resolution and at the same time recover potentially high T_e. Finally, the T_e results estimated from three different window sizes are merged to obtain the final T_e map. This is done by calculating a weighted average of the T_e estimated from each of the three windows following the approach of Pérez-Gussinyé et al. (2009b). This approach combines the information content regarding abrupt T_e gradients recovered by small windows and the more reliable information on high T_e recovered by the larger windows.

2.2. Wavelet method

The wavelet method convolves a range of scaled wavelets with the whole data set to map and invert the coherence at each grid point, and achieves good wavenumber resolution over long length scales and good spatial resolution over short length scales. Here we employ a Morlet wavelet of high spatial resolution in the fan wavelet transform (Kirby and Swain, 2011). The value of the central wavenumber of the Morlet wavelet, denoted by $|\mathbf{k}_0|$, governs the resolution of the wavelet in the space and wavenumber domains. Larger values of $|\mathbf{k}_0|$ give better wavenumber resolution but poorer spatial resolution, and vice versa for smaller values (Addison, 2002). The choice of the value of $|\mathbf{k}_0|$, described in Kirby and Swain (2011), is governed by the amplitude of the first sidelobes of the simple wavelet. If this amplitude is a fraction $1/p$ ($p > 1$) of the amplitude of the central peak of the real part of the space-domain wavelet, then $|\mathbf{k}_0| = \pi\sqrt{2/\ln p}$. The $|\mathbf{k}_0|$ value used in this study is 2.668, which give a space-domain wavelet whose first sidelobes is 1/16 of the magnitude of the central amplitude (Kirby and Swain, 2011).

Table 1
Symbols and values of constants.

Constant	Symbol	Value	Units
Young's modulus	E	100	GPa
Poisson's ratio	υ	0.25	
Newtonian gravitational constant	G	6.67259×10^{-11}	$m^3\,kg^{-1}\,s^{-2}$
Gravity acceleration	g	9.79	$m\,s^{-2}$
Seawater density	ρ_w	1030	$kg\,m^{-3}$
Crust density	ρ_c	2670	$kg\,m^{-3}$
Mantle density	ρ_m	3300	$kg\,m^{-3}$

To recover T_e, the Bouguer gravity anomaly and topography are mirrored about their edges prior to Fourier transformation, which, when used with the wavelet transform does not generally bias the results significantly, as it can with the periodogram method (Kirby and Swain, 2008). The wavelet transform is then applied to both datasets to calculate the auto and cross-spectra at different azimuths and scales. We follow Kirby and Swain (2009) and invert the square of the real part of the wavelet coherency (SRC), rather than the coherence, because it is less sensitive to correlations between the initial loads on the plate and to "gravitational noise", both of which can cause incorrect recovery of T_e (Kirby and Swain 2009, 2011).

2.3. Regional topography, gravity and crustal structure

The elevation data used in our analysis are obtained from the ETOPO1 digital elevation model, a 1 arc-minute global relief model of Earth's surface that integrates land topography and ocean bathymetry (Amante and Eakins, 2009). Our area contains both continental and oceanic lithosphere, with the latter being subject to an additional water load. To treat mixed land and marine environments, we adopt the approach of Stark et al. (2003) and Kirby and Swain (2008). This approach scales ocean bathymetry (h) to an equivalent topography $[h' = (\rho_c - \rho_w)h/\rho_c]$ prior to Fourier transformation, with subsequent application of the land loading deconvolution equations to the entire data set. Kirby and Swain (2008) showed that although this approach may bias T_e in ocean areas, the bias is small. Values of the densities are given in Table 1. The equivalent topography represents the bathymetry that would be expected if there were no water present (provided Airy isostasy operates). This allows the loading equations for a land environment to be used for the whole area, rather than performing two separate analyses and inversions on land and ocean areas (Pérez-Gussinyé et al., 2004).

The regional free-air gravity anomaly data are taken from the V18 Global Gravity Anomaly model of Sandwell and Smith (2009), on a $1' \times 1'$ grid over both land and ocean. The Bouguer gravity anomaly has been calculated applying the complete Bouguer correction at regional scales to free-air data using the FA2BOUG code (Fullea et al., 2008). We calculated terrain corrections using the ETOPO1 digital elevation model (see above), with a reduction density of 2670 $kg\,m^{-3}$. The Bouguer gravity anomaly of the study area obtained following this procedure is shown in Fig. 2.

The deconvolution requires detailed information on the internal structure of the crust and uppermost mantle. To define the internal density profile and lateral variation of the different interfaces, we use the global crustal model CRUST2.0 (Laske and Masters, 1997; Bassin et al., 2000; Laske et al., 2000). CRUST2.0 includes three crustal and two sediment layers, whose 7th layer describes the Moho depth. Forsyth's (1985) original formulation of the predicted coherence assumes that all internal density variations and loading occurs at the Moho. In this study we assumed that internal loading occurs at the interface between upper and mid-crust. Since the observed coherence can be reproduced equally well by either low T_e and shallow loading or a larger T_e and deeper loading, there

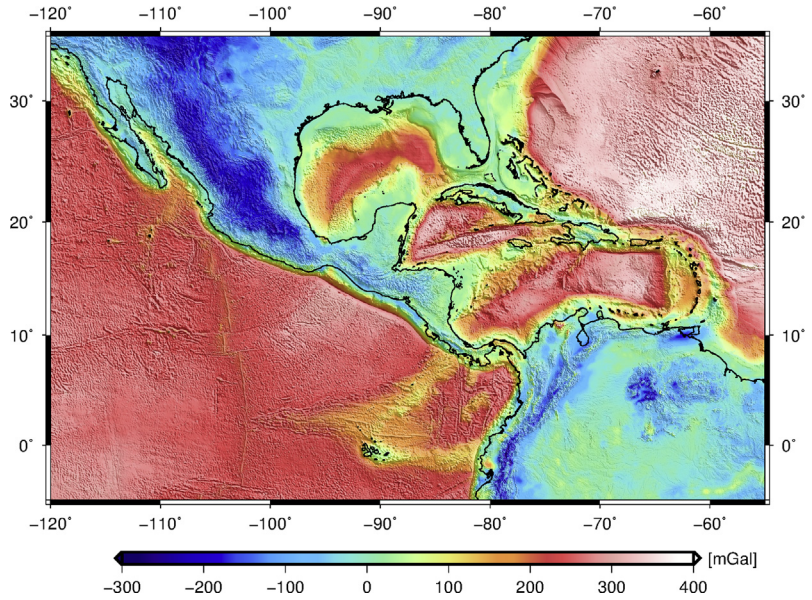

Fig. 2. Bouguer gravity anomaly used for the analysis. Topography shaded relief superimposed.

is a trade-off between T_e and assumed depth of loading. However, Pérez-Gussinyé and Watts (2005) tested the sensitivity of T_e to loading depth in Europe and found that changing the loading depth from the mid-crust to Moho changed T_e by ∼5 km, but the general patterns of variations remained the same (Pérez-Gussinyé and Watts, 2005; Pérez-Gussinyé et al., 2007). Other constants are given in Table 1.

We project all data sets to a Cartesian coordinate system using the Mercator projection to mitigate errors arising from the planar treatment of curvilinear coordinates. The data cover a much larger area than the study area to mitigate boundary effects.

3. Results

3.1. Spatial variations of T_e

The effective elastic thickness obtained from the multitaper and wavelet methods are shown in Fig. 3. Fig. 3a shows the final T_e from multitaper method after merging results from three different window sizes. Fig. 3b shows T_e estimated from the wavelet method with $|\mathbf{k}_0| = 2.668$. In the following, we present our results and describe only those T_e variations present in the results obtained with both multitaper and wavelet methods.

The pattern of T_e variations in Central America and surrounding regions agrees well with the tectonic provinces in the area, and it is closely related to major tectonic boundaries (Fig. 3). The stable platforms of the North and South American plates have relatively high values. Otherwise, both methods give low values over the southern Cordillera and Baja California areas of North America. A steep T_e gradient separates this region from the southerly regions of the Interior Platform, which are characterized by intermediate to high T_e values (50–100 km). To the east, T_e decreases smoothly towards the Atlantic plain. Over northern South America, we also recover a high T_e within the stable platform. Both methods give very large values (>90 km) over the northern part of the Amazonia craton, where a linear SW–NE trending of much lower T_e values characterize the eastern part of the Guyana Shield within the rigid cratonic interior. Northward along the Northern Andes there is an increase of T_e to intermediate values at the junction with the boundary between the South American and Caribbean plates.

The northern part of the Maya block shows a linear SW–NE trend of intermediate to high T_e values. The Trans-Mexican Volcanic Belt is characterized by very low T_e values, which are bounded to the south by a narrower band of relatively higher T_e. The Maya–Chortis and Chortis–Chorotega active boundaries (i.e., the Polochic–Motagua Fault System and Santa Elena shear zone, respectively) show steep gradients with lower T_e values than the surrounding regions, such that the interaction between these blocks has reduced the strength of the lithosphere near their boundaries. Our results also show a linear NW–SE trending zone of low T_e associated with the Central American volcanic arc, probably associated with high heat flow related to magma transport along the arc (see below). Within the Chortis block, which shows low T_e values, there are two areas of relatively high T_e that coincide with the Nicaraguan depression and the eastern passive margin of this block.

Low to intermediate T_e values characterize the Eastern Pacific Ocean, where both methods give extremely low values (<5 km) along region under intensive extension and volcanism, e.g., the East Pacific Rise, around the Galapagos hotspot, Cocos Ridge, Carnegie Ridge and the Cocos–Nazca spreading center, as well as the Cayman spreading center in the Caribbean Sea. The Eastern Pacific also shows contrasting patches of high and low T_e. The Middle American subduction zone is characterized by a narrower band of high T_e on the downgoing slab, greater than 30 km, over the outer rise seaward of the trench. These T_e values decrease sharply under the Middle American Trench (MAT) offshore of Central America. In this zone, the Tehuantepec Ridge (TR) represents a major limit which separates the oceanic lithosphere into two distinct tectonic regions with a maximum T_e offset of ∼30 km, such that seaward of the trench show higher T_e values in the northwest of the TR than to the southeast of the TR.

Over the Gulf of Mexico there is a linear SW–NE trend of intermediate to high T_e values (20–40 km) associated with old oceanic crust (seafloor ages of ∼160–120 Myr; Müller et al., 2008) which outcrops in this area. Moreover, most of the Caribbean oceanic domain seems to be uniformly weak. In addition, several patches of intermediate to high T_e are also visible in the Colombian and Venezuelan basins. Westward, the Cocos–Nazca slab window beneath southeastern Costa Rica and northwestern Panamá is characterized by extremely low T_e (<4 km). Finally, T_e increases to

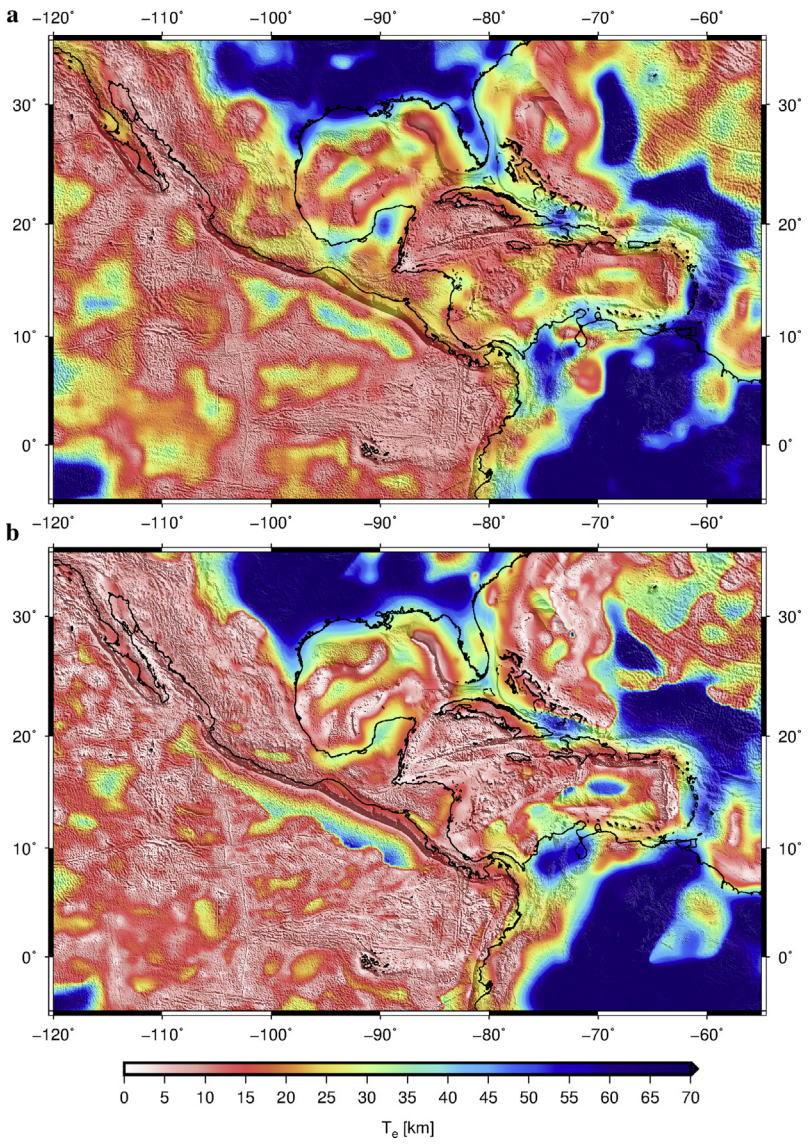

Fig. 3. Effective elastic thickness, T_e, over Central America and surrounding regions from: (a) multitaper method, and (b) wavelet method. In both images, topography shaded relief is superimposed. (a) shows final T_e after merging the results from the three different window sizes (see Section 2 and Supp. Fig. 1). The final T_e structure retains the primary characteristics of the largest window, but it better resolves the sharp gradient between low and high T_e areas and the short wavelength variations in T_e. (b) shows T_e estimated from the wavelet method with $|\mathbf{k}_0| = 2.668$.

high values clearly delineated along the transform plate boundary between the South American and Caribbean plates and Lesser Antilles Trench, which connect northward with the high T_e values in the Puerto Rico Trench, western North Atlantic margin and the Bermuda Rise region.

Regardless of the technical differences between the two methods, there is a good overall agreement in the relative spatial variations of T_e recovered from both techniques. Although absolute T_e values can vary in both maps, the qualitative T_e structure and location of the main T_e gradients are very similar. The greater discrepancies between both methods are local spatial variations of T_e in the stable platforms of the North and South American plates. Other differences are observed in T_e values recovered along the plate boundary between the South American and Caribbean plates, northward of the Lesser Antilles Trench and Bermuda Rise region. Since this study focuses on spatial variations of T_e and its geodynamic implications for Central America and surrounding regions, we do not discuss here the differences in absolute values between both maps produced by the methods, and the interested reader can find a more thorough comparison between the wavelet and multitaper methods in, for example, Daly et al. (2004), Audet et al. (2007), Pérez-Gussinyé et al. (2007, 2009a), and Kirby and Swain (2011).

As mentioned above, there are several 'key' parameters used in the analysis that lead to small (but perhaps significant) changes in resolution and accuracy of the results from both methods. Here we follow the approach of Pérez-Gussinyé et al. (2009b) and Kirby and Swain (2011) to obtain high spatial resolution and at the same time recover potentially high T_e from both methods. We have included an extensive description of the choice of parameters and its influence on the results, as well as the biases in T_e estimation, in the Supplementary Material. It should also be noted that "gravitational noise" (McKenzie and Fairhead, 1997; McKenzie, 2003; Kirby and Swain, 2009) does exist in the study area, which casts doubt upon T_e values in some regions, especially where we have recovered very high values; we will return to this issue in the Discussion.

3.2. Comparison with previous T_e estimates

Direct comparison of T_e values and its variations is possible between our results and the previous study of T_e from the multitaper method by Lowry and Pérez-Gussinyé (2011) for the western United States, and with T_e computed by Tassara et al. (2007) and Kirby and Swain (2011) for northern South America using $|\mathbf{k}_0| = 2.668$ and $|\mathbf{k}_0| = 5.336$ wavelets (Supp. Fig. 6 shows our results obtained from wavelet method with $|\mathbf{k}_0| = 5.336$). Our results are consistent with these and other previous regional studies of North America (Kirby and Swain, 2009), and South America (Pérez-Gussinyé et al. 2007, 2008, 2009a). This consistency indicates the viability of our results over Central America and surrounding regions.

Regarding the Central America region, there are numerous studies of oceanic T_e performed for given places (for a compilation see Watts, 2001). For the Middle America Trench, Caldwell and Turcotte (1979) estimated a T_e of 18.6 ± 2.2 km for seafloor age of 32.5 ± 2.5 Myr. Meanwhile, McNutt (1984) obtained a T_e of 17.5 ± 2.5 km for 20 ± 5 Myr, McAdoo and Martin (1984) a T_e of 29.7 ± 2.2 km for 20 ± 5 Myr, and Levitt and Sandwell (1995) a T_e of 27.3 ± 10 km for 19.9 ± 8 Myr. Feighner and Richards (1994) studied the Galápagos region using a variety of compensation models, obtaining a T_e of 12 ± 2 km and 3 ± 3 km for 7.5 ± 1 Myr. McAdoo et al. (1985) obtained a T_e of 31.7 ± 5.2 km for 80 ± 5 Myr over the Puerto Rico Trench, and Levitt and Sandwell (1995) a T_e of 40.7 ± 5 km for 101.6 ± 12 Myr over the Antilles Trench. Furthermore, in their study Manea et al. (2005) estimated T_e of the oceanic lithosphere beneath Tehuantepec Ridge by means of an admittance analysis of a set of profiles across this structure. These authors obtained a T_e of ~5–10 km in the NW area of the TR, while in the SE area T_e is of ~10–15 km. As mentioned above, we recover a complex pattern of T_e associated with the TR, with a maximum offset of ~30 km.

Finally, our results are in a good agreement with previous global studies as in e.g., Watts et al. (2006), who obtained T_e estimates from a wide range of submarine volcanic features in the East Pacific Ocean. Recently, Kalnins (2011) produced a global map of elastic thickness in the world's oceans, and recovered T_e at major constructional volcanic features in our study area, as the Bermuda Rise (T_e of 15–21 km), Carnegie Ridge (3–4 km), Cocos Ridge (3–4 km), Galapagos Islands (3–4 km) or Nazca Ridge (4–5 km). Furthermore, our results are also in a good agreement with the worldwide T_e map obtained by Audet and Bürgmann (2011) from the Bouguer coherence using the continuous wavelet transform, and with T_e results of Tesauro et al. (2012) from a rheological approach based on the lithospheric strength distribution, although our results have higher resolution due to the regional nature of the present work.

4. Discussion

4.1. T_e, surface heat flow and thermal age

Due to the dependence of lithosphere strength on temperature, T_e should show an inverse correlation with heat flow (McNutt, 1984; Lowry and Smith, 1995): higher surface heat flow implies higher lithospheric temperatures and hence lower lithospheric strength. Several studies examining the dependence of the strength of the lithosphere on the temperature structure (e.g., Watts and Burov, 2003; Afonso and Ranalli, 2004; Burov and Watts, 2006), found that there is not a simple relation between T_e and surface heat flow for continental areas, due to local differences in crustal structure and composition (which implies differences in radioactive heat production and thermal and rheological properties of the rocks) and lithosphere flexure (which affects the vertical distribution of elastic stresses). Otherwise, the situation is relatively simpler for oceanic areas, because oceanic crust is thinner and comparatively devoid of radioactive elements, implying that the strength of the lithosphere is mostly controlled by the cooling history (i.e., thermal age) of the oceanic lithosphere, although flexural effects can be important.

Fig. 4a shows the regional surface heat flow in the study area from the updated global heat flow database of the International Heat Flow Commission (Hasterok, 2010). Despite some uncertainties, there is a relatively good (inverse) correlation between surface heat flow and T_e values in Central America and surrounding regions. Low T_e values observed in the southern Cordillera and Baja California are associated with relatively high heat flow. Similarly, high T_e values recovered for southern regions of the Interior Platform match the observed low heat flow (Fig. 3 and Fig. 4a). By contrast, there are extensive areas with no measurements, e.g., the northern South America. Pérez-Gussinyé et al. (2007, 2008) examined the relationship of T_e to heat flow in South America, concluding that both parameters correlate well. Our relatively high T_e values observed in the northern part of the Maya block and in the southern boundary of the Trans-Mexican Volcanic Belt are well correlated with the low surface heat flow of these areas. The Trans-Mexican Volcanic Belt is characterized by intermediate to high heat flow and low T_e values. The southern Maya block and northwestern Chortis block, including the northwestern Central American volcanic arc, are also characterized by high surface heat flow and low T_e values. By contrast, the southeastern part of the Central American volcanic arc and Chorotega block are characterized by low heat flow and low T_e values (Fig. 3 and Fig. 4a), such that it's possible that due to the narrow width of the Central American land bridge in this area, the T_e recovered over the continent is very influenced by the low T_e values of the surrounding oceanic regions.

As illustrated in Fig. 4a, high heat flow is observed in the Eastern Pacific Ocean in regions under intensive extension and volcanism, e.g. the East Pacific Rise, around the Galapagos hotspot, Cocos Ridge, Carnegie Ridge and the Cocos–Nazca spreading center, as well as over the Cayman spreading center in the Caribbean Sea. This first-order pattern of surface heat flow variation is in accord with our low T_e estimates for these areas (Fig. 3). However, a low heat flow is observed within the Cocos plate where there is not a clear correlation with the T_e signature associated to the Middle American subduction zone (see below). The western Caribbean region shows moderate surface heat flow, where the Cocos–Nazca slab window beneath Central America, characterized by extremely low T_e, does not show a high surface heat flow. Meanwhile the eastern Caribbean region is characterized by lower values, with several contrasting patches of high surface heat flow as in the central part of the Hess Escarpment or over the Aves Ridge associated with the Lesser Antilles.

It is commonly accepted that T_e reflects a fossil lithospheric equilibrium developed at the time of loading (for a review see Artemieva, 2011). If loading occurs when the lithosphere is weak and no mass redistribution occurs afterwards, there is no need for stress to re-equilibrate, and isostatic analyses might yield a low T_e estimate even after subsequent cooling and strengthening of the lithosphere, as is the case for oceanic lithosphere (Pérez-Gussinyé et al., 2009b). Fig. 4b shows the age–area distribution of the ocean floor from Müller et al. (2008) in the study area. If we compare our T_e results with the age of the ocean crust in the study area (Fig. 4c), a direct relationship between them is not evident. This is consistent with the scatter observed in previous works on other oceanic regions (e.g., Tassara et al., 2007; Kalnins and Watts, 2009). Watts (2001) notes that the load age, which is not necessarily the same of the crust age, would explain much of this scatter. Other contributing sources could be

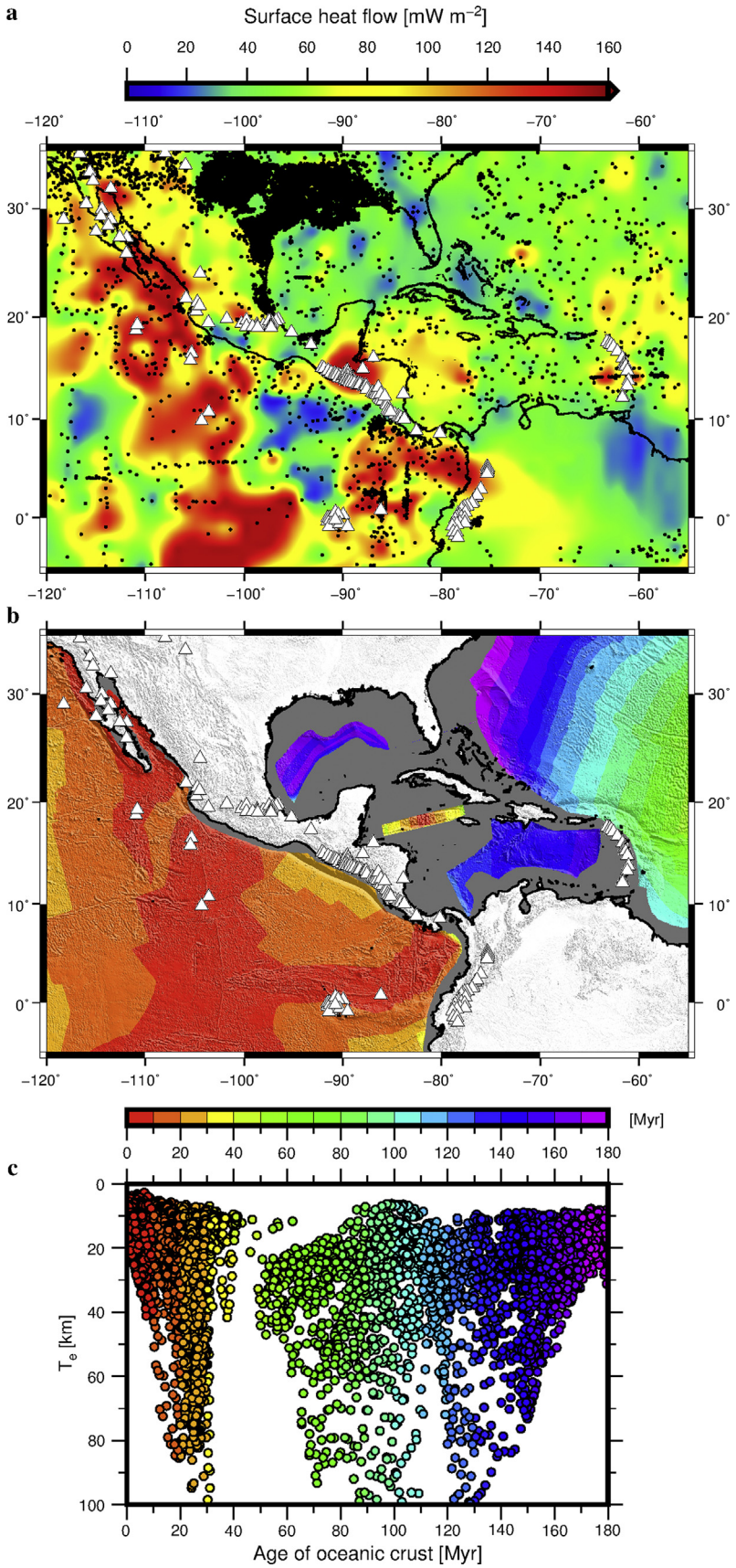

Fig. 4. (a) Regional surface heat flow from the updated global heat flow database of the International Heat Flow Commission (Hasterok, 2010). Black circles indicate measurement sites. White triangles show the position of Holocene volcanoes (Siebert and Simkin, 2002). (b) Age–area distribution of ocean floor from Müller et al. (2008). (c) Effective elastic thickness, T_e, from the multitaper method versus age of the oceanic crust (Müller et al., 2008).

uncertainties in load, infill and mantle densities, thermal perturbations due to hot and cold spots (e.g., Tassara et al., 2007), viscoelastic stress relaxation (Watts and Zhong, 2000), yielding in regions of large loads and high curvature (McNutt and Menard, 1982), or spatial variations in the controlling isotherms that determine T_e (Kalnins and Watts, 2009).

Otherwise, as stated above, the thermal state and rheological behavior of the lithosphere in continental areas are largely a consequence of local conditions, such that there is a complex relationship between T_e and the age of the continental lithosphere. Surface processes of erosion and deposition constantly redistribute continental surface mass loads. In any case, the high T_e values recovered here for the stable platforms of the North and South American plates (see Fig. 3) are consistent with previous studies for these regions (Tassara et al., 2007; Pérez-Gussinyé et al. 2007, 2009a; Kirby and Swain 2009, 2011).

4.2. Loading of the lithosphere

A fundamental assumption of the load deconvolution method developed by Forsyth (1985) is that surface and subsurface loads are statistically uncorrelated. In many cases, however, surface and subsurface loading are likely to be tectonically related processes and, therefore, spatially correlated (Forsyth, 1985). Subsurface loads include mafic intrusions, accreted lower crustal material, thermal anomalies and compositional variations, which cause lateral variations of density at depth and may have a strong influence on T_e estimates (Stark et al., 2003). Meanwhile, surface loading is caused by topography and large-scale variations in surface density (e.g., mountains and sedimentary basin). Macario et al. (1995) showed that when the degree of correlation of initial surface and subsurface loading increases, the T_e values estimated using Forsyth's (1985) deconvolution method can be biased downward. Furthermore, erosion and sedimentation may play an important role in modifying the relationship between surface topography and subsurface density anomalies (e.g., Forsyth, 1985; McKenzie and Fairhead, 1997). Both processes can reduce the landscape to a perfectly flat surface, removing the topographic expression of subsurface loads. The presence of topographically unexpressed internal loading, known as "noise" or "gravitational noise" (McKenzie and Fairhead, 1997; McKenzie, 2003; Kirby and Swain, 2009), biases the T_e upward. As pointed out by Kirby and Swain (2009), this problem can occur in regions of subdued topography, and predominantly affects areas where the coherence method indicates high T_e (see Suppl. Fig. 7).

The load deconvolution wavelet method can also estimate the ratio between the initial internal and surface load amplitudes (the loading ratio, f; Forsyth, 1985). We can display the loading ratio results in terms of the F parameter, the internal load fraction (McKenzie, 2003), where purely surface loading gives $F = 0$, purely internal loading gives $F = 1$, while equal surface and internal loading gives $F = 0.5$ (see Supplementary Material for an extended explanation). Fig. 5a shows best fitting F values corresponding to the T_e recovered from the wavelet method (Fig. 3b). For North America, our results are consistent with Kirby and Swain's (2009) F results, which show that subsurface loading has dominated continental tectonics, or at least been equal in magnitude to surface loading, in North America. Our results are also consistent with the pattern of the flexural loading ratio, f_F, obtained by Tassara et al. (2007) in northern South America, which suggest that below the north–eastern limit of the Amazonia craton there are strong lateral variations in density not compensated by surface topography. Subsurface loading dominates along the East Pacific Rise, around the Galapagos hotspot, Cocos Ridge, Carnegie Ridge and the Cocos–Nazca spreading center (Fig. 5a). In this zone, the Tehuantepec Ridge represents, again, a major limit which separates the oceanic lithosphere into two distinct load regions, such that the northwest TR is dominated by surface loading while the southeast TR is dominated by internal loads. The Caribbean region is characterized by all range of F values. Higher F values are observed over the eastern Cayman spreading center, the Caribbean Large Igneous Province, the Cocos–Nazca slab window beneath Central America, the Aves Ridge, and along the Lesser Antilles Trench and east North American margin.

Fig. 5b shows seafloor sediment thickness (Divins, 2003; Whittaker et al., 2013) in the study area. Large amount of sediments are located on the Gulf of Mexico basin, along of the western North Atlantic margin, the Colombian, Venezuelan and Grenada basins, and on the Barbados Accretionary Complex associated to the Lesser Antilles. In many cases sediment thickness exceeds 10 km. However, most of the Caribbean lithosphere, where both methods recovered low T_e values (see Fig. 3), seems to be uniformly weak, suggesting that the effect of the sediments on T_e estimates is very small. The continental shelf of the Gulf of Mexico, which shows a smooth surface, is characterized by moderate to high T_e values (between 40 and 50 km; see Fig. 3) and low F values, with surface loads dominating. Seaward, high T_e values are recovered for the Mississippi delta system (Fig. 3). Southwestward in the Gulf of Mexico, over the old oceanic crust which outcrops in this area, both methods recover a linear SW–NE trending of intermediate to high T_e values associated with a high F value. The Venezuelan basin also shows high T_e values associated with a subsurface loading domain, possibly related to the oceanic basement underneath the Caribbean Large Igneous Province. Müller et al. (2008) found prominent negative residual basement depth anomalies (in a range between 750 and 1500 m) associated with the Gulf of Mexico, northeast of Venezuela, and off the east coast of North America, which may be related to subducted slab material descending in the mantle or to asthenospheric flow. In the case of the Colombian basin, the presence of sediments on the continental shelf may play a major role on the estimation of T_e (~40 km; Fig. 3 and Fig. 5b). Interestingly, the presently active Nicaraguan depression, which experienced significant extension in the Cenozoic, shows intermediate T_e values (~25 km) and a F value of 0.5, such that it is possible that in this case T_e values are overestimated due to the effect associated with its sediment fill (see Suppl. Fig. 7).

4.3. The Middle American and Lesser Antilles subduction zones

The results over the Middle American and Lesser Antilles subduction zones should be interpreted with caution. As exposed in the Results Section, the Middle American subduction zone is characterized by a narrower band of high T_e on the downgoing slab seaward of the trench (Fig. 3). These T_e values decrease sharply under the MAT offshore of Central America, indicating a substantial degree of weakening within the downgoing plate due to the flexure of the lithosphere (see McNutt and Menard, 1982; Judge and McNutt, 1991; Billen and Gurnis, 2005; Contreras-Reyes and Osses, 2010). In fact, the bathymetry of the MAT offshore of Central America shows a complex response of the crust to the subduction process, with widespread outer-rise normal faulting subparallel to the trench axis due to the plate bending, increasing in number and offset where the bending is more pronounced (Ranero et al. 2003, 2005; Harders et al., 2011; Manea et al., 2013). This high T_e signature is very evident (broader and even exceeding 50 km at the Lesser Antilles Trench; see Fig. 3), and can also be observed in other subduction zones, as e.g. along the Peru–Chile Trench (Tassara et al., 2007; Pérez-Gussinyé et al., 2009a; Kirby and Swain, 2011), or over the Japan, Izu–Bonin, and Mariana trenches and at the northernmost tip of the Tonga–Kermadec trench (Kalnins and Watts, 2009).

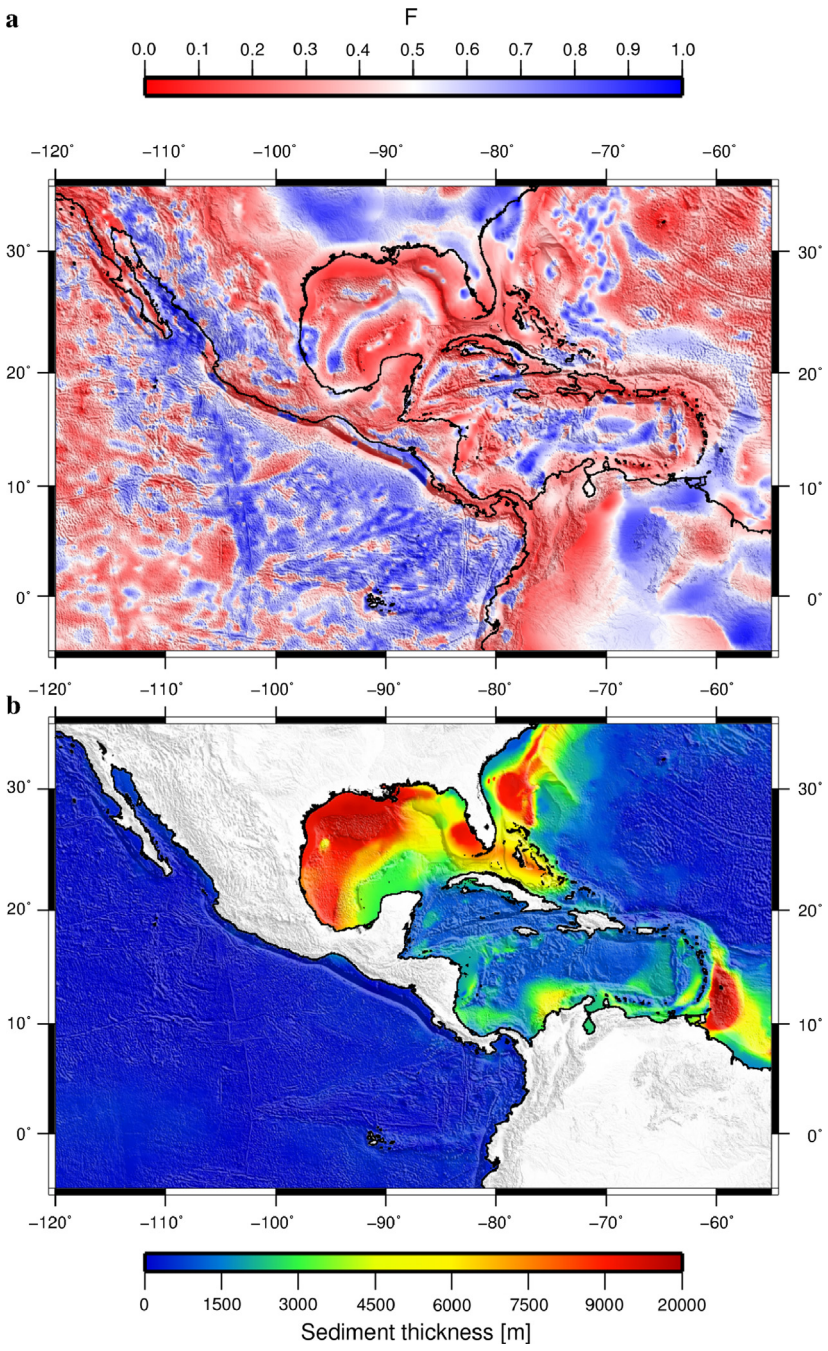

Fig. 5. (a) Loading ratio (F) corresponding to the T_e obtained from the wavelet method (Fig. 3b). (b) Sediment thickness (meters) on the seafloor in the study area from the 5 arc-minute digital total-sediment-thickness database for the world's oceans and marginal seas (Divins, 2003; Whittaker et al., 2013).

Subsurface loads, such as those due to a dense downgoing slab, should be taken into account when interpreting the results over subduction zones (Kalnins and Watts, 2009). We have found that the high T_e values over the Middle American and Lesser Antilles subduction zones are dominated by internal loads (and in the case of the southernmost tip of the LAT also associated with a large amount of sediments; see Fig. 5), where the corresponding noise levels are high (see Suppl. Fig. 7) and thus, these results may be biased upward. If T_e over the Middle American subduction zone is actually low (at least relatively), it would be in accordance with they reflecting a "frozen in" signal which is not affected in this zone by subsequent cooling and strengthening of the oceanic lithosphere. Interestingly, this is not the case of the Lesser Antilles subduction zone, where the high T_e values are free of noise (excepting the southernmost tip of the LAT associated with a large amount of sediments; see Fig. 5b and Suppl. Fig. 7), and persist in all our results from different window sizes and $|\mathbf{k}_0|$ in both multitaper and wavelet methods, respectively (see Fig. 3 and Supp. Figs. 1 and 6). This is in accordance with the strength of the oceanic lithosphere is being in this case controlled by the thermal age of the lithosphere at the time of loading (Watts, 2001; Kalnins and Watts, 2009), such that T_e values increase with cooling of the oceanic lithosphere away from the ridge. Furthermore, it should be noted that the results over the Middle American and Lesser Antilles subduction zones, especially in relation to the high gradient that limits these bands of higher T_e, are highly dependent on the choice of spectral parameters in both multitaper and wavelet methods (see Fig. 3 and Supp. Figs. 1 and 6).

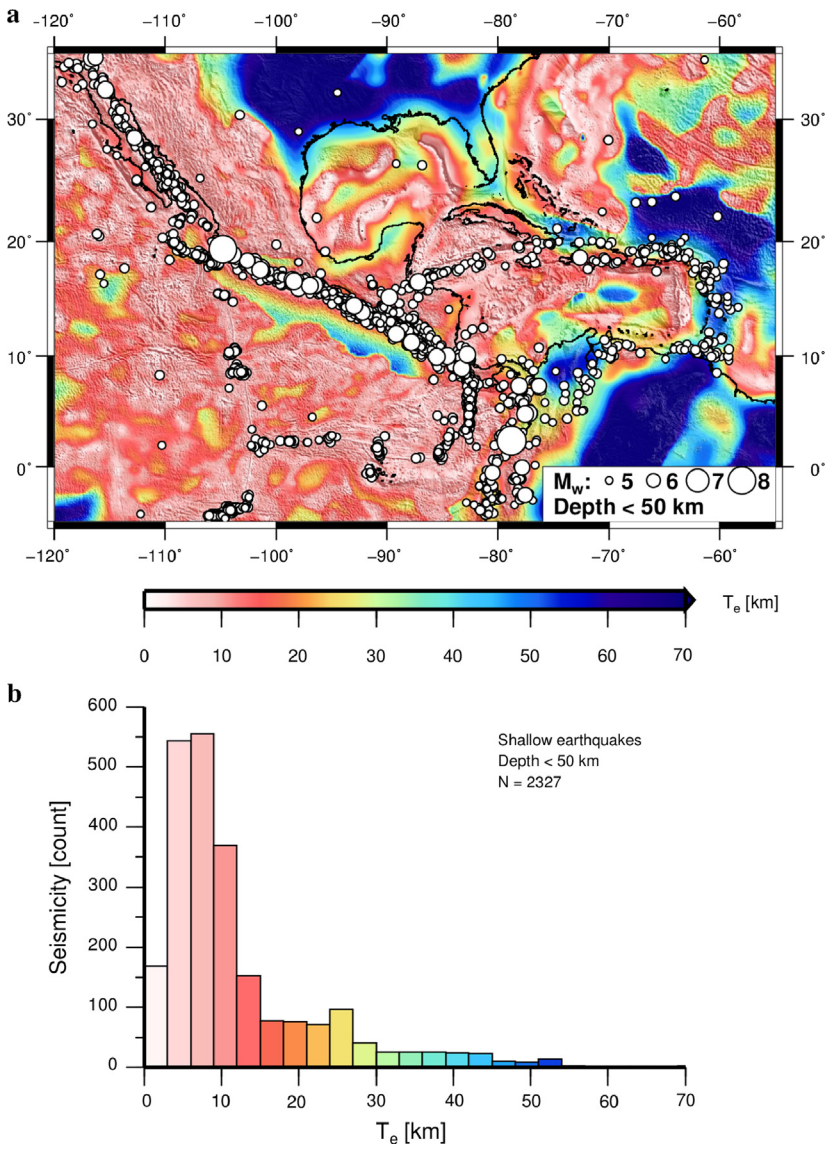

Fig. 6. (a) Correlation between distribution of the shallow seismicity (depth <50 km) from the Global CMT seismic catalog (Ekström et al., 2012) with T_e derived from the wavelet method. (b) Histogram shows shallow earthquake events versus T_e.

4.4. T_e and seismicity

The magnitude and spatial variations of T_e could control the degree, style and localization of deformation in response to long-term tectonic loads, and potentially the distribution of seismic activity (e.g., Lowry and Smith, 1995; Tassara et al., 2007; Audet and Bürgmann, 2011; Chen et al., 2013). The seismotectonics of the circum-Caribbean area is complex, and essentially related to plate boundaries, with intraplate activity being very scarce (Fig. 6a). Comparison of the spatial variation of T_e with the shallow (<50 km deep) earthquake distribution indicates that most of the seismic activity is located in regions with low T_e or steep T_e gradient, while the lack of seismicity in stable tectonic provinces characterized by high T_e values is evident (Fig. 6a). As illustrated in Fig. 6b, shallow earthquakes are very frequent in regions with low T_e (<20 km), and are relatively scarce in regions with higher values. This suggests that the stronger lithosphere resists deformation and transfers the stress effectively, while the weak lithosphere and areas with steep change of T_e are prone to accumulate and then release tectonic stresses causing earthquakes (Mao et al., 2012; Chen et al., 2013).

5. Conclusions

We have used two different spectral methods (multitaper and wavelet) to calculate the coherence between the Bouguer gravity anomaly and the topography in order to estimate the spatial variations in effective elastic thickness in Central America and surrounding regions. We have generated, for the first time, high-resolution maps of spatial variations of T_e for this region. Regardless of the technical differences between the two methods, there is a good overall agreement in the spatial variations of T_e recovered from both methods. Although absolute T_e values can vary in both maps, the qualitative T_e structure and location of the main T_e gradients are very similar, such that estimation of T_e is relatively insensitive to the choice of spectral estimator.

The pattern of the T_e variations in Central America and surrounding regions agrees well with the tectonic provinces in the region, and it is closely related to major tectonic boundaries. There is a relatively good correlation, despite some uncertainties, between surface heat flow and our T_e results. These results suggest that although this area is geologically complex, the thermal state of the lithosphere has profound influence on its strength, such that

T_e is strongly governed by thermal structure. Otherwise, in general there is not a direct relationship between T_e and the age of the ocean crust in of our study area (contrary to that expected if T_e is exclusively controlled by the thermal structure of the oceanic lithosphere), which could be explained for other factors, maybe mainly differences in age loading.

The Middle American and Lesser Antilles subduction zones are characterized by a band of high T_e on the downgoing slab seaward of the trenches. These high T_e values are related to internal loads (and in the case of the southernmost tip of the LAT also associated with a large amount of sediments); showing high noise levels and they may be biased upward. Thus, the results over subduction zones should be interpreted with caution, and warrant further analysis.

Finally, future research should also evaluate the relationship between T_e, as well as its anisotropy, Moho structure and mantle structure within a geodynamical perspective, in order to improve our understanding on the evolution of the Caribbean plate.

Acknowledgements

We thank Pascal Audet, an anonymous reviewer, and Editor Yanick Ricard for their useful reviews that significantly improved this manuscript. We also thank Javier Fullea for providing the FA2BOUG code. A.J.-D. especially thanks Pilar Llanes and Yangfan Deng for fruitful discussion on various topics of the methodology. The figures have been produced with the GMT software (Wessel et al., 2013). A.J.-D. work was supported by a grant of the Universidad Complutense de Madrid. J.R. work was supported by a contract Ramón y Cajal co-financed from the Ministerio de Economía y Competitividad of Spain and the European Social Fund. This work was carried out in the projects CGL2008-03463 and CGL2009-14405-C02-02. This work is a contribution from the Active Tectonics, Paleoseismology and Associated Hazards research group (UCM-910368; http://tectact.wordpress.com/).

Appendix A. Supplementary material

Supplementary material related to this article can be found online at http://dx.doi.org/10.1016/j.epsl.2014.01.042.

References

Addison, P.S., 2002. The Illustrated Wavelet Transform Handbook. Institute of Physics Publishing, Bristol, UK.
Afonso, J.C., Ranalli, G., 2004. Crustal and mantle strengths in continental lithosphere: is the jelly sandwich model obsolete?. Tectonophysics 394, 221–232.
Amante, C., Eakins, B.W., 2009. ETOPO1 1 arc-minute global relief model: procedures, data sources and analysis. NOAA Technical Memorandum NESDIS NGDC-24. 19 pp.
Artemieva, I., 2011. The Lithosphere: An Interdisciplinary Approach, vol. 773. Cambridge University Press. 773 pp.
Audet, P., Bürgmann, R., 2011. Dominant role of tectonic inheritance in supercontinent cycles. Nat. Geosci. 4, 184–187.
Audet, P., Jellinek, A.M., Uno, H., 2007. Mechanical controls on the deformation of continents at convergent margins. Earth Planet. Sci. Lett. 264, 151–166.
Bassin, C., Laske, G., Masters, T.G., 2000. The current limits of resolution for surface wave tomography in North America. Eos Trans. AGU 81, F897.
Billen, M.I., Gurnis, M., 2005. Constraints on subducting plate strength within the Kermadec trench. J. Geophys. Res. 110, B05407.
Bird, P., 2003. An updated digital model of plate boundaries. Geochem. Geophys. Geosyst. 4 (3), 1027. http://dx.doi.org/10.1029/2001GC000252.
Bürgmann, R., Dresen, G., 2008. Rheology of the lower crust and upper mantle: evidence from rock mechanics, geodesy, and filed observations. Annu. Rev. Earth Planet. Sci. 36, 531–567.
Burov, E.B., 2011. Rheology and strength of the lithosphere. Mar. Pet. Geol. 28, 1402–1443.
Burov, E.B., Diament, M., 1995. The effective elastic thickness of (Te) continental lithosphere. What does it really means?. J. Geophys. Res. 100 (B3), 3905–3927.
Burov, E.B., Watts, A.B., 2006. The long-term strength of continental lithosphere: "jelly sandwich" or "crème brûlée"?. GSA Today 16 (1), 4–10.
Caldwell, J.G., Turcotte, D.L., 1979. Dependence of the elastic thickness of the oceanic lithosphere on age. J. Geophys. Res. 84, 7572–7576.
Chen, B., Chen, C., Kaban, M.K., Du, J., Liang, Q., Thomas, M., 2013. Variations of the effective elastic thickness over China and surroundings and their relation to the lithosphere dynamics. Earth Planet. Sci. Lett. 363, 61–72.
Contreras-Reyes, E., Osses, A., 2010. Lithospheric flexure modeling seaward of the Chile trench: implications for oceanic plate weakening in the Trench Outer Rise region. Geophys. J. Int. 182 (1), 97–112.
Daly, E., Brown, C., Stark, C.P., Ebinger, C.J., 2004. Wavelet and multitaper coherence methods for assessing the elastic thickness of the Irish Atlantic margin. Geophys. J. Int. 159, 445–459.
DeMets, C., Gordon, R.G., Argus, D.F., 2010. Geologically current plate motions. Geophys. J. Int. 181, 1–80. http://dx.doi.org/10.1111/j.1365-246X.2009.04491.x. See also: Erratum. Geophys. J. Int. 187 (2011) 538. http://dx.doi.org/10.1111/j.1365-246X.2011.05186.x.
Divins, D.L., 2003. Total Sediment Thickness of the World's Oceans & Marginal Seas. NOAA National Geophysical Data Center, Boulder, CO.
Ekström, G., Nettles, M., Dziewoński, A., 2012. The global CMT project 2004–2010: centroid-moment tensors for 13,017 earthquakes. Phys. Earth Planet. Inter. 200–201, 1–9.
Feighner, M.A., Richards, M.A., 1994. Lithospheric structure and compensation mechanism of the Galápagos Arc. J. Geophys. Res. 99, 6711–6729.
Forsyth, D.W., 1985. Subsurface loading estimates of the flexural rigidity of continental lithosphere. J. Geophys. Res. 90, 12,623–12,632.
Fullea, J., Fernàndez, M., Zeyen, H., 2008. FA2BOUG – A FORTRAN 90 code to compute Bouguer gravity anomalies from gridded free air anomalies: application to the Atlantic–Mediterranean transition zone. Comput. Geosci. 34, 1665–1681.
Harders, R., Ranero, C.R., Weinrebe, W., Behrmann, J.H., 2011. Submarine slope failures along the convergent continental margin of the Middle America Trench. Geochem. Geophys. Geosyst. 12, Q05S32.
Hasterok, D., 2010. Thermal state of the Oceanic and Continental lithosphere. Ph.D. Thesis. University of Utah.
Hasterok, D., Chapman, D.S., 2011. Heat production and geotherms for the continental lithosphere. Earth Planet. Sci. Lett. 307, 59–70.
Judge, A.V., McNutt, M.K., 1991. The relationship between plate curvature and elastic plate thickness: a study of the Peru–Chile trench. J. Geophys. Res. 96 (B10), 16625–16639.
Kalnins, L.M., 2011. Spatial variations in the effective elastic thickness of the lithosphere and their tectonic implications. Ph.D. Thesis. University of Oxford.
Kalnins, L.M., Watts, A.B., 2009. Spatial variations in effective elastic thickness in the Western Pacific Ocean and their implications for Mesozoic volcanism. Earth Planet. Sci. Lett. 286, 89–100.
Kirby, J.F., Swain, C.J., 2008. An accuracy assessment of the fanwavelet coherence method for elastic thickness estimation. Geochem. Geophys. Geosyst. 9 (3), Q03022. Correction: Geochem. Geophys. Geosyst. 9 (5) (2008) Q05021.
Kirby, J.F., Swain, C.J., 2009. A reassessment of spectral Te estimation in continental interiors: the case of North America. J. Geophys. Res. 114, B08401.
Kirby, J.F., Swain, C.J., 2011. Improving the spatial resolution of effective elastic thickness estimation with the fan wavelet transform. Comput. Geosci. 37, 1345–1354.
Laske, G., Masters, G., 1997. A global digital map of sediment thickness. Eos Trans. AGU 78, F483.
Laske, G., Masters, G., Reif, C., 2000. A new global crustal model at 2 × 2 degrees (CRUST2.0). http://igppweb.ucsd.edu~gabi/rem.dir/crust/crust2.html.
Levitt, D.A., Sandwell, D.T., 1995. Lithospheric bending at subduction zones based on depth soundings and satellite gravity. J. Geophys. Res. 100, 379–400.
Lowry, A.R., Pérez-Gussinyé, M., 2011. The role of crustal quartz in controlling Cordilleran deformation. Nature 471 (7338), 353–357. http://dx.doi.org/10.1038/nature09912.
Lowry, A.R., Smith, R.B., 1995. Strength and rheology of the western U.S. Cordillera. J. Geophys. Res. 100, 17,947–17,963.
Lowry, A.R., Ribe, N.M., Smith, R.B., 2000. Dynamic elevation of the Cordillera, western United States. J. Geophys. Res. 105, 23,371–23,390.
Macario, A., Malinverno, A., Haxby, W.F., 1995. On the robustness of elastic thickness estimates obtained using the coherence method. J. Geophys. Res. 100 (D8), 15,163–15,172.
Manea, M., Manea, V.C., Kostoglodov, V., Guzman-Speziale, M., 2005. Elastic thickness of the lithosphere below the Tehuantepec Ridge. Geofis. Int. 44, 2157–2168.
Manea, V.C., Manea, M., Ferrari, L., 2013. A geodynamical perspective on the subduction of Cocos and Rivera plates beneath Mexico and Central America. Tectonophysics 609, 56–81.
Mao, X., Wang, Q., Liu, S., Xu, M., Wang, L., 2012. Effective elastic thickness and mechanical anisotropy of South China and surrounding regions. Tectonophysics 550–553, 47–56.
Mareschal, J.-C., Jaupart, C., 2013. Radiogenic heat production, thermal regime and evolution of Continental Crust. Tectonophysics 609, 524–534.
McAdoo, D.C., Martin, C.F., 1984. Seasat observation of geoid anomalies due to subducting slabs. J. Geophys. Res. 87, 8684–8692.
McAdoo, D.C., Martin, C.F., Poulose, S., 1985. Seasat observations of flexure: Evidence for a strong lithosphere. Tectonophysics 116, 209–222.
McKenzie, D., 2003. Estimating Te in the presence of internal loads. J. Geophys. Res. 108 (B9), 2438.

McKenzie, D.P., Fairhead, J.D., 1997. Estimates of the effective elastic thickness of the continental lithosphere from Bouguer and free air gravity anomalies. J. Geophys. Res. 102 (B12), 27523–27552.

McNutt, M.K., 1984. Lithospheric flexure and thermal anomalies. J. Geophys. Res. 89 (11), 11180–11194.

McNutt, M.K., Menard, H.W., 1982. Constraints on yield strength in the oceanic lithosphere derived from observations of flexure. Geophys. J. R. Astron. Soc. 71, 363–394.

Müller, R.D., Sdrolias, M., Gaina, C., Roest, W.R., 2008. Age, spreading rates, and spreading asymmetry of the world's ocean crust. Geochem. Geophys. Geosyst. 9, Q04006.

Percival, D.B., Walden, A.T., 1993. Spectral Analysis for Physical Applications, Multitaper and Conventional Univariate Techniques. Cambridge Univ. Press, New York, pp. 1–190.

Pérez-Gussinyé, M., Watts, A.B., 2005. The long-term strength of Europe and its implications for plate forming processes. Nature 436, 381–384.

Pérez-Gussinyé, M., Lowry, A.R., Watts, A.B., Velicogna, I., 2004. On the recovery of the effective elastic thickness using spectral methods: examples from synthetic data and from the Fennoscandian Shield. J. Geophys. Res. 109.

Pérez-Gussinyé, M., Lowry, A.R., Watts, A.B., 2007. Effective elastic thickness of South America and its implications for intracontinental deformation. Geochem. Geophys. Geosyst. 8 (5), Q05009.

Pérez-Gussinyé, M., Lowry, A.R., Phipps Morgan, J., Tassara, A., 2008. Effective elastic thickness variations along the Andean margin and their relationship to subduction geometry. Geochem. Geophys. Geosyst. 9, Q02003.

Pérez-Gussinyé, M., Swain, C.J., Kirby, J.F., Lowry, A.R., 2009a. Spatial variations of the effective elastic thickness, Te, using multitaper spectral estimation and wavelet methods: examples from synthetic data and application to South America. Geochem. Geophys. Geosyst. 10, Q04005.

Pérez-Gussinyé, M., Metois, M., Fernández, M., Vergés, J., Fullea, J., Lowry, A.R., 2009b. Effective elastic thickness of Africa and its relationship to other proxies for lithospheric structure and surface tectonics. Earth Planet. Sci. Lett. 287, 152–167.

Ranalli, G., 1997. Rheology of the lithosphere in space and time. Geol. Soc. (Lond.) Spec. Publ. 121, 19–37.

Ranero, C.R., Morgan, J.P., McIntosh, K., Reichert, C., 2003. Bending-related faulting and mantle serpentinization at the Middle America trench. Nature 425, 367–373.

Ranero, C.R., Villaseñor, A., Morgan, J.P., Weinrebe, W., 2005. Relationship between bend-faulting at trenches and intermediate-depth seismicity. Geochem. Geophys. Geosyst. 6, Q12002.

Ross, M.I., Scotese, C.R., 1988. A hierarchical tectonic model of the Gulf of Mexico and Caribbean region. Tectonophysics 155, 139–168.

Sandwell, D.T., Smith, W.H.F., 2009. Global marine gravity from retracked Geosat and ERS-1 altimetry: ridge segmentation versus spreading rate. J. Geophys. Res. 114, B01411.

Siebert, L., Simkin, T., 2002. Volcanoes of the world: an illustrated catalog of Holocene volcanoes and their eruptions. In: Smithsonian Institution, Global Volcanism Program Digital Information Series, GVP-3. http://www.volcano.si.edu/world/.

Simons, F.J., Zuber, M.T., Korenaga, J., 2000. Isostatic response of the Australian lithosphere: estimation of effective elastic thickness and anisotropy using multitaper spectral analysis. J. Geophys. Res. 105 (B8), 19,163–19,184.

Stark, C.P., Stewart, J., Ebinger, C.J., 2003. Wavelet transform mapping of effective elastic thickness and plate loading: validation using synthetic data and application to the study of southern African tectonics. J. Geophys. Res. 108 (B12), 2558.

Sykes, L.R., McCann, W.R., Kafka, A.L., 1982. Motion of Caribbean Plate during last 7 million years and implications for early Cenozoic movements. J. Geophys. Res. 87 (B13), 10656–10676.

Tassara, A., Swain, C.J., Hackney, R.I., Kirby, J.F., 2007. Elastic thickness structure of South America estimated using wavelets and satellite-derived gravity data. Earth Planet. Sci. Lett. 253, 17–36.

Tesauro, M., Kaban, M.K., Cloetingh, S.A.P.L., 2012. Global strength and elastic thickness of the lithosphere. Glob. Planet. Change 90–91, 51–57.

Thomson, D.J., 1982. Spectrum estimation and harmonic-analysis. Proc. IEEE 70 (9), 1055–1096.

Walden, A.T., McCoy, E.J., Percival, D.B., 1995. The effective bandwidth of a multitaper spectral estimator. Biometrika 82 (1), 201–214.

Watts, A.B., 2001. Isostasy and Flexure of the Lithosphere. Cambridge University Press. 472 pp.

Watts, A.B., Burov, E.B., 2003. Lithospheric strength and its relation to the elastic and seismogenetic layer thickness. Earth Planet. Sci. Lett. 213, 113–131.

Watts, A.B., Zhong, S., 2000. Observations of flexure and the rheology of oceanic lithosphere. Geophys. J. Int. 142 (3), 855–875.

Watts, A.B., Sandwell, D.T., Smith, W.H.F., Wessel, P., 2006. Global gravity, bathymetry, and the distribution of submarine volcanism through space and time. J. Geophys. Res. 111 (B8).

Wessel, P., Smith, W.H.F., Scharroo, R., Luis, J.F., Wobbe, F., 2013. Generic mapping tools: Improved version released. Eos Trans. AGU 94, 409–410.

Whittaker, J., Goncharov, A., Williams, S., Müller, R.D., Leitchenkov, G., 2013. Global sediment thickness dataset updated for the Australian–Antarctic Southern Ocean. Geochem. Geophys. Geosyst. 14 (8), 2547–3313. http://dx.doi.org/10.1002/ggge.20181.

Anexo III

Ruiz, J., McGovern, P.J., **Jiménez-Díaz, A.**, López, V., Williams, J.P., Hahn, B.C., Tejero, R. The thermal evolution of Mars as constrained by paleo-heat flows. *Icarus* 215, 508-517, 2011.

Icarus 215 (2011) 508–517

Contents lists available at SciVerse ScienceDirect

Icarus

journal homepage: www.elsevier.com/locate/icarus

The thermal evolution of Mars as constrained by paleo-heat flows

Javier Ruiz [a,*], Patrick J. McGovern [b], Alberto Jiménez-Díaz [a], Valle López [c,d], Jean-Pierre Williams [e], Brian C. Hahn [f], Rosa Tejero [a,d]

[a] Departamento de Geodinámica, Facultad de Ciencias Geológicas, Universidad Complutense de Madrid, 28040 Madrid, Spain
[b] Lunar and Planetary Institute, 3600 Bay Area Boulevard, Houston, TX 77058, USA
[c] Instituto de Geología Económica, CSIC-UCM, 28040 Madrid, Spain
[d] Instituto de Geociencias, CSIC-UCM, 28040 Madrid, Spain
[e] Department of Earth and Space Sciences, University of California, Los Angeles, CA 90095, USA
[f] Department of Earth and Planetary Sciences, University of Tennessee, Knoxville, TN 37996, USA

ARTICLE INFO

Article history:
Received 10 May 2011
Revised 24 July 2011
Accepted 28 July 2011
Available online 3 August 2011

Keywords:
Mars
Mars, Interior
Thermal histories

ABSTRACT

Lithospheric strength can be used to estimate the heat flow at the time when a given region was deformed, allowing us to constrain the thermal evolution of a planetary body. In this sense, the high (>300 km) effective elastic thickness of the lithosphere deduced from the very limited deflection caused by the north polar cap of Mars indicates a low surface heat flow for this region at the present time, a finding difficult to reconcile with thermal history models. This has started a debate on the current heat flow of Mars and the implications for the thermal evolution of the planet. Here we perform refined estimates of paleo-heat flow for 22 martian regions of different periods and geological context, derived from the effective elastic thickness of the lithosphere or from faulting depth beneath large thrust faults, by considering regional radioactive element abundances and realistic thermal conductivities for the crust and mantle lithosphere. For the calculations based on the effective elastic thickness of the lithosphere we also consider the respective contributions of crust and mantle lithosphere to the total lithospheric strength. The obtained surface heat flows are in general lower than the equivalent radioactive heat production of Mars at the corresponding times, suggesting a limited contribution from secular cooling to the heat flow during the majority of the history of Mars. This is contrary to the predictions from the majority of thermal history models, but is consistent with evidence suggesting a currently fluid core, limited secular contraction for Mars, and recent extensive volcanism. Moreover, the interior of Mars could even have been heating up during part of the thermal history of the planet.

1. Introduction

A very interesting and productive debate on the present-day heat flow and thermal state of Mars, and their implications for the thermal evolution of the planet, is currently occurring (Phillips et al., 2008; Kiefer and Li, 2009; Grott and Breuer, 2009, 2010; Ruiz et al., 2010; Dombard and Phillips, 2010). The very high (>300 km) effective elastic thickness of the lithosphere implied by the very limited (if any) deflection caused by the loading due to the north polar cap of Mars (Phillips et al., 2008) indicates a low surface heat flow at the present-time that is difficult to reconcile with most thermal history models. This low heat flow could be indicative of sub-chondritic heat-producing elements abundances (Phillips et al., 2008), a limited influence of secular cooling and fossil heat (Ruiz et al., 2010), or simply a regional variability of surface heat flow (Phillips et al., 2008; Kiefer and Li, 2009; Grott and Breuer, 2009, 2010). This debate clearly shows the profound implications that current or ancient surface heat flow estimates, deduced from geological or geophysical indicators of the thermal state of the lithosphere, have for understanding the thermal history of Mars.

Previous works estimated surface heat flows for diverse regions and epochs of Mars from the effective elastic thickness of the lithosphere (Solomon and Head, 1990; Anderson and Grimm, 1998; Zuber et al., 2000; Nimmo, 2002; Kiefer, 2004; McGovern et al., 2002, 2004; Grott et al., 2005; Ruiz et al., 2006a,b, 2008, 2010; Kronberg et al., 2007; Ruiz, 2009; Dohm et al., 2009a; Ritzer and Hauck, 2009) or from the depth to the brittle–ductile transition (BDT) beneath large thrust faults (Schultz and Watters, 2001; Grott et al., 2007; Ruiz et al., 2008, 2009); such heat flow estimates correspond to the time when the lithosphere was loaded or faulted. These previous works find a general decrease of heat flows with time, as expected for a cooling planet (McGovern et al., 2002, 2004; Montesi and Zuber, 2003), although there were some

* Corresponding author.
E-mail address: jaruiz@geo.ucm.es (J. Ruiz).

0019-1035/$ - see front matter © 2011 Elsevier Inc. All rights reserved.
doi:10.1016/j.icarus.2011.07.029

indications of regional variations in surface heat flows since comparatively higher heat flows are found for volcanic regions (McGovern et al., 2004).

However, the values of material parameters used to derive heat flow estimates varies widely, limiting the ability to integrate the results of different studies to collectively constrain the thermal history of Mars. Specifically, the amount and distribution of lithospheric heat-producing elements (HPE) and the values of the thermal conductivity of crust and mantle can affect the results substantially (Ruiz et al., 2006a, 2010). Heat flow estimates typically have not included HPE in the calculations: this omission reduces the calculated surface heat flow but increases calculated mantle heat flow and temperatures in the lower crust. Similarly, most workers used a very high mantle lithosphere thermal conductivity, which overestimates the surface heat flow for high effective elastic thicknesses but underestimates temperatures in the mantle lithosphere.

In this work we carefully calculate in a consistent manner paleo-heat flow for 22 martian regions of different ages and geological contexts (Fig. 1). We improve the heat flow calculations by taking into account realistic thermal conductivities for the crust and mantle lithosphere (including a temperature-dependent thermal conductivity, appropriate for olivine, for the mantle lithosphere), and two extreme cases for the abundance and distribution of HPE: we use refined HPE values based on Mars Odyssey GRS measurement and zero lithospheric HPE to calculate upper and lower limits, respectively, for the surface heat flows. For the heat flow calculations that use the effective elastic thickness of the lithosphere we also consider the respective contributions of crust and mantle components to the total strength of the lithosphere. Finally, we compare our results with estimates of radioactive heat production deduced from compositional models and with predictions from thermal history models, in order to obtain constrains on the thermal evolution of Mars. Since heat flow upper limits are more useful to constrain thermal evolution, we have been very careful to provide very robust upper limit calculations for the analyzed regions.

2. Strength of the lithosphere

The effective elastic thickness is a measure of the total strength of the lithosphere, integrating contributions from brittle and ductile layers and from elastic cores of the lithosphere (for a review see Watts and Burov (2003)). Effective elastic thickness estimates can be converted to estimates of heat flow following the equivalent strength envelope procedure described by McNutt (1984). This methodology is based on the condition that the bending moment M of the mechanical lithosphere must be equal to the bending moment of the equivalent elastic layer of thickness T_e, and so,

$$\frac{EKT_e^3}{12(1-\nu^2)} = \int_0^{T_m} \sigma(z)(z-z_n)\,dz, \tag{1}$$

where E is the Young's modulus, K is the topography curvature, T_e is the effective elastic thickness, ν is the Poisson's ratio, T_m is the mechanical thickness of the lithosphere, $\sigma(z)$ is the least, at depth z, of the brittle strength, the ductile strength, or the fiber stress due to plate flexure, and z_n is the depth to the neutral stress plane. Additionally, the condition of zero net axial force is imposed,

$$\int_0^{T_m} \sigma(z)\,dz = 0. \tag{2}$$

The case of a rheologically stratified lithosphere with mechanically decoupled crust and mantle is more complicated (see, for example, McNutt et al., 1988; Burov and Diament, 1992; Ruiz et al., 2006c), and the total bending moment is given by

$$M = M_{crust} + M_{mantle}, \tag{3}$$

where the subindex refers to the crust and mantle lithosphere contributions to the total bending moment. Also, in this case the condition of zero net axial force must be imposed on both the crust and lithospheric mantle.

The brittle strength is calculated according to the expression (e.g., Ranalli, 1997)

$$(\sigma_1 - \sigma_3)_b = \alpha\rho g(1-\lambda)z, \tag{4}$$

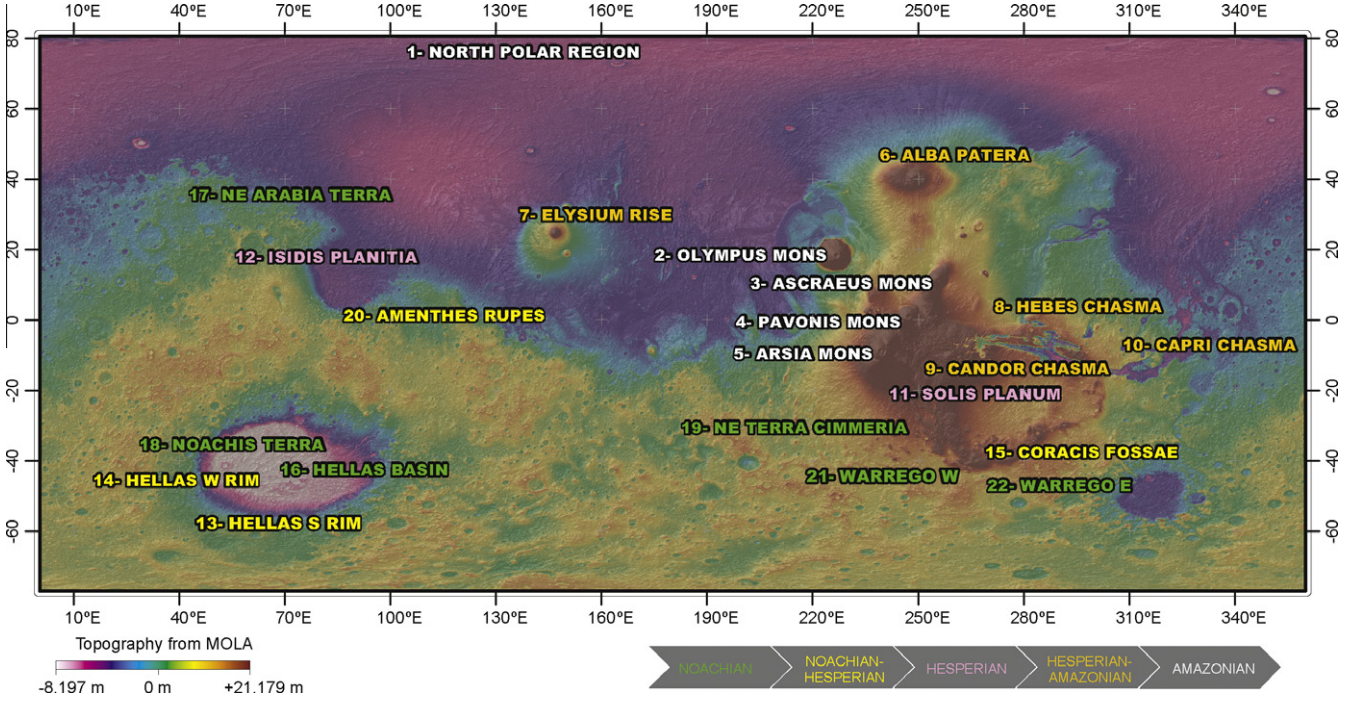

Fig. 1. MOLA topography map showing the analyzed regions.

where α is a coefficient depending on the stress regime (which is 3 and 0.75 for pure compression and tension respectively; e.g., Ranalli, 1997), ρ is the density, g is the acceleration due to the gravity (3.72 m s^{-2} for Mars), λ is the pore pressure, and z is the depth. The brittle strength of the crust is here calculated directly from Eq. (4) by using the density of the crust. The brittle strength of the lithospheric mantle is calculated for a density of 3500 kg m^{-3} and starting from the brittle strength at the base of the crust. The ductile strength (which does not depend on the stress regime) is given by

$$(\sigma_1 - \sigma_3)_d = \left(\frac{\dot{e}}{A}\right)^{1/n} \exp\left(\frac{Q}{nRT}\right), \quad (5)$$

where $\dot{e}$ is the strain rate, A, Q, and n are laboratory-determined constants, R (= 8.31447 J mol^{-1} K^{-1}) is the gas constant, and T is the absolute temperature. The fiber stress is in turn calculated from

$$\sigma_{fib} = \frac{EK(z - z_n)}{1 - \nu^2}. \quad (6)$$

The link between the strength envelope procedure and heat flow comes from the dependence of the ductile strength on temperature.

We analyze regions for which estimates of effective elastic thickness and topography curvatures of the equivalent elastic layer are available (see Table 1). Also, the elastic parameters in these estimates must be consistent with the nominal values of E = 100 GPa and ν = 0.25, which are widely used for Mars (e.g., McGovern et al., 2002; Phillips et al., 2008). The density of the crust is taken as 2900 kg m^{-3}, unless a different value has been inferred from geophysical modeling (e.g., McGovern et al., 2004) for a given region, and the mantle lithosphere density is taken as 3500 kg m^{-3}. The admittance modeling of McGovern et al. (2004), from which derive the majority of effective elastic thicknesses in Table 1, was performed for a mean crustal thickness of 50 km, whereas the crustal thickness maps of Neumann et al. (2004, 2008) were constructed for a mean crustal thickness of 45 km. Thus, for our calculations we assume local crustal thicknesses based on regional trends in Neumann et al. (2008) but increased by 5 km, in order to be consistent with the mean value of McGovern et al. (2004). Positive and negative topography curvatures are concave downward and upward, respectively, which implies that the part of the elastic plate above the neutral stress plane is under tension or compression, respectively (e.g., Turcotte and Schubert, 2002). This determines the value of the parameter α used for each case in Eq. (4). For several regions in Table 1 T_e upper (lower) limits are unavailable; for these regions we cannot obtain lower (upper) limits for the heat flow.

We perform calculations for zero pore pressure and hydrostatic pore pressure. Increasing the pore pressure decreases the total strength of the lithosphere, and the heat flow must be lowered in order to maintain the total strength consistent with a given T_e. Thus, for equal T_e, zero and hydrostatic pore pressures serve to place upper and lower limits, respectively, to the obtained surface heat flow.

For creep parameters of the martian crust we use the constants for the flow law of diabase: A = 0.0612 MPa^{-n} s^{-1}, n = 3.05 and Q = 276 kJ mol^{-1} (Caristan, 1982). The use of a wet diabase law is appropriate for a basaltic martian crust and is consistent with extensive evidence for water-related geological activity in early Mars (e.g., Head et al., 2001; Dohm et al., 2009b); moreover, the water amount needed to "wet" the diabase is certainly modest (lower than 1%; see Caristan, 1982). The ductile strength of the mantle lithosphere is calculated for dry and wet olivine dislocation creep rheologies, which give upper and lower limits, respectively, to the surface heat flow. For wet olivine, we use the flow law of the Anita Bay dunite: A = 9550 MPa^{-n} s^{-1}, n = 3.35 and Q = 444 kJ mol^{-1} (Chopra and Paterson, 1984). This flow law places a lower limit on the strength of wet olivine due to its relative weakness (compared with other wet dunites, such as Aheim dunite). For dry olivine we use the flow law obtained for artificially dried dunites (which is valid for both Anita Bay and Aheim dunites): A = 28840 MPa^{-n} s^{-1}, n = 3.6 and Q = 535 kJ mol^{-1} (Chopra and Paterson, 1984). Zhao et al. (2009) have recently reported that

Table 1
Values used for the calculation of heat flows from the effective elastic thickness (T_e) of the lithosphere.

Feature	Centered on	Surface age	T_e (km)	Curvature (10^{-7} m^{-1})[h]	Crustal density (kg m^{-3})	Crustal thickness (km)
1. North Pole[a]	90°N, 0°E	Current	>300	0	2900	30
2. Olympus Mons[b]	19°N, 226.5°E	A	>70	−1.6	2900	55
3. Ascraeus Mons[b]	11.5°N, 256°E	A	⩽80[g]	−0.69	2900	70
4. Pavonis Mons[b]	0.5°N, 247°E	A	<100	−1.0	2900	75
5. Arsia Mons[b]	9°S, 239°E	A	>20	−13	2900	85
6. Alba Patera[b]	42°N, 249°E	A–H	38–65	−1.8 to −0.55	2900	65
7. Elysium rise[b]	25°N, 147°E	A–H	15–45	−9.9 to −2.3	2900	45
8. Hebes Chasma[b,c]	1°S, 284°E	A–H	⩾60	−1.2	2900	65
9. Candor Chasma[b,c]	8°S, 295°E	A–H	⩾80	−1.2	2200	70
10. Capri Chasma[b,c]	12°S, 310°E	A–H	>100	−0.6	2500	55
11. Solis Planum[b]	25°S, 270°E	H	24–37	+6.4 to +3.0	2900	70
12. Isidis Planitia[d]	13°N, 87°E	H	100–180	−0.09 to −0.02	2900	10
13. Hellas S rim[b]	64°S, 66°E	H–N	20–120	+6.4 to + 0.34	2900	55
14. Hellas W rim[b]	42°S, 39°E	H–N	<20	−3.9	2650	55
15. Coracis Fossae[e]	34.5°S, 274.5°E	H–N[f]	10.3–12.5	+6.4 to + 4.9	2900	75
16. Hellas Basin[b]	42°S, 66°E	N	<13	−7.6	2750	15
17. NE Arabia Terra[b]	36°N, 40°E	N	<16	−2.4	2500	50
18. Noachis Terra[b]	35°S, 26°E	N	<12	−3.1	2800	65
19. Terra Cimmeria[b]	30°S, 180°E	N	<12	−4.2	2950	60

[a] Phillips et al. (2008).
[b] McGovern et al. (2004); the maximum lithospheric curvature in the vicinity of each feature/region was determined directly from the lithospheric deflection, for the models that correspond to the upper and/or lower bounds on effective elastic thickness.
[c] There are alternative best fit T_e values (McGovern et al., 2004), but we use values maximizing the heat flow range.
[d] Ritzer and Hauck (2009).
[e] Grott et al. (2005).
[f] A surface age of 3.5–3.9 Ga has been reported for this feature by Grott et al. (2005).
[g] The effective elastic thickness range for this feature is 2–80 km (McGovern et al., 2004); because the very low lower bound, we have only calculated the lower limit heat flows for this feature.
[h] Curvature values correspond to the quoted T_e values; positive and negative values indicate, respectively, concave upward and downward curvatures.

anhydrous olivine is considerably weaker when it is proportionally iron-rich, as expected for the martian mantle, which would reduce mantle strength and hence the obtained heat flows. Thus, the use of rheology of Chopra and Paterson (1984) provides a generous upper limit for heat flows obtained from lithospheric strength. (There are not similar published experiments for iron-rich wet olivine.) Strain rates of 10^{-16} and 10^{-19} s^{-1} are used in the calculations, based on the range usually considered for Mars (McGovern et al., 2002, 2004). To make a comparison, terrestrial strain rates are typically $\sim 10^{-16}$ s^{-1} in active continental interiors (e.g., Tesauro et al., 2007), and $\sim 10^{-19}$–10^{-17} s^{-1} in stable plate interiors (Kumar and Gordon, 2009).

The base of the mechanical lithosphere is here defined as the depth at which the ductile strength reaches a low value of 10 MPa (see Ranalli, 1994; Ruiz et al., 2006a), and below which there are no further significant increases in strength, although varying the exact value selected does not produce substantial changes in the calculations due to the exponential dependence of ductile strength on temperature (see McNutt, 1984).

The depth of the brittle–ductile transition (BDT) can also be used in order to calculate surface heat flows (Ruiz and Tejero, 2000). This depth can be deduced by estimating the depth of faults that are thought to extend down until the crustal BDT, and hence the temperature at the BDT depth is obtained by equating the brittle and ductile strength for the depth $z = z_{BDT}$,

$$T_{BDT} = \frac{Q}{R}\left[\ln\frac{A(\sigma_1-\sigma_3)^n_{BDT}}{\dot{e}}\right]^{-1}, \quad (7)$$

where $(\sigma_1 - \sigma_3)_{BDT}$ is the strength at the BDT depth from Eq. (4). The heat flow is then obtained by matching T_{BDT} to a temperature profile. Here we use this procedure for three prominent lobate scarps (Table 2), interpreted to be the surface expression of large thrust faults. It must be noted that pore fluid pressure reduces brittle strength, and hence increases temperature at the BDT depth. Thus, upper and lower limits for the surface heat flow are calculated, respectively, for hydrostatic conditions and zero pore pressure, the opposite to the case for calculations based on the effective elastic thickness of the lithosphere.

3. Temperature profiles

Surface heat flows obtained from lithospheric strength are higher, for a fixed T_e or BDT depth, if lithospheric radioactive heat sources are included in the calculations than if purely thermal gradients are used (see Ruiz et al., 2006a, 2008, 2009). Thus, we calculate surface heat flow upper limits by including HPE in the crust and the mantle lithosphere, whereas lower limits are obtained by using zero lithospheric heat sources.

The significant homogeneity of elemental abundances measure by Mars Odyssey GRS suggests that the martian crust is much less geochemically varied than the Earth's crust (Taylor et al., 2006), which is consistent with a strong mixing by cratering (e.g. Taylor et al., 2006), and with the absence of large-scale crustal recycling, at least since the early part of the history of Mars (e.g., Frey, 2006). Indeed, some authors have suggested that Mars experienced an early phase of plate tectonics (e.g., Sleep, 1994; Baker et al., 2007), although high-resolution topography and radar sounding have revealed a large population of buried impact basins on Mars, implying a similar, and very early (>4 Ga), age of the basement throughout the entire planet (Frey, 2006; Watters et al., 2006). Temperature profiles in the crust are therefore calculated by assuming a homogeneous distribution of radioactive heat sources. Although it is possible that crustal HPE abundances decrease with depth, a homogeneous distribution gives higher surface heat flow and therefore is useful for our upper limit calculations. Also, we use a constant thermal conductivity for the crust, and therefore the temperature at a given depth z is given by

$$T_z = T_s + \frac{Fz}{k_c} - \frac{\rho_c H_c z^2}{2k_c}, \quad (8)$$

where T_s is the surface temperature, F is the surface heat flow, k_c is the thermal conductivity of the crust, ρ_c is the density of the crust, and H_c is the crustal heat production rate per unit mass. We use a surface temperature of 220 K, the present-day mean surface temperature on Mars (Kieffer et al., 1977), which is consistent with the inference of low near-surface temperatures deduced for most of the past 4 Ga from ALH84001 thermochronology (Shuster and Weiss, 2005). Also, we use $k_c = 2$ W m^{-1} K^{-1}, a value appropriate for intact basaltic rocks; this value is in the uppermost part of the range for intact (non-porous) basalts (see the compilation by Beardsmore and Cull (2001)).

Crustal potassium and thorium abundances for each analyzed region (Table 3) have been obtained from 5° × 5° pixel maps of GRS abundances renormalized considering the volatile content, in order to reflect a volatile/alteration-free composition, more likely to be representative of the total crust, and not surface contamination (Hahn et al., 2011). Uranium abundances are estimated using a Th/U ratio of 3.8. Potassium and thorium abundance values of the pixels corresponding to the analyzed features are good regional approximations due to the regional scale of the GRS footprint; the footprint of the GRS instrument from which 50% of the gamma ray signal originates is between 480 and 600 km in diameter (roughly 8–10° measured at the equator) depending upon energy (e.g., Boynton et al., 2007). For the North Polar Region, where GRS measurements are absent, we use global averages. For Hellas south rim, for which there are potassium and thorium GRS measurements but no volatile values, we use the same volatile abundances as for Hellas west rim. Heat dissipation rates are calculated for decay constants from Van Schmus (1995), and regional ages are listed in Table 1. The effective elastic thicknesses from the admittance study of McGovern et al. (2004) were estimated for regions including surfaces of different epochs (see also Tanaka, 1986). For these regions we use the age range embracing the appropriate periods. Absolute ages for period boundaries are derived from the cratering chronologies of Hartmann and Neukum (2001); when Hartmann's and Neukum's chronologies differ (for the Late Hesperian epoch or younger) we use the mean value as representative.

Table 2
Values used for the calculation of heat flows from the brittle–ductile transition (BDT) depth.

Feature	Centered on	Surface age	BDT depth (km)	Crustal density (kg m^{-3})	Crustal thickness (km)
20. Amenthes Rupes[a]	2°N, 249°E	H–N	27–35	2900	50
21. Warrego W[b]	41°S, 263°E	N[c]	27–35	2900	80
22. Warrego E[b]	43°S, 267°E	N[c]	21–28	2900	75

[a] Ruiz et al. (2008).
[b] Grott et al. (2005).
[c] A surface age of 3.7–4.0 Ga has been reported Grott et al. (2005) for this feature.

Table 3
Heat-producing element abundances.

Feature	K (ppm)	Th (ppm)	U (ppm)
1. North Pole	3652[a]	0.69[a]	0.18[a]
2. Olympus Mons	3390	0.63	0.17
3. Ascraeus Mons	3220	0.67	0.18
4. Pavonis Mons	3540	0.68	0.18
5. Arsia Mons	3630	0.63	0.17
6. Alba Patera	3070	0.51	0.13
7. Elysium rise	2900	0.53	0.14
8. Hebes Chasma	3670	0.54	0.14
9. Candor Chasma	3850	0.54	0.14
10. Capri Chasma	4310	0.65	0.17
11. Solis Planum	2540	0.42	0.11
12. Isidis Planitia	4590	0.86	0.23
13. Hellas S rim	2850	0.36	0.10
14. Hellas W rim	3750	0.77	0.20
15. Hellas Basin	3030	0.36	0.09
16. Coracis Fossae	2960	0.51	0.13
17. NE Arabia Terra	3640	0.79	0.21
18. Noachis Terra	3850	0.75	0.20
19. Terra Cimmeria	4830	0.97	0.26
20. Amenthes Rupesa	3540	0.68	0.18
21. WarregoW	3100	0.60	0.16
22. Warrego E	3260	0.57	0.15

[a] Average values for the martian crust.

The thermal conductivity of olivine (the main mineral in the mantle) is strongly temperature-dependent, and therefore we calculate temperature profiles in the mantle lithosphere from

$$\frac{dT}{dz} = \frac{F_{cb} - \rho_m H_m (z - b_c)}{k_m(T)}, \tag{9}$$

where $F_{cb} = F - \rho_c H_c b_c$ is the heat flow at the base of the crust, ρ_m and H_m are, respectively, the density and heat production rate per mass unity of the mantle lithosphere, b_c is the base of the crust, and k_m is the thermal conductivity of the mantle lithosphere. The value of H_m is poorly constrained, and here we use $H_m = 0.1 H_{c(av)}$, where $H_{c(av)}$ is the average value for the martian crust. This choice is based on a ratio between crustal and primitive mantle HPE abundances higher than ~10 for Mars (Taylor and McLennan, 2009), and represents a reasonable upper limit for H_m (melt extraction would reduce mantle HPE abundances), which in turn results in an upper limit to the obtained surface heat flow (the lower limit is obtained for $H_c = 0$ and $H_m = 0$).

For k_m we use the thermal conductivity of olivine, the main mineral in lithospheric mantle rocks, according to the expression (McKenzie et al., 2005)

$$k_m = \frac{a}{1 + c(T - 273)} + \sum_{i=0}^{3} d_i T^i, \tag{10}$$

where $a = 5.3$, $c = 0.0015$, $d_0 = 1.753 \times 10^{-2}$, $d_1 = -1.0364 \times 10^{-4}$, $d_2 = 2.2451 \times 10^{-7}$ and $d_3 = -3.4071 \times 10^{-11}$, for calculating an upper limit for the thermal conductivity of olivine as a function of temperature. Results obtained from Eq. (10) are similar to those of Hofmeister (1999) for forsterite olivine. The thermal conductivity of some silicate minerals somewhat decreases with the increasing of the proportion of iron (Hofmeister, 1999). The martian mantle is considered to be iron-rich (e.g., Halliday et al., 2001), and for this reason Eq. (10) gives an upper limit to the thermal conductivity of the mantle lithosphere of Mars. However, there are not, to our knowledge, similar expressions to Eq. (10) accounting for iron content of olivine. Eq. (10) applied to the martian mantle lithosphere would overestimate the thermal conductivity (by less than 1 W m^{-1} K^{-1}), which is useful for calculation of surface heat flow upper limits; on the other hand, for the calculation of surface heat flow lower limits this effect is balanced by the assumption of zero lithospheric heat sources.

For the case of the North Polar Region we additionally consider the effect of the polar cap above (but not included in) the lithosphere. The polar cap is assumed to be composed of water–ice. The thermal conductivity of cold water–ice is high, and the presence of rocks or other ices (e.g., CO_2) would reduce the bulk thermal conductivity, and hence the calculated heat flow. For this reason, non-water–ice components are not taken into account in our upper-limit calculation. The thermal conductivity of water–ice is strongly temperature-dependent, and therefore the temperature profile in the polar cap is given by

$$T_{pcb} = T_s \exp\left(\frac{F b_{pc}}{k_0}\right), \tag{11}$$

where T_s is the surface temperature, F is the surface heat flow (equal to the heat flow reaching the polar cap from below), b_{pc} is the thickness of the polar cap, and $k_0 = 621$ W m^{-1} (Petrenko and Whitworth, 1999). Here we use $T_s = 155$ K and $b_{pc} = 2$ km as representative of the martian polar regions (Plaut et al., 2007; Phillips et al., 2008; Wieczorek, 2008).

4. Results

Surface heat flows are calculated by constructing thermal profiles (Section 3) that satisfy the constraints imposed by indicators of lithospheric strength (Section 2). Calculations based on faulting depth only consider the thermal structure of the crust above the BDT depth, since the lithosphere below it does not influence the results. Calculations based on the effective elastic thickness of the lithosphere consider the entire thickness of the mechanical lithosphere. Also, the condition of non-negative sublithospheric heat flow is imposed for calculations using lithospheric heat sources. A negative sublithospheric heat flow could occur if assumed lithospheric HPE abundances are higher than the actual ones for a particular region (for example, the crust could be stratified, with a HPE-poor lower crust; see Ruiz et al., 2006b, 2009). If the sublithospheric heat flow is negative, then the thermal profile is adjusted to enforce zero sublithospheric heat flow and permit a ductile strength higher than 10 MPa at the base of the mechanical lithosphere. This is appropriate for calculating a generous upper limit to the surface heat flow since, as above noted, higher lithospheric strength increases the surface heat flow for a given T_e.

Results are shown in Fig. 2 as a function of age. Fig. 2 also shows the average surface heat flow corresponding to the total radioactive heat production of Mars after the compositional model of Wänke and Dreibus (1988). From Fig. 2 it is evident that most of the estimated heat flow upper limits, and all the lower limits, are below the radioactive heat flow curve (although lower limits from features for which an upper limit is not available give a limited constraint on the thermal history). Also, the obtained heat flows are lower than predicted for the majority of thermal history models of Mars (e.g., Hauck and Phillips, 2002; Williams and Nimmo, 2004; Grott and Breuer, 2010; Fraeman and Korenaga, 2010).

Our results can also be interpreted in terms of the Urey number *Ur*, the ratio of the internal heat production to the total surface heat loss in a planet. Fig. 2 indicates very low heat flows relative to expected heat output, consistent with very little secular cooling, i.e., a bulk-Mars *Ur* for Mars approaching 1.0 or perhaps even exceeding that value. Current estimates of the bulk-Earth *Ur* are in the range 0.35–0.53 (e.g., Jaupart et al., 2007; Korenaga, 2008), and somewhat higher (but usually <0.75) values are predicted for most martian thermal history models (see Fig. 3).

If $Ur > 1$ the martian interior (as an average) would be heating up. For illustrative purposes, we have estimated the mantle

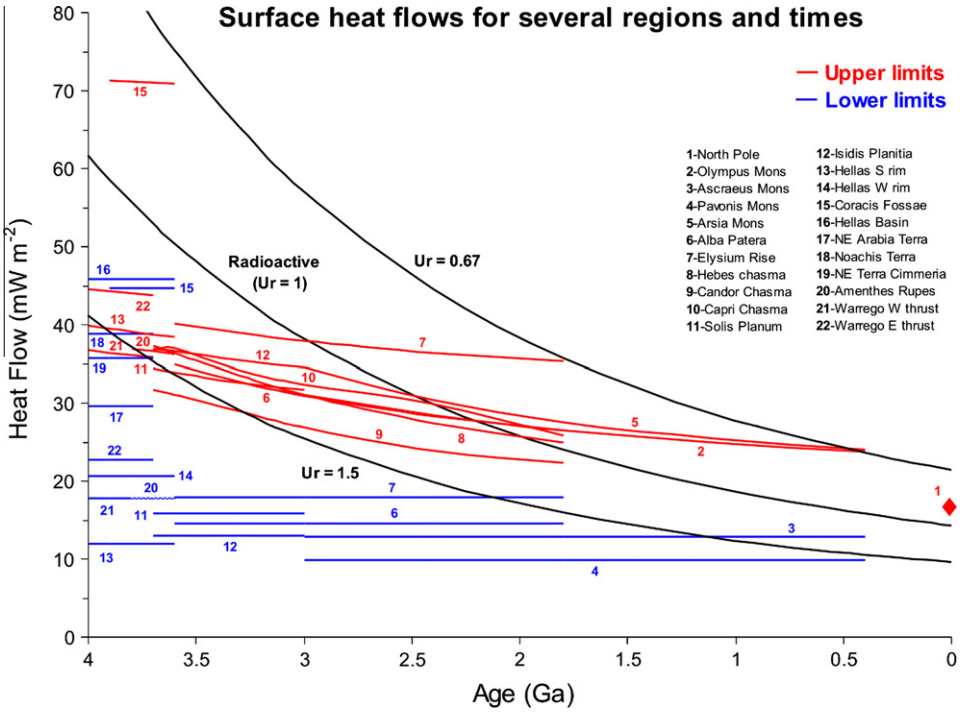

Fig. 2. Upper (red) and lower (blue) limits for the surface heat flows for several regions and times of Mars. For several regions only upper or lower limits are obtained, since lower or upper limits on effective elastic thickness are not available. Curves and horizontal lines indicate uncertainty related to surface age (and hence also to radioactive heating in the lithosphere), not to temporal evolution. The black curves show surface heat flows for three values of the Urey number (the ratio of the internal heat production to the total surface heat loss in a planet), calculated according to the composition model of Wänke and Dreibus (1988). Thus, the curve labeled "Radioactive ($Ur = 1$)" corresponds to the average surface heat flow which is equivalent to the total radioactive heat production of Mars. (For interpretation of the references to color in this figure legend, the reader is referred to the web version of this article.)

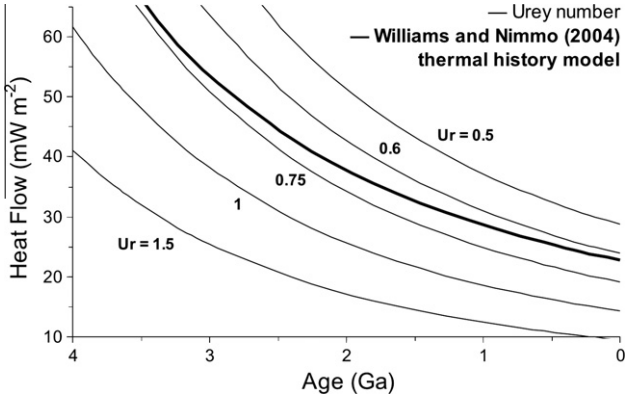

Fig. 3. Heat flows as a function of age and Urey number compared with the predictions of a thermal history model of Mars (calculated according to Williams and Nimmo (2004)), which obtain results similar to those of other thermal history models for Mars (e.g., Hauck and Phillips, 2002; Grott and Breuer, 2010). The Urey number is between 0.75 and 0.6 through the entire history of Mars.

temperature change for constant representative values for the Urey number by integrating the mantle heat balance equation from McGovern and Schubert (1989) using martian interior heat production values deduced from the HPE abundances of Wänke and Dreibus (1988). We obtain mantle temperature increases of 160 and 320 K for, respectively, Urey numbers of 1.2 and 1.5 integrated over the entire history of Mars. These values would be in any case generous upper limits given that the time period for which *Ur* could have been higher than 1 is likely to be significantly less than 4.6 Gyr. Under appropriate conditions ($Ur > 1$ and surface heat flow higher than the radioactive contribution from the lithosphere), heating of the convective mantle and cooling (and thickening) of the lithosphere could simultaneously occur.

Fig. 4 shows upper limits to the surface heat flow as a function of feature age and type of terrain (Fig. 5 shows the location, period and relative value of these upper limits). The only terrains for which surface heat flow could clearly exceed the equivalent radioactive heat flow are volcanic regions (Coracis Fossae is a rift zone with associated magmatism; Dohm et al., 2001; Grott et al., 2005), although uncertainties in feature age and effective elastic thickness preclude a definitive conclusion. Also, regional heat flow variations related to differences in crustal HPE abundances and/or crustal thickness (which influences the total amount of crustal HPE in the lithospheric column), are also expected (e.g., Grott and Breuer, 2010; Hahn et al., 2011), although our results lack the resolution to reveal these variations.

The estimates of effective elastic thickness for Isidis Planitia are comparatively high (Ritzer and Hauck, 2009), but the obtained surface heat flow is similar to other regions due to the very low curvatures and thin crust (which increases the mantle contribution to the total strength of the lithosphere) in this region. Similarly, the very high lower limits of the effective elastic thickness estimated for the North Polar Region (Phillips et al., 2008) gives a heat flow upper limit slightly higher than the equivalent radioactive heat flow due to the absence of flexure (and also to a relatively thin crust) in this region. On the other hand, the heat flow lower limits obtained for non-volcanic Noachian terrains (for which only upper limits are available for the effective elastic thickness) do not rule out a very high surface heat flow when the large-scale topography of these regions was formed. However, the absence of upper limit estimates for the surface heat flow in these regions greatly diminishes their relevance as constraints on the thermal evolution of Mars.

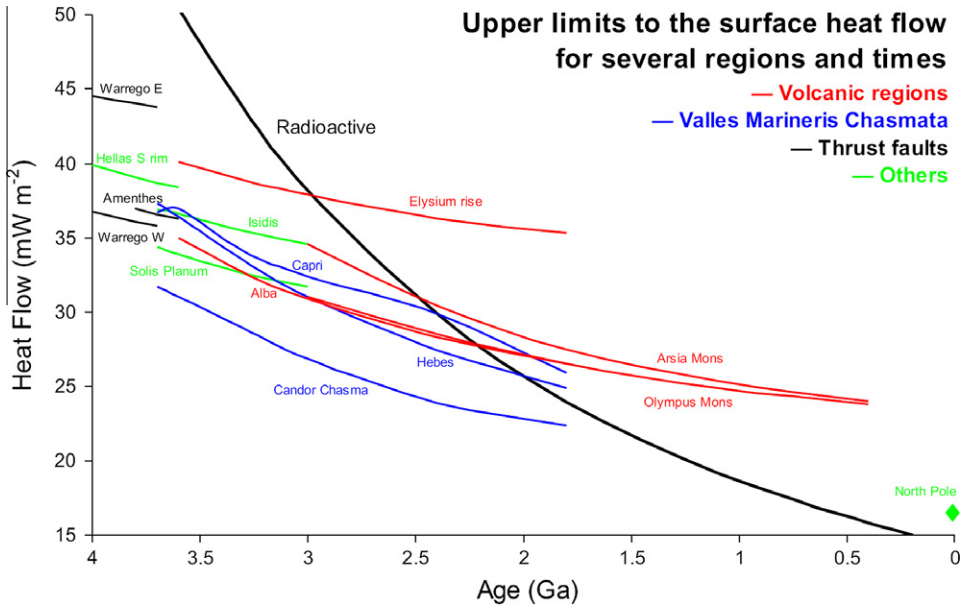

Fig. 4. Upper limits for the surface heat flows for several regions and times of Mars. Several categories of geological features are also indicated. Coracis Fossae, a rift zone with associated magmatism is not represented due to scale considerations (see Fig. 3). Curves indicate uncertainty related to surface age (and hence to radioactive heating in the lithosphere), not to temporal evolution. The black curve is the average heat flow equivalent to the total radioactive heat production of Mars according to the composition model of Wänke and Dreibus (1988). (For interpretation of the references to color in this figure legend, the reader is referred to the web version of this article.)

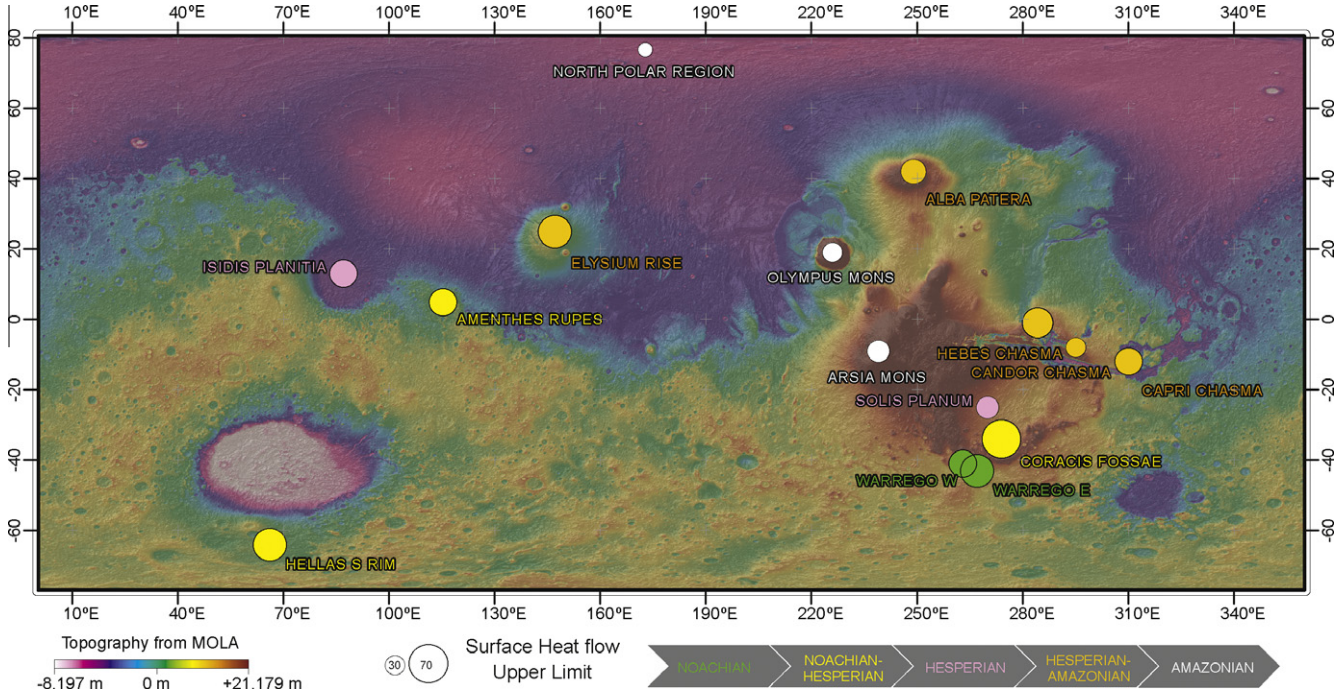

Fig. 5. Regional distribution of upper limits for the surface heat flow shown on MOLA topography. Most estimates correspond to the Tharsis region of Mars, where geological activity is concentrated.

5. Discussion

Our results indicate that the contribution from secular cooling to the surface heat flow has been limited during the majority of the history of Mars, contrary to the predictions of most thermal history models (e.g., Hauck and Phillips, 2002; Grott and Breuer, 2010). Further, the heat flow estimates in Fig. 2 suggest that the martian mantle was heating up during a significant fraction of the history of the planet (at least during Hesperian and Early Amazonian periods). These results are robust due to the conservative assumptions applied in generating our heat flow upper bounds.

Fig. 6 shows upper limits for sublithospheric heat flows (in essence the heat flow from the convective mantle), calculated in the same way as upper limits in Figs. 2 and 4 except by assuming $H_c = 0$ and $H_m = 0$: in absence of lithospheric heat sources the surface heat flow equals the sublithospheric heat flow. Calculated

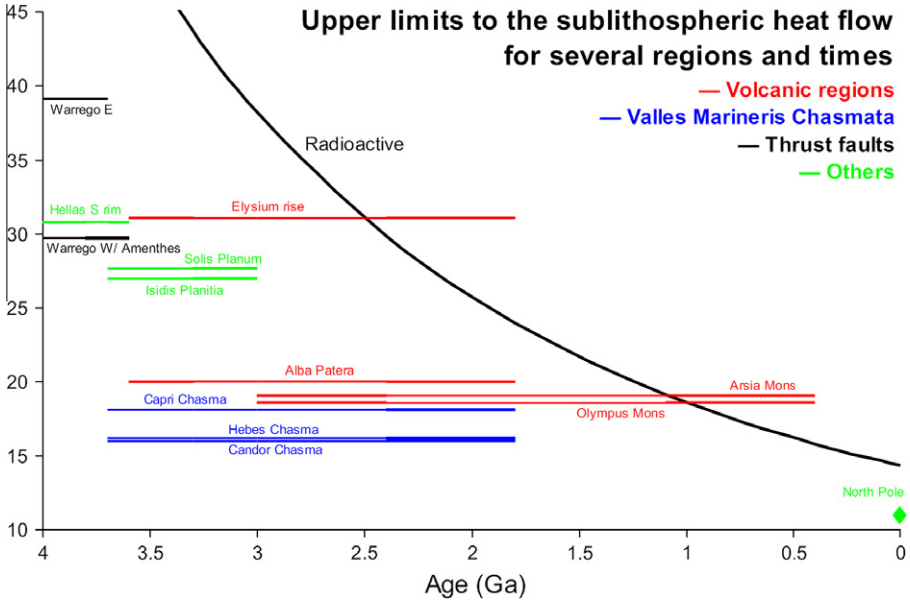

Fig. 6. Upper limits for the sublithospheric heat flow for several regions and times of Mars, calculating by imposing the condition of zero lithospheric heat sources. Coracis Fossae is not represented due to scale considerations (the sublithospheric heat flow upper limit is 68 mW m^{-2} for this feature). Several categories of geological features are also indicated. Black curve as in Fig. 4. (For interpretation of the references to color in this figure legend, the reader is referred to the web version of this article.)

upper limits for sublithospheric heat flows are again lower than predicted from the majority of thermal history models (e.g., Hauck and Phillips, 2002; Grott and Breuer, 2010). These low sublithospheric heat flow values also suggest that mantle convection has been less efficient than has been appreciated in many studies of martian thermal evolution.

Our results are consistent with several independent geophysical and geological observations. For example, high mantle temperatures reduce core cooling, possibly contributing to the present-day existence of a, at least partly, fluid core (deduced from the response to the solar tide; Yoder et al., 2003), and to the simultaneous absence of an endogenic magnetic field (e.g., Acuña et al., 2001) due to the reduction (or even suppression) of core convection (e.g., Nimmo and Stevenson, 2000). Our results are also consistent with a lower amount of global contraction since the Early Noachian than expected from thermal history models, as deduced from thrust faults recorded on the surface (Nahm and Schultz, 2011); indeed, the lack of mantle cooling (and maybe mantle heating) limits the thermal contraction that can drive surface contraction. Finally, the evidences for recent extensive volcanism (Hauber et al., 2011) also suggest the retention of a substantial amount of internal heat.

Our results are also supported by parameterized mantle convection models that couple convective vigor with the rheologic weakening effect of interior volatiles suggesting that high Urey ratios are also favored by inefficient cycling of volatiles to and from the mantle (McGovern and Schubert, 1989; Sandu et al., 2011), as might be expected for Mars, which has lacked a plate tectonic cycle to efficiently degas and (especially) replenish the mantle volatiles at least since the early part of the evolution of Mars. Further, High Urey ratios might typify all planets lacking the thermal efficiency of plate tectonics.

Alternatively, a substantial amount of heat could be transported by hydrothermal cooling of the upper crust (Parmentier and Zuber, 2007). However, hydrothermal circulation could only operate above the brittle–ductile transition, since below porosity is mostly eliminated by viscous creep (Hanna and Phillips, 2005). This implies that, for a given temperature at the BDT, the obtained temperature profile below the BDT depth (and the sublithospheric heat flow) is the same if hydrothermal cooling is occurring or not (although in our calculations surface heat flows are increased with respect to the value at the BDT depth due to radioactive heating in the brittle crust). Magmatic activity could enhance hydrothermal circulation and heat flow on space scales lower than resolved by admittance studies, but to justify in this way average heat flows higher than those obtained here for the majority of the history and regions of Mars seems unrealistic.

On the other hand, Baratoux et al. (2011a,b) have recently modeled melting pressures and degrees of partial melting from GRS data for 12 Hesperian and Amazonian volcanic provinces, and hence potential mantle temperatures and (using linear thermal gradients and a constant thermal conductivity for the entire lithosphere) heat flows, suggesting bulk-Mars *Ur* ~0.6–0.7 or lower, in accordance with most thermal history models. However, volcanic regions are expected to be associated with higher than average heat flows (see Figs. 2 and 4), making any *Ur* value based on those regions a lower limit. Thus, the melting pressures and degrees of partial melting obtained by Baratoux et al. (2011a,b) do not alter our conclusions.

6. Conclusions

Our results strongly suggest that Mars has been losing less heat than conventionally thought during, at least, a substantial part of its history. This would be indicative of less efficient mantle convection than commonly thought (perhaps related to stagnant lid convection with inefficient volatile cycling) and/or a reduced contribution from fossil heat to the surface heat flow, which would result in a lower heat flow from the convective mantle, and possibly elevated lower mantle and core temperatures. Also, there is evidence favoring a heterogeneous heat flow depending on the geological province (volcanic versus non-volcanic provinces), although it cannot presently be definitively demonstrated. Moreover, if the interior of Mars is in fact heating up (*Ur* > 1), there is the potential for a future increase in mantle convective vigor and/or melting, and there may ultimately be a resurgence of volcanic and tectonic activity.

It is clear that a better understanding of the thermal evolution of Mars requires a feedback between thermal history models and heat flow calculations based on the evolution of the strength of the lithosphere.

Acknowledgments

We thank James Dohm and an anonymous reviewer for their comments and suggestions; also, we thank Matthias Grott for his comments on an early version of this work. J.R. was supported by a contract Ramón y Cajal co-financed from the Ministerio de Ciencia e Innovación of Spain and the Fondo Social Europeo (ESF). LPI contribution number LPI-001630.

References

Acuña, M.H. et al., 2001. Magnetic field of Mars: Summary of results from the aerobraking and mapping orbits. J. Geophys. Res. 106, 23403–23417.
Anderson, S., Grimm, R.E., 1998. Rift processes at the Valles Marineris, Mars: Constraints from gravity on necking and rate-depending strength evolution. J. Geophys. Res. 103, 11113–11124.
Baker, V.R., Maruyama, S., Dohm, J.M., 2007. Tharsis superplume and the geological evolution of early Mars. In: Yuen, D.A., Maruyama, S., Karato, S.-I., Windley, B.F. (Eds.), Superplumes: Beyond Plate Tectonics. Springer, Berlin, pp. 507–523.
Baratoux, D., Toplis, M.J., Monnereau, M., Gasnault, O., 2011a. Thermal history of Mars inferred from orbital geochemistry of volcanic provinces. Nature 472, 338–341.
Baratoux, D., Toplis, M.J., Monnereau, M., Gasnault, O., 2011b. Corrigendum: Thermal history of Mars inferred from orbital geochemistry of volcanic provinces. Nature 475, 254.
Beardsmore, G.R., Cull, J.P., 2001. Crustal Heat Flow: A Guide to Measurement and Modelling. Cambridge University Press, Cambridge, 324 pp.
Boynton, W.V. et al., 2007. Concentration of H, Si, Cl, K, Fe, and Th in the low and mid latitude regions of Mars. J. Geophys. Res. 112, E12S99. doi:10.1029/2007JE002887.
Burov, E.B., Diament, M., 1992. Flexure of the continental lithosphere with multilayered rheology. Geophys. J. Int. 109, 449–468.
Caristan, Y., 1982. The transitions from high temperature creep to fracture in Marylan diabase. J. Geophys. Res. 87, 6781–6790.
Chopra, P.N., Paterson, M.S., 1984. The role of water in the deformation of dunite. J. Geophys. Res. 89, 7861–7876.
Dohm, J.M., Tanaka, K.L., Hare, T.M., 2001. Geologic map of the Thaumasia region of Mars. USGS Misc. Inv. Ser. Map I-2650, scale 1:5000,000.
Dohm, J.M. et al., 2009a. Claritas rise, Mars: Pre-Tharsis magmatism? J. Volcanol. Geotherm. Res. 185, 139–156.
Dohm, J.M. et al., 2009b. GRS Evidence and the possibility of paleooceans on Mars. Planet. Space Sci. 57, 664–684.
Dombard, A.J., Phillips, R.J., 2010. Viscoelastic finite-element simulations of the flexure under the north polar cap of Mars. Proc. Lunar Planet. Sci. Conf. 41. Abstract 1865.
Fraeman, A.A., Korenaga, J., 2010. The influence of mantle melting on the evolution of Mars. Icarus 210, 43–57.
Frey, H.V., 2006. Impact constraints on, and a chronology for, major events in early Mars history. J. Geophys. Res. 111, E08S91. doi:10.1029/2005JE002449.
Grott, M., Breuer, D., 2009. Implications of large elastic thicknesses for the composition and current thermal state of Mars. Icarus 201, 540–548.
Grott, M., Breuer, D., 2010. On the spatial variability of the martian elastic lithosphere thickness: evidence for mantle plumes? J. Geophys. Res. 115, E03005. doi:10.1029/2009JE003456.
Grott, M., Hauber, E., Werner, S.C., Kronberg, P., Neukum, G., 2005. High heat flux on ancient Mars: Evidence from rift flank uplift at Coracis Fossae. Geophys. Res. Lett. 32, L21201. doi:10.1029/2005GL023894.
Grott, M., Hauber, E., Werner, S.C., Kronberg, P., Neukum, G., 2007. Mechanical modelling of thrust faults in the Thaumasia region, Mars, and implications for the Noachian heat flux. Icarus 186, 517–526.
Hahn, B.C., McLennan, S.M., Klein, E.C., 2011. Martian surface heat production and crustal heat flow from Mars Odyssey gamma-ray spectrometry. Geophys. Res. Lett. doi:10.1029/2011GL047435, in press.
Halliday, A.N., Wänke, H., Birck, J.L., Clayton, R.N., 2001. The accretion, composition and early differentiation of Mars. Space Sci. Rev. 96, 197–230.
Hanna, J.C., Phillips, R.J., 2005. Hydrological modeling of the martian crust with application to the pressurization of aquifers. J. Geophys. Res. 110, E01004. doi:10.1029/2004JE002330.
Hartmann, W.K., Neukum, G., 2001. Cratering chronology and the evolution of Mars. Space Sci. Rev. 96, 165–194.
Hauber, E., Broz, P., Jagert, F., Jodlowski, F., Platz, T., 2011. Very recent and widespread basaltic volcanism on Mars. Geophys. Res. Lett. 38, L10201. doi:10.1029/2011GL047310.
Hauck, S.A., Phillips, R.J., 2002. Thermal and crustal evolution of Mars. J. Geophys. Res. 107, 5052. doi:10.1029/2001JE001801.
Head, J.W. et al., 2001. Geological processes and evolution. Space Sci. Rev. 96, 263–292.
Hofmeister, A.M., 1999. Mantle values of thermal conductivity and the geotherm from phonon lifetimes. Science 283, 1699–1706.
Jaupart, C., Labrosse, S., Mareschal, J.C., 2007. Temperatures, heat and energy in the mantle of the Earth. In: Bercovici, S. (Ed.), Treatise on Geophysics: Mantle Dynamics, vol. 7. Elsevier, Amsterdam, pp. 253–303.
Kiefer, W.S., 2004. Gravity evidence for a extinct magma chamber beneath Syrtis Major, Marts: A look at the magmatic plumbing system. Earth Planet. Sci. Lett. 222, 349–361.
Kiefer, W.S., Li, Q., 2009. Mantle convection controls the observed lateral variations in lithospheric thickness on present-day Mars. Geophys. Res. Lett.. doi:10.1029/2009GL039827.
Kieffer, H.H. et al., 1977. Thermal and albedo mapping of Mars during the Viking primary mission. J. Geophys. Res. 82, 4249–4291.
Korenaga, J., 2008. Urey ratio and the structure and evolution of Earth's mantle. Rev. Geophys. 46, 1–32.
Kronberg, P. et al., 2007. Acheron Fossae, Mars: Tectonic rifting, volcanism, and implications for lithospheric thickness. J. Geophys. Res. 112, E04005. doi:10.1029/2006JE002780.
Kumar, R.R., Gordon, R.G., 2009. Horizontal thermal contraction of oceanic lithosphere: The ultimate limit to the rigid plate approximation. J. Geophys. Res. 114, B01403. doi:10.1029/2007JB005473.
McGovern, P.J., Schubert, G., 1989. Thermal evolution of the Earth: Effects of volatile exchange between atmosphere and interior. Earth Planet. Sci. Lett. 96, 27–37.
McGovern, P.J. et al., 2002. Localized gravity/topography admittance and correlation spectra on Mars: Implications for regional and global evolution. J. Geophys. Res. 107, 5136. doi:10.1029/2002JE001854.
McGovern, P.J. et al., 2004. Correction to localized gravity/topography admittance and correlation spectra on Mars: Implications for regional and global evolution. J. Geophys. Res. 109, E07007. doi:10.1029/2004JE002286.
McKenzie, D., Jackson, J., Priestley, K., 2005. Thermal structure of oceanic and continental lithosphere. Earth Planet. Sci. Lett. 233, 337–349.
McNutt, M.K., 1984. Lithospheric flexure and thermal anomalies. J. Geophys. Res. 89, 11180–11194.
McNutt, M.K., Diament, M., Kogan, M.G., 1988. Variations of elastic plate thickness at continental thrust belts. J. Geophys. Res. 93, 8825–8838.
Montesi, L.G.J., Zuber, M.T., 2003. Clues to the lithospheric structure of martian from wrinkle ridge sets and localization instability. J. Geophys. Res. 108, 5048. doi:10.1029/2002JE001974.
Nahm, A.L., Schultz, R.A., 2011. Magnitude of global contraction on Mars from analysis of surface faults: Implications for martian thermal history. Icarus 211, 389–400.
Neumann, G.A. et al., 2004. The crustal structure of Mars from gravity and topography. J. Geophys. Res. 109, E08002. doi:10.1029/2004JE002262.
Neumann, G.A., Lemoine, F.G., Smith, D.E., Zuber, M.T., 2008. Marscrust3-A crustal thickness inversion from recent MRO gravity solutions. Proc. Lunar Planet. Sci. Conf. 39. Abstract 2167.
Nimmo, F., 2002. Admittance estimates of mean crustal thickness and density at the martian hemispheric dichotomy. J. Geophys. Res. 107, 5117. doi:10.1029/2000JE001488.
Nimmo, F., Stevenson, D.J., 2000. Influence of early plate tectonics on the thermal evolution and magnetic field of Mars. J. Geophys. Res. 105, 11969–11979.
Parmentier, E.M., Zuber, M.T., 2007. Early evolution of Mars with mantle compositional stratification or hydrothermal crustal cooling. J. Geophys. Res. 112, E02007. doi:10.1029/2005JE002626.
Petrenko, V.F., Whitworth, R.W., 1999. Physics of Ice. Oxford Univ. Press, Oxford, 366pp.
Phillips, R.J. et al., 2008. Mars north polar deposits: Stratigraphy, age, and geodynamical response. Science 320, 1182–1185.
Plaut, J.J. et al., 2007. Subsurface radar sounding of the south polar layered deposits of Mars. Science 316, 92–95.
Ranalli, G., 1994. Nonlinear flexure and equivalent mechanical thickness of the lithosphere. Tectonophysics 240, 107–114.
Ranalli, G., 1997. Rheology of the lithosphere in space and time. Geol. Soc. Spec. Pub. 121, 19–37.
Ritzer, J.A., Hauck, S.A., 2009. Lithospheric structure and tectonic at Isidis Planitia, Mars. Icarus 201, 528–539.
Ruiz, J., 2009. The very early thermal state of Terra Cimmeria: Implications for magnetic carriers in the crust of Mars. Icarus 203, 454–459.
Ruiz, J., Tejero, R., 2000. Heat flows through the ice lithosphere of Europa. J. Geophys. Res. 105, 23283–23289.
Ruiz, J., McGovern, P.J., Tejero, R., 2006a. The early thermal and magnetic state of the cratered highlands of Mars. Earth Planet. Sci. Lett. 241, 2–10.
Ruiz, J., Tejero, R., McGovern, P.J., 2006b. Evidence for a differentiated crust at Solis Planum, Mars, from lithospheric strength and heat flow. Icarus 180, 308–313.
Ruiz, J., Gómez-Ortiz, D., Tejero, R., 2006c. Effective elastic thicknesses of the lithosphere in the Central Iberian Peninsula from heat flow: Implications for the rheology of the continental lithospheric mantle. J. Geodyn. 41, 500–509.
Ruiz, J. et al., 2008. Ancient heat flow, crustal thickness, and lithospheric mantle rheology in the Amenthes region, Mars. Earth Planet. Sci. Lett. 270, 1–12.
Ruiz, J., Williams, J.P., Dohm, J.M., Fernández, C., López, V., 2009. Ancient heat flows and crustal thickness at Warrego rise, Thaumasia Highlands, Mars: Implications for a stratified crust. Icarus 203, 47–57.
Ruiz, J., López, V., Dohm, J.M., 2010. The present-day thermal state of Mars. Icarus 207, 631–637.

Sandu, C., Lenardic, A., McGovern, P., 2011. The effects of volatile cycling on planetary thermal evolution. J. Geophys. Res., submitted for publication.
Schultz, R.A., Watters, T.R., 2001. Forward mechanical modeling of the Amenthes Rupes thrust fault on Mars. Geophys. Res. Lett. 28, 4659–4662.
Shuster, D.L., Weiss, B.P., 2005. Martian surface paleotemperatures from thermochronology of meteorites. Science 309, 594–597.
Sleep, N.H., 1994. Martian plate tectonics. J. Geophys. Res. 99, 5639–5655.
Solomon, S.C., Head, J.W., 1990. Heterogeneities in the thickness of the elastic lithosphere of Mars: Constraints on heat flow and internal dynamics. J. Geophys. Res. 95, 11073–11083.
Tanaka, K.L., 1986. The stratigraphy of Mars. J. Geophys. Res. 91, E139–E158.
Taylor, S.R., McLennan, S.M., 2009. Planetary Crusts: Their Composition, Origin and Evolution. Cambridge Univ. Press, Cambridge.
Taylor, G.J. et al., 2006. Bulk composition and early differentiation of Mars. J. Geophys. Res. 111, E03S10. doi:10.1029/2005JE002645 (Printed 112 (E3), 2007).
Tesauro, M., Kaban, M.K., Cloetingh, S.A.P.L., Hardebol, N.J., Beekman, F., 2007. 3D strength and gravity anomalies of the European lithosphere. Earth Planet. Sci. Lett. 263, 56–73.
Turcotte, D.L., Schubert, G., 2002. Geodynamics, second ed. Cambridge Univ. Press, Cambridge, 456pp.
Van Schmus, W.R., 1995. Natural radioactivity of the crust and mantle. In: Ahrens, T.J. (Ed.), Global Earth Physics: A Handbook of Physical constants. AGU Reference Shelf 1. American Geophysical Union, Washington, DC, pp. 283–291.
Wänke, H., Dreibus, G., 1988. Chemical composition and accretion history of terrestrial planets. Philos. Trans. Roy. Soc. London: Ser. A 325, 545–557.
Watters, T.R. et al., 2006. MARSIS radar sounder evidence of buried basins in the northern lowlands of Mars. Nature 444, 905–908.
Watts, A.B., Burov, E.B., 2003. Lithospheric strength and its relation to the elastic and seismogenetic layer thickness. Earth Planet. Sci. Lett. 213, 113–131.
Wieczorek, M.A., 2008. Constraints on the composition of the martian south polar cap from gravity and topography. Icarus 196, 506–517.
Williams, J.-P., Nimmo, F., 2004. Thermal evolution of the martian core: Implications for an early dynamo. Geology 32, 97–100.
Yoder, C.F., Konopliv, A.S., Yuan, D.N., Standish, E.M., Folkner, W.M., 2003. Fluid core size of Mars from detection of the solar core. Science 300, 299–303.
Zhao, Y.-H., Zimmerman, M.E., Kohlstedt, D.L., 2009. Effect of iron content on the creep behavior of olivine: 1. Anhydrous conditions. Earth Planet. Sci. Lett. 287, 229–240.
Zuber, M.T. et al., 2000. Internal structure and early thermal evolution of Mars from Mars Global Surveyor. Science 287, 1788–1793.

UNIVERSIDAD
COMPLUTENSE
DE MADRID